Imaging polarimetry of planetary and proto-planetary nebulae

Bowlzer, S. L.

Imaging Polarimetry of Planetary and Proto-Planetary Nebulae

S. L. Bowlzer B.Sc.

A thesis submitted to the University of Durham

for the degree of Doctor of Philosophy

Department of Physics

August 1997

Dedication

I dedicate this doctoral thesis to the memory of my father. Together with my mum, his sacrificial help and support enabled me to finally complete the path that I started on such a long time ago. It is, therefore, with many mixed emotions that this work is finished. On the one hand, relief and joy to have, at last, brought this to a successful conclusion, but on the other, great sadness that my dad could not remain here to see this day, for it is as much to his credit as anyone. I wish that that I could tell him these thoughts face to face. One day, in a better world, I believe that I will ...

Abstract

Optical imaging polarimetry has been performed on a small sample of objects which are associated with that stage of stellar evolution occurring between the Asymptotic Giant Branch and full Planetary Nebula. Three such systems are considered, specifically, the young planetary nebulae M 1-16 and Mz 3, and the protoplanetary nebula, IRAS 09371+1212 (the 'Frosty Leo' nebula). The work is based upon CCD polarimetry obtained with the Durham Imaging Polarimeter.

Planetary nebulae are believed to form as a low to intermediate mass star evolves from the main sequence, through the mass-loss stages of the Red Giant Branch and Asymptotic Giant Branch, towards its final destiny as a White Dwarf. A brief review of the relevant aspects of post-main sequence stellar evolution is given as a basis for understanding the transitionary planetary nebula phase in relation to the character of the central star and its role in the creation of a nebula.

The theory of light scattering from both homogeneous and core-mantle spherical dust grains (Mie theory) is discussed. The results of a series of scattering calculations, using the theory, for dust grains composed of those materials believed to be abundant in the atmospheres of late-type stars and planetary nebulae are presented. The levels of polarization and scattered intensities predicted in the scattering analysis have been applied in the interpretation of the polarimetric data for the three planetary nebulae. Constraints upon the nature of the dust component, the size distribution of the dust and the nebula geometry are suggested for each of the nebulae. The inferred character of the dust material is in good agreement with the classification of the nebulae using the two-colour diagram for the *IRAS* fluxes.

Preface

The body of work presented within this thesis deals mainly with the study of proto-planetary and planetary nebulae using the techniques of optical polarimetry. All the data, with the exception of IRAS 09371+1212, were recorded by the author using the Durham Imaging Polarimeter during observing time allocated to Dr. S. M. Scarrott at the Anglo-Australian Telescope, New South Wales and the South African Observatory in January/March 1994 and February 1997 respectively. Data reduction and analysis for all the objects was performed by the author, again with the exception of IRAS 09371+1212 for which the author carried out a fresh analysis and interpretation of data originally reduced and published by other members of the Durham Polarimetry Group (Scarrott & Scarrott, 1994, 1995). In the data analysis of Mz 3, some use is made of the results of V-band optical polarimetry observations published in Scarrott & Scarrott (1995).

None of the material presented within this thesis has been previously submitted for a degree at the University of Durham, or any other university.

The data in this thesis were taken on telescope allocations made to Dr. S. M. Scarrott and Mr. S. Bowlzer and their permission must be obtained by anyone wishing to publish or use the results beyond this thesis.

Contents

List of Figures

List of Tables

Chapter 1

An Introduction to Planetary Nebulae

1.1 Introduction

The first planetary nebulae were discovered, or at least observed, by Charles Messier (1730-1817) during the compilation of his famous catalogue of '*nebulae*'[1], the most comprehensive version of which was published in 1784. The catalogue lists a well-known planetary nebula, the Dumbbell nebula (NGC6853), as Messier 27 for example. However, due to the limitations of telescopic instrumentation at that time, the 'nebulae' were poorly understood and although there were clearly some differences in appearance between individual objects, their intrinsic nature remained a topic of tremendous debate for some while. William Herschel (1738-1822) became the first astronomer to employ the term '*planetary nebulae*' to categorize that class of celestial objects as they are known today. In a paper published in 1785, Herschel set aside a number of nebulae which he considered to be observationally distinct from the others, naming them 'planetary nebulae' purely because they displayed some visual similarity with the greenish disk of the outer solar system planet Uranus when viewed through his telescopes. The name is retained solely for historical reasons and there is no physical connection between planetary nebulae and planets. Herschel argued that the faint nebulosity which he observed in the planetary nebulae could not be due to the combined light of many individual stars, since he was persuaded that the observed central star and the nebula must be associated.

[1] *nebulae* is the Latin word for 'clouds'

The very low probability of a relatively bright star being located so perfectly at the centre of many of these nebulae by pure coincidence indicates that the star and its surrounding nebula must lie at the same distance. A paper of 1791 reports an observation that Herschel made on 13 November 1790.

> "A most singular phenomenon! A star of about the 8th magnitude with a faint luminous atmosphere, of circular form. The star is perfectly in the centre, and the atmosphere is so diluted, faint and equal throughout that there can be no surmise of its consisting of stars; nor can there be a doubt of the evident connection between the atmosphere and the star".

If the nebula were to consist of stars, this would imply that they are either very faint, or that the central star is of an implausibly large size. As more planetary nebulae came to be discovered, their similar appearance and general morphology began to indicate that some common mechanism of creation and subsequent development must be involved.

Concurrent with the development of optical spectroscopic techniques in astronomy during the late nineteenth century came a greater understanding of the true nature of planetary nebulae, most notably through the investigations of W. Huggins, W. H. Wright, and H. D. Curtis, amongst others. The strong emission-line optical spectra of planetary nebulae enabled them to be easily distinguished from other astronomical objects, such as spiral galaxies, which exhibited a continuum spectrum with a few absorption lines, so that by the early twentieth century, about 150 planetary nebulae were known beyond doubt. In addition, at this time, the observed number ratio of planetary nebulae to stars was of the order of 10^{-5} or less, so that Curtis was led to comment that a planetary nebula would "appear to be an exceptional case, a sporadic manifestation of a path which has been but rarely followed in stellar evolution". Alternatively, the planetary nebula could be regarded as being "a stage of existence of a relatively brief duration through which most stars have long since passed". Assuming the latter, Curtis argued that the time period for a star to evolve through its planetary nebula stage would be less than ten thousand years. With additional evidence gained from the average space velocity of planetary nebulae, Curtis concluded that "it would seem much more reasonable to regard them (planetary nebulae) as merely sporadic cases of stellar evolution, presumably of cataclysmic origin".

At about this same time it also became clear that planetary nebulae were "an integral part of our own galactic system". The main evidence in support of this claim included the

observed distribution of planetary nebulae in the galactic plane, their apparent concentration toward the galactic centre, and their kinematic properties. Alongside an increasing knowledge of the dimensions of the Galaxy there was a corresponding, and important, attempt to develop an accurate distance scale for planetary nebulae. Even today, the distance to any particular planetary nebula unfortunately remains an uncertain factor which can present serious difficulties. The precision of many of the derived physical parameters of a planetary nebula and its central star depend ultimately upon an accurate knowledge of the distance. The earliest attempts to estimate the distance of planetary nebulae were based essentially upon an inverse function of the nebular observed angular dimensions. However, it later transpired that planetary nebulae were found to be expanding radially, and as a consequence their apparent angular size is not only distance but also age dependent. The fundamentally flawed basis of this elementary distance scale meant that inaccurate results were unavoidable, and as a consequence, the method soon came to be discarded. The distance determination of planetary nebulae still remains a matter of much controversy, with a particular object being assigned distances which can differ by factors of more than two or three.

Throughout the 1920's and 1930's progressive developments in spectroscopy and atomic physics gradually revealed the chemical composition of planetary nebulae and the physical processes occurring therein. Observational data of planetary nebulae was particularly instrumental in the discovery of several interesting and important physical phenomena, such as forbidden lines (O^{++} low level energy transitions by I. S. Bowen in 1928, for example) and two-photon emission (cf., Pottasch 1984; Osterbrock 1989). It became clear through analysis of their optical spectra that planetary nebulae, generally speaking, consist of an ionized and expanding gaseous shell surrounding a hot central star. The observed size and measured expansion velocities of planetary nebulae enabled another estimate of their age to be determined. Values of the order of 10^4 years were inferred, providing the first persuasive evidence that many, possibly the majority of, stars evolve through the planetary nebula stage.

The last thirty years or so have seen enormous progress in observational techniques and instrumentation, computational resources and the theoretical framework of stellar evolution. Theories of planetary nebula evolution have been steadily refined as more discriminating data have become available. The data obtained from the *Infrared Astronomical Satellite* (IRAS) sky survey in 1983, in particular, has led to a number of significant ad-

vances in planetary nebula research. Many more planetary nebulae have been catalogued (currently in excess of some 1600; Acker *et al.* 1992) and there is now a much clearer understanding of many aspects of planetary nebulae which formerly presented numerous theoretical difficulties and posed many questions. In the 1950's, the prediction was that cool giant stars were likely to be the progenitors of planetary nebulae. The validity of this proposal has since been verified many times by the observational data, so that planetary nebulae, once regarded as objects far removed from the main drama of stellar evolution, are now recognized as late stages in the life of many a common star as it descends from the brilliance of a giant into the relative obscurity of white dwarfdom.

Although planetary nebulae are now known without doubt to be objects that are highly representative of the final stages of intermediate-mass stellar evolution, there remain many unresolved difficulties concerning their evolutionary scheme. Mass loss processes during the progenitor stars' Asymptotic Giant Branch phase (see §1.2.3) certainly play a crucial role but are not yet fully understood, and there continues to be lively debate as to the relative importance which binarity, stellar rotation and magnetic fields may assume in the formation of a planetary nebula. The continuing observation of the structure and composition of planetary nebulae, over the whole range of the electromagnetic spectrum, will eventually resolve those problems which remain.

The introductory review of planetary nebulae presented in this chapter firstly locates their overall position in the general design of stellar evolution, briefly describes and comments on some of the more important aspects of our current knowledge of these objects, and concludes with a discussion of those properties of planetary nebulae of which optical polarimetry may be a useful diagnostic.

1.2 Red Giants To Planetary Nebulae

Within the accepted 'standard model' of stellar astrophysics, it is currently well established that a star, subsequent to its formation within molecular clouds and associations of molecular clouds, evolves through a further three main phases over its remaining lifetime.

- **pre-main sequence**
- **main sequence**
- **post-main sequence**

A number of texts are available which describe in detail the process of stellar formation and the *pre-main sequence* period during which the star derives most of its energy from gravitational contraction (see, for example, Gledhill 1987). This early phase of the stars' evolution, although fundamental to an accurate and comprehensive understanding of stellar astrophysics, can be regarded as having little significant influence upon the stars behaviour much later on in its history, particularly at the stage where planetary nebulae are believed to be formed. Although there are similarities in the appearance of bipolar post-main sequence objects and the bipolar flows observed in many pre-main sequence objects, which might suggest some common mechanism behind their formation, it is not considered likely that bipolarity at the pre-main sequence stage is retained through the intervening main sequence evolution to effect bipolarity in the post-main sequence or planetary nebula phase. In this section, I therefore disregard the evolutionary history of the star prior to its joining the *main sequence*, where stars spend the major fraction of their total lifespan, and present a general summary of main sequence and post-main sequence evolution for stars of moderately low mass.

1.2.1 Main Sequence Evolution

It is usually assumed that a particular star joins the main sequence (at some point known as the *zero-age main sequence*), fully radiative and with a well-mixed and homogeneous chemical composition which is essentially that of the interstellar gas cloud from which it was formed. The central temperature of the star is an increasing function of the stellar mass, so that the continuing evolution of the star is mass dependent. The detail of precisely how a particular star might evolve from its formation through to its demise is therefore strongly dependent upon the initial mass of the star, and to a lesser extent,

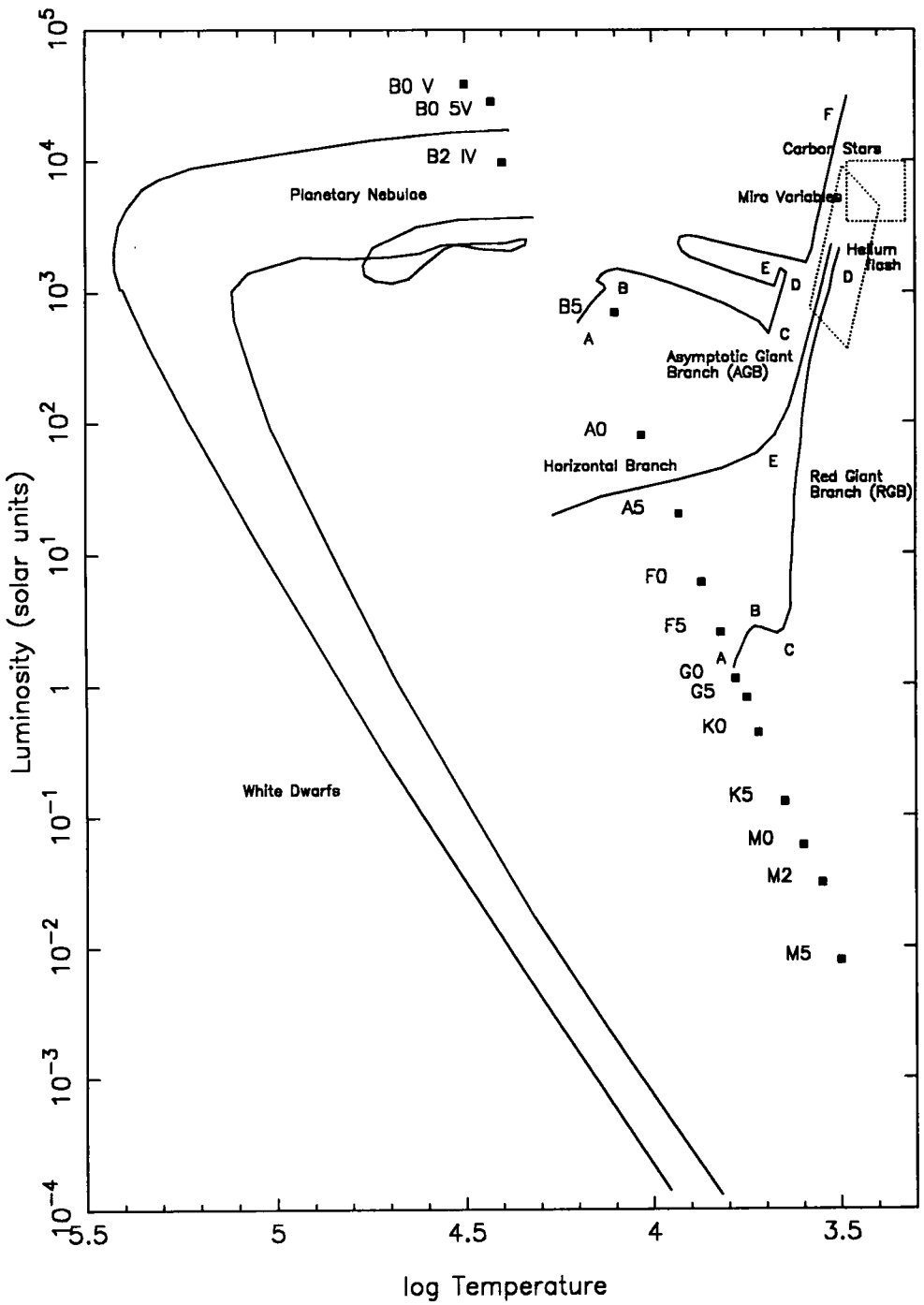

Figure 1.1: Hertzsprung-Russell diagram. Post-main sequence evolutionary paths are shown for stars of approximate masses $1.0\,M_\odot$ and $5.0\,M_\odot$(adapted from Pottasch 1984)

upon its original chemical composition. Accordingly, the initial position on the main sequence is determined solely by the mass of the star, as long as it consists mainly of hydrogen.

Generally, for the purposes of understanding their evolution subsequent to the main sequence, stars can loosely be classified according to their initial mass: *low-mass* stars, *intermediate-mass* stars and *massive* stars. The three groupings are defined more sharply by the existence of certain physical processes

- a natural sequence of nuclear reactions able to burn hydrogen to silicon
- the amount of energy liberated per unit mass by gravitational contraction which increases with stellar mass
- a tendency of the material in the stars central region to become electron degenerate with increasing density
- the existence of threshold values for the central temperature and density at each nuclear step
- a relation between these threshold values and the minimum stellar core mass at which nuclear burning can start and that the minimum core mass for any particular nuclear burning reaction is different for electron degenerate and non-degenerate gas
- the explosive nature of nuclear burning in a degenerate gas

The behaviour of a star as it evolves may be demonstrated on the Hertzsprung-Russell (HR) diagram. This is a graphical representation portraying the fundamental relationship between the absolute luminosity of the star and its effective surface temperature, or equivalently, its spectral classification. It is traditional to plot $\log L$ against $\log T$, and is one of the most widely employed techniques for the comparison of stellar evolution theory with observational data. Figure 1.1 is typical of such a diagram, adapted from Pottasch (1984), and displaying evolutionary tracks for stars of mass around $1.0\,M_\odot$ and $5.0\,M_\odot$. The main sequence is shown ascending from the cooler, less luminous and less massive stars in the bottom right corner, up to the hot, bright and massive stars at the top of the diagram. The spectral classifications of stars are shown at the relevant points on the main sequence. Stars leave the main sequence as they evolve, according to certain criteria

which are briefly discussed in the next section, and ascend to the top right corner of the HR diagram. Important stages in their evolution are marked by the letters **A**,**B**, etc, and are referenced when appropriate.

A star will remain on the main sequence for a length of time which is dependent upon its mass (and luminosity) according to the approximate relation

$$t \simeq \frac{M}{L} \times 10^{10} \quad \text{years}$$

This implies total main sequence lifetimes of around 10^6 years for stars of spectral type O5, increasing up to 10^{12} years for M5 stars.

1.2.1.1 Low-mass stars

Low-mass stars are somewhat loosely defined as those which, shortly after leaving the main sequence, develop an electron degenerate core composed of helium. As the mass of the helium core grows to a critical value[2] of $0.45\,M_\odot$, a helium-burning runaway reaction occurs which continues until the degeneracy has been removed. The maximum initial stellar mass for this to occur is 1.8 to $2.2\,M_\odot$, and is again dependent upon the exact chemical composition. In stars of mass lower than a limiting value of around $1.0\,M_\odot$, core hydrogen burning on the main sequence continues radiatively with little or no convective core region developing, whereas in stars more massive than this limit, the transfer of nuclear and gravitational energy is predominantly convective. The central temperature and density of the star both grow in response to an increasing molecular weight, with the conversion of hydrogen to helium taking place via the *p*-*p* chain process (deuterium burning). Hydrogen only becomes exhausted in a very small central region and as a result, a small isothermal helium core develops. The core must be supported against its own gravity as well as providing support to the rest of the star, and its energy sources are all on the outside of the core. It is therefore impossible for the hydrogen shell to establish a temperature gradient within the helium core.

The energy within the helium core can only be released by a gravitational contraction of the core, which begins to contract long before its mass becomes comparable with the Chandrasekhar-Schönberg Limit.[3]

[2] The precise value is weakly dependent upon the chemical composition, mass and input physics

[3] The limit of the maximum mass of material that the isothermal core can support. This depends solely upon the mass fraction of the isothermal core and the mean molecular weights of the core and envelope

For a helium core, this value is some 10 to 13% of the total mass of the star. Once the core begins to exceed this limiting mass fraction, it must contract in order to provide the required temperature and pressure gradients necessary to support the remainder of the star as well as itself. Except for this source of energy, the core must be isothermal with its temperature determined by the surrounding hydrogen burning shell. It follows that evolution off the main sequence is less rapid for the lower mass stars than for those of higher mass. The duration of the core hydrogen-burning period strongly decreases with increasing stellar mass. A typical $0.7\,M_\odot$ star will evolve through this phase in about 15×10^9 years, with a $1.7\,M_\odot$ star achieving the same in roughly 10^9 years. This period of the stars evolution is represented by the sequence **A** to **B** on the HR diagram.

The star now leaves the main sequence, crossing what is known as the *Hertzprung Gap*, while the central helium core temporarily cools and becomes electron degenerate with hydrogen burning becoming established in a shell surrounding the core. Energy liberated by gravitational contraction in the core flows outward by electron conduction, delaying the increase in the central temperature which would be required to ignite the helium in the core. The central temperature eventually reaches a minimum, which is approximately equal to the temperature in the surrounding hydrogen shell. From this point, the helium core continues to contract but increases in mass through the action of the hydrogen-burning shell, and the temperatures of both core and shell begin to increase. The luminosity of the star is proportional to the shell temperature. In addition, the rate at which matter is added to the core by the shell, and as a consequence, the rate of release of gravitational energy and core heating, is proportional to the luminosity. Simultaneously, the star is expanding and the outer layers become convective. The star eventually reaches the *Hayashi Limit* where convection extends deeply inward (in mass) from the stellar surface, and the star begins to ascend the (first) *giant branch*, becoming a *Red Giant*. The convective envelope extends into the region where partial hydrogen burning has occurred earlier in the evolution. This material is still mostly hydrogen but with some products of carbon-nitrogen-oxygen (CNO) cycling, notably ^{14}N and ^{13}C, besides ^4He. These are brought by convection to the stellar surface, in a phase known as the '*first dredge-up*'.

The electron degeneracy ensures that all low-mass stars, regardless of their precise initial mass, develop a helium core of approximately the same mass of about $0.45\,M_\odot$. As the ^4He core continues to contract and heat, energy is lost via neutrinos from the central

region causing the temperature maximum to move radially outward. Violent helium-burning commences at some point outside the core and as the nuclear burning progresses inwards, the core degeneracy is removed, and quiescent nuclear burning initiates in the core. This terminates the stars Red Giant Branch (RGB) evolutionary period. The duration of the RGB phase is again dependent upon the stellar mass with 2.0×10^9 years for a $0.7\,M_\odot$ star down to 2.7×10^8 years for a $1.7\,M_\odot$ star. The points labelled **C** through **D** represent this period in the stars evolution on the HR diagram.

The main sequence evolution of stars with initial masses between 1.0 and $2.2\,M_\odot$ is essentially the same as that given above, although stars towards the upper mass limit will display many aspects of the evolution seen in intermediate and massive stars.

1.2.1.2 Intermediate and Massive stars

In a more massive star, with a higher central temperature, main sequence core hydrogen-burning generates its energy by the CNO cycle. Furthermore, the high temperature dependence of these reactions causes a convective core to develop, radiation alone not being sufficient to carry the energy away from the central regions. The opacity (due mainly to electron scattering and therefore proportional to the hydrogen content) decreases and the extent of the convective core decreases with time. The size of the convective core is customarily fixed by the classical Schwarzschild criterion and increases with stellar mass. On the other hand, the duration of the core hydrogen-burning phase decreases with increasing mass because of the effects of increasing luminosity. In addition, there is a steady increase in the luminosity and radius of the star and a decrease in the effective temperature.

Following core hydrogen depletion there is a phase of hydrogen burning in a thin shell above a rapidly contracting and heating core, composed essentially of helium, and the star evolves rapidly to the RGB. Again, the inward penetration of the convective envelope reaches into regions where there has been partial hydrogen burning earlier in the stars evolution and these products (primarily ^{13}C and ^{14}N, produced at the cost of ^{12}C) are brought to the surface in the first dredge-up, as for lower mass stars.

However, for these more massive stars, ignition of ^4He occurs in the centre and under non-degenerate conditions, and the star begins a period of quiescent ^4He burning in a

convective core, together with hydrogen burning in a shell. When the core ^{4}He is depleted there is a structural re-adjustment to shell ^{4}He burning resulting in a strong expansion.

The theoretical understanding of the processes underlying and provoking a stars' evolution to a red giant remains far from satisfactory and has been a matter of debate for many years (e.g., Weiss, 1989).

The development of the He-flash at the tip of the RGB has been subject to many investigations. There exist arguments which support both a violent disruption of the star at this point as a supernova event, or extensive mixing between the core and envelope (Iben & Renzini, 1984; Renzini & Fusi-Pecci, 1988). Following core He-flash at the termination of the RGB, stars less massive than about $2.2\,M_\odot$ quiescently burn helium in a convective core. Their location on the HR diagram is dependent upon a number of other factors such as metallicity, and the mass of the H-rich envelope which is depleted by mass-loss processes (see §1.2.3), but the star moves to the *Horizontal Branch* (labelled as **E** in the HR diagram of Figure 1.1) to continue burning ^{4}He gently in a convective core and hydrogen in a shell. This provides most of the stars luminosity. Helium burning increases the mass fraction of ^{12}C and ^{16}O. The outer layers of the stars convective core become stable to the Schwarzschild convection criterion but unstable to that of Ledoux. These are differing theoretical conditions which reflect the limits of chemical neutrality in the system. This situation is referred to as *semiconvection* and causes the composition profile to adjust itself to produce convective neutrality. Following exhaustion of ^{4}He in the core, the star ascends the giant branch for the second time. This is the *Asymptotic Giant Branch* phase (see §1.2.2).

The hydrogen shell is extinguished as the star begins to ascend the Asymptotic Giant Branch. With this entropy barrier removed, the inner edge of the convective envelope is free to penetrate the hydrogen shell, and the products of complete hydrogen burning are brought to the surface in what is termed the *second dredge-up*. This again alters the surface composition of ^{4}He, ^{12}C, ^{13}C and ^{14}N, and actually reduces the mass of the hydrogen exhausted core, because in the process of mixing ^{4}He outward, hydrogen is also mixed inward. There is a critical mass (of about $4\,M_\odot$, but dependent on composition) below which the second dredge-up does not occur.

Those stars with initial main sequence masses greater than about $8\,M_\odot$ ignite carbon in a non-degenerate carbon-oxygen core and are believed to become *supergiants*. They then continue to produce energy by burning successively more complex elements until a central core of iron is formed. Lacking any further source of available fuel, the core will collapse violently to form a *neutron star* and explosively shed its outer envelope in a *supernova* event.

Stars of initial mass less than about $1\,M_\odot$ have not had sufficient time to evolve off of the main sequence during the known lifetime of the Galaxy (eg., Iben & Rood 1970).

Consequently, it is now widely believed that those stars with initial main sequence masses within the broad range 1 to $8\,M_\odot$ become *red giants* and thereafter evolve away from the main sequence. Such stars eventually find their way to the AGB and, with particular relevance to this work, the formation of a planetary nebula commences.

Table 1.1 summarizes the pathways of main sequence and post-main sequence evolution for single stars of a given initial mass.

Table 1.1: Typical post-main sequence stellar evolutionary paths

Mass ($M_\odot$)			Path	Final Status
< 0.25		.	never a star	brown dwarf
0.25	–	2.00	MS[a] - PMS(He flash) - PN	C,N,O white dwarf
2.00	–	8.00	MS - PMS[b] - PN[c]	C,N,O white dwarf
8.00	–	25.00	MS - PMS - SN II[d]	neutron star
25.00	–	100.00	MS - PMS - SN II	black hole
> 100.00		.	unstable	

[a]main sequence
[b]post-main sequence
[c]planetary nebula
[d]type II supernova

1.2.2 Post-Main Sequence Evolution

Essentially, the evolution of the star after leaving the main sequence (the *post-main sequence* phase) represents the response of the star to a depletion in its available fuel supply, and can be understood by considering the response of the stars' core and envelope to the attempts of the nuclear burning regions to adjust to the diminution of available hydrogen. This stage of the stars' evolution is characterized by an ever increasing central density, burning temperature, surface luminosity and radius, with the star seeking continually to exploit new nuclear energy sources where possible.

1.2.2.1 Asymptotic Giant Branch stars

When the helium, like the hydrogen before it, has become critically depleted in the stars core, shell burning commences again. However, there are two possible shell sources now present, the hydrogen shell envelope and a new helium-burning shell immediately surrounding the compact, but stable, carbon-oxygen and electron degenerate core of the star. Stellar evolutionary models predict that the mass of the core is of the order of $0.8\,M_{\odot}$ for all initial main sequence masses (Vassiliadis & Wood, 1993). It is the interaction and symbiotic relationship between the hydrogen and helium shells that is the principle cause for the unusual properties of AGB stars.

As the ^{4}He shell is burning, the temperature gradient of the stellar interior results in increased convection, suppressing the rate of hydrogen fusion in the outer shell to practically zero. The helium is quickly consumed over a period which is a small fraction of the stars main sequence lifetime, the helium fusion processes cease, and hydrogen fusion is allowed to resume once again. This permits some contraction in the helium layer leading to further degeneracy and eventually the ignition of triple-α helium fusion in the degenerate material. The material at the base of this layer undergoes a *helium flash*, which then triggers a large-scale expansion of the stellar envelope. This also serves as a potential mechanism for massive dredge-up and disruption of the hydrogen burning layer above it. The repetitive cycle of the burning of hydrogen into helium in the shell, followed by intermittent helium flashes is manifested in a series of recurring *thermal pulses*. The AGB period of the stars evolution can then be subdivided into two consecutive, but distinct, phases: the early AGB, prior to (and at lower luminosities than) the first thermal pulse, and the thermally-pulsing AGB (TP-AGB) beyond this. The character of the thermal pulses are dependent upon the internal properties of the star and its energy generation. Empirical dependence on the mass, age and prior history of the star

have been demonstrated in many evolutionary models (e.g., Vassiliadis & Wood, 1993). The pulsing period, which is inversely proportional to the mass of the star, is found to be typically of the order of 10^4 years for the most massive stars, increasing to 10^5 years for lower masses. The thermal pulse process introduces significant disturbances in the star which results in moderate atmospheric mixing and initiates prodigious mass loss for a short period (see §1.2.3). For the more massive AGB stars, the thermal pulses dominate the evolutionary changes in the star over the early period of its lifetime on the AGB.

In addition to the thermal pulses, AGB stars are pulsationally unstable as a consequence of the structure of their envelopes. The relatively low temperatures in the outer regions of the envelope result in the HI opacity triggering some pulsational instability. These pulsating AGB stars are known as Mira variables[4].

Envelope expansion results in a drop in effective temperature and the peak wavelength of the blackbody emission rising out of the opacity regime. The envelope is thereby allowed to contract once more and this returns the temperature back into the HI opacity regime. Despite some controversy concerning the precise underlying mechanism, empirical evidence demonstrates that Mira pulsations lead to the high mass loss rates observed in AGB stars. It is widely believed that the pulsations impel carbon-rich material into the outer atmosphere of the star where temperatures become low enough to permit the formation of dust grains. The presence of the grains promotes the development of a radiatively-driven stellar wind.

The total period of time spent by the star in the AGB phase is of the order of 10^6 years (see Iben & Renzini 1984; Vassiliadis & Wood 1993), no more than some 1% of the stars' main-sequence lifetime, and the first 90% of the stars' AGB phase is spent in the early AGB. In addition, whilst on the AGB, the mass of the envelope is steadily reduced by nuclear burning on the inside (increasing the mass of the carbon-oxygen core) and mass loss through a stellar wind on the outside. As the mass of the envelope drops below about $0.05\,M_\odot$, the temperature of the star starts to increase and the *post*-AGB phase commences. The temperature at this stage can attain values of the order of 10^5 K (depending upon mass) before nuclear burning ceases and the star begins to cool towards a white dwarf.

[4]The prototype star of this class of variable stars is o Ceti, commonly known as *Mira*. The amplitude of its visual brightness ranges over more than 6 magnitudes which corresponds to changes in its intrinsic luminosity by a factor of more than 100.

1.2.3 Mass loss on the Asymptotic Giant Branch

The occurrence of mass loss from stars throughout the RGB and AGB phases cannot yet be derived from a satisfactory theory, but it is essentially justified by the observational data and it is generally believed that all AGB stars are characterized by intense mass loss processes. During the first giant branch (red-giant phase) and the initial stages of the AGB, mass loss occurs with a steady rate of around 10^{-10} $M_{\odot}\,yr^{-1}$. Indeed, the process of mass loss is thought to drive the stellar evolution forward (Schönberner, 1990). A combination of pulsation and radiation pressure effects on dust, which condenses in the stellar atmosphere and which transfers its momentum to the gas through collisions, gives rise to a gradual build up of a circumstellar envelope (CSE) around the star and also amplifies the mass-loss rate. The rate at which an AGB star loses mass increases with its luminosity, and in turn, the average luminosity increases with the mass of the inert carbon and oxygen core.

As a star evolves upward in the HR diagram, along the AGB, the mass-loss rate intensifies to such an extent that, at some point, almost all of the matter remaining in the hydrogen-rich envelope is stripped from the star. The core remnant contracts rapidly at nearly constant luminosity (to form a white dwarf star) whilst the ejected nebular material drifts outward, and later becomes detectable as a planetary nebula under certain favourable conditions.

Various models for the mass loss during the AGB phase have been proposed that differ particularly in the later stages. These include an abrupt increase of mass-loss rate at the tip of the AGB (Renzini, 1981), slowly increasing mass-loss rate with time (Baud & Habing, 1983), and interrupted mass loss leading to multiple detached shells (Olofsson *et al.*, 1990).

The best observationally-established mass-loss relationship to date is given by Judge & Stencel (1991) for a sample of RGB and AGB stars as

$$\frac{\mathrm{d}M}{\mathrm{dt}} = (2.3 \pm 1.3) \times 10^{-14} \left(\frac{R^2}{M}\right)^{1.43 \pm 0.23} \quad M_{\odot}\, yr^{-1}$$

The above relation is similar to the well-known Reimers law for mass-loss rates which is believed to predict rates which are too low from late AGB stars. However, these equations do accurately predict that the mass-loss rate increases with time on the AGB and that significant short-term variations should occur following a thermal pulse. The mass loss process will determine the mass of the core at the final white dwarf stage of the star, and therefore the initial-final mass relation.

This is poorly constrained by observational data, but applying the above mass-loss relationship to the theoretical models of AGB stars does give results consistent with the few observations available (Weidemann, 1987; Vassiliadis & Wood, 1993; Groenewegen & de Jong, 1994). The above relation also implies that stars with masses within the range 1 to $3\,M_{\odot}$ become white dwarfs with masses around $0.6\,M_{\odot}$. Higher mass stars result in heavier white dwarfs but the Chandrasekhar-Schönberg Limit is never reached. The most massive AGB stars leave 1 to $1.2\,M_{\odot}$ remnants.

Recent observations of high rotational CO emission lines in the post-AGB object GL 2688 and the planetary nebulae GL 618 and NGC 7027 (Justtanont *et al.*, 1997) reveal copious amounts of warm, dense molecular gas ($n \sim 10^7\,\mathrm{cm}^{-3}$; $T \sim 100\,\mathrm{K}$). These results imply that the AGB is indeed terminated by a short-lived phase of high mass-loss rate, and that once the star leaves the AGB, the mass-loss rate returns again to a lower value.

1.2.4 Post-AGB and the formation of planetary nebulae

There is now no doubt that PNs, as a class of celestial objects, constitute a short-lived evolutionary link between stars at the tip of the AGB and the white dwarf stars. A subset of PNs are those objects referred to as protoplanetary nebulae (PPNs). These are somewhat loosely defined as objects which are in transition between the AGB and PN phase of evolution. However, the concept that PNs have their origin in the outer atmospheres of red giant stars was initiated by the work of Shklovsky (1956). This idea was given added support by Abell & Goldreich (1966), who used the expansion velocities of PNs and the escape velocities of red giant stars to argue that PNs are the suddenly ejected atmospheres of red giants.

One of the earliest features of oxygen-rich red giant envelopes (RGE) to be observed was mid-IR emission at 9.7μm due to the presence of silicates (Woolf & Ney, 1969; Merrill & Stein, 1976).

This feature was also detected in young PNs (Aitken *et al.*, 1979), and taken to be further evidence for some probable evolutionary connection between the two. Gradually, it became clear that there was indeed a very real evolutionary transition between late-type stars and PNs. Far infrared studies of PNs suggested the presence of two dust grain components of very different temperatures (Telesco & Harper, 1977; Moseley, 1980). The implication was that the cooler component had been emitted by the remnant of the red giant envelopes and the hotter component by dust grains which had newly condensed after the transition to planetary nebula (Kwok, 1980). Giant optical haloes were observed around PNs and were understood to be the remnants of the RGE illuminated by the central star of the PNs. The sharp outlines which are observed in these haloes were considered to be the result of an abrupt stopping of the red giant wind by the interstellar medium. Alternatively, such haloes have also been interpreted as multiple PN ejections (cf., Capriotti 1978).

Observational and theoretical studies have indeed conclusively confirmed the validity of Shklovsky's original arguments, but the most promising advance in the understanding of the formation of PNs came with the emergence of the various 'wind' theories for stellar mass loss and planetary nebula evolution. These theoretical models are reviewed in §1.3.

The formation of a PN is now known to be a process which is critically dependent upon the evolutionary behaviour of the central star, since the star is the source of both the wind(s) and the photons which will ultimately determine the appearance and shape of the resultant nebula. As a consequence, the most successful theoretical models for the formation of PNs bring together the physics of hydrodynamics and photo-ionization in their calculations (e.g., Marten & Schönberner, 1991; Mellema, 1994, 1995).

The transition period from red giant to PN is believed to be very short ($< 10^4$ years), and is fundamentally dependent on the mass of the hydrogen envelope at the end of the AGB phase (Vassiliadis & Wood, 1994; Blöcker, 1995). In addition, the central star must evolve from an effective temperature of $\sim 3000\,\mathrm{K}$ to $\sim 30000\,\mathrm{K}$ within this same time scale. If the AGB is ended by a sudden ejection, there will always be an undetermined amount of mass left around the core and this results in a long delay in the evolution to higher temperatures. Accordingly, if the central star evolves too slowly, the nebular material will have totally dispersed before the central star becomes sufficiently hot to ionize it and no PN will form (Renzini, 1981).

However, as an alternative to sudden ejection, should the hydrogen envelope on the AGB be steadily depleted by a stellar wind, the wind will continue until the stellar temperature has changed significantly, therefore ensuring the minimum amount of transition time between AGB and PN phases. The observational data, however, does not seem to support a large transition time between the end of the AGB superwind and the beginning of the PN ionization phase as adopted in the models of Vassiliadis & Wood (1994) according to Tylenda *et al.* (1994).

If, on the other hand, the central star evolves too quickly, then the nebula becomes illuminated for only a very brief period before the star finishes nuclear burning and becomes a white dwarf. Paczynski (1970, 1971) attempted to resolve this theoretical difficulty by assuming that the central star of the PN was undergoing hydrogen shell burning in a layer outside an electron degenerate carbon-oxygen core, basing this assumption on PNs being descendants of AGB stars, as described above. The evolution of the central star was found to be highly dependent on the core mass of the star. A low core mass star will evolve too slowly to become a PN, whereas a high core mass star ($\gtrsim 1.2\,M_\odot$) will be luminous too briefly to be detectable. Consequently, only stars possessing core masses within a very narrow mass range (~ 0.6 to $1.2\,M_\odot$) will later become observable as PNs.

The mass of a PN can be estimated from its density (deduced from forbidden-line ratios) and its apparent angular dimensions. Comparisons of nebular masses in the Small Magellanic Cloud (SMC) and Large Magellanic Cloud (LMC), where the PNs can then be assumed to lie at the same distance, results in a mass function which increases monotonically with radius from a lower limit of $0.01\,M_\odot$ and asymptotically approaching an upper limit of $0.27\,M_\odot$. This is usually interpreted as the total mass of the PN when the nebula is completely ionized. It is also clear that the ionized nebular mass evolves with time as a consequence of photo-ionization and the dynamics of the nebular expansion.

Both of these processes probably contribute to the increase of the nebular mass over time, so that the common assumption that PNs are ionization bounded is probably too simplistic. It is also possible to explain the mass-radius relationship, with the nebular mass increasing with age, by modelling the PN evolution as an interacting winds process (§1.3).

A typical *post*-AGB evolutionary track in the HR diagram consists of two distinct parts. Initially the central star contracts, evolving to higher effective temperatures at a constant

luminosity. As the stellar energy production ceases, the luminosity begins to decrease and the effective temperature starts to fall. The star reaches its highest temperature at the transition from the contraction to the cooling phase. In the contraction phase, the more massive stars are more luminous and can reach higher effective temperatures than the lower mass ones. The most striking difference is the evolutionary time scales involved. The lowest mass stars can take upwards of 10^4 years to attain their highest temperature, whereas the highest mass stars manage the same in less than 10^2 years. As a consequence, there is a low probability of observing a more massive central star in the contraction phase. Figure 1.2 (adapted from Kwok 1993) displays a graphical representation of the *post*-AGB evolutionary path.

A survey of 18 cms OH maser emission in the direction of 196 IRAS point sources (te Lintel Hekkert & Chapman, 1996) revealed that appreciable changes have occurred in the OH spectral profile of several *post*-AGB objects over very rapid timescales of only a few years. Such rapid changes in the nature of the stellar winds associated with these objects is seen as possible evidence for an interaction between the star and a companion in a binary system, or alternatively, the result of unusually rapid stellar evolutionary processes occurring in the *post*-AGB star itself.

Radio observations of the CO emission in the *post*-AGB object V Hydrae (Kahane *et al.*, 1996) have revealed both high and low velocity bipolar flows with substantial asymmetric mass loss. V Hydrae is also known to possess a high rotation speed (Kahane *et al.*, 1988; Barnbaum *et al.*, 1995) and this can be expected to amplify any slight deviations from spherical symmetry in the system, particularly in the dust formation zone where the dust condensation process is strongly temperature and density dependent (Dorfi & Hoefner, 1996).

Accordingly, the material lost from the AGB star in the mass loss process is preferentially deposited in the equatorial plane of the star. The mass loss rate and flow velocity is also believed to be a function of the angle out of the equatorial plane and provides a natural explanation for the observed asymmetries seen in many PNs.

The relative merits of these processes, binarity, stellar rotation and magnetic fields, in relation to the formation of bipolar PNs particularly, is discussed further in §1.4.

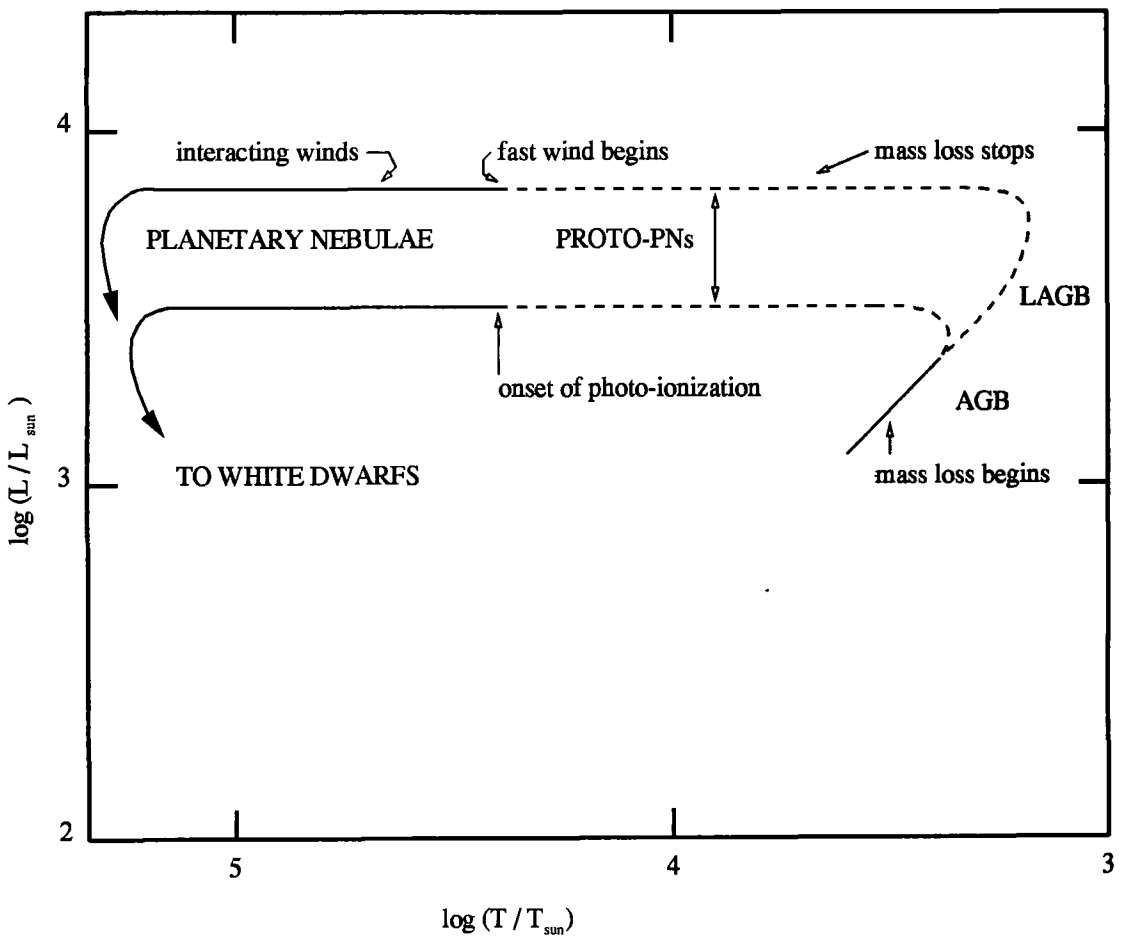

Figure 1.2: A HR diagram representing some important elements of the *post*-AGB stellar evolution phase. The two tracks indicate the evolution of stars of different core masses (adapted from Kwok 1993)

Mid-IR narrow band studies of a number of carbon rich PPNs have provided further insight into asymmetric mass loss. IRAS 07134+1005, IRAS 22272+5435, IRAS 04296 +3429 (Meixner *et al.*, 1994, 1997) and IRAS 19500-1709 (Meixner *et al.*, 1997) have been observed at 9.7 and 11.8μm. Of these four objects, 07134+1005, 22272+5435 and 19500-1709 were discovered to possess axially symmetric dust shells. IRAS 07134+1005, in particular, displays an elliptical outer shell surrounding two aligned peaks which are interpreted as the limb-brightened peaks of an optically thin, elliptical shell with an equatorial density enhancement. This is in sharp contrast with that observed in the better studied carbon-rich PPNs AFGL 2688, AFGL 915 and AFGL 618, which display bright, unresolved cores, probably created by optically thick inner regions, and bipolar extensions that align with their optical reflection nebulosity.

The young carbon rich PN, IRAS 21282+5050, has been studied at 3.3, 8.5, 10.0, 11.3 and 12.5μm (Meixner *et al.*, 1993). Again, the object is observed to possess a toroidal dust nebula with bipolar structure, remarkably similar to that seen in the more evolved object NGC 7027. The observed structure in the dust shells of three carbon rich PPNs and a young PN implies a strong evolutionary link between these objects and tends to reinforce the common perception that bipolar structure is developed very early in the carbon rich atmospheres of *post*-AGB objects. Modelling of the emission and spectral energy distribution of the dust shells of these PPNs and PNs using 0.01μm amorphous carbon grains implies that they have experienced a phase of enhanced mass loss at a rate of some $3 \times 10^{-5}\,M_{\odot}\,yr^{-1}$ and with an equatorial rate which was greater than the polar rate by a factor of between 18 and 90 as a result of an axially symmetric superwind. Dynamical estimates of the objects evolutionary status indicate that they moved off of the AGB between 300 and 1400 years ago, following the termination of the superwind phase.

1.3 Interacting Stellar Winds

The interacting stellar winds (ISW) model of Kwok, Purton and FitzGerald (1978) (in addition, see also Kwok 1982; Kahn 1983; Balick 1987; Balick *et al.* 1987; Icke *et al.* 1992; Aller 1993; Kwok 1994; Frank & Mellema 1994; Mellema & Frank 1995; Dwarkadas *et al.* 1996) is presently the most widely accepted scenario for the formation and evolution of PNs from AGB stars. Briefly, according to this model, a PN is formed through the in-

teraction between a 'fast' stellar wind, originating from the post-AGB central star, and a 'slow' wind which is the remnant of a somewhat earlier AGB-wind. Reliable observations of the fast wind have been made in many PN central stars (cf., Perinotto 1989) and the extensive faint halos seen around many PNs may be identified with the remnant of the slower AGB-wind.

Since Renzini (1981) it has become commonplace to consider two mass loss phases for a star evolving along the AGB. Both stellar winds during these phases have roughly the same outflow velocity ($\sim 10\,\mathrm{km\,s^{-1}}$), but the rate at which mass is lost differs significantly. The first phase is identified with Mira-type stars which have typical mass-loss rates of 10^{-8} to $10^{-6}\,\mathrm{M_\odot\,yr^{-1}}$. The second phase can be matched to that observed in OH/IR stars. This is called the *superwind*, where appreciable mass loss occurs steadily from the AGB star at an increased rate of around 10^{-4} to $10^{-5}\,\mathrm{M_\odot\,yr^{-1}}$. Ejection of the progenitor red giant envelopes occurs throughout both these phases over a time period of around 10^4 years. The length of this period is strongly dependent on the core mass of the progenitor, being shorter for high-mass stars and more protracted for low-mass stars (see §1.2). Towards the end of the stars AGB phase, the mass loss rate decreases again to around 10^{-8} to $10^{-6}\,\mathrm{M_\odot\,yr^{-1}}$, but the wind velocity increases to about $2000\,\mathrm{km\,s^{-1}}$. This 'fast' wind catches up with the material previously lost through the slower wind phases and drives a shock front through it, compressing the gas in a high density shell at the contact interface and heating it to temperatures of 10^5 to $10^7\,\mathrm{K}$. The shell of condensed gas is pushed outwards by the central-star 'fast' wind and retarded by the gas from the red-giant wind, quickly reaching a constant velocity but increasing in mass. Some of the shell will be ionized by radiation from the central star and will then present the classical appearance of a PN, with an emission line spectrum and radio radiation. The ionizing radiation may penetrate to the remnant of the red-giant wind beyond the shell, depending on the initial conditions and elapsed time. Both the size and mass of the shell are believed to increase linearly with time. One of the most attractive features of this model is that it assumes no physical processes which have not been observed. It offers definite predictions for comparison with observations. The model predicts three gas components in a PN system; a remnant RGE, a high-velocity wind from the central star, and a dense shell at the interface of the two winds. All of these components have good observational evidence for their existence in a large number of PNs. Balick (1987) proposed that the diverse variety of morphologies observed in PNs results from differences in the density contrast in the slow wind between the equatorial and polar directions.

A strong contrast results in those nebulae referred to as "butterfly" or bipolar shape. Balick *et al.* (1987) extended this thought, suggesting that the fast wind can be collimated by the inner shock and that the interacting winds can produce the ansae (knots) which are observed in some, mainly elliptical, PNs. It is believed that ansae form when higher density regions are cooled along the long axis of the ellipse. In turn, these knots cool and recombine more easily.

This particular theoretical model is very satisfactory in providing an explanation for the formation of the classical, spherically symmetric PNs through the action of isotropic stellar winds. However, observations of PNs reveal that most do not exhibit perfect spherical symmetry and in fact display a wide range of morphologies (see §1.5). Indeed, somewhat less than 20% of all PNs are thought to be spherically symmetric (Zuckerman & Aller, 1986). These deviations from sphericity are widely ascribed as being due to some degree of non-uniformity in the early, slow "superwind", which then propagates through to impart some degree of asymmetry in the shape of the PN shell (Kahn & West, 1985; Icke, 1988; Icke *et al.*, 1989). The origin of this asymmetry is not fully known and understood. However, explanations generally considered to be plausible include the presence of a central close binary, high stellar rotation speeds or the existence of magnetic fields.

Although it is accepted that the common envelope (CE) phase in the evolution of binary systems will lead to preferential mass outflow in the equatorial (orbital) plane of the system (Livio & Soker, 1988), it is rather less than clear as to whether this mechanism would produce the required degree of envelope asymmetry. If the spiraling-in process occurs within the envelope of a highly evolved AGB star, then a relatively mild density contrast ensues. A high contrast results from less evolved (less centrally condensed) AGB stars or from normal giants.

Hence, CE evolution is considered a natural mechanism for the production of the density contrast upon which the ISW model can operate to produce different morphologies (in PNs containing binary nuclei). Extreme contrasts result from relatively non-centrally condensed configurations (not very evolved AGB stars or normal giants) and relatively massive secondary stars. Mild contrasts are obtained from very centrally condensed configurations (highly evolved AGB stars).

However, it is plainly evident that a central binary is extremely unlikely to be present in every PN, and so other mechanisms must also be considered for the production of the density contrast. On the other hand, a significant fraction of stars, perhaps as many as one third (Renzini, 1983), are binaries which experience Roche lobe contact and significant mass transfer during their evolution, so that many PNs might be expected to display some degree of collimation in their mass loss history. The validity of binary interactions as a suitable mechanism is discussed in more detail in section §1.4.

For a single star, stellar rotation could, in principle, generate equatorial density enhancements up to a factor of 5. By the time the star expands to become an AGB star, its surface velocity is very likely to be a very small fraction of the escape velocity, thereby making a large effect of the rotational velocity on mass-loss rate somewhat implausible. Friend & Abbot (1986) found no evidence for a dependence of the mass-loss rate on rotational velocity. On the other hand, IRAS observations do seem to indicate mass-loss rates around the equator which are considerably higher than those found from IUE observations (Waters, 1986). There is also the possibility that a suitable magnetic field (Pascoli *et al.*, 1992) or the presence of a fossil protostellar disk (Balick & Preston, 1987) might create the required conditions. However, the rotation velocities and magnetic fields of single stars and supergiants are low, while the required red giant envelope density contrasts are uncomfortably high.

In the models of Icke *et al.* (1989), Icke (1991), Icke *et al.* (1992) and Mellema *et al.* (1991), the elongated shapes of bipolar nebulae are determined by the interaction of the fast wind with an initially aspherical, but axisymmetric, RGE mass distribution. Consequently, the shock front driven by the fast wind propagates anisotropically, shaping the nebula gas in the form of a bipolar nebula. Integrating the nebula evolution up to around 500 years shows that the development of the nebula is highly sensitive to the density distribution of the gas expelled prior to the onset of the fast wind, which is deflected and focussed by inner shocks. The timescale over which a strong aspherical flow is established is determined by the equator to pole density contrast. The steepness with which the RGE density rolls over from the polar to equatorial value determines the degree of collimation of the flow. Lower steepness values produce elliptical PNs, whereas higher values lead to jet structures and a more spherical inner shock. The ISW model is quite complete for systems of a spherical geometry (Weaver *et al.*, 1977; Kwok, 1982; Kahn, 1983) but remains somewhat lacking in modelling and explaining many features of the more com-

plicated bipolar nebulae. Balick (1987, 1989) suggested that all PNs could perhaps be explained by the ISW mechanism, if the RGE was expelled with cylindrical symmetry and with a density higher at the equator than at the poles. planetary nebula morphology and evolution then becomes simply a result of the mass distribution in the RGE and the properties of the fast stellar wind. However, the true form of the RGE is not fully understood (Johnson & Jones, 1991).

The question remains as to what causes asphericity in the RGE in the first place. A close companion in a binary system is usually viewed as the most likely mechanism (Livio *et al.*, 1979; Livio & Soker, 1988; Soker, 1989). However, if the central source is a binary system, the RGE may require an even higher equatorial density to polar density contrast (Livio *et al.*, 1979).

The Interacting Stellar Winds mechanism has also been utilized to explain the phenomena of jets and ansae in, mainly elliptical, PNs and PPNs (Frank *et al.*, 1996), via a wind blown bubble driven by an evolving fast wind. The fast wind expands into a previously ejected aspherical slow wind circumstellar envelope. During the early PPN stage, when the velocity of the fast wind is $< 160\,\mathrm{km\,s^{-1}}$, the bubble will be in the momentum conserving phase. The presence of an equatorial to pole density contrast in the slow wind makes the bubble elliptical (prolate). The fast wind will encounter the shocks bounding the bubble obliquely and the post-shock fast wind flow will be focused towards the equator forming a converging conical stream. It has been shown by Cantó *et al.* (1988) that well collimated jets can be produced by such converging streams at the tip of the conical flow. The theoretical calculations of Frank *et al.* (1996) show that jets produced by converging streams in the bubbles of PPNs have characteristic velocity and size scales which are well matched to observations of PN ansae. The momentum conserving phase has a finite lifetime and the proposed mechanism should not work in the energy conserving phase, so that this scenario provides definite time and velocity scales for the production of jets and ansae in PNs. Frank *et al.* (1996) also find large densities in the model jets which implies short recombination timescales and can therefore explain the observed low ionization states in these objects.

An alternative mechanism for the production of multiple shell PN could be the result of radiation pressure effects provoked by Lyman-α photons, and thereby removing the requirement for invoking any gas-dynamic effects. It has been shown that double enve-

lope PNs could possibly be formed by the dynamical separation of one envelope into two under the action of Lyman-α pressure (Gurzadyan, 1996).

Applying the standard ISW models to the late-AGB/PPN stage of evolution is beset with difficulties. Typical AGB slow-wind mass-loss rates are 10^{-7} to $10^{-4}\,M_{\odot}\,yr^{-1}$ at velocities around $5 - 25\,kms^{-1}$. After the AGB star evolves from a cool ($\sim 5000\,K$) to a much hotter star ($\sim 150\,000\,K$), the levels of ionizing radiation increase. In addition, the fast wind accelerates, increasing from velocities of about $100\,kms^{-1}$ up to $\sim 4000\,kms^{-1}$ with mass-loss rates reducing to some 10^{-9} to $10^{-7}\,M_{\odot}\,yr^{-1}$.

In the general ISW models, the fast wind remains unnaturally constant. In addition, as radiative effects are added in to the model, it is usual to temporarily halt the evolution of the central star (cf., Soker & Livio, 1989; Mellema *et al.*, 1991; Mellema, 1995; Icke *et al.*, 1992; Frank & Mellema, 1994; Mellema & Frank, 1995). However, the reality is that the star is evolving on the same timescale as the nebula gas-dynamics. This is also true of the fast wind since it is related to the central star parameters. AGB stars are thought to lose mass through the process of radiation pressure on dust (Bowen & Willson, 1991), whereas the hot central stars of PNs lose mass through radiation pressure on lines (Pauldrach *et al.*, 1988). It is not fully understood where the first mass-loss process ends and the second one starts. Indeed, the mass-loss character of stars with temperatures between 5000 K and 25 000 K is not known with confidence, though there are indications that radiation pressure on lines may also support stars with effective temperatures above about 10 000 K (Abbott, 1982).

1.4 Binary Star Interactions

A number of planetary nebulae, such as M 1-16 and Mz 3, are believed to have developed their distinctive bipolar morphology as a result of undergoing pronounced axisymmetric mass loss during their AGB and early PPN stages of evolution. The mass loss era of AGB evolution has been discussed in section §1.3, but leaves unanswered some fundamental questions regarding the sort of physical processes which might be expected to lead to the formation of the required flattened initial dust density distributions.

One of the most plausible candidates for such a mechanism, and possibly the most natural explanation, is mass loss occurring in a close, interacting binary system, involving a mass losing red giant in the presence of a binary companion in a detached or common envelope configuration (Morris, 1981). The observational data strongly favours the binary model on the basis of the large mass-loss rates and outflow velocities observed in bipolar nebulae. The primary component in the system is evolving as an RGB star. The secondary pulls material from the primary atmosphere as the primary approaches its tidal radius and ejects the material out of the system. The ejected matter is naturally concentrated towards the equatorial plane. This process also removes angular momentum from the system, permitting a quick evolution to a revised configuration as the secondary spirals towards the primary. This attractive hypothesis has been discussed in relation to very close binary stars (Bond & Livio, 1990), wider interacting binaries as symbiotic stars (Morris, 1987) and even non-accreting systems (Kolesnik & Pilyugin, 1986; Pilyugin, 1987). There are a number of PNs which clearly display a marked bipolarity (Schwarz *et al.*, 1992) but it is extremely difficult to confirm the binary nature of the exciting source involved since it is more often than not hidden from direct observation by circumstellar material.

Recent observations of symbiotic stars, which are commonly accepted as accreting binary star systems, have provided convincing evidence of some evolutionary link between these systems and PNs (Schwarz *et al.*, 1989; Balick, 1989; Schwarz & Corradi, 1992; Corradi & Schwarz, 1993). Corradi (1995) presents optical spectroscopy data for the highly collimated bipolar nebulae He 2-25 and Th 2-B. These objects are found to have very dense ($n_e \sim 10^7\,\mathrm{cm}^{-3}$) cores which are characterized by emission lines of low to intermediate ionization species, including rich [FeII] emission. The Hα profiles display broad non-Gaussian wings, and these are spectral characteristics which are known to be common features in some bipolar PNs, including the well-studied M 2-9, as well as bearing a close resemblance to those of interacting binary system symbiotic stars. Goodrich (1991) performed long-slit optical spectroscopy measurements of M 2-9 and M 1-91, both of which are bipolar nebulae, concluding that the overall bipolar morphology of these nebulae might be a consequence of the orbital motions of binary central stars. Secondary symmetries in these nebulae, such as the point-symmetric knots in M 1-91, are thought to be due to other possible influences in the system, such as the rotation axis of one of the individual stars or the polar axis of an accretion disk. Corradi & Schwarz (1993) provide a further example of the connection between binarity and bipolarity in their observations

of the bipolar PN He 2-36, noting that a second, hotter companion star is required to explain the high excitation levels and nebula morphology.

Long-slit spectra of high spectral and spatial resolution of the compact planetary nebula Hu 2-1 (Miranda, 1995) show a bipolar shell consisting of a compact (radius about 0.9 arcseconds), slowly expanding ($\sim 15\,\mathrm{kms}^{-1}$) bright equatorial toroid and two faint bipolar lobes expanding at $\sim 30\,\mathrm{kms}^{-1}$ surrounded by a faint spherical halo (radius $\sim$ 12 arcseconds). A ring-like region (radius $\sim$ 2 arcseconds) is concentric with the equatorial toroid and its formation seems to have preceded that of the bipolar shell suggesting that the formation of the ring-like region - corresponding to anisotropic mass ejection - occurred in the very last stages of the AGB phase of the Hu 2-1 progenitor. A mass exchanging binary can qualitatively and convincingly account for the observed components in Hu 2-1, and Miranda (1995) proposed that the ring-like region might represent the remnant of a common envelope or of a circumbinary disk. The highly collimated components could easily be connected with the effects of an accretion disk around a compact secondary and the different orientation of the compact components may be attributed to precession of that disk. A complex geometry of mass accretion may lead to asymmetries in the physical conditions around the secondary so that the collimated bipolar ejections present different properties.

In Chapter 3 of this work, observational data for the object M 1-16 is presented. The images display clearly a precessional rotation of the bipolar outflow axis for which the most reasonable, and possibly the only, explanation is that the object has evolved as an interacting binary system, with the geometry of mass accretion affecting the mass loss symmetry axes periodically.

1.5 Classification of Planetary Nebulae

The apparent wide range in the visual appearance of PNs as a single class of object has prompted many attempts to establish a comprehensive classification scheme, all of which are essentially based upon one, or the other, of two distinct determining characteristics

- purely visual categories extrapolated from the two-dimensional observed appearance of the nebula
- a consideration of the physics and three-dimensional structure of the nebula

The first catalogues of planetary nebulae were published by Keeler in 1908 and by Curtis in 1918. Additional catalogues were published by Evans & Thackeray (1950), Voroncov-Vel'jaminov (1961) and Westerlund & Henize (1967). More recent and extensive catalogues became available with Perek & Kohoutek (1967) and Acker *et al.* (1982, 1992). Statistical analysis of these data, however, is very difficult since the images are derived using a wide variety of instruments and methods. Catalogues based upon more comparable images are available in Jewitt *et al.* (1986) (47 images of 47 nebulae), Balick (1987) (223 images of 51 nebulae) and Schwarz *et al.* (1992) (507 images of 255 nebulae).

The first attempt to establish a possible link between the morphology and evolution of PNs was made by Stoy in 1933. This was a complex system, classifying a sample of PNs into six groups according to the observed structure and the spectrum and brightness of the central star. A simpler, and more extensively used system, was introduced by Voroncov-Vel'jaminov in 1934, using only the observed shape to define six morphological classes. There have been several other systems which may be mentioned briefly; in 1962, Gurzadyan used eleven classes of objects based upon shape. In 1968, Khromov & Kohoutek arranged the nebulae into three groupings using the main structure appearance (round, elliptical and effectively bipolar) and three groupings using the shape of the outer parts of the nebula (regular arclike closed filaments, torn diverging filaments, and faint regular rings). It became clear that it is very difficult to classify, in a simple way, even a small sample of nebulae. Khromov & Kohoutek also attempted to construct one single underlying three-dimensional nebula which could explain all the observed shapes by viewing at different angles.

The most recent classification scheme based upon morphology is that of Schwarz *et al.* (1993), classifying 361 nebulae from Hα images, with the aim of revealing possible links between morphological class and other fundamental parameters such as central star evolution in the Hertzsprung-Russell, galactic distribution and kinematics, expansion velocity, etc. This method of classification yields four distinct groups; elliptical **e** (with inner structure **es**, or multiple shells **em**), bipolar **b** (with multiple events **bm**), point-symmetrical **p** (with multiple events **pm**) and irregular **i** (a general group into which a nebula is placed if it does not fit naturally into any of the preceding classes).

A number of schemes also exist which classify PNs according to various characteristics of their chemical structure or composition. Peimbert (1978) (also Peimbert & Torres-

Peimbert, 1983; Peimbert, 1990) proposed a classification scheme for PNs based essentially upon the differences in the observed chemical abundances in the shells of PNs. According to this widely used scheme, PNs are of four basic types: **Type I** (helium-nitrogen rich); **Type II** (disk or intermediate population); **Type III** (high velocity) and **Type IV** (halo population). It can be argued that this scheme is not solely a chemical classification but also displays some correlation with the initial or main sequence mass of the PN progenitor stars (M_i), with the approximate masses shown in Table 1.2.

Table 1.2: PN mass ranges according to the Peimbert classification

Classification	Mass range ($M_\odot$)
Type I	2.4 – 8.0
Type II	1.2 – 2.4
Type III	1.0 – 1.2
Type IV	0.8 – 1.0

These values in turn correspond with a range of core masses for the central star (M_c), after shell ejection, of $0.54 - 0.8\,M_\odot$. For any PN, the difference between M_i and M_c will vary in the range 0.3 to a few solar masses. This difference is comprised of the mass lost during the red giant stage and the mass of any ejected shell. The PN shell mass appears to range from about $0.02\,M_\odot$ for the extreme Type IV PNs up to about $1.0\,M_\odot$ for the most extreme Type I PNs. Maciel (1989) has proposed that PNs within the bulge of the Galaxy should be called **Type V**.

Type I

These are defined as those objects with $n(\mathrm{He})/n(\mathrm{H}) \geq 0.125$ or $\log n(\mathrm{N})/n(\mathrm{O}) \geq -0.30$. Most of the objects in this category are very filamentary, their spectra show very strong forbidden lines ranging from [O I], [N I] and [S II] up to [Ne V], and they also display a bipolar morphology. In Greig's classification scheme (Greig, 1971, 1972), there are four main classes of PN: A (annular), B (binebulous or bipolar), C (centric, the surface brightness increases towards the PN centre) and E (egg shaped). There appears to exist

a strong correlation between PNs of Peimbert's Type I and Greig's class B. Numerous studies of the kinematic and galactic distribution of PNs indicate that class B (Greig, 1972; Cudworth, 1974) and Type I objects (Acker, 1980, 1983; Dutra & Maciel, 1990) correspond as a group to having evolved from more massive progenitor stars than the other classes of PN. Gorny *et al.* (1997) have recently shown that bipolar PNs have a wider distribution of central star masses than other PNs, and that the distribution is also shifted towards higher values. In addition, they generally lie closer to the galactic plane than the point symmetric nebulae, which appear to correspond to a rather short evolutionary stage of PNs.

There are a number of Type I PNs for which estimates of their main sequence progenitor mass (M_i) have been proposed in the astronomical literature. NGC 2346, for example, is known to be a binary system with a current orbital separation of $38\,R_\odot$. Iben & Tutukov (1989), assuming that the system evolved with a common envelope, estimate M_i to be around $2-3\,M_\odot$. Similar values of M_i have been derived for GL 618 and NGC 2818 (Kwok & Bignell, 1984).

It has been observed by a number of authors that the central stars of Type I PN generally lie on higher-mass tracks in the HR than the central stars of other PN types. This observed trend implies that Type I PNs possess a higher M_i than the other classes, as shown in Table 1.2 above (e.g., Pottasch, 1989).

Greig's class B PNs, strongly identified with Peimbert's Type I, are found to remain optically thick for much of their evolution, whereas class C PNs are essentially optically thin (Sabbadin, 1986). This again supports the hypothesis that class B nebulae evolve from higher mass progenitor stars than class C.

Type II

PNs that are classed as Type II in the Peimbert scheme are defined as having $n(\mathrm{He})/n(\mathrm{H}) < 0.125$, $\log n(\mathrm{N})/n(\mathrm{O}) < -0.30$, $\log n(\mathrm{O})/n(\mathrm{H}) > -3.90$, $|\Delta v_{pr}| < 60\,\mathrm{km\,s^{-1}}$, and $|z| < 0.8\,\mathrm{kpc}$, where $|v_{pr}|$ is the peculiar radial velocity relative to the galactic rotation curve and z is the distance from the galactic plane. Some 80% of PNs in close proximity to the solar neighbourhood are found in this grouping. The average height of these nebulae is 150 pc, corresponding to progenitor masses of some $1.5\,M_\odot$. Such values are found to be typical of intermediate population I stars.

Type II PN were subsequently subdivided into Types IIa and IIb by Faúndez-Abans & Maciel (1987a), with IIa displaying $\log n(\mathrm{N})/n(\mathrm{H}) \geq -4.00$ and IIb with $\log n(\mathrm{N})/n(\mathrm{H}) < -4.00$.

Type III

These PNs have $|\Delta v_{pr}| > 60\,\mathrm{km\,s^{-1}}$ and $\log n(\mathrm{O})/n(\mathrm{H}) > -3.90$. Most of these nebulae may also be identified with the Population II PNs of Kaler (1970).

Type IV

There are few known Type IV PNs, or halo PNs. They are defined as having $\log n(\mathrm{O})/n(\mathrm{H}) \leq -3.90$, often with $|\Delta v_{pr}| > 60\,\mathrm{km\,s^{-1}}$ and $|z| > 0.8\,\mathrm{kpc}$.

There have been occasional claims of the existence of apparent correlations between the morphological classes and various physical parameters. Stanghellini *et al.* (1993) demonstrated that the different classes occupied distinctive points on the Hertzsprung-Russell diagram. The bipolar nebulae are distributed more evenly over mass than the general class of nebulae, and those classed as irregular PNs are heavily concentrated in one place in the Luminosity-Temperature plane (implying that irregulars are not only of the same mass but are at the same evolutionary stage). Bipolar nebulae are found to be more concentrated towards the Galactic plane, are predominantly Type I PNs (He and N rich), as mentioned above, and have an average expansion velocity of $170\,\mathrm{kms^{-1}}$ (the average for all PNs is $20\,\mathrm{kms^{-1}}$). They also appear to contain neutral material, have a smaller radial velocity dispersion ($24\,\mathrm{kms^{-1}}$ as opposed to $80\,\mathrm{kms^{-1}}$ for elliptical PNs), and have higher central star temperatures ($140 \times 10^3\,\mathrm{K}$ versus $75 \times 10^3\,\mathrm{K}$ for the ellipticals). Greig (1971, 1972) found that the presence of strong [NII] and [OII] lines correlates with the bipolar morphology, as do Type I nebulae, suggesting that bipolar PNs evolved from giant (of spectral type G, K or M) and symbiotic progenitor stars, while the other nebulae have evolved from long period variable stars.

1.6 Summary

The origin and characteristics of PNs have been reviewed and summarized in this chapter, with the aim of placing these objects into their proper place within the general framework of stellar evolution. It is seen that PNs form a relatively brief transitory period during the much longer total lifetime of low to intermediate mass stars. Much still remains to be understood concerning the physical processes which constrain main sequence stars of a limited mass range to become PNs. Mass-loss from stars is obviously the key fundamental mechanism which promotes the transition and it is now clear that stars begin to lose mass early on as they leave the main sequence and evolve along the Red Giant and Asymptotic Giant Branches towards their final destiny as a white dwarf and ultimate obscurity.

From an optical polarimetry point of view, the most interesting phase of PN evolution must be the period between the tip of the AGB and a fully ionized PN status. At this point, the progenitor star is enshrouded within the products of the mass loss history. Radiative and hydrodynamic effects result in an abundant diversity of morphologies and chemical environments, the physics of which are only just becoming accessible as the data increasingly allows for better discrimination between competing theories. Regardless of the lack of complete understanding in some areas, observations of the immediate circumstellar environments in these objects will enable the theories of mass-loss processes, in particular the formation of astrophysical solid materials, to be refined accordingly. It is here that optical polarimetry can be applied as a powerful diagnostic and analytical tool in the study of grain properties and the dust distribution within and around PPNs and PNs. In addition, more evolved PNs display interesting structural phenomena in the form of jets, ansae and emission-like knots.

In the majority of instances, such structure is found to be purely the result of emission, via shock excitation for instance. Optical polarimetry provides an effective means of investigating the true nature and geometry of these structures by a determination of their intrinsic polarization. The polarization data enables us to differentiate between the various possibilities.

In the following section, I review the phenomena of polarization in relation to potential polarizing mechanisms within PPNs and PNs, with particular regard to the nature and properties of the solid dust material which is known to be a major component of PN structure and, potentially, an important factor in the formation and evolution of all PNs.

Chapter 2

Polarization and Planetary Nebulae

2.1 Introduction

There are a number of studies of polarization and scattering in post-AGB objects which have been published in the astronomical literature. Those of particular relevance in regard to this present study involve observations of PNs and PPNs carried out by the Durham Polarimetry Group. These include, for example, V-band imaging polarimetry data for Mz 3, Roberts 22, Hen 401, NGC 2346, IC 4406, J 320 (Scarrott & Scarrott, 1995), multi-waveband polarimetry of IRAS 07131-0147 (Scarrott *et al.*, 1990) and IRAS 09371+1212 (Frosty Leo nebula) (Scarrott & Scarrott, 1994, 1995), broadband and emission-line polarimetry of M 2-9 (King *et al.*, 1981; Aspin & McLean, 1984; Scarrott, Scarrott & Wolstencroft, 1993), and continuum observations of the evolved star OH 231.8+4.2 (Scarrott *et al.*, 1990).

The conclusions of the V-band polarization data of Scarrott & Scarrott (1995) for Mz3 will be reviewed and discussed in conjunction with the new Hα data presented in Chapter 4 of this thesis.

The multiwaveband data for IRAS 09371+1212 has been re-analysed and interpreted in Chapter 5 of this work, with particular emphasis on the optical properties of the dust grains responsible for the observed polarization, as well as the scattering geometry of the nebula.

Both Roberts 22 and Hen 401 are small PPNs which display many similarities with IRAS 09371+1212. The available polarization data for each of these three PPNs reveals that the central evolved source is hidden from direct view by a dense circumstellar disk of dust/gas. The high levels of linear polarization are believed to be a consequence of moderately sized dust grains thinly coated with a volatile material, such as water ice.

NGC 2346, IC 4406, and J 320 are more evolved PNs for which the V-band polarization data infers that they are seen mainly by emission from hot gas rather than scattered light from dust grains.

IRAS 07131-0147 is a PPN of intermediate age formed during the post-AGB evolution of the central source. In this case, light scattering from small ($\leqslant 0.2\mu$m) dust grains and the overall geometry of the nebula results in high levels of observed linear polarization.

M 2-9 is a bipolar object, generally considered to be a PPN, which displays significant levels of linear polarization (both in the continuum and emission line) as a result of scattering of the central starlight by dust in the nebula bipolar lobes.

The polarization observed in the maser/OH source OH 231.8+4.2 reveals that the object possesses a circumstellar disk and that the scattering dust is composed of very small 'Rayleigh particles', again with the possibility of the grains being thinly coated with ice material.

It is clearly evident from the published polarization data for these objects, as well as that available for a few late-type stars (see, for example, Jura, 1994), that it is predominantly the nature and distribution of dust grains in the nebulae, combined with the effects of the nebula geometry, which invests each individual object with it's intrinsic polarization properties.

Physical mechanisms for the production of polarized light have been adequately reviewed and discussed elsewhere (e.g., Berry, 1985; Gledhill, 1987; Martin, 1989; Alton, 1996). Polarization in PPNs and PNs, such as presented in this work, almost certainly arises as a result of scattering from dust particles. I therefore neglect other potential causes of polarization (synchrotron emission and dichroic extinction by aligned grains in a magnetic

field, for example), and concentrate solely on the process of scattering, in particular, scattering by associations of astrophysical solids. In the remaining sections of this chapter, I review the fundamentals of the polarization of light and the basics of scattering theory, with an emphasis on scattering from spherical particles, and then outline some aspects of current thinking on the nature and distribution of astrophysical dust in the immediate environment of AGB stars, PPNs and PNs.

The chapter concludes with a description of a number of scattering calculations carried out in an investigation of the optical properties of both homogeneous and core-mantle dust grains, ending with a commentary on the scattering properties of the types of dust grain materials which are considered to be important in understanding the dust content of PPNs and PNs.

2.2 Polarization via scattering

A full treatment of the absorption and scattering of light by small particles is a problem in electromagnetic theory and is beyond the scope of this thesis. A number of texts are available which present detailed accounts of the principles involved (see, for example, van de Hulst (1957); Bohren & Huffman (1983). Essentially, however, light can be considered as a transverse electromagnetic wave, in which case it is described mathematically by the equations of Maxwell.

2.2.1 The polarization of light

For a time dependent harmonic field, Maxwell's equations may be written (Bohren & Huffman, 1983)

$$\nabla \cdot (\epsilon \mathbf{E}) = 0 \tag{2.1}$$

$$\nabla \times \mathbf{E} = i\omega\mu\mathbf{H} \tag{2.2}$$

$$\nabla \cdot \mathbf{H} = 0 \tag{2.3}$$

$$\nabla \times \mathbf{H} = -i\omega\epsilon\mathbf{E} \tag{2.4}$$

where $\mathbf{E}$ is the complex representation of the real *electric field*, $\mathbf{H}$ is similarly the *magnetic field*, ω is the *angular frequency* of the harmonic field, μ is the *permeability* of the medium and ϵ is the *complex permittivity*.

Plane wave solutions to equations 2.1 through 2.4, for a wave travelling in the positive z-direction, have the form

$$\mathbf{E} = \mathbf{E}_o \exp\left(-\frac{2\pi kz}{\lambda}\right) \exp\left(\frac{i2\pi nz}{\lambda} - i\omega t\right) \tag{2.5}$$

where k and n are the non-negative parts of the complex refractive index of the medium in which the wave propagates. These pair of quantities are often referred to as "*optical constants*". However, this is a somewhat misleading term as neither k nor n are constant and are almost universally a strong function of the wavelength.

The Poynting vector of the plane wave in the positive z-direction is

$$\mathbf{S} = \frac{1}{2} \mathrm{Re}\left\{\sqrt{\frac{\epsilon}{\mu}} |\mathbf{E}_o|^2 \exp\left(-\frac{4\pi kz}{\lambda}\right)\right\} \tag{2.6}$$

the magnitude of which, $|\mathbf{S}|$, is the *irradiance* (I), or *intensity* of the wave, with dimensions of energy per unit area and time. As the wave traverses the medium, the irradiance is exponentially attenuated

$$I = I_o e^{-\alpha z} \tag{2.7}$$

where the *absorption coefficient*, α, is given by

$$\alpha = \frac{4\pi k}{\lambda} \tag{2.8}$$

and I_o is the irradiance at $z = 0$.

In addition to the irradiance and wavelength, a monochromatic (time-harmonic) electromagnetic wave has a property known as its *state of polarization*. Consider a plane monochromatic wave with angular frequency ω and wave number k, propagating in the positive z-direction in a non-absorbing medium. In discussions of polarization it is usual to focus attention upon the electric field $\mathbf{E}$

$$\mathbf{E} = \mathrm{Re}\{(\mathbf{A} + i\mathbf{B}) \exp(ikz - i\omega t)\} \tag{2.9}$$

or

$$\mathbf{E} = \mathbf{A} \cos(\mathrm{k}z - \omega t) - \mathbf{B} \sin(\mathrm{k}z - \omega t) \tag{2.10}$$

where $\mathbf{A}$ and $\mathbf{B}$ are real vectors which are independent of position and represent the amplitude of the $\mathbf{E}$ vector. The electric field vector at any point lies in a plane, the normal to which is parallel to the direction of wave propagation. In any particular plane, $z = 0$ for example, the endpoint of the electric vector describes a curve

$$\mathbf{E}_{z=0} = \mathbf{A} \cos \omega t + \mathbf{B} \sin \omega t \tag{2.11}$$

Equation 2.11 has the form of an ellipse (often called the *vibrational ellipse*).

If $\mathbf{A} = 0$ (or $\mathbf{B} = 0$), the vibrational ellipse collapses to a straight line and the wave is said to be *linearly polarized* (or occasionally, *plane polarized*). If $|\mathbf{A}| = |\mathbf{B}|$ and $\mathbf{A} \cdot \mathbf{B} = 0$, then the vibrational ellipse is a circle and the wave is said to be *circularly polarized*. In general, a monochromatic wave is *elliptically polarized*. For natural light, which can be thought of as the superposition of many individual waves, the $\mathbf{E}$ vector displays no preferred direction of orientation and the light is then *unpolarized*.

2.2.2 Stokes parameters

The phenomenon of polarization in a monochromatic wave of a given wavelength may be fully described by certain properties of the vibrational ellipse. However, these ellipsometric parameters are not easily visualized or very useful in understanding the transformations which occur to the state of polarization as the light is scattered, absorbed

or reflected, for example. In addition, apart from the irradiance of the light, they are difficult to measure directly.

Sir George Stokes introduced an alternative, but equivalent, set of parameters which are particularly useful in the description of polarized light. Although the Stokes parameters are even less easily visualized than the ellipsometric parameters, their important advantage is that they are operationally defined in terms of the measurable quantities of irradiance (intensity).

For a beam of light, travelling in a certain direction, the exact specification of the Stokes parameters allows the determination of the intensity, the degree of polarization and the plane of polarization of the light. The Stokes parameters may be defined using both real, trigonometric wave functions and complex exponential functions. Following van de Hulst (1957), consider a monochromatic beam of light travelling in the positive z-direction. Complex oscillating functions for the components of the electric field are

$$E_{||} = a_{||} \exp(-i\epsilon_1) \exp(-ikz + i\omega t) \tag{2.12}$$

$$E_{\perp} = a_{\perp} \exp(-i\epsilon_2) \exp(-ikz + i\omega t) \tag{2.13}$$

where $a_{||}$ and $a_{\perp}$ are non-negative real quantities representing the amplitude, ϵ_1 and ϵ_2 are constants which incorporate the phase, k$= 2\pi/\lambda$, and λ is the wavelength. The physical quantities are assumed to be the real parts of these expressions.

The Stokes parameters are now defined as the real quantities

$$I = E_{||}E_{||}^* + E_{\perp}E_{\perp}^* \tag{2.14}$$

$$Q = E_{||}E_{||}^* - E_{\perp}E_{\perp}^* \tag{2.15}$$

$$U = E_{||}E_{\perp}^* + E_{\perp}E_{||}^* \tag{2.16}$$

$$V = i\left(E_{||}E_{\perp}^* - E_{\perp}E_{||}^*\right) \tag{2.17}$$

where the asterisk denotes the complex conjugate value.

Applying these relations to Equations 2.12 and 2.13 leads to

$$I = a_{\|}^2 + a_{\perp}^2 \tag{2.18}$$
$$Q = a_{\|}^2 - a_{\perp}^2 \tag{2.19}$$
$$U = 2a_{\|}a_{\perp}\cos(\epsilon_1 - \epsilon_2) \tag{2.20}$$
$$V = 2a_{\|}a_{\perp}\sin(\epsilon_1 - \epsilon_2) \tag{2.21}$$

Here

$$a_{\|}^2 + a_{\perp}^2 = a^2 \tag{2.22}$$

is equal to the specific intensity of the beam. Consequently, the Stokes parameters are four real quantities with the same physical dimensions.

When the light is not strictly monochromatic, $a_{\|}$, $a_{\perp}$ and $(\epsilon_1 - \epsilon_2)$ are, in general, time-dependent, so that time averages must be considered. It is found that (see, for example, Berry, 1985)

$$I^2 \geqslant Q^2 + U^2 + V^2 \tag{2.23}$$

where the equality holds if the light is polarized and is equivalent to the square of the polarized intensity. For unpolarized light, $Q = U = V = 0$.

The inequality leads naturally to the concept of *degree of polarization*, where for *linear polarization*

$$P(\%) = \frac{\sqrt{Q^2 + U^2}}{I} \times 100$$

The direction, or *position angle*, of polarization ϕ can be determined from

$$\tan 2\phi = \frac{U}{Q}$$

and identifies the orientation of the plane to which the **E** vector is confined relative to some reference direction.

Light of arbitrary polarization may be represented by a column vector, the *Stokes vector*, the four elements of which are the Stokes parameters. In general, the state of polarization of light is altered upon interaction with some optical element (polarizer, reflector, scatterer, for example), and the Stokes vector undergoes a transformation. The optical elements may be represented by a 4×4 matrix which describes the relation between the "incident" and "transmitted" Stokes vectors. The design principle of the Durham Imaging Polarimeter is such that the linear polarization of extended astronomical objects may be obtained by measurement and analysis of the observed intensities transmitted through an intervening linear polarizer or retarder (Draper, 1988). Further details on the principles involved may be found in Warren-Smith (1979), Scarrott *et al.* (1983) and Scarrott (1991).

2.2.3 The scattering of light by small particles

Light impinging upon a particle of specified characteristics will either be scattered or absorbed. The quantity and angular distribution of the scattered light, as well as the amount absorbed, is completely dependent upon the nature of the particle, that is, its size, shape and optical properties. Obtaining solutions to the Maxwell equations, both inside and outside a particle of arbitrary shape with appropriate boundary conditions, when illuminated by arbitrarily polarized light is a very difficult theoretical problem which has been solved only for relatively simple geometries (van de Hulst, 1957; Bohren & Huffman, 1983).

For particles which are very much smaller than the wavelength of the incident light, the problem is simplified somewhat, and is generally referred to as *Rayleigh scattering*.

For unpolarized incident light, the polarization of the scattered light (P) is given by

$$P(\theta) = \frac{1 - \cos^2(\theta)}{1 + \cos^2(\theta)} \times 100\%$$

where θ is the angle between the incident and scattered light (see Figure 2.2). This function is seen to be symmetrical about a scattering angle of 90° and with the polarization attaining its maximum value of 100% at that same angle. Figure 2.1 shows a plot of the levels of polarization obtained as a function of the scattering angle for small Rayleigh particles. In addition, Figure 2.1 also displays the total intensity scattered into unit solid angle for unit incident flux.

This is known as the *differential scattering cross-section* and, for Rayleigh particles, is obtained from the proportionality

$$I(\theta) \propto \cos^2(\theta) + 1$$

Figure 2.1 shows that the scattered intensity is also symmetrical about a scattering angle of 90 degrees.

For particles of arbitrary size, a rigorous solution for smooth, homogeneous spheres was derived independently by Mie (1908) and Debye (1909). A full account of this solution is given in van de Hulst (1957). As interstellar particles must certainly display a range of geometrical shapes to explain observed features, such as interstellar polarization, rigorous solutions have also been obtained for infinite cylinders (van de Hulst, 1957) and spheroids (Asano & Yamamoto, 1975). There are also a number of numerical methods which can be used for certain nonspherical particles (Draine, 1988; Matsumura & Seki, 1991).

For the purposes of the present study, light scattering from smooth, homogeneous spheres (Mie scattering) is a sufficiently accurate theoretical framework to enable an analysis of the polarization observations of PNs in relation to the nature of the dust grains responsible.

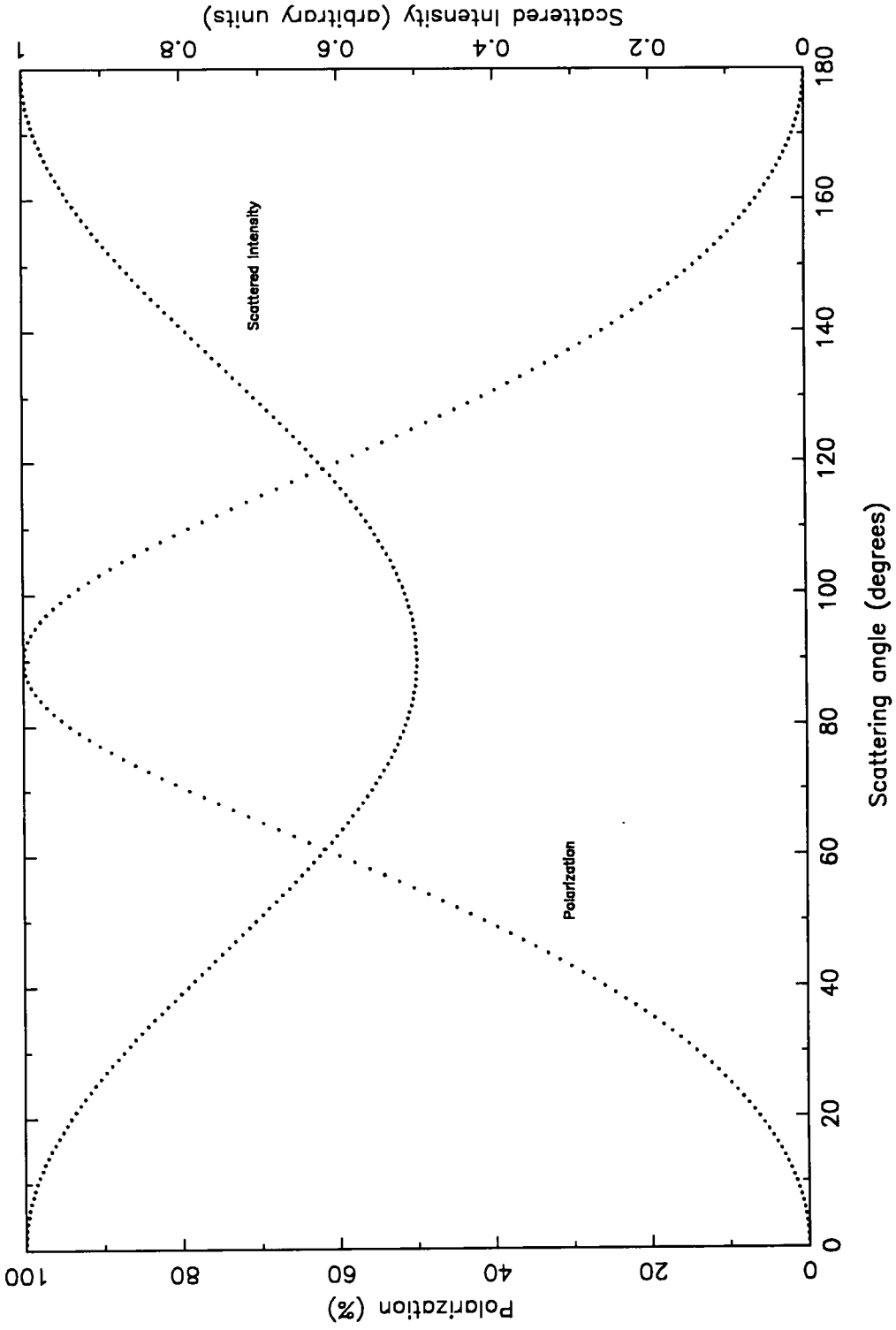

Figure 2.1: Polarization and scattered intensity as a result of light scattering from small Rayleigh particles

Practical algorithms for the calculation of the Mie scattering functions for homogeneous spherical particles have been developed by a number of authors including Wickramasinghe (1973) , Warren-Smith (1979), Bohren & Huffman (1983) and de Rooij & van der Stap (1984). However, it is relevant to describe the basic relationships and derived functions here.

Suppose a beam of light is scattered by a single particle or a small volume element of particles. The geometry of an appropriate scattering coordinate system is shown in Figure 2.2. The light beam is scattered by an angle θ and the plane containing the incident and scattered beams is called the *scattering plane*. The scattering plane is uniquely determined by the azimuthal angle ϕ (except when the scattered beam is parallel to the z axis). It is convenient to resolve both the incident and scattered electric fields into components which are parallel and perpendicular to the scattering plane, $E_{\|}$ and $E_{\perp}$ respectively. The outgoing scattered wave in the far-field can then be written as

$$\begin{pmatrix} E'_{\perp} \\ E'_{\|} \end{pmatrix} = \begin{pmatrix} S_1(\theta) & 0 \\ 0 & S_2(\theta) \end{pmatrix} \frac{e^{-ik(R+z)}}{ikR} \begin{pmatrix} E_{\perp} \\ E_{\|} \end{pmatrix} \tag{2.24}$$

The distance to the particle is represented by R and θ is the scattering angle.

The scattering amplitude functions $S_1(\theta)$ and $S_2(\theta)$ are given by

$$S_1(\theta) = \sum_{n=1}^{\infty} \frac{2n+1}{n(n+1)} \{a_n \pi_n(\cos\theta) + b_n \tau_n(\cos\theta)\} \tag{2.25}$$

and

$$S_2(\theta) = \sum_{n=1}^{\infty} \frac{2n+1}{n(n+1)} \{b_n \pi_n(\cos\theta) + a_n \tau_n(\cos\theta)\} \tag{2.26}$$

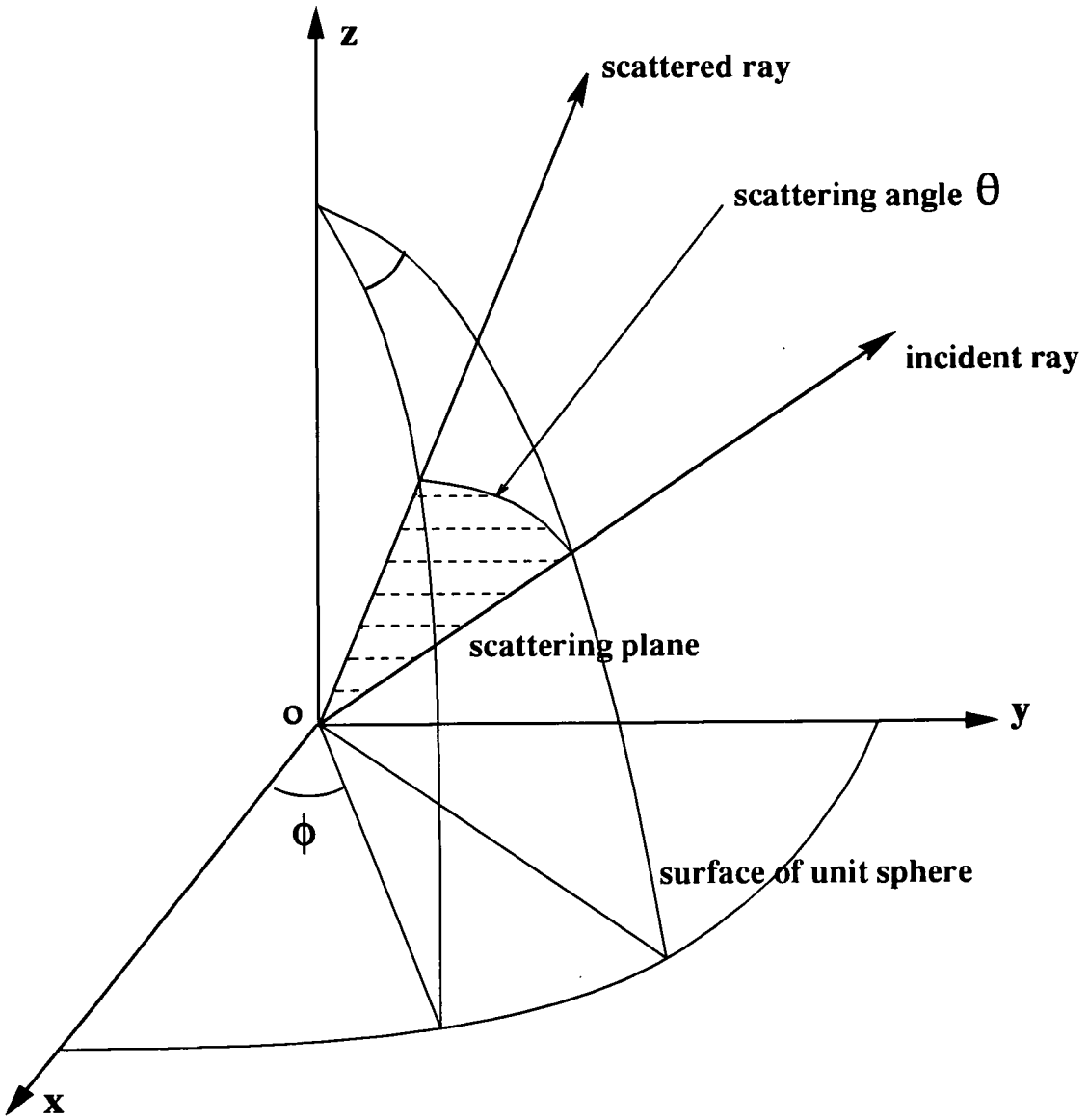

Figure 2.2: The geometry of scattering

where the angular functions of $\cos(\theta)$ can be expressed in terms of associated Legendre functions P_n^1 as

$$\pi_n(\cos\theta) = \frac{1}{\sin(\theta)} P_n^1(\cos\theta) \tag{2.27}$$

and

$$\tau_n(\cos\theta) = \frac{d}{d\theta} P_n^1(\cos\theta) \tag{2.28}$$

The Mie scattering coefficients a_n and b_n can be written as

$$a_n = \frac{\{[D_n(z)/m] + n/x\}\psi_n(x) - \psi_{n-1}(x)}{\{[D_n(z)/m] + n/x\}\zeta_n(x) - \zeta_{n-1}(x)} \tag{2.29}$$

and

$$b_n = \frac{\{mD_n(z) + n/x\}\,\psi_n(x) - \psi_{n-1}(x)}{\{mD_n(z) + n/x\}\,\zeta_n(x) - \zeta_{n-1}(x)} \tag{2.30}$$

where $m = n_r - in_i$ is the complex refractive index of the particle material, $x = kr = 2\pi r/\lambda$ is a dimensionless size parameter and r is the radius of the particle.

In addition, $z = mx$ and

$$\psi_n(x) = xJ_n(x) \tag{2.31}$$

$$\zeta_n(x) = \psi_n(x) + i\chi_n(x) \tag{2.32}$$

with

$$\chi_n(x) = -xY_n(x) \tag{2.33}$$

where $J_n(x)$ and $Y_n(x)$ are spherical Bessel functions of the first and second kind respectively. The logarithmic derivative function $D_n(z)$ is defined as

$$D_n(z) = \frac{d}{dz}\ln\psi_n(z) = -\frac{n}{z} + \frac{\psi_{n-1}(z)}{\psi_n(z)} \tag{2.34}$$

The relationship between the Stokes vectors of the incident $\mathbf{I} = I, Q, U, V$ and scattered $\mathbf{I}' = I', Q', U', V'$ waves, in the far field, can be written as

$$\mathbf{I}' = \frac{1}{k^2R^2}\,\mathbf{T}(\theta)\,\mathbf{I} \tag{2.35}$$

The non-zero elements of the transformation matrix $\mathbf{T}(\theta)$ are

$$T_{11} = T_{22} = \frac{1}{2}\left(S_1S^*{}_1 + S_2S^*{}_2\right) \tag{2.36}$$

$$T_{33} = T_{44} = \frac{1}{2}\left(S_1S^*{}_2 + S_2S^*{}_1\right) \tag{2.37}$$

$$T_{12} = T_{21} = -\frac{1}{2}\left(S_1S^*{}_1 - S_2S^*{}_2\right) \tag{2.38}$$

$$T_{34} = -T_{43} = \frac{i}{2}\left(S_1S^*{}_2 - S_2S^*{}_1\right) \tag{2.39}$$

The scattering matrix of the particle, $\mathbf{F}(\theta)$, is proportional to the transformation matrix $\mathbf{T}(\theta)$. From the normalization condition

$$\frac{1}{4\pi}\int_{4\pi} \mathrm{F}_{11}(\theta)\,d\Omega = \alpha \tag{2.40}$$

where α is the single scattering *albedo* of the particle (the fraction of intercepted light scattered), given by

$$\alpha = \frac{C_{sca}}{C_{ext}} \tag{2.41}$$

it is found that

$$\mathbf{F}(\theta) = \frac{4\pi}{k^2 C_{ext}} \mathbf{T}(\theta) \tag{2.42}$$

C_{sca} is the total scattering cross-section and is obtained through the integral of the scattering function over all solid angles

$$C_{sca} = \frac{1}{k^2} \int_{4\pi} \mathrm{T}_{11}(\theta)\, d\Omega = \frac{2\pi}{k^2} \sum_{n=1}^{\infty} (2n+1) \left\{ |a_n|^2 + |b_n|^2 \right\} \tag{2.43}$$

C_{ext}, the total extinction cross-section, defined as

$$C_{ext} = \frac{4\pi}{k^2} \mathrm{Re}\{S_1(0)\} = \frac{2\pi}{k^2} \sum_{n=1}^{\infty} (2n+1) \mathrm{Re}\{a_n + b_n\} \tag{2.44}$$

has the dimensions of area and represents the *effective* cross-sectional area presented to the incident light. This is normally not the same value as the geometrical cross-section.

It is usual to consider the extinction efficiency by defining the ratio of the extinction cross-section to the geometrical cross-section, which for homogeneous spheres of radius a is

$$Q_{ext} = \frac{C_{ext}}{\pi a^2} \tag{2.45}$$

Similar relationships are defined for the scattering and absorption efficiencies.

The degree of scattering in the forward direction is known as the *asymmetry factor* and is defined as

$$g = \langle \cos\theta \rangle = \frac{1}{k^2} C_{sca} \int F(\theta, \phi) \cos\theta \, d\omega \tag{2.46}$$

Considering a volume element of N independent scattering particles, the Stokes vectors of the waves scattered by the individual particles are summed over N to obtain the total Stokes vector of the scattered light. It can be shown that the above relations all hold for this situation with all the quantities being averaged over N individual particles.

2.3 The origin of astrophysical solids

In the review of PN evolution presented in Chapter 1 of this thesis, it was stated that an important component in the mass loss mechanism from red giant and AGB stars is the astrophysical solid material which is processed in the circumstellar environment of the evolving AGB star. It is generally believed that the dust grains which compose a significant element of the interstellar medium (ISM) and the dust grains which inhabit the outer atmospheres of AGB stars have a very similar chemical composition. This leads to the distinct probability that there exists some fundamental link between the two grain species. Estimates of the numbers of carbon stars and their mass-loss rates, for example, indicate that these stars may inject up to $0.03\,M_\odot\,yr^{-1}$ of carbonaceous material into the galactic ISM and may dominate the carbon stardust budget (Gehrz, 1989). Indeed, mass-losing late-type carbon stars are understood to be responsible for some 50% of the total solid matter returned into the general ISM (Jura, 1986).

Asymptotic Giant Branch stars are cool, luminous stars, with effective surface temperatures typically between 2000 and 3000 K, luminosities of the order of $10^4\,L_\odot$ and radii up to about $10^3\,R_\odot$. Their spectral classification depends upon the composition of the stars' photosphere. Oxygen-rich CSEs ([C]/[O] < 1 by number) are associated with M giants, C-rich envelopes ([C]/[O] > 1) mainly exist around carbon, or C, stars, with S stars positioned somewhere in between the two. Naturally in the circumstellar environments of carbon stars, carbon atoms and compounds are readily available to form dust grains of carbonaceous material. Oxygen-rich stars, however, have available molecules such as magnesium oxide (MgO), silicon oxide (SiO) and water (H_2O) to form silicate grains.

It is widely believed that the M-S-C spectral classification of AGB stars portrays an evolutionary sequence, with the stars outer atmosphere progressively becoming enriched with carbonaceous material. The stellar pulsation and mixing processes, or "dredge ups"(see §1.2.2), lead to the carbon-rich matter from the stars core being deposited in the outer envelope.

The transition from an O-rich to a C-rich envelope is controlled by the extent of the third dredge-up, and it can occur only for AGB stars in a narrow mass range. Indeed, stars with core masses lower than $\sim 0.6\,M_\odot$ (Straniero *et al.*, 1995) will not undergo the third dredge-up, while hydrogen burning at the base of the convective envelope (so-called *hot bottom burning*) is expected to deplete carbon in the envelope of stars more massive than about $5\,M_\odot$ (Wood *et al.*, 1983; Boothroyd *et al.*, 1993), preventing them from becoming C-rich. Despite the low dust-to-gas mass ratio (in the range $\sim 0.001 - 0.01$), the optical properties of AGB CSEs are mainly determined by the dust grains; silicates in O-rich envelopes (Pégourié & Papoular, 1985) and a mixture of hydrogenated amorphous carbon (Jones *et al.*, 1990; Duley, 1993) with inclusions of SiC (Skinner & Whitmore, 1988) and possibly polycyclic aromatic hydrocarbons (PAH's) (Puget & Léger, 1989; Cherchneff & Barker, 1992) in C-rich CSEs. Table 2.1 (adapted from Gehrz 1989) reviews the current understanding concerning the chemical composition of stellar outflows, and Table 2.2 (again from Gehrz 1989) lists the contributions to the ISM of the relevant stellar populations. Both oxidic and carbonaceous dust is characterized by vibrational bands positioned in the mid-IR window (at 9.7 and $18\,\mu$m for silicates, at $11.3\,\mu$m for SiC and at $3.3, 6.2, 7.7, 8.6$ and $11.3\,\mu$m for PAHs). Furthermore, most of the continuous thermal radiation from the dusty optically opaque envelope is emitted in the same wavelength range. Although it has been reported that hydrocarbons may produce anomalous IR emission from some carbon stars, there is currently only sparse evidence that hydrocarbon grains are an abundant constituent of the dust in stellar outflows. Upper limits on the PAH content of carbon returned to the ISM by carbon stars have been set around $\lesssim 10\%$ (Greenberg *et al.*, 1993). If this is indeed the case, then the production of hydrocarbon grains or mantles on dust may be mainly an ISM process. Generally, it appears that circumstellar hydrocarbon emission is seen only in sources with high excitation nebular conditions.

Both the ISM and AGB solid materials are similarly composed mainly of refractory elements, but it is improbable that the two populations are exactly identical in nature as some of the gas-phase depletion of refractory elements onto interstellar particles occurs within the ISM itself. The supposition that the two grain species will be markedly

different is given added weight through the observed spectral differences (e.g., Papoular & Pégourié, 1983) besides good theoretical and observational evidence for some progressive evolution of interstellar dust grains (e.g., Mckee *et al.*, 1987). Although there are some highly developed models describing the size distribution of interstellar grains (e.g., Mathis, Rumpl & Nordsieck, 1977; Kim *et al.*, 1994), much less is known concerning the size distribution of the dusty material which is formed in the circumstellar environment despite a number of theoretical proposals (e.g., Dominik *et al.*, 1993; Egan & Leung, 1995).

Table 2.1: Types of dust grains in stellar outflows

Stellar Type	Input to ISM dust relative to all stars	Gas/dust ratio (by mass)	Silicate	Carbon	SiC	PAHs
M stars (Miras)[a]	35%	100-300	Yes	No	No	No
M Supergiants[a]	4%	100-300	Yes	No	No	No
OH/IR stars[b]	32%	100-300	Yes	No	No	No
Carbon stars[b]	20%	100	No	Yes	Yes[c]	?
Supernovae[d]	8%	50-100?	?	?	?	?
Planetary Nebulae	0.2%	3000	Yes	Yes	Yes	Yes

[a]Silicates in O-rich stars contain a "dirty" component (Draine & Lee, 1984)
[b]Near-IR absorption features due to ices are sometimes seen
[c]Trace amounts only
[d]Can contribute significant amounts of gas-phase condensibles into the ISM

Table 2.2: Dust production in the Galaxy

Stellar Type	Total Number	Gas to Dust ratio	$< dM/dt >$ $M_\odot\, yr^{-1}$	$(dM/dt)_{dust}$ $M_\odot\, yr^{-1}$
M stars (Miras)	9×10^6	100-300	1.3-2.8	0.004-0.028
M Supergiants	5211	100-300	0.05-0.5	$1.7 - 50 \times 10^{-4}$
OH/IR stars	5.9×10^4	100-300	1.0-3.0	0.003-0.03
Carbon stars	$3 - 6 \times 10^4$	100-200	0.34-0.96	0.003-0.01
Supernovae	1/(30-50) yrs	50-100	0.1-0.3	0.001-0.006
Planetary Nebulae	3.8×10^4	3000	0.05-0.5	$1.7 - 17 \times 10^{-5}$

The notion that dust grains would form in the atmospheres of cool giant stars appears to be due to O'Keefe (1939) and conjectured as a result of the well-known sporadic variability in the observed magnitude of R Coronae Borealis. The formation of small graphite grains of around 0.1 μm diameter is believed to take place as the partial pressure of carbon exceeds the vapour pressure of graphite in the receding and cooling gas. Classical grain nucleation theory shows that the supersaturation ratio[1] would need to be only about 2.2 for graphite grains to form (Donn *et al.*, 1968). Gilman (1969) proposed that aluminium and magnesium silicates would form in oxygen-rich atmospheres, while carbon with quantities of silicon carbide would be found to condense in carbon-rich stars.

The mechanism by which the mass loss is driven is believed to be the accelerating action of radiation pressure on the dust grains which in turn drag the gas outward (Gehrz & Woolf, 1971; Gilman, 1972; Kwok, 1975). Mass loss rates of the order of 10^{-7} to $10^{-4}\,M_{\odot}$ per year can be expected to occur by this process.

In recent years it has become clear that the interstellar grain size distribution extends to much smaller sizes than were previously believed to exist in the ISM environment. Polycyclic Aromatic Hydrocarbons particularly, containing as few as 20 carbon atoms, are now considered to be very abundant in the general ISM and consequently ought to be considered an important factor in dust formation around carbon stars (e.g., Omont, 1986; Tielens, 1993). However, as mentioned above, the verdict in favour of hydrocarbon abundance in circumstellar environments awaits the availability of more convincing data.

3.4 μm and 12 μm absorption band data for the PPN CRL 618 (Lequeux & Jourdain de Muizon, 1990) display features which are attributable to the C-H stretching vibrational mode in hydrogenated carbon compounds. This band has not been seen previously in a circumstellar (carbonaceous) envelope, indicating that the corresponding material is formed in such envelopes. The ratio of band depth to extinction is smaller in CRL 618 than in the ISM generally, perhaps due to a smaller degree of hydrogenation of the material. The absorption band at 12 μm has been identified as due to silicon carbide (SiC). The SiC/amorphous carbon grain ratio in CRL 618 is found to be similar to that seen in the archetypal carbon star IRC +10216. In addition, the apparent lack of PAHs in CRL 618 compared to more evolved objects suggests that PAHs are formed from amorphous carbon grains rather than the reverse.

[1] The supersaturation ratio is that of the partial pressure in the receding gas to the vapour pressure of, in this case, graphite

Theoretical models of mass-losing stars, such as IRC +10216 (Jura, 1994), suggest dust grain diameters (for amorphous carbon spheres in this case) near 0.1 μm, and also that the size distribution of particles formed in an outflow from a star consist mostly of small grains, following a power law with exponential cut off (see §2.2.7). The scattering and polarizing properties of circumstellar grains allow for a sensitive and discriminating method for evaluating their sizes and optical properties (see §2.4). Previous studies of sizes of particles around a variety of mass-losing red giants have focussed mainly upon oxygen-rich rather than carbon-rich stars, indicating sizes less than 1 μm. Around α Orionis, for example, the maximum grain size is believed to be of the order of 0.12 μm (Mauron & Le Borgne, 1986). Seab & Snow (1989) argue for a minimum grain radius of 0.08 μm in the ejecta of α Scorpii, but Papoular & Pégourié (1983) find that grain sizes up to 4 μm may be required to model the 9.7 μm feature seen in the spectra of a number of mass-losing oxygen-rich red giant stars.

Ice mantles can, and do, accumulate on dust grain surfaces under suitable conditions. One of the possible environments where this may occur is the cool, oxygen-rich atmosphere of an evolved star whose optically thick dust shell is associated with an OH maser source. Whereas interstellar ices will form in a situation where both O and C are generally available as monomers in the gas, the shells of OH/IR stars do not contain free carbon, as C is almost entirely locked up in gas phase CO. The circumstellar gas is too warm for CO itself to condense, and any solid materials which do form are therefore expected to be deficient in carbon.

2.4 Dust in planetary nebulae

The fact that dust comprises a major component of many PNs is implied by several factors. Firstly, there is an observed depletion of condensable elements. Secondly, the nebulae display internal extinction and thirdly, the detection of IR emission. Indeed, a significant fraction of the total luminosity of the PN emerges in the IR through thermal emission.

The discovery of strong 10 μm emission from NGC 7027 (Gillett *et al.*, 1967), at levels which were significantly greater than what was expected of free-free and line fluxes at the time, provoked no small amount of controversy over the nature of infrared excesses in PNs. The infrared continuum from NGC 7027 was interpreted as being emission from

small graphite particles heated in the nebula by resonantly trapped Lyman-α photons generated in the ionized nebular gas, and originating in the envelope of the progenitor red-giant star (Krishna Swamy & O'Dell, 1968; Cohen & Barlow, 1974; Moseley, 1980). Until 1983 only some of the brightest PNs had been observed in the near IR and 10 μm windows, and very few in the FIR.

The *Infrared Astronomical Satellite* (IRAS) mission data provided a wealth of valuable new information on the nature of dust in PNs, and it is now widely accepted that dust grains are indeed responsible for infrared emission from PNs, although the details of the chemical composition and the spatial distribution of the dust remain somewhat unclear.

There are many PNs now known to display continuum emission in the FIR, in excess of the expected nebular continuum emission, due to dust heated to about 100 – 150 K. The nebular flux usually peaks in the range 25 to 60 μm. It is possible to calculate the flux expected if all the Lyman-α photons produced by recombinations in the nebula heat the dust, using the observed radio continuum emission to estimate the number of recombinations. The expected IR flux is then compared with the total observed flux and an IR excess is defined as the ratio of observed total IR emission to the energy available in Lyman-α photons. The IR excess is related to properties of the planetary nebula (PN) and Lyman-α heating is able to explain the amount of observed IR radiation, in particular that seen in large, old PNs. Values of IR flux slightly larger than expected could be explained by absorption of other strong nebular lines, such as the C[IV] UV doublet. High values of IR excess (> 10) are found in compact, probably very young, PNs. In this case, heating by direct starlight is the most plausible cause of dust heating.

Significant problems remain in understanding the grain component of PNs. The number of PNs observed to possess the silicate feature is small. On the other hand, thousands of AGB stars have been observed to have this feature (Volk & Kwok, 1987). It has been proposed that a majority of PNs evolve from carbon-rich progenitors (Zuckerman & Aller, 1986), but if this is correct, then it is far from clear what the large number of oxygen-rich AGB stars will evolve to.

Zhang & Kwok (1990) studied the 18 μm silicate dust feature in 11 young PNs, concluding that oxygen-rich PNs were more common than previously believed. The silicate dust probably originates from the circumstellar envelope remnant of the AGB progenitor.

It was also found that a significant number of PNs displayed both oxygen and carbon-rich dust features. It might be possible that an oxygen-rich progenitor star will be classified as carbon-rich as the silicate feature is diminished and UV-excited PAH bands become more prominent as the PN evolves.

However, the question remains as to how the dust is distributed within the nebula. The dust could be mixed homogeneously with the ionized gas or in neutral inclusions, or perhaps concentrated in a disk around the central star. The effects of dust on the visible and UV emission from PNs can be seen in the absorption and scattering of light. In most PNs this effect is small and it becomes difficult to measure with sufficient accuracy to put useful constraints on the nature of the dust grains responsible. It is seen later in this work, however, that optical polarimetry provides a sensitive means of investigating these dusty environments.

Leroy *et al.* (1986) discovered polarization levels of up to 1% in the O[III] spectral emission lines in a number of PNs. This was attributed to scattering from dust particles. In order to account for observations of UV resonance lines, there must be some dust in the ionized regions. The precursors of PNs are known to be the AGB stars, typically cool stars immersed in thick circumstellar envelopes produced by heavy mass loss. Condensation theory predicts that these stars condense copious amounts of dust in their CSE and this is indeed what is observed. Different species of grains are produced according to the details of the stellar outflow and depending upon the chemical abundances of the circumstellar material. It is expected that the grains reflect the conditions present in the precursor wind, though the ionizing flux from the PN will affect the grains, which may in turn influence the development of the ionized nebula. Elements such as Fe, Mg and Si are underabundant in the gas phase compared to the expected values (Shields, 1983) and it is just these type of materials which are expected to condense out as refractory grains in PNs. The depletions of other species, notably C and O, whose total abundances in the PN may be altered by nuclear processing, are much less certain. It is clear that carbon is not depleted by the factors $10 - 20$ that are found for iron, but some depletion must occur, and in C-rich objects some form of carbon may well account for most of the dust. The $10\,\mu$m emission from NGC 7027 observed by (Gillett *et al.*, 1967) has been confirmed many times and the photometric surveys of Cohen & Barlow (1974, 1980), for example, have shown that many PNs display strong IR emission from dust. Near-IR photometry (1-4 μm) has been obtained by several groups (e.g. Whitelock, 1985; Aspin *et al.*, 1993)

pinpointing those PNs which contain hot dust with colour temperatures up to 1000 K. Mid-IR spectra have been collected in ground-based observations (e.g., Aitken & Roche, 1982; Roche & Aitken, 1986; Slijkhuis *et al.*, 1991) or utilizing data obtained with the Low Resolution Spectrometer on the *IRAS* satellite (e.g. Garcia Lario *et al.*, 1991).

Measurement of spectral features due to dust grains can, in principle, identify the species producing the emission features and permit investigation of the chemistry of the nebular ejecta. Principally through spectroscopy near to 10 μm, it has been established that IR spectral signatures, and therefore the composition of the dust grains, vary from PN to PN. Broad features at 9.7 μm and 11.2 μm were first seen in the spectra of CSE around late-type O-rich and C-rich stars, and later identified as emission from silicate and silicon carbide grains respectively (Treffers & Cohen, 1974).

It is likely then that dust seen in PNs could also be designated as having formed in O-rich or C-rich environments where the silicate or silicon carbide signatures were detected. This has been verified by abundance determinations made by careful modelling of optical and UV emission lines. All objects which show strong silicate emission bands, that have been modelled, have been found to have a C/O ratio < 1; conversely those PNs with silicon carbide emission proved to have C/O > 1 (Seaton, 1983). The emission lines between 3 and 13 μm appear likely to be produced by the excitation of small (0.001 μm) C-rich grains, possibly the PAHs proposed by Duley & Williams (1981) and Leger & Puget (1984).

Through the identification of these spectral features then, it is possible to classify the dust in PNs as O-rich, C-rich or very C-rich. The excellent agreement between the gas-phase C/O ratios and those predicted from 10 μm spectra clearly indicate that the basic view of PN dust is correct. Although the 10 μm spectral observations yield much information about the warm (300 K) dust in PNs, most of the dust is at considerably lower temperatures, and has not been studied in as great a detail. Spectra beyond 20 μm are available for some objects (Forrest *et al.*, 1981). A strong broad emission feature peaking near 30 μm can be seen which has also been observed in several carbon stars and has been attributed to the presence of MgS (Goebel & Moseley, 1985), possibly as a mantle on grains of some other composition.

The precise location and distribution of dust within PNs remains somewhat uncertain. It would help to know this with greater precision as it will yield information on whether dust plays a significant role in softening the radiation field in the ionized region by selective absorption of high energy photons, whether emission from dust grains is important as a coolant of the ionized gas and whether the mass of dust calculated from the IR emission can be compared with the mass of ionized gas in order to derive the dust to gas ratio. The absorption of trapped UV resonance lines gives the idea that some dust at least is mixed in with the ionized gas but it is possible that these are the warm grains emitting at wavelengths below 20 μm rather than the bulk of the dust emitting in the FIR. Data generally shows that the extent of the dust emitting region is similar, but not necessarily identical, to that of the ionized region. Studies of NGC 7027 have shown that grains emitting the 11.3 μm feature lie outside the ionized zone and are probably contained in a neutral shell, so that the grains responsible for the narrow emission bands are destroyed in the ionized zone. The dust in PNs is likely to vary in both composition and mean grain size between the ionized and neutral regions. In some objects, disk-like structures are evident where there is a substantial amount of dust girdling the central star. In others, the dust seems to be well mixed with the ionized gas, but it appears certain that the emission from some grain species is seen only from neutral shells.

Dust which is warmer than about 30 K will have been seen by IRAS, but it is possible that there could be a substantial amount of dust outside the ionized regions which may be cooler than this. Dust at 10 K emits very weakly in the FIR but strongly in the submillimetre spectral region (300 μm to 2 mm).

2.5 The scattering properties of dust grains

An extremely sensitive diagnostic tool for the analysis of the sizes and distribution of dust grains in whatever environment, is their optical scattering and polarization properties. The characteristics and degree of both scattering and polarization by dust grains are very sensitive to the grain size, geometrical distribution and optical constants of the scattering dusty medium.

The Mie scattering functions described in section 2.2.3 allow the scattering and absorbing properties of single spherical dust grains to be computed. In astrophysical situations, such as are relevant to the present work, it is more usual to consider a collection of many

dust grains, distributed over a range of sizes, within a given volume. The scattered light from such a cloud of particles possesses a total Stokes vector equal to the sum of the individual Stokes vectors scattered from each particle. This is calculated by performing an integration of the scattering functions for a single particle over the range of particle sizes which are present in the cloud.

2.5.1 The size distribution of grains

The extinction curve for starlight passing through interstellar material is found to be inconsistent with attenuation by dust grains of a single uniform size, and it is clear that there exists a distribution of grain sizes which is responsible for the observed reddening. It is usual to describe the grain size distribution by a function of the grain radius $n(a)$, such that the probability of a grain possessing a radius between a and $a+\mathrm{d}a$ is $n(a)\mathrm{d}a$ and normalized to

$$\int_0^\infty n(a)\,\mathrm{d}a = 1$$

It is then possible to determine cross sections and scattering functions for an imaginary "average" grain by integrating the product of the grain size distribution function and the required scattering function over the amount of light scattered by spheres of each size (Warren-Smith, 1979).

The usual problem is the choice of a physically realistic form of the function $n(a)$ for any particular situation. Observations of the interstellar extinction curve at visual wavelengths have often led to the use of a power-law size distribution in subsequent models (Mathis *et al.*, 1977; Draine & Lee, 1984)

$$n(a) \propto a^{-\gamma}$$

where γ is the *power-law index*. The value of γ can be adjusted and controls the relative weighting of small particles in the distribution.

For models of the ISM, γ often takes the value of ~ 3.5. In modelling other situations, γ has often been allowed to take higher values; $\sim 4.0 - 4.5$ in regions associated with star formation or in pre-main sequence nebulae (Warren-Smith, 1979; Shirt, 1984; Ageorges *et al.*, 1996), $\sim 5.0 - 5.5$ for PPNs (Scarrott *et al.*, 1990; Scarrott & Scarrott, 1994).

For core-mantle grains, the distribution is less straightforward and may be applied to

- a varying core radius with a constant, uniform mantle thickness
- a constant (small) core radius with a varying mantle thickness
- a varying core radius with a mantle thickness which is a constant fractional volume of the total grain size

The case in favour of the power-law size distribution is very strong on both observational and theoretical grounds (Biermann & Harwit, 1979; Mathis, 1989).

An alternative to the pure power-law distribution is a power-law with added exponential decay (Kim *et al.*, 1994; Jura, 1996)

$$n(a) \propto a^{-\gamma} \exp\left(-a/a_o\right)$$

with a_o as a cut-off size to the distribution, beyond which the number of particles of size a falls off very rapidly.

A different form of size distribution is occasionally used and is based upon the theory of grain growth and destruction. It is often applied in order to increase the relative number of larger particles within the distribution, and is described by

$$n(a) \propto \exp\left[-5\left(\frac{a - a_c}{a_o}\right)^q\right]$$

for core-mantle grains, where a, a_c, and a_o are the total radius of the core-mantle grain, the radius of the core and the cut-off size of the distribution respectively.

q is adjusted to weight the relative numbers of small and large grains and usually takes the values of 2 (Gaussian) or 3. The function actually describes a distribution of the mantle thickness for a constant core radius. For homogeneous grains, the function simply becomes

$$n(a) \propto \exp\left[-5\left(\frac{a}{a_o}\right)^q\right]$$

2.5.2 An investigation into polarization by scattering from grains

In this section, I investigate the scattering and polarization properties of dust grains comprised of those materials which are considered to be abundant in PNs. This exercise was carried out in order to gain a deeper understanding of the optical behaviour of the grain materials with the intention of providing a means to explain some of the features of the polarization observed in the PNs under study. I have not attempted to investigate every detail of the parameter space, merely to determine the effects on scattering and polarization that results from varying certain parameters. Fortran computer routines have been developed, based upon inherited code written by former members of the Durham Polarimetry Group, to evaluate the Mie scattering functions for both homogeneous and core-mantle, spherical dust grains (Warren-Smith 1979; see also Bohren & Huffman 1983). A number of modifications were made to improve some aspects of the numerical stability and utilize algorithms given by de Rooij & van der Stap (1984), which promote the use of both upward and downward recursion in the calculation of the functions $\chi_n(x)$, $\psi_n(x)$ and $D_n(z)$ as defined in Equations 2.31, 2.33 and 2.34 of section 2.2.3. The use of upward recurrence in the calculation of $\psi_n(x)$ can lead to numerical instability when the number of summed terms in the series expansions exceeds the value of the size parameter x. The paper of de Rooij & van der Stap (1984) was corrected for two mistakes in the recurrence relations and initial conditions given by them.

The computer routines evaluate the complex Mie scattering amplitude functions $S_1(\theta)$ and $S_2(\theta)$ for specific size distributions of spherical grains (either homogeneous or core-mantle) over the scattering angle (θ). This permits the degree of polarization (which is always *linear* for single scattering of unpolarized incident light) and total phase function, or scattered intensities, to be calculated, as well as the cross-sections of scattering, extinction, absorption, etc., according to the expressions outlined in section 2.2.3.

2.5.2.1 Dust grain composition

Table 2.3 lists the dust grain materials investigated and their adopted optical properties. At each of the four wavelengths, values for the real (n) and imaginary (k) parts of the grain refractive index (m), where m=n−*i*k, are shown. These particular materials were chosen on the basis of that they are all good candidates for a possible presence in the cool and dusty circumstellar environments of mass-losing AGB stars. There is very good observational evidence that each of these grain materials can be regarded as a possible inhabitant of PNs and PPNs, as well as AGB envelopes. It was decided not to attempt the calculations with PAH as a grain material, for two reasons. Firstly, it appears that hydrocarbons are only excited at UV wavelengths, a region of the spectrum which is beyond the scope of this work. Secondly, accurate and established optical data for hydrocarbons is still found wanting. Graphite is another material often used in investigations of this nature. However, in the objects under scrutiny here, the spectral signature of graphite is rarely, if ever, observed. Pure water ice was included in the calculations as there is strong evidence in favour of its presence in a number of objects (see, for example, the references given in Chapter 5 concerning the 'Frosty Leo' nebula). However, pure ice was only used as a coating material for the other grains, following Draine (1985).

The optical constants for the silicates were taken from Ossenkopf, Henning & Mathis (1992).[2] The amorphous carbon and "dirty" ice (containing 10% amorphous carbon) data was taken from Preibisch *et al.* (1993). For silicon carbide, I use the values given in Pégourié (1988).

Table 2.3: Optical Data for Grain Materials

	Wavelength (μm)/Refractive index							
	0.440		0.515		0.630		0.800	
Grain material	n	k	n	k	n	k	n	k
Oxygen-rich silicate	1.7985	0.0828	1.8158	0.0699	1.8270	0.0590	1.8270	0.0434
Oxygen-deficient silicate	1.8275	0.0919	1.8413	0.0751	1.8460	0.0636	1.8500	0.0573
Amorphous carbon	1.8789	0.7743	2.0376	0.7985	2.1960	0.8005	2.3179	0.7734
Silicon carbide	2.6170	0.1010	2.5800	0.1084	2.6030	0.1040	2.4960	0.1250
Water Ice[a]	1.3300	0.0000	1.3300	0.0000	1.3300	0.0000	1.3300	0.0000
Dirty Ice[b]	1.3876	0.0652	1.3960	0.0621	1.4037	0.0593	1.4197	0.0534

[a]imaginary part of refractive index (k) $\simeq 10^{-8}$ at visual wavelengths
[b]contains 10% amorphous carbon

[2]See also http://www.astro.uni-jena.de/Users/ossk/tables.html

2.5.2.2 Dust model

In the light of the discussion in §2.3, it is reasonable to assume that the dust which inhabits the circumstellar environment of late-type stars and PNs is characterized by a grain size distribution made up of several different components, which may be similar in form to, and in some way related to, those distributions known to exist in the general ISM.

I consider three variants of size distribution, all of which have been invoked on numerous occasions by many authors. Table 2.4 gives details on each of the size distributions used in the scattering calculations, with reference to section 2.5.1.

Table 2.4: Details of the size distributions used in Mie scattering calculations

Distribution	Parameter values	Comments
$n(a) \propto a^{-\gamma}$	$3.5 \leqslant \gamma \leqslant 6.0$	power law index
	$a_{min} \leqslant a \leqslant a_{max}$	
	$0.005\,\mu\text{m} \leqslant a_{min} \leqslant 0.500\,\mu\text{m}$	minimum grain core size
	$0.250\,\mu\text{m} \leqslant a_{max} \leqslant 1.000\,\mu\text{m}$	maximum grain core size
	$0.005\,\mu\text{m} \leqslant dm \leqslant 0.500\,\mu\text{m}$	mantle thickness
normal power law varying core size with a fixed mantle thickness		
$n(a) \propto a^{-\gamma}$	$3.5 \leqslant \gamma \leqslant 6.0$	power law index
	$0.005\,\mu\text{m} \leqslant a_{core} \leqslant 0.100\,\mu\text{m}$	grain core size
	$0.005\,\mu\text{m} \leqslant dm \leqslant 1.000\,\mu\text{m}$	mantle thickness
power law varying mantle thickness with a fixed core size		
$n(a) \propto \exp\left[-5\left(\frac{a-a_c}{a_o}\right)^q\right]$	$q = 2$ and $q = 3$	exponential power
	$a_{core} = 0.100\,\mu\text{m}$	fixed core size
	$0.005\,\mu\text{m} \leqslant dm \leqslant 0.900\,\mu\text{m}$	mantle thickness
	$a_{max} = 1.000\,\mu\text{m}$	maximum grain cut-off size
exponential function varying mantle thickness with a fixed core size		

2.5.2.3 The properties of uncoated grains

A selection of the results of the Mie scattering calculations for 'bare' uncoated grains are presented in Chapter 7. Figures 7.1 through 7.23 and display curves of polarization and, in some cases scattered intensity, for grains composed of the different materials and size distributions detailed in Table 2.3 and Table 2.4.

The effects of varying the free parameters are summarized in Tables 2.5 and 2.6.

Table 2.5: Polarization as a function of the power law index (γ) for 'bare' grains

	$\gamma = 3.5$		$\gamma = 4.0$		$\gamma = 4.5$	
Material	P_{max} (%)	$\theta_{P_{max}}$ (°)	P_{max} (%)	$\theta_{P_{max}}$ (°)	P_{max} (%)	$\theta_{P_{max}}$ (°)
Oxygen-rich silicate	12	88	23	95	37	98
Oxygen-deficient silicate	12	87	23	95	36	98
Amorphous carbon	56	90	63	93	71	94
Silicon carbide	8	76	14	106	23	108
Dirty Ice	50	101	63	100	75	99
	$\gamma = 5.0$		$\gamma = 5.5$		$\gamma = 6.0$	
Material	P_{max} (%)	$\theta_{P_{max}}$ (°)	P_{max} (%)	$\theta_{P_{max}}$ (°)	P_{max} (%)	$\theta_{P_{max}}$ (°)
Oxygen-rich silicate	51	99	64	99	76	97
Oxygen-deficient silicate	50	99	63	99	75	97
Amorphous carbon	78	94	85	94	90	93
Silicon carbide	34	105	45	103	58	102
Dirty Ice	84	97	90	95	95	94

$n(a) = n_o a^{-\gamma}$; $a_{min} = 0.005\,\mu$m $a_{max} = 1.000\,\mu$m ; $\lambda = 0.515\,\mu$m

Table 2.6: Wavelength dependence of polarization for 'bare' grains

	$\lambda = 0.440\,\mu$m		$\lambda = 0.515\,\mu$m		$\lambda = 0.630\,\mu$m		$\lambda = 0.800\,\mu$m	
Material	P_{max} (%)	$\theta_{P_{max}}$ (°)	P_{max} (%)	$\theta_{P_{max}}$ (°)	P_{max} (%)	$\theta_{P_{max}}$ (°)	P_{max} (%)	$\theta_{P_{max}}$ (°)
Oxygen-rich silicate	41	99	37	98	34	98	31	97
Amorphous carbon	74	93	70	94	67	95	64	96
Silicon carbide	21	108	23	107	22	106	25	107
Dirty Ice	74	99	73	99	72	99	69	99

$n(a) = n_o a^{-\gamma}$; $a_{min} = 0.005\,\mu$m $a_{max} = 1.000\,\mu$m ; $\gamma = 4.5$

2.5.2.4 Comments

The scattering properties of the two forms of pure silicates, oxygen-rich and oxygen-deficient, appear to be almost identical. This is not entirely unexpected as their optical properties given in Table 2.3 are naturally very similar. For this reason, only one of the silicate forms (oxygen-rich) was used in the subsequent studies of the scattering from core-mantle grains. Table 2.5 and Figures 7.1 and 7.2 in Chapter 7 show the levels of polarization as a function of scattering angle. Maximum polarization occurs at angles close to and greater than 90 degrees and the level increases with increasing values of γ. As γ is increased then the polarization becomes more Rayleigh-like as the relative numbers of small particles increases within the distribution. In a standard power law size distribution there is no specific mean grain size. However, an effective grain size (a_o) may be calculated from the product of the total scattering cross section, $s(a)$, and the size distribution, $n(a)$. Figure 7.3 shows the results of such a calculation for power law indices of 3.5 and 6.0 using oxygen-rich silicate grains at a wavelength of 0.515 μm over the range of core sizes $a_{min} = 0.005\,\mu$m to $a_{max} = 1.000\,\mu$m. The plotted values have been normalized to enable comparison. It can be seen that a_o is 0.14 μm and 0.06 μm for $\gamma = 3.5$ and 6.0 respectively. Therefore, as γ increases, the effective mean grain size decreases and the scattering becomes progressively more Rayleigh-like. The scattered intensity from silicate grains is shown in Figure 7.4. Note the highly asymmetric nature of the scattered intensity. This is typical of Mie scattering behaviour, in contrast to the symmetric nature of Rayleigh scattering (compare with Figure 2.1).

The optical properties of amorphous carbon are considerably different to the silicates and this is seen clearly in the nature of the polarization due to scattering from grains formed from this material. Figure 7.5 and Figure 7.6 show the polarization and scattered intensity respectively for a standard power law size distribution and a wavelength of 0.515 μm. The curves show a marked increase in the levels of polarization above the silicates for a given power law index (refer also to Table 2.5) and in addition, peak polarization occurs closer to 90 degrees and is much more symmetrical between forward and backward scattering angles. The reason for this is that the effective mean grain size (a_o) for amorphous carbon is significantly smaller than for silicate grains under the same set of circumstances. Figure 7.7 shows the results of an effective mean grain size calculation for power law indices of 3.5 and 6.0 using amorphous carbon grains at a wavelength of 0.515 μm over the range of core sizes $a_{min} = 0.005\,\mu$m to $a_{max} = 1.000\,\mu$m. a_o is found to be 0.10 μm and 0.05 μm for $\gamma = 3.5$ and 6.0 respectively. Again, the plotted values have been normalized for comparative purposes.

Silicon carbide displays, perhaps not unexpectedly, scattering characteristics which lie somewhere between those of the silicates and amorphous carbon. Table 2.5 and Figure 7.8 show that only moderate levels of polarization can be achieved, even with a high weighting of small grains. At the standard power law index of 3.5, peak polarization is low $\sim 5\%$ over almost all scattering angles. For higher values of γ, the level of maximum polarization increases accordingly and peaks consistently at scattering angles greater than 100 degrees. The effective mean grain size (a_0) is the same as amorphous carbon at low γ but is significantly higher than both amorphous carbon and the silicates at higher values of γ ($a_o = 0.08\,\mu$m for $\gamma = 6.0$). The scattered intensity from silicon carbide grains is shown in Figure 7.9.

For the 'dirty ice' grains, the effects of the small amorphous carbon component is immediately seen in the polarization curve of Figure 7.10. The curves have the almost Rayleigh-like nature of pure amorphous carbon but the peak polarization is shifted somewhat to angles greater than 90 degrees and negative polarization appears at scattering angles close to 180 degrees, in a similar manner to the silicate behaviour. Interestingly, the effective mean grain size at low γ ($a_o = 0.25\,\mu$m) is much higher than that found in the other grain materials under the same grain parameters but also becomes the smallest ($a_o = 0.005\,\mu$m) as γ is increased. The scattered intensity is shown in Figure 7.11.

The wavelength dependence of polarization for 'bare' grains is demonstrated in Table 2.6 and Figures 7.12 through 7.15. The general trend appears to be a moderate reduction in the maximum levels of polarization with increasing wavelength, except for silicon carbide grains where the trend is for increasing polarization. However, the wavelength dependence of Mie calculations is also a function of the grain size limits of the distribution, such that fitting to observed $BVRI$ polarization data would require consideration of grain size distribution limits in addition to the theoretical levels of polarization at a given wavelength. Table 2.7 shows how the wavelength dependence of the polarization for 'bare' grains is essentially reversed when the smallest grains are removed from the size distribution (compare with Table 2.6).

The effect on the character of the polarization by removing the smaller grain sizes from the distribution and moving to a large grain model, at a single wavelength, is more complex than is implied from Table 2.7. Referring to Figures 7.16 through 7.23, the scattering becomes progressively more asymmetric and variable over small changes in scattering angle as the grains are made larger.

Table 2.7: Wavelength dependence of polarization for a larger grain model using 'bare' grains

	$\lambda = 0.440\,\mu$m		$\lambda = 0.515\,\mu$m		$\lambda = 0.630\,\mu$m		$\lambda = 0.800\,\mu$m	
Material	P_{max} (%)	$\theta_{P_{max}}$ (°)	P_{max} (%)	$\theta_{P_{max}}$ (°)	P_{max} (%)	$\theta_{P_{max}}$ (°)	P_{max} (%)	$\theta_{P_{max}}$ (°)
Oxygen-rich silicate	2	47	5	65	14	86	21	93
Amorphous carbon	36	65	35	70	40	85	51	96
Silicon carbide	6	152	2	158	2	159	10	96
Dirty Ice	45	100	56	101	63	101	66	100

$n(a) = n_o a^{-\gamma}$; $a_{min} = 0.100\,\mu$m $a_{max} = 1.000\,\mu$m ; $\gamma = 4.5$

2.5.2.5 The properties of core-mantle grains

Several appropriate core-mantle combinations of materials were selected as input to the Mie scattering routines from those listed in Table 2.3 and Table 2.4. The effects of varying the free parameters are summarized in Tables 2.8, 2.9, 2.10 and 2.11.

2.5.2.6 Comments

Generally the addition of a thin mantle, regardless of the exact material of both core and mantle, increases the maximum levels of polarization that can be obtained. Figures 7.24 through 7.35 in Chapter 7 show the polarization and scattered intensity Mie scattering curves for the core-mantle combinations listed in Tables 2.8 to 2.10.

The wavelength dependence curves show a similar trend as for the 'bare' grain models. However, it is expected that the different combinations of core and mantle material will display a more complicated wavelength dependence and this is indeed reflected in the results shown in Table 2.10. Certain core-mantle combinations show increasing polarization levels with increasing wavelength, while the reverse is true for others. Again, it is important to note that the polarization level as a function of wavelength also depends upon the grain size cut-offs. Compare the results in Table 2.11 with those of Table 2.10. The curves derived from the calculations are shown in Figures 7.36 to 7.40.

The effect of increasing the mantle thickness is more complex and again depends upon the material forming both the core and mantle. In some cases, the polarization increases with increasing mantle thickness, whereas in other combinations, the polarization can be increased up to a point and then is reduced again with continued further increases in mantle thickness (see Figures 7.41 through 7.46). In all cases, a mantle thickness which exceeds some 10% of the maximum grain core size results in wildly fluctuating polarization over the range of scattering angles.

Table 2.8: Polarization as a function of the mantle thickness (dm) for core-mantle grains

	Mantle thickness					
	0.010 μm		0.050 μm		0.100 μm	
Material	P_{max} (%)	$\theta_{P_{max}}$ (°)	P_{max} (%)	$\theta_{P_{max}}$ (°)	P_{max} (%)	$\theta_{P_{max}}$ (°)
O-rich silicate core Water Ice mantle	51	98	98	91	100	95
O-rich silicate core Amorphous carbon mantle	71	97	98	93	64	94
Amorphous carbon core Water Ice mantle	78	95	99	91	100	95
Amorphous carbon core Silicon carbide mantle	83	97	97	98	9	66
Silicon carbide core Water Ice mantle	35	105	96	92	100	95
Silicon carbide core Amorphous carbon mantle	56	100	98	93	61	94
$n(a) = n_o a^{-\gamma}$; $a_{min} = 0.005\,\mu$m $a_{max} = 1.000\,\mu$m ; $\lambda = 0.515\,\mu$m ; $\gamma = 4.5$						

Table 2.9: Polarization as a function of the power law index (γ) for core-mantle grains

	$\gamma = 3.5$		$\gamma = 4.0$		$\gamma = 4.5$	
Material	P_{max} (%)	$\theta_{P_{max}}$ (°)	P_{max} (%)	$\theta_{P_{max}}$ (°)	P_{max} (%)	$\theta_{P_{max}}$ (°)
O-rich silicate core Water Ice mantle	20	92	34	96	51	98
O-rich silicate core Amorphous carbon mantle	33	97	52	98	71	97
Amorphous carbon core Water Ice mantle	60	91	68	93	77	94
Amorphous carbon core Silicon carbide mantle	63	99	74	99	84	97
Silicon carbide core Water Ice mantle	14	90	23	107	35	105
Silicon carbide core Amorphous carbon mantle	29	100	38	102	59	99
	$\gamma = 5.0$		$\gamma = 5.5$		$\gamma = 6.0$	
Material	P_{max} (%)	$\theta_{P_{max}}$ (°)	P_{max} (%)	$\theta_{P_{max}}$ (°)	P_{max} (%)	$\theta_{P_{max}}$ (°)
O-rich silicate core Water Ice mantle	68	97	83	95	94	92
O-rich silicate core Amorphous carbon mantle	87	94	96	94	99	91
Amorphous carbon core Water Ice mantle	85	93	91	92	96	91
Amorphous carbon core Silicon carbide mantle	92	95	97	93	99	91
Silicon carbide core Water Ice mantle	49	103	65	99	81	95
Silicon carbide core Amorphous carbon mantle	75	96	87	94	97	92

$n(a) = n_o a^{-\gamma}$; $a_{min} = 0.005\,\mu$m $a_{max} = 1.000\,\mu$m ; $\lambda = 0.515\,\mu$m ; mantle thickness = $0.01\,\mu$m

Table 2.10: Polarization as a function of the wavelength for core-mantle grains

	$\lambda = 0.440\,\mu$m		$\lambda = 0.515\,\mu$m		$\lambda = 0.630\,\mu$m		$\lambda = 0.800\,\mu$m	
Material	P_{max} (%)	$\theta_{P_{max}}$ (°)	P_{max} (%)	$\theta_{P_{max}}$ (°)	P_{max} (%)	$\theta_{P_{max}}$ (°)	P_{max} (%)	$\theta_{P_{max}}$ (°)
O-rich silicate core Water ice mantle	57	98	51	98	46	98	40	97
O-rich silicate core Am carbon mantle	55	99	64	98	71	97	77	96
Am carbon core Silicon carbide mantle	74	98	79	97	84	97	86	97
Silicon carbide core Water ice mantle mantle	36	95	35	95	32	95	33	96
Silicon carbide core Am carbon mantle	62	98	58	100	52	102	48	103
$n(a) = n_o a^{-\gamma}$; $a_{min} = 0.005\,\mu$m $a_{max} = 1.000\,\mu$m ; $\gamma = 4.5$; mantle thickness = 0.01 μm								

Table 2.11: Wavelength dependence of polarization for a larger grain model using core-mantle grains

	$\lambda = 0.440\,\mu$m		$\lambda = 0.515\,\mu$m		$\lambda = 0.630\,\mu$m		$\lambda = 0.800\,\mu$m	
Material	P_{max} (%)	$\theta_{P_{max}}$ (°)	P_{max} (%)	$\theta_{P_{max}}$ (°)	P_{max} (%)	$\theta_{P_{max}}$ (°)	P_{max} (%)	$\theta_{P_{max}}$ (°)
O-rich silicate core Water ice mantle	4	49	7	64	17	86	25	93
O-rich silicate core Am carbon mantle	6	48	7	58	13	83	24	97
Am carbon core Silicon carbide mantle	16	58	22	64	30	82	50	100
Silicon carbide core Water ice mantle mantle	12	149	5	155	3	154	14	123
Silicon carbide core Am carbon mantle	17	149	7	154	6	148	18	119
$n(a) = n_o a^{-\gamma}$; $a_{min} = 0.100\,\mu$m $a_{max} = 1.000\,\mu$m ; $\gamma = 4.5$; mantle thickness = 0.01 μm								

The results from using the modified second power law distribution (essentially a fixed core size with a distribution of mantle thicknesses) are shown in Figures 7.47 to 7.51. The main difference with the results of the normal power law distribution appears to be a broadening of the polarization curve with a less well defined peak and a decreasing level of polarization with increasing core radius. No further investigations were carried out with this distribution as it appeared obvious that either the levels of polarization obtained were insufficiently high to match the observed polarization in the PPNs and PNs, else the polarization was too forward scattering to be a possible candidate, or lastly, the polarization curves were too broad to enable realistic constraints to be placed upon the possible inclinations of the nebulae axes (see sections 3.4, 4.4 and 5.4).

The exponential function produced results which were also not applicable to the observational data obtained for the nebulae. Again, the polarization dependence on the scattering angle was not comparable with that seen in the PPNs and PNs in this study. However, examples of the results are to be found in Figures 7.52 through 7.54. Curves are only presented for the function power $q = 2$ as there appeared to be very little difference between the $q = 2$ and $q = 3$ results.

Chapter 3

M 1-16

M 1-16, at position RA $07^h\,37^m\,18^s.3$ Dec $-09°\,38'\,43''$ (2000.0), was discovered by Minkowski in 1946 as an emission line object and has subsequently been classified as a compact PN (Acker *et al.*, 1982). Observations at optical wavelengths and in narrow band filters show clearly that M 1-16 displays unusual high velocity multiple bipolar lobes which are characteristic of a series of episodic mass ejections. Spectroscopic and photometric observations of the object indicate that M 1-16 is a PN in formation. Schwarz (1992) refers to the object as a PPN, although many of the objects often referred to as PPNs should be more accurately defined as very young PNs. In this chapter, optical polarimetry maps of M 1-16 are presented and discussed with reference to the limited number of imaging and spectroscopic observations of this object that are available. The polarization data enables tighter constraints to be placed upon the geometry of the nebula and provides additional insight into the nature of the dust component.

3.1 Previous studies of M 1-16

M 1-16 is catalogued by Acker *et al.* (1982) as a PN with an optical diameter of 3 arcseconds. Radio continuum images of the object (Kwok, 1985; Aaquist & Kwok, 1990) also indicate a diameter of around 3 arcseconds, present a circular ring-like morphology which is considered to be typical of a classical PN and confirm it's non-stellar nature. However, recent optical, infrared and millimetre wave data suggest that M 1-16 is considerably more unusual than has been previously supposed (Schwarz, 1992; Corradi & Schwarz, 1993; Aspin *et al.*, 1993; Sahai *et al.*, 1994). Prior to this current study, no optical polarimetry data has been obtained for this PN.

Figure 3.1 shows an optical continuum V-band greyscale image of M 1-16 derived from the observational data presented later in this chapter. The orientation of the figure is north towards the top and east towards the left, with an approximate image scale of 68 arcseconds in the east-west direction by 95 arcseconds in the north-south direction. The intensity contours are spaced logarithmically at intervals of 0.8 magnitudes.

The central region of the object appears essentially featureless, although there are regions of nebulosity which can be seen extending radially towards the southeast and somewhat less prominently towards the northwest directions. In this image, the mean optical diameter of the central region is estimated to be approximately 15 arcseconds, somewhat greater than the catalogue value of 3 arcseconds listed in Acker *et al.* (1982). The presumed stellar source of M 1-16 appears to be hidden from direct viewing by circumstellar material since there is no sharply defined stellar feature within this central region.

Figure 3.2, however, shows a Hα + [NII] narrowband filter image of M 1-16 kindly provided by R. Corradi[1] and H. Schwarz[2] and published in Corradi & Schwarz (1993). This is a ten minute exposure through a filter centred on a wavelength of 657 nm and with a FWHM bandwidth of 7.2 nm. The orientation and image scale are the same as in Figure 3.1. The contour spacing in this image is also 0.8 magnitudes.

The narrowband image of Figure 3.2 reveals considerably more detail in the extended nebulosity. Three distinct and highly collimated bipolar-type emission lobes are clearly visible. The more extensive, and presumably the oldest, of the lobes (labelled as **A** in Figure 3.2) can be traced out to radial distances of some 45 arcseconds from the position of the central source in both the northwest and southeast directions. Adopting a value of 1.8 kpc as the distance to M 1-16, and a possible inclination to the line of sight of 45 degrees for the nebula axis (see the discussions of both distance and inclination later in this section), the outermost lobes appear to have attained an expansion distance of some 0.56 parsecs, or $\sim 115 \times 10^3$AU. In addition, there are two fainter, less extensive (and progressively younger) pairs of lobes, labelled as **B** and **C** respectively in Figure 3.2. Lobe **B** extends some 23 arcseconds ($\sim 59 \times 10^3$AU) southeast but no equivalent northwestern emission is seen. Lobe **C** is appreciably smaller again, extending roughly 17 arcseconds ($\sim 43 \times 10^3$AU) to the southeast and overlying the northeastern rim of lobe **B**. This third lobe has a counterpart which is also visible out to about 17 arcseconds toward the northwest.

[1] IAC Planetary Nebula Research Group, Instituto de Astrofisica de Canarias, Tenerife
[2] Astronomer in Charge, Nordic Optical Telescope

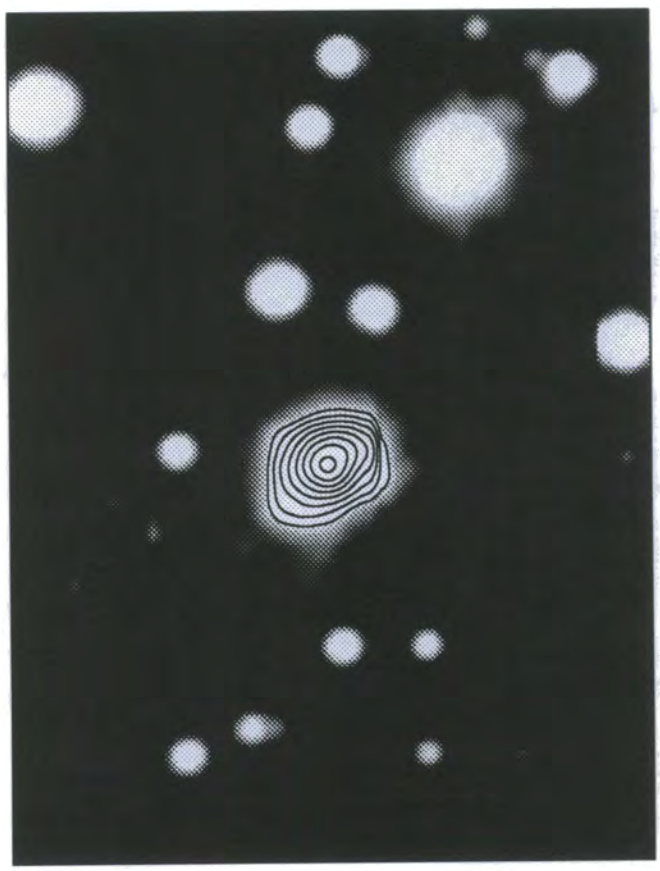

Figure 3.1: A greyscale intensity contour image of M 1-16 in the V-band

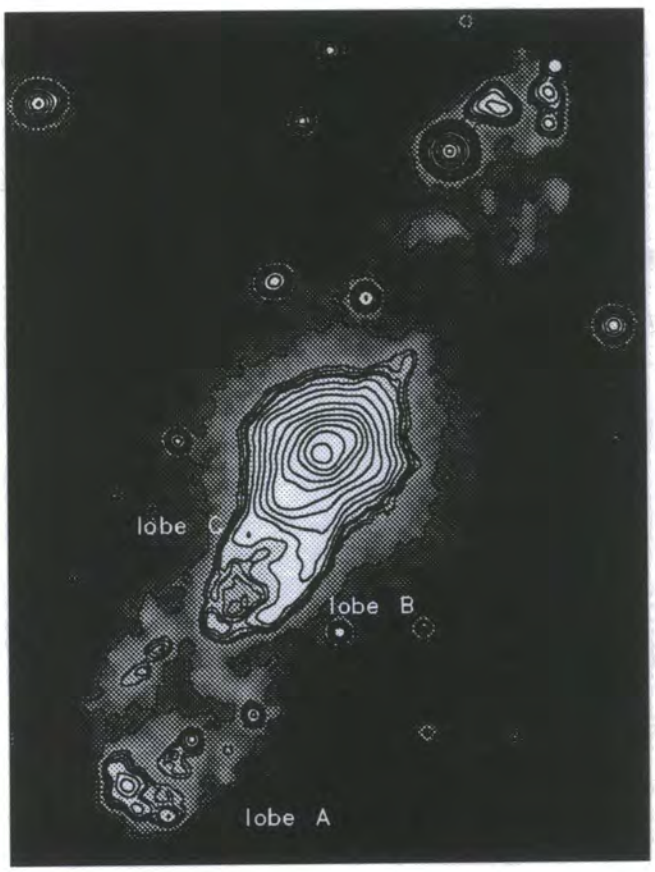

Figure 3.2: A greyscale intensity contour image of M 1-16 in Hα+N[II]

Schwarz (1992) has previously published a similar Hα image, and as a result of the detection of the three sets of lobes, argued that this was the first data which provided direct observational evidence of apparent multiple mass ejections from an evolved object. There are other PNs which are thought to have undergone similar mass ejection events, such as M 2-9 (Balick, 1989) and He 2-104 (Schwarz *et al.*, 1989), but for M 1-16 it is clearly seen that the major axis of each lobe system has a different position angle, indicating that the axis along which any mass ejection may be occurring appears to be changing its direction with time. The major axis of lobe system **A** lies at an angle[3] of 152 degrees, lobe **B** at 145 degrees and lobe **C**, 135 degrees. It is also noticeable that the inner $3-4$ intensity contours of Figure 3.2 are rotated slightly northwards with respect to what would appear to be the most recent large-scale mass ejection axis of lobe **C**, and that it is quite possible that the current mass ejection axis, if any, lies northward of lobe **C**, at a position angle around 120 degrees. The most probable mechanism by which this rotation of the ejection axis takes place is thought to be the effect of a large-scale circumstellar gas/dust disk in an interacting binary star system which is constraining the mass ejections to its precession cone (e.g. Morris, 1987; Balick & Preston, 1987).

In both of these images, the southern lobes are observed to be somewhat optically brighter than their northern counterparts. This is naturally explained by requiring that the nebula be tilted out of the plane of the sky such that the northern lobes are tilted backwards away from the line of sight. In addition, any circumstellar disk which is present would also be similarly tilted and thereby increase the levels of obscuration of the northern area of the nebula close to the inner emission region. However, the validity of this assumption has been found to be somewhat questionable in other objects (see, for example, the case of OH 231.8+4.2 Morris & Bowers, 1980; Morris *et al.*, 1982; Cohen *et al.*, 1985; Woodward *et al.*, 1989; Scarrott *et al.*, 1990), and as such, must be applied with some caution.

Long slit spectra of the outer lobes indicate that they are pure line emission features from shocked gas and not reflected continuum light from the central source (Schwarz, 1992; Corradi & Schwarz, 1993). The spectral line profiles may be interpreted as bow-shock signatures, and a comparison with model line profiles derived from bow shock models of Herbig-Haro objects (Hartigan *et al.*, 1987), adjusting the parameters of orientation angle and shock velocity, infer that the inclination angle of the bipolar lobes in M 1-16 lies within the range $20 \leq i \leq 45$ degrees, with the southern lobes inclined toward us. Surprisingly, all of the lobes remained undetected in a previous spectroscopic observation of the object by Baessgen & Grewing (1989).

[3]The position angles of the lobe axes given here are approximate values and are measured from the north increasing towards the east

The [NII] line is observed to be stronger than Hα in the lobes of M 1-16, a phenomenon which is also frequently seen in the lobes of other bipolar PNs and due in part to nitrogen overabundance in these nebulae, most of which are Type I PNs (§1.5.1). The emission of low ionization species is also enhanced by shocks (Icke *et al.*, 1989). Shock-excitation is expected to be more predominant in bipolar PNs because of the higher outflow velocities that are present. The shock velocity from the [NII] profiles is observed to be 290 kms^{-1} and from the Hα line to be 340 kms^{-1}.

Extensive millimetre-wave observations of the molecular gas in M 1-16 show that there is a molecular envelope of the object containing both a slow and a fast outflow with expansion velocities of 19 kms^{-1} and greater than 34 kms^{-1} (a lower limit) respectively (Huggins & Healey, 1989), (Schwarz, 1992) and (Sahai *et al.*, 1994). The fast outflow is collimated along an axis which has the same position angle as that of the very high velocity optically emitting gas reported by Schwarz (1992) and orthogonal to the major axis of the mildly elliptical, slowly expanding outflow. The bipolar axis of the fast outflow is also inclined with the southern lobe directed toward us, like that of the optical emission. The $^{13}CO/^{12}CO$ abundance ratio is 0.33, a very high value, possibly the largest found in an evolved object. The observed abundances of numerous molecular species in M 1-16 are generally consistent with its supposed AGB origin and reveals a largely intact circumstellar envelope. This supports the perception that M 1-16 is a very young PN. On the other hand, HCO^+/HCN and CN/HCN abundance ratios (0.9 and 8.5 respectively) are significantly greater than those found in the circumstellar envelopes of AGB stars and find more similarity with evolved planetary nebulae, such as IC 4406 and NGC 6072 (Sahai *et al.*, 1994). Enhanced abundance ratios can result from chemistry driven by shocks and photodissociation by stellar UV radiation. In AGB circumstellar envelopes the rotational lines of HCN, CN, and HCO^+ are usually excited by infrared radiation emitted by the central source. In M 1-16 this source of excitation is very weak and this results in strongly subthermal excitation. Time-dependent chemistry calculations within an interacting-winds planetary nebula model (Howe, Millar & Williams, 1992), show that most of the existing molecules in an AGB envelope (except H_2 and CO which are self-shielded against photodissociation) are destroyed in about 100 years from the time when the central source reaches an effective temperature of about 30000 K. All polyatomic species that are within the unshocked regions of the slow outflow are destroyed very quickly. In a thin, shocked region at the inner boundary of the slow outflow, a few small hydrogenated molecules and molecular ions can attain abundances of the order of 10^9 in this same time period, for a stellar luminosity of $10^3\,L_\odot$.

These abundances decline rapidly, however, with radial distance and the passage of time. It is observed that the abundances of these molecular species is much larger than what would be expected from the model of Sahai *et al.* (1994), so that some mechanism is active to protect and/or regenerate these molecules.

To explain the excitation of high-dipole moment molecules in M 1-16, Sahai *et al.* (1994) postulate that the molecular gas is distributed in small, dense clumps with H_2 densities of the order of 10^5 to 10^6. The clumpiness is thought to be an inherent factor in the mass-loss process which produced the slow outflow from M 1-16, and would result in a lower net photodissociation of the high-dipole moment molecules. The molecular envelope of M 1-16 appears to extend from radial distances of about 4.8×10^{11} km out to about 3.0×10^{12} km with corresponding expansion timescales of 850 to 5250 years, and this implies that the observed abundances of CN and HCN are probably consistent with the clumpy chemical model of Howe, Millar & Williams (1992).

There is also the suggestion of the existence of an equatorial density enhancement in the slow molecular outflow (Sahai *et al.*, 1990), and the most plausible explanation is that of an equatorial disk structure. A comparison of spectra along the NE-SW direction appears to confirm the presence of an inclined disk and the conclusion is that the slow outflow material, perhaps in the form of a disk, may act to collimate the fast outflow in the polar directions. Such a disk may arise either from the material regained from a planetary system (Sahai *et al.*, 1991) or produced by the gravitational capture of material around an unseen close companion from the precursor giant star slow wind (Morris, 1987). The mass of material in the fast outflow is estimated to be of the order of $7.5 \times 10^{-3}\,M_\odot$ and that of the slow outflow to be $0.068\,M_\odot$. The mass of the proposed disk structure is estimated to be about $6.4 \times 10^{-3}\,M_\odot$. Mass loss rate for the fast outflow is estimated to be $5.0 \times 10^{-6}\,M_\odot\,yr^{-1}$ and $2.8 \times 10^{-5}\,M_\odot\,yr^{-1}$ for the slow outflow (lower limits which are dependent on distance estimates). Very few red giant stars have mass-loss rates exceeding $10^{-4}\,M_\odot\,yr^{-1}$ and this implies that M 1-16 cannot lie much beyond 1.8 kpc in distance.

The distance to M 1-16 has been reviewed a number of times and in common with most PNs, is subject to a considerable degree of uncertainty. A reasonably comprehensive set of literature values for the distance parameter are listed for reference in Table 3.1.

Table 3.1: Distance values for M 1-16

Distance (kpc)	Source	Comment
8.40	Acker (1978)	
3.00	Amnuel *et al.* (1984)	
5.50	Maciel (1984)	see text for details
1.10	Whitelock (1985)	see text for details
16.50	Shaw & Kaler (1989)	
< 2.80	Zijlstra & Pottasch (1991)	see text for details
1.80	Schwarz (1992)	see text for details
2.40	Stanghellini *et al.* (1993)	
6.80	Zhang (1995)	see text for details

All of these distance estimates have been statistical determinations of necessity. Maciel (1984) applied the modified Shklovsky method. The accuracy of this particular method depends crucially on the value used for the optical diameter (θ) and scales as $\theta^{-3.5}$. Since the original diameter of M 1-16 was accepted as being of the order of 3 arcseconds, the derived distance of 5.5 kpc would appear to be overestimated. Whitelock (1985) finds a distance of 1.1 kpc based upon the observed reddening towards M 1-16. Schwarz (1992) applies a weighted mean diameter of 24 arcseconds to take into account the new observations of the inner and outer emission lobes, deriving a distance estimate of 1.6 kpc. Alternatively, assuming that M 1-16 lies at the nominal scale height accepted for PNs, about 140 pc, then the Galactic latitude of M 1-16 (5°.1) again fixes the object at a distance of some 1.6 kpc. Zijlstra & Pottasch (1991), however, have proposed a scale height of between 190 and 250 pc depending on the galactic disk model used. These values would place M 1-16 at the slightly greater distance of between 2.1 and 2.8 kpc. A weighted mean of all these estimated values for the distance parameter is then determined to be 1.8 kpc (Schwarz, 1992).

Once a value for the distance to M 1-16 has been established, it allows for an estimate of the dynamical ages for the expansion of the lobes. The linear dimension of the lobes (r) is related to the observed angular size (θ) in arcseconds and the distance d in parsecs by the relation

$$r(\mathrm{pc}) = \frac{\theta(\mathrm{arcsec})d(\mathrm{pc})}{206265}$$

Assuming that the nebula expansion velocity has been constant during the lifetime of the lobes at $\sim 350\,\mathrm{kms}^{-1}$ (Schwarz, 1992), and with a maximum nebula inclination of 45°, the ages of the lobes **A**, **B** and **C** are approximately 1550, 800 and 520 years respectively. With a supposed minimum nebula tilt of 20°, the ages increase to values of 2060, 1055 and 690 years.

Recently, Zhang (1995) proposed a statistical distance scale for PNs based upon the correlation between the ionized mass and the radius and the correlation between the radio continuum surface brightness temperature and the radius. The distance scale is an average of the two distances obtained from each correlation, calibrated using a database of 132 PNs with well-determined individual distances and is in good agreement with that recently proposed by van de Steene & Zijlstra (1995a,b). However, employing this distance scale, M 1-16 appears to lie at the greater distance of 6.8 kpc (Zhang, 1995). Consequently, the dynamical ages of the emission lobes increase to the somewhat implausible values of 5900, 3000 and 1950 years for lobes **A**, **B** and **C** respectively with a 45 degree inclination. With a reduced nebula tilt of 20 degrees, the ages increase even further to values of 7800, 4000 and 2600 years.

Near-infrared (NIR) photometry (Whitelock, 1985; Aspin *et al.*, 1993) reveals that M 1-16 has a significant NIR excess (J-H$= -0.22$, H-K$= 1.0$, E(B-V) $= 0.65$). This confirms that the source is not a typically reddened normal main sequence or red giant star and indicates significant continuum emission of a thermal origin. The NIR excess probably arises as a result of thermal emission from heated dust in the near vicinity of the source. The observed NIR colours can be modelled with black-body continuum emission from a stellar photosphere and thermal emission from dust. Aspin *et al.* (1993) find a best fit to their data to be a stellar source at 10^4 K with a dust component at about 1500 K in the ratio 70 : 30.

The IR flux measured by *IRAS* for M 1-16 indicate that its far-infrared emission reaches a peak in the 60 to 100 μm range, indicating significant emission at wavelengths greater than 100 μm. Sahai *et al.* (1994), applying a two-component dust model, determine values for the temperatures and masses of the dust components to be 53 K, $4.3 \times 10^{-4}\,\mathrm{M}_\odot$ and 131 K, $3.1 \times 10^{-6}\,\mathrm{M}_\odot$ for an emissivity power-law index of 1 and 41 K, $1.7 \times 10^{-3}\,\mathrm{M}_\odot$ and 114 K, $2.7 \times 10^{-6}\,\mathrm{M}_\odot$ for an emissivity power-law index of 2, assuming a 60 μm dust emissivity of $150\,\mathrm{cm}^2\mathrm{g}^{-1}$. However, it should be noted that calculations of dust masses in

this fashion scale as the distance squared and inversely as the emissivity. Most of the stellar luminosity is re-emitted in the far-infrared as thermal emission from dust grains since the near-infrared photometry shows a sharp decrease in the flux at wavelengths less than $10\,\mu$m. Integrating the dust component emission over all frequencies gives a luminosity of about $120\,L_{\odot}$, which is in agreement with the value derived by Schwarz (1992). This sort of modelling, although probably too simplistic, does reveal that there is a substantial mass of cool dust present in M 1-16, most probably associated with the cool molecular gas seen in the CO emission. The estimate of the gas-to-dust ratio is $M_{gas}/M_{dust} \sim 500$, but this is rather uncertain since it is relies upon assumptions concerning the radial extent of the molecular material. There is also the possibility that there exists substantial quantities of cold dust ($< 15\,$K) which is observable only at very long wavelengths.

Near-infrared (NIR) imaging photometry of M 1-16 (Aspin *et al.*, 1993) also suggests the presence of a circumstellar disk structure. Narrow band L filter images (central wavelength at $3.4\,\mu$m with 6% bandpass) display an apparent elongation in a northeast/southwest direction, that is, along a direction approximately normal to the axis of the optical bipolar lobes. The authors speculate that, following Morris (1987), a large accretion/excretion disk has formed around a binary system and, again, that this provides a suitable mechanism for the creation of the bipolar lobes.

Long-slit NIR spectroscopy (Aspin *et al.*, 1993) shows that, at $2\,\mu$m, the nebulosity outside of the central 3 arcsecond region consists entirely of H_2 emission with no obvious continuum flux. Within the central 3 arcsecond region, strong H and He lines are present. Schwarz (1992) detected optical continuum flux only directly on this central region, the lobes being detectable only in Hα and [NII]. The authors conclude that no significant continuum emission is seen from the bipolar lobes, which indicates that **there is no component of scattered light present**.

Additionally, emission from the bipolar lobes is present in both J and H bands, which must also be of H_2 emission line origin. This arises either as a result of radiative excitation in photo-dissociation regions, that is, excitation by UV absorption and the associated cascade to the ground vibrational state, or by collisional (shock) excitation. The line ratios obtained by Aspin *et al.* (1993) suggest that within the bipolar lobes of M 1-16, excitation of H_2 is not consistent with pure shock-excitation. This is contrary to the apparent excitation mechanism for the optical line emission (Schwarz, 1992). However, above a certain gas density ($\sim 10^5\,\mathrm{cm}^{-3}$), collisional de-excitation of radiatively excited H_2 emission can mimic shock-excited emission.

Assuming a distance of 1.8 kpc, an estimate of the total molecular mass within a 3 arcsecond sphere centred on M 1-16, gives a value of $0.08\,M_{\odot}$ (see Huggins & Healey, 1989). Assuming a uniform spherical distribution of molecular gas around M 1-16 then implies a H_2 number density of $\sim 2 \times 10^5\,cm^{-3}$. This value suggests that the H_2 close to M 1-16 may still be UV-excited. Aspin *et al.* (1993) also admit the possibility that the observed lobe emission could be purely shock excitation, and is a combination of the physical parameters of the lobes and the relatively poor signal-to-noise ratio in some of their data. This could conspire to suggest a dominant UV-excitation mechanism.

Wavelength shifts in echelle spectra of the lobes are usually taken as representing velocity variations along the bipolar axis. In M 1-16 it is seen that the velocity of the H_2 emission increases linearly with distance (that is, an accelerating outflow) from the central source in both lobes, increasing to a maximum of $\sim \pm 25\,kms^{-1}$. Aspin *et al.* (1993) assert that the most probable cause of this is a pure geometric effect similar to a pre-main sequence model developed by Shu *et al.* (1991). However, in the case of M 1-16, it is observed that the H_2 emitting gas is found in a linear jet rather than located in the cavity walls of a stellar wind inflated bubble as conjectured in Shu's model.

Applying an angle of 45° for the inclination of the bipolar major axis with respect to the plane of the sky, the deprojected maximum velocity of the H_2 outflow is found to be $35\,kms^{-1}$ (Aspin *et al.*, 1993). This in turn suggests a dynamical timescale for the expansion of the outermost H_2 to be of the order of 8000 years. This is not consistent with the dynamical ages of the optical lobes derived by Schwarz (1992), where a value closer to 1600 years was offered. However, the optical emission is created by the fast stellar wind (deprojected velocity $\sim 350\,kms^{-1}$) shock-exciting previously ejected low-velocity material. To expand out to the extremes of the optical emission at the velocity associated with the molecular gas would require timescales of the order 16000 years. More typical expansion velocities for progenitor envelopes are in the range $5-20\,kms^{-1}$, which suggests that the H_2 expansion is either unusually rapid or the gas is being accelerated.

The H_2 emission appears to be confined to a 'jet', but it is also possible that H_2 gas is present throughout the optical lobes and beyond. This would suggest that it is only the molecular gas within the jet that is being excited. Overlaying the H_2 emission on the optical Hα image reveals that the emission jet appears to lie close to the western edge of the northern bipolar lobe and the eastern edge of the southern lobe (Aspin *et al.*, 1993).

The H_2 emission may be occurring within the boundary layer between the shock excited high velocity gas and the neutral low velocity material. This sort of effect is seen more commonly in young pre-main sequence objects. Other explanations invoked include a non-isotropic excitation of a fairly uniform distribution of molecular gas in the remnant RGE or physical density enhancements in the outflowing gaseous material.

Assuming an electron number density of $10^3\,\mathrm{cm}^{-3}$ (Stanghellini & Kaler, 1989), Aspin *et al.* (1993) estimate the effective temperature of the central star in M 1-16 to be $\sim 3.4 \times 10^4\,\mathrm{K}$. For higher electron number densities, this is lowered to $\sim 3.2 \times 10^4\,\mathrm{K}$. Temperatures at least as high as this are certainly to be expected for stars completing their evolution to white dwarfs.

The major axes of the optical bipolar emission lobes are seen to be rotated with respect to each other and do indicate some precessional effect on the direction of the stellar wind. Assuming a binary system for the central source of M 1-16 does provide a logical explanation for such an effect. This type of mechanism has often been considered as explanation for structure in other PNs. In the same way that a circumstellar dust disk confines the stellar wind to the polar directions, the stellar radiation might also be so constrained such that the UV flux exciting the H_2 may not be irradiating the bipolar lobes isotropically. The current orientation of the H_2 jets would then define the present direction of the fast stellar wind axis. There are some difficulties with this explanation, however. Firstly, the central photo-ionization region appears to be approximately circular (spherical in projection), which suggests that the proposed disk is larger in size than 3 arcseconds, so that it surrounds the ionized gas. Large scale disks have been postulated in other PNs. Secondly, it is required that the molecular species survive dissociation in a collimated, high velocity wind. Thirdly, the optical cavities appear to have been created by a sweeping up of RGE material which suggests that the cavities themselves are evacuated.

Other interpretations may be placed on the jet-like structure of the H_2 emission, such as physical structure in the outflowing gas, or density enhancements in the expanding RGE. Balick *et al.* (1987) proposed a hydrodynamic mechanism whereby outflowing material is collimated by passage through a prolate shock front associated with a fast stellar wind. The result is the production of a jet-like structure with associated density enhancement knots or 'ansae'. M 1-16 does possess a high-velocity stellar wind which would allow for the possibility of an internal shock front close to the object. The K-band image of Aspin *et al.* (1993) does display suggestions of emission knots. This is consistent with the idea that the bipolar cavities are evacuated by material being 'snowploughed' into the cavity walls, since near to the source, material entrained in the stellar wind is focussed

into a jet-like structure. However, there remains the problem of the H_2 gas surviving a fast stellar wind/mass outflow. On the other hand, the velocities found in M 1-16 appear to be at the lower end of the scale suggested by Balick *et al.*, so that the molecular gas may survive destruction.

The narrow band L filter image of Aspin *et al.* (1993) appears distinctly elongated in a northeast/southwest direction, that is, approximately perpendicular to the bipolar lobe structure, and it is probable from the images of close field stars that this elongation is intrinsic to the object. The limited data available is, however, not conclusive in this respect. The model of Morris (1987) proposes a scenario where a large accretion disk forms around an interacting binary system. The model of Pringle (1989) invokes a collimating disk which is the remnant of the original protostellar disk formed in the early stages of the central stars evolution. At the assumed distance of M 1-16 (1.8 kpc), the observed 3 arcsecond size of such a disk would represent a structure with a diameter of the order of $\sim 5 \times 10^3$ AU.

The $JHKL$ photometry data of Aspin *et al.* (1993) implies that the frictional heat input to the gaseous material from any dust component is negligible in the envelope of M 1-16, unlike other AGB circumstellar envelopes where this mechanism is believed to be the predominant source of heating. The most likely alternative process for heating in the molecular outflow of M 1-16 is that due to photoelectric emission from dust grains due to far-UV stellar radiation.

Combining the optical photometry data of Shaw & Kaler (1989) and the near infrared photometry of Whitelock (1985), with the fluxes, over the wavelength range 0.43 to 100 μm, shows that the form of the energy distribution is typical of that of PPNs or PNs (Schwarz, 1992). The bolometric luminosity of M 1-16 is estimated to be $3.6 \times 10^{-5}\, d^2\, L_\odot$, where d is the objects distance in parsecs. At 1.8 kpc, $L_{bol} \sim 120\, L_\odot$ (Schwarz, 1992; Aspin *et al.*, 1993), rising to $1700\, L_\odot$ at 6.8 kpc.

The calculated luminosity of M 1-16 is, however, somewhat perplexing for a supposed AGB object. At a distance of 1.8 kpc, the luminosity is of the order of $120\, L_\odot$, but typical AGB luminosities are in the region of $3000\, L_\odot$. The arguments against M 1-16 being a young object are well defined by Schwarz (1992). Firstly, the CO spectrum of the object is typical of circumstellar shells and OH/IR stars, that is, a broad emission line coming from a point source.

There are no narrow lines seen, nor any extended emission. This suggests that M 1-16 is not associated with a molecular cloud or star forming region. Secondly, M 1-16 is a radio continuum source with a morphology typical of a young PN, that is, a ring of ionization. Furthermore, the shocked line profiles clearly show that the [NII] lines are stronger than the Hα emission. In the models of Hartigan *et al.* (1987), this is impossible unless nitrogen is overabundant, and that again implies an evolved object. However, the luminosity problem requires a response. There are other examples of low luminosity PN central stars. One PN in particular, NGC 6565, could be the result of an unusually rapid evolution of the central star (Pottasch, 1989). For M 1-16, this would have to have occurred on a timescale of about 1600 years, the dynamical age of the outermost lobes. Another suggestion is that the mass loss history of M 1-16 may have been considerably different to that of typical AGB stars (Schwarz, 1992). Mass exchange in a binary system may be sufficient to explain the low core mass necessary to yield such a low luminosity. The bipolar morphology of M 1-16 would, of course, fit nicely with the model of Morris (1987), explaining the different position angles of the various lobes and the multiple mass ejections.

A further possibility is that a star might become a PN directly from the RGB without passing through the AGB phase (Slijkhuis *et al.*, 1991). Schwarz (1992) notes that the luminosity of M 1-16 is reasonable for a normal giant star and that there could be some connection with the peculiar, highly evolved and dusty, yellow symbiotic stars. The PN nature of one of these symbiotic stars (AS201) had been confirmed in previous work by Schwarz (1988, 1991), with a binary star system again being suggested.

The relatively strong molecular line emission seen in M 1-16 implies that it has a largely intact circumstellar envelope, presumably from the red giant phase. This again supports the idea that the object is indeed a very young PN. It is estimated from the data that the time elapsed since the onset of ionization (when the slow outflow ceases) is of the order of 850 years. The expansion ages of the three optical lobes which are formed by the action of the very high velocity optical outflow are 1600, 1050 and 740 years respectively. It is concluded that at least the older of the two lobes were formed before the formation of the ionized nebula. The chemical composition of the molecular gas in M 1-16 is substantially different to that measured in the circumstellar envelopes of red giant stars, and this is probably due to the evolution of the central source from a cool red giant to a white dwarf which emits copiously in the UV. In order to drive the slow CO outflow by radiation

pressure on dust grains (typical in AGB stars) certainly does require a level of luminosity higher than 120 $L_{\odot}$, but in M 1-16 we see levels of momentum in the slow outflow which are roughly two orders of magnitude less than what is needed. Attempting to establish M 1-16 on the currently accepted evolutionary tracks for post-AGB stars encounters difficulties using the inferred values of age, luminosity and effective temperature of the source. The very low luminosity of M 1-16 cannot be explained if it is a very young PN. On the other hand, if the low luminosity is considered to result from an extremely rapid evolution of the central source, then the low effective temperature is a problem. M 1-16 does not then fit the post-AGB evolutionary tracks of single stars.

The attractive alternative is to consider a binary system for the central source. A binary central star with mass exchange could have produced the extensive mass loss without the need for a large luminosity. Additionally, a binary system provides a means of explaining the bipolarity of the very fast optical outflow and the energy requirements in order to power these outflows. Such a model was proposed by Morris (1987). The slow outflow from a red giant is captured into a large accretion disk by a main-sequence or compact companion. The disk powers a fast collimated outflow via it's rotational energy. Comparing the kinetic energy in the very fast outflow with the possible range of values for the rotational energy in a disk, it is found that the rotational energy is insufficient for driving the very fast outflow by many orders of magnitude. However, it is possible that stellar rotation may also play an important role in the mass loss form stars as they evolve from red giants, so that it would still be within reason that rotationally driven mass loss could be the mechanism involved.

M 1-16 shows a high $^{13}C/^{12}C$ abundance ratio which can only be reached in equilibrium CNO-nucleosynthesis. Such levels are also seen in oxygen-rich circumstellar envelopes (Morris *et al.*, 1987) and also in a rare class of carbon stars known as J-type (Lambert *et al.*, 1986). The observations infer that the slow outflow in M 1-16 is carbon-rich. It is thought that the cool J-type carbon stars are evolved examples of early R stars which also exhibit ^{13}C-rich envelopes without *s*-process element enhancement typical in normal carbon stars (Lambert *et al.*, 1990; Dominy, 1984). These stars are then expected to possess much lower luminosities than normal AGB carbon stars. The ^{13}C enrichment, possible carbon-rich nature and the low luminosity of M 1-16 suggest that it has evolved from an R star. A small fraction of J-type carbon stars exhibit a 10 μm silicate emission feature which is indicative of oxygen-rich material (Willems & de Jong, 1986; Lambert *et al.*, 1990). The similarity of the frequency of binary occurrence for R stars and normal K giants implies that the formation of an R star is independent of the presence of a companion star.

A low-mass main sequence companion could feasibly capture some of the mass lost from the giant progenitor of the J-type star into an accretion disk, which produces the silicate emission (Lloyd-Evans, 1990). It is possible that M 1-16 has evolved from a silicate-carbon star, but unfortunately high-resolution 10 μm spectra do not exist for M 1-16 to test this hypothesis. Additionally, no measurable CO emission has been detected in any silicate-carbon star to date, indicating a lack of an extended envelope. However, if silicate-carbon stars are significantly less luminous than AGB stars, then their mass-loss rates should be much higher, since the circumstellar gas may be sufficiently cold to result in non-detectable levels of CO emission. As the primary star in these systems evolves toward higher temperatures, grain-photoelectric heating begins to become a significant factor which gives rise to the CO emission as observed in M 1-16.

M 1-16 is denoted as point source IRAS 07349-0932 with flux data in all four bands; 12, 25, 60 and 100 μm. The peak flux is at 60 μm, and this is known to be typical of PNs. Table 3.2 shows both the IRAS point source catalogue and the colour corrected flux densities for M 1-16. The IRAS point source catalogue lists flux densities at the effective wavelengths of its survey bands for an input energy distribution that is flux constant per logarithmic frequency interval, so that a wavelength dependent correction factor should be applied to obtain the true source emission (e.g. Iyengar, 1986; Kwok *et al.*, 1986).

Table 3.2: IRAS flux densities for M 1-16

	IRAS flux density (Jy)			Colour corrected (Jy)		
F_{12}	0.32	$\pm$	0.04	0.41	$\pm$	0.05
F_{25}	2.33	$\pm$	0.14	2.52	$\pm$	0.15
F_{60}	9.45	$\pm$	0.76	8.84	$\pm$	0.71
F_{100}	7.59	$\pm$	0.68	7.19	$\pm$	0.65

The IRAS data can be used to infer important characteristics of the object and put constraints upon the nature of the source. A few examples include the *IRAS Point Source Catalogue* (1985) and the *IRAS LRS Atlas* (1986) being used to categorize and identify late-type stars (e.g. Zuckerman & Dyck, 1986; Thronson *et al.*, 1987, 1988) and PNs specifically (e.g. Iyengar, 1986; Zhang & Kwok, 1990) as well as wider samples of source types (e.g. van der Veen & Habing, 1988; Walker & Cohen, 1988; Walker *et al.*, 1989).

Adopting the definitions of van der Veen & Habing (1988), M 1-16's IRAS colours (using the non-colour corrected flux densities in Jy) are

$$\begin{aligned}
[12]-[25] &= 2.5\log(F_{25}/F_{12}) &= 2.16 &\pm 0.15\\
[25]-[60] &= 2.5\log(F_{60}/F_{25}) &= 1.52 &\pm 0.11\\
[60]-[100] &= 2.5\log(F_{100}/F_{60}) &= -0.24 &\pm 0.13
\end{aligned}$$

With these values, M 1-16 is found to lie in region VIII on the IRAS two-colour diagram of van der Veen & Habing (1988) (60 μm/25 μm versus 25 μm/12 μm). These authors refer to this class as composing different types of objects, from PNs to galaxies. They note that these objects may be extreme cases of stars at the end of their AGB mass loss phase or early PN phase.

Alternatively, adopting the definitions of Walker & Cohen (1988) and Walker *et al.* (1989), the colours of M 1-16 (again non-colour corrected values in Jy) are

$$\begin{aligned}
[12]-[25] &= 1.56+2.5\log(F_{25}/F_{12}) &= 3.72 &\pm 0.15\\
[25]-[60] &= 1.88+2.5\log(F_{60}/F_{25}) &= 3.40 &\pm 0.11\\
[60]-[100] &= 1.11+2.5\log(F_{100}/F_{60}) &= 0.87 &\pm 0.13
\end{aligned}$$

M 1-16, under this classification scheme, most closely matches the properties of the 'red' PN, showing atomic line emission and broader molecular features in the IR spectrum. The implication is that the circumstellar dust material surrounding the object is likely to be carbon-rich rather than silicates (cf., Scarrott *et al.*, 1990). This is consistent with the observed $^{13}C/^{12}C$ abundances, carbon-rich slow outflow and supports the suggestion of its evolution from an R star or rare J-type carbon star.

3.2 Observational details

M 1-16 was observed on 16 January 1994 at the f/15 Cassegrain focus of the 3.9 metre Anglo-Australian Telescope (AAT) using the Mark IV Durham imaging CCD polarimeter (Scarrott *et al.*, 1983; Scarrott, 1991) and an EEV P8603 CCD blue-coated detector. The observations were made using a broadband V filter which has a passband centred on a wavelength of 515 nm and a FWHM bandwidth of 150 nm. Exposures of 300 seconds duration were taken at each of the four polarimeter half-waveplate positions, and this was repeated at 3 telescope positions to provide complete coverage of the object (12 CCD frames totalling 60 minutes exposure time). An unfortunate error in the positioning of the telescope resulted in the loss of some 5 pixel columns (1.6 arcseconds) of data, 4 arcseconds to the west of the object. The effective seeing at the time of the observations was approximately 1.6 arcseconds (the mean seeing disk size determined from field star images in the combined data), at an image scale corresponding to 0.32 arcseconds per pixel.

In addition, M 1-16 was also observed on 17 February 1997 at the f/15 Cassegrain focus of the South African Astronomical Observatory's 1.0 metre telescope. In this case, a EEV P86000 CCD AstroChrome^{TM} coated detector was employed.

These observations were made using a narrowband Hα filter, centred on a wavelength of 656 nm with a FWHM bandwidth of 5 nm. Four CCD frames, each of 900 seconds exposure, were taken at a single telescope position, in conditions when the atmospheric seeing was approximately 3.5 arcseconds and with an image scale of 1.2 arcseconds per pixel.

In both cases, the data were reduced in the standard manner (Draper, 1988).

3.3 Results

3.3.1 Intensity images

A comparison of the Hα image of Figure 3.2 with the V-band continuum image of Figure 3.1 clearly implies an emission-line nature for the prominent bipolar lobe structures, as continuum flux is significantly observed only on the central region of the object. This is in agreement with the results of Schwarz (1992) and Corradi & Schwarz (1993) derived

from their long slit spectra of the object, at least in the more extensive, oldest lobes. However, the intermediate southern lobe, indicated as **B** in Figure 3.2, although not immediately apparent in the reproduction of Figure 3.1 is certainly present to some degree in the V-band data, although it's northern counterpart is undetectable in both images. The intensity images alone strongly point to the absence of scattered light in the lobes. This point can be confirmed by measurements of the polarization in these regions (see §3.3.2).

The intensity isophotes of the inner emission region in both Figure 3.1 and Figure 3.2 display an elongation in the NW-SE direction, corresponding to the orientation of the major axis of lobe **C** at position angle 135 degrees. There is also an obvious distortion, in both images, along an axis approximately normal to the **C** lobe axis, at position angle 225 degrees. This would appear to coincide with the elongation seen in the near-IR images of Aspin *et al.* (1993), for which the authors propose a large circumstellar disk.

Figure 3.3 displays the logarithm of the intensity in arbitrary units as a function of distance from the central source along an axis at position angle 135 degrees, corresponding with the major axis of lobe **C**.

It is observed that the intensity falls off fairly smoothly with increasing offset distance from the source. There is, however, some variation, particularly at 12 arcseconds SE where the intensity profile indicates a slight enhancement. This point corresponds with a patch of limb brightened nebulosity along the NE rim of lobe **B** and can be seen in the Hα image of Figure 3.2 and in the intensity contour image of Figure 3.4. The intensity also falls away more rapidly towards the SE as opposed to the NW, with a 'plateau' at some $6 - 7$ arcseconds offset SE. It is not known whether there is an equivalent feature offset to the NW as this would fall within the region for which no data is available.

3.3.2 The effects of interstellar polarization

The effect on the polarization of starlight which passes through a medium of aligned, non-spherical interstellar grains is well-known and can provide important insight into the nature of the dust grains responsible. The radiation suffers both extinction and a phase shift, the magnitude of which is dependent upon the orientation of the electric (**E**) vector relative to the dust grain cross-section. For typical grain sizes, the differential extinction at optical wavelengths leads to linearly polarized light whose **E**-vector is orientated with the minor axis of the dust grain profile.

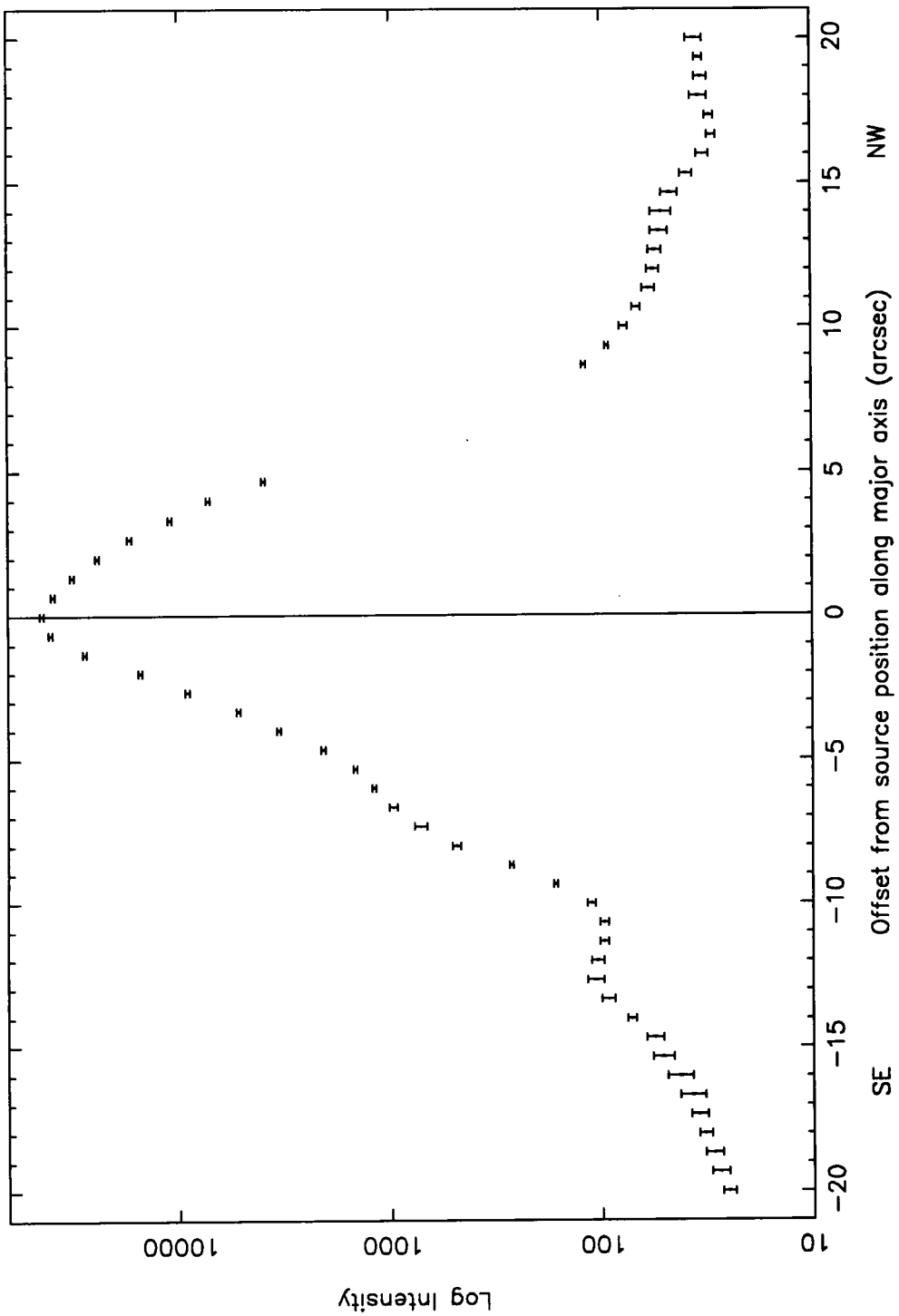

Figure 3.3: Profile of the total intensity of M 1-16 measured along an axis orientated at a position angle of 135 degrees

Although this phenomena provides an excellent means of probing the nature of the Galactic magnetic field, it also can pose some difficulties in extracting the intrinsic polarization of objects when observations close to the Galactic plane are attempted.

M 1-16 has Galactic coordinates of $l = 226.80, b = +5.63$, and it might be expected that the observed levels of polarization would include a small contribution which arises from the extinction effects of magnetically aligned dust grains in the diffuse interstellar medium.

This can reach levels of up to around 3 percent polarization per magnitude of visual extinction when the light path is perpendicular to the Galactic magnetic field (Scarrott, Scarrott & Wolstencroft, 1993). In the direction of M 1-16, at an assumed distance of 1.8 kpc, it is expected that the interstellar polarization (ISP) attains levels of between $0.5 - 0.8\%$ at position angles of around $300 - 320$ degrees (Axon & Ellis, 1976). The resultant effect of an interstellar component on the levels and orientation of the intrinsic polarization of a simple reflection nebula, for instance, are to distort the familiar centrosymmetric pattern and impart a more elliptical appearance. Following Scarrott, Scarrott & Wolstencroft (1993), it is assumed that the level of polarization corresponding to the position of the stellar source is zero, so that the observed level of 0.63 ± 0.21 percent polarization at a position angle of 310 ± 10 degrees, consistent with Axon & Ellis (1976), is solely due to the effects of the ISM. The following polarization data has therefore been corrected for this level of ISP. In addition, if the measured levels of polarization on the source are attributed solely to the effects of the ISM, then the stellar linear polarization data of Axon & Ellis (1976) constrains the distance parameter of M 1-16 to be not less than 1 kpc.

3.3.3 Polarization Maps

Figure 3.4 displays a V-band linear polarization map of M 1-16 superimposed on an intensity contour image, derived from the data obtained with the Anglo-Australian Telescope. The image coordinate system is in arcseconds and includes the object central region together with the full extent of lobes **B** and **C**. At the adopted distance to M 1-16 (1.8 kpc), one arcsecond in the image corresponds to a distance of some 0.01 parsecs or ~ 2000 AU in the plane of the sky. The contours are spaced logarithmically at intervals of 0.8 magnitudes.

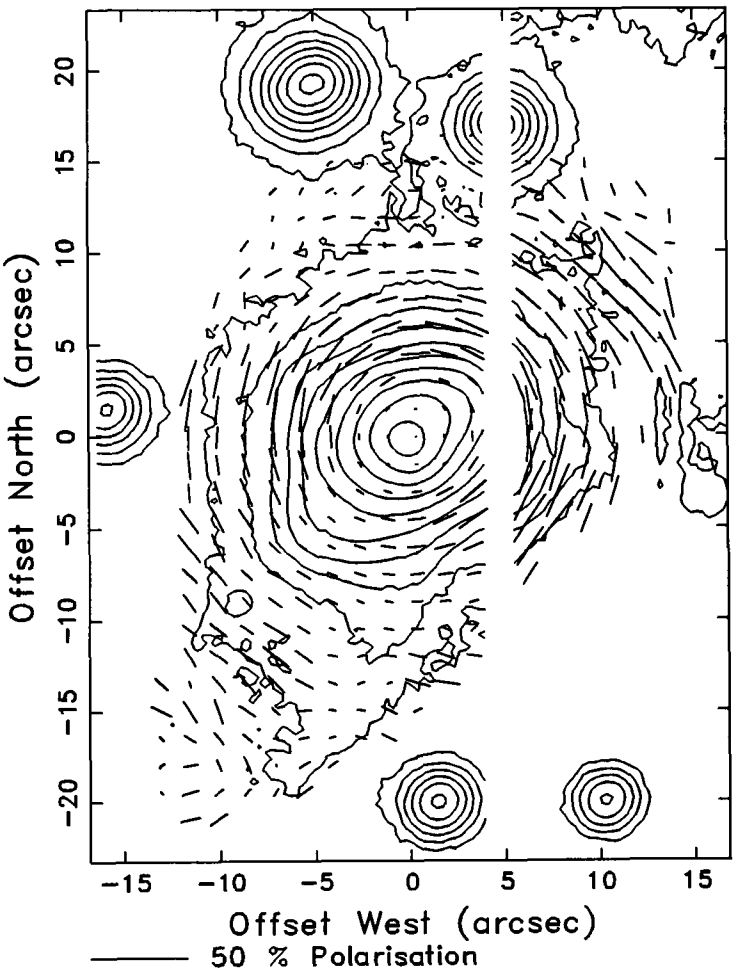

Figure 3.4: An intensity contour and linear polarization map of M 1-16 in the V waveband

The vectors[4] representing the magnitude and position angle of the linear polarization correspond to data which has been placed into square bins of dimensions 7 pixels (2.24 arcseconds) and spaced at intervals of 5 pixels (1.6 arcseconds). Levels of polarization of up to 40% are seen to the west and north of the object, with somewhat lower levels found towards the south and east ($\sim 10-12\%$ maximum). Uncertainties in the levels of polarization and position angle are of the order of $1-2$ percent and $6-8$ degrees respectively for the measurements in the regions of reasonable signal to noise ratio, although the degree of uncertainty increases in the fainter regions of the image where signal levels are low and close to the level of the general sky background.

There are no significant levels of polarization in the faint outermost lobe **A**, both to the northwest and southeast. Any polarized emission from these regions is clearly either non-existent or at a sufficiently low level to be lost in the noise of the random background sky polarization. This would again imply that there is little or no dust present in these regions to scatter light from the central source, at least not at the wavelengths of the continuum data presented here, and tends to confirm that the lobes are purely emission features with no contribution from scattered light.

The position of the central source, as defined by the intensity maximum, appears to correspond, within the measurement uncertainty, with the location of the centre of the centrosymmetric polarization vector pattern and is strong confirmation for the existence of a single primary illuminating source inducing polarization via scattering from a surrounding reflection nebula.

Figure 3.5 displays a Hα intensity contour and linear polarization map of M 1-16 derived from data obtained with the SAAO 1 metre telescope. The image coordinate system is again in arcseconds. The intensity contours are logarithmically spaced at 0.8 magnitudes.

In this instance, the linear polarization data has been integrated over square bins of dimensions 3 pixels (3.6 arcseconds) and spaced at intervals of 2 pixels (2.4 arcseconds). Uncertainties in the levels of polarization and position angle are of the order of 0.3 percent and $4-6$ degrees respectively, increasing to some $10-12\%$ and 20 degrees in the fainter and noisier regions of the polarization data.

[4]The commonly accepted convention for the figurative representation of polarization data is a line (vector) whose length is proportional to the magnitude of the polarization and whose orientation is parallel to the electric (**E**) vector of the polarized light

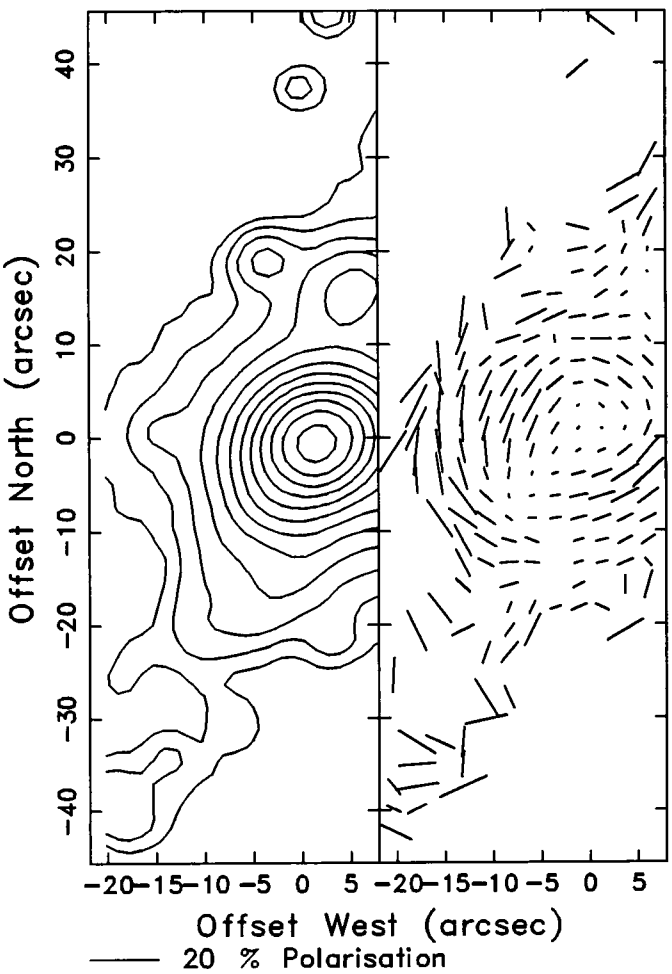

Figure 3.5: An intensity contour and linear polarization map of M 1-16 in Hα

The central 15 arcsecond diameter region displays a centrosymmetric vector pattern in linear polarization very similar to that observed in the continuum, but with reduced levels of observed polarization to the west of around 10 – 15%. The same trend for lower polarization south and east of the object, as noted for the V-band data, is apparent. However, outside the central region, the lobes show no significant levels of polarization above the random sky background. This again confirms that the lobes are seen purely by emission with no persuasive evidence for scattering material being present at these locations.

Figure 3.6 displays an intensity contour and polarization map for the central 30 arcsecond diameter region of M 1-16 only, including the system of lobes **C**, again derived from the AAT data. The intensity contours are spaced logarithmically at 0.72 magnitudes. Each polarization vector represents data integrated over square bins of 5 pixels (1.6 arcseconds), with an inter-bin spacing of 3.3 pixels ($\sim$ 1.1 arcseconds).

Figure 3.7 shows the levels of polarized intensity over the same region and spacial extent as Figure 3.6. The spacing of the intensity contours and binning of the data is also the same as applied in the previous figure, and the levels of polarized intensity are plotted as vectors over the same intensity contour image. The levels of polarization generally increase with radial distance from the source position in both the continuum and Hα data. However, the symmetry of the polarization vector magnitudes is not completely perfect with lower levels of polarization observed along certain radial directions and maximum values more apparent towards the west of the object. Notably, lower levels of polarization are seen along a position angle of 135 degrees which coincides with the SE major axis of lobe system **C**.

The radial distribution of the levels of polarization are shown in Figure 3.8 and Figure 3.9 which trace the measured linear polarization around 360 degree arcs at varying radial distances from the source for the V-band data. The levels of polarization were determined by applying a 1.5 arcsecond software aperture to an image isolating the polarization (and corrected for the effects of interstellar polarization) with measurement positions spaced at 5 degree intervals around circles of varying radii from the source. Within the inner 2 arcsecond region, the polarization is low and fairly constant. However, moving out to 4 arcseconds and beyond shows a marked increase in the levels of polarization along directions lying at position angles of 60 and 240 degrees, roughly east and west of the source along an axis normal to the major bipolar axis of the lobe system.

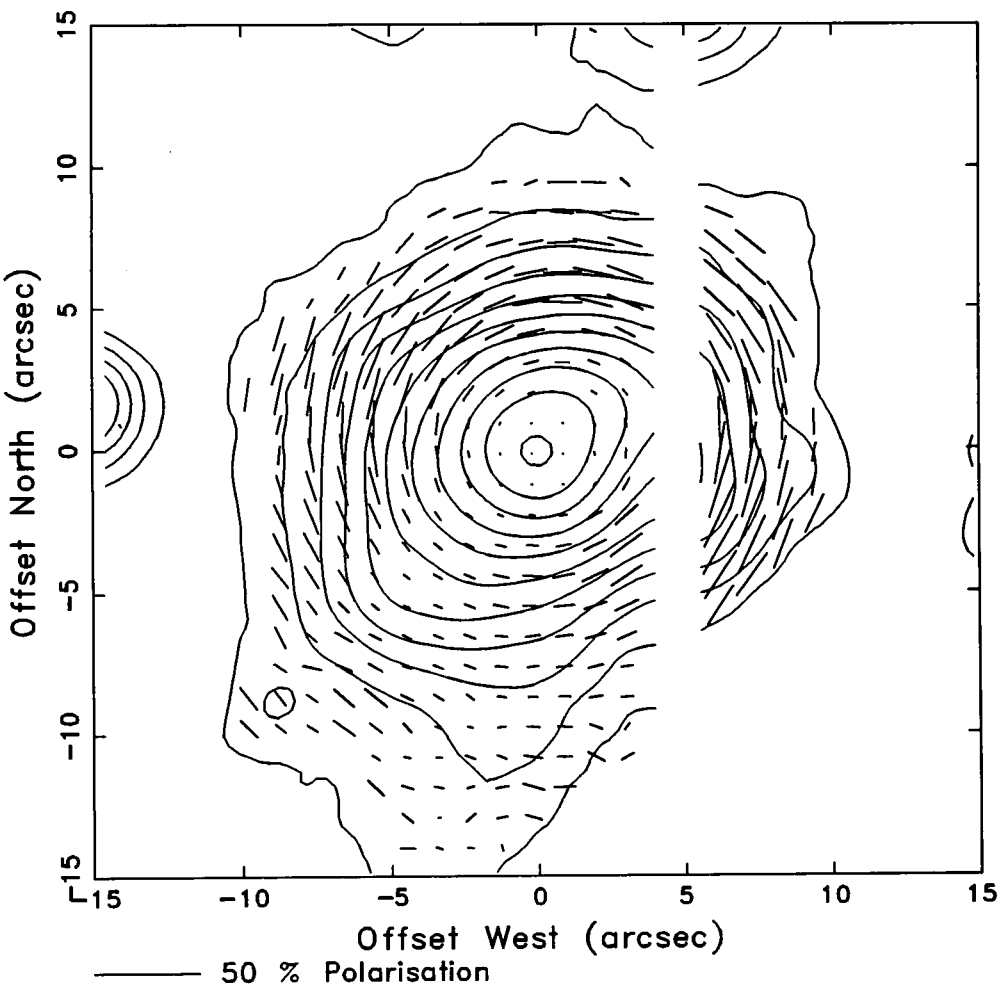

Figure 3.6: An intensity contour and linear polarization map of M 1-16 in the V-waveband at a higher spacial resolution

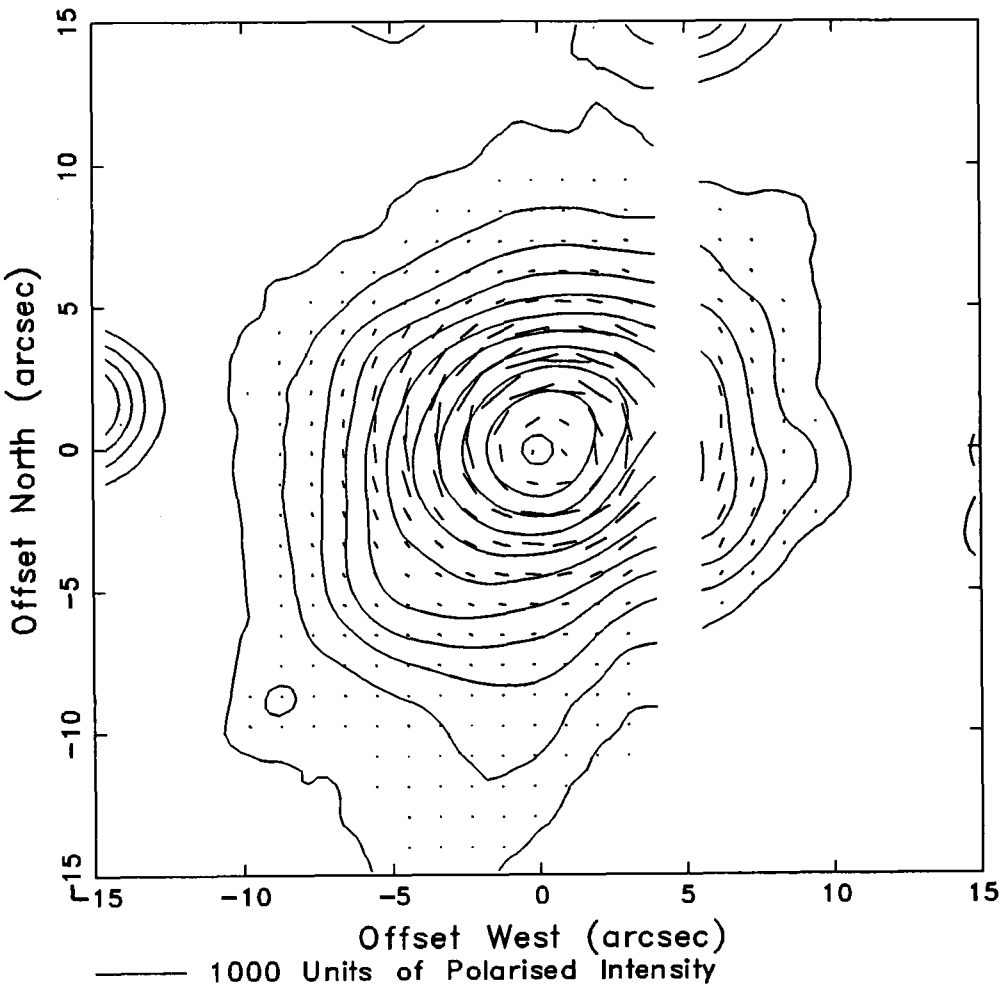

Figure 3.7: An intensity contour and polarized intensity map of M 1-16 in the V-waveband

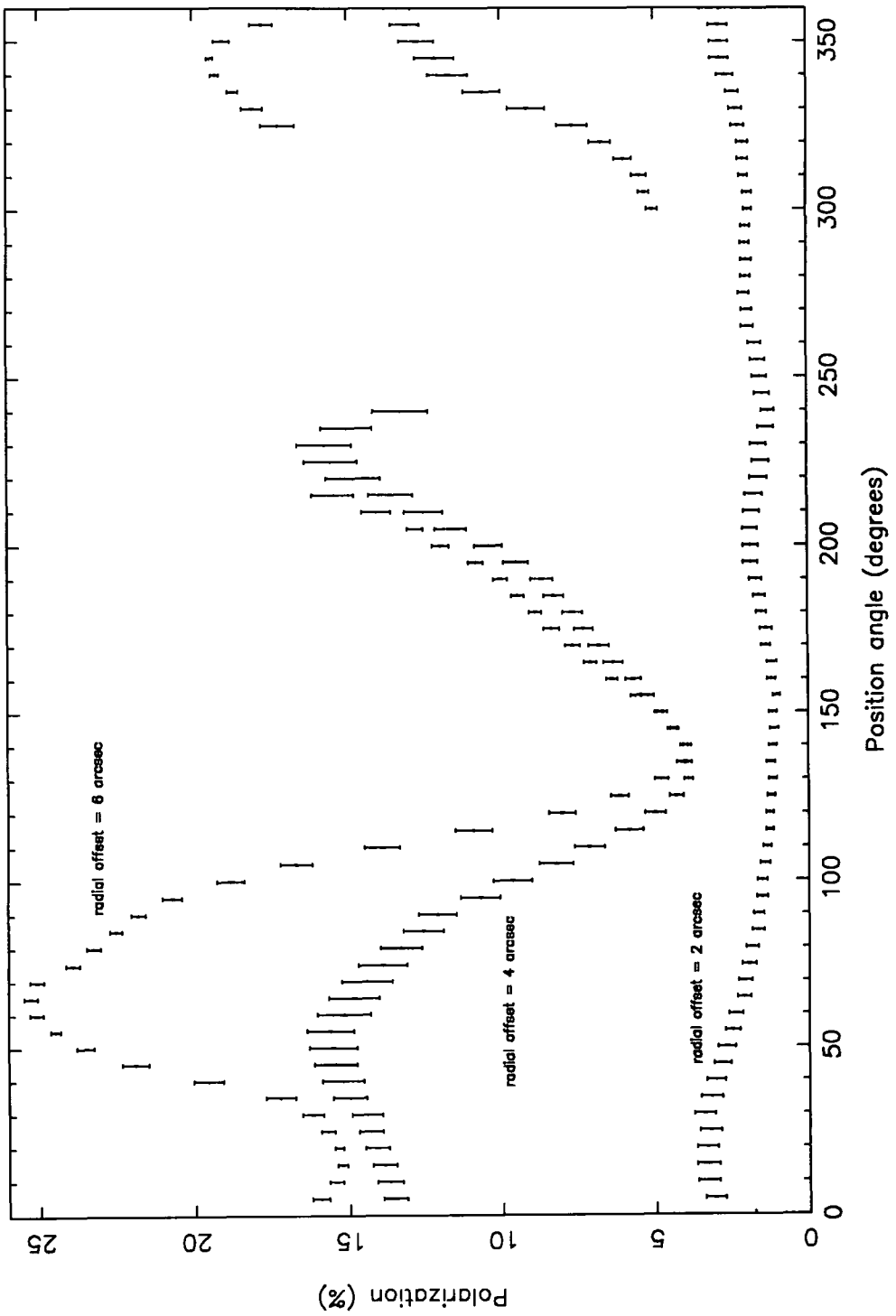

Figure 3.8: A trace of linear polarization for M 1-16 in the V-waveband as a function of position angle and radial offsets of 2,4 and 6 arcseconds

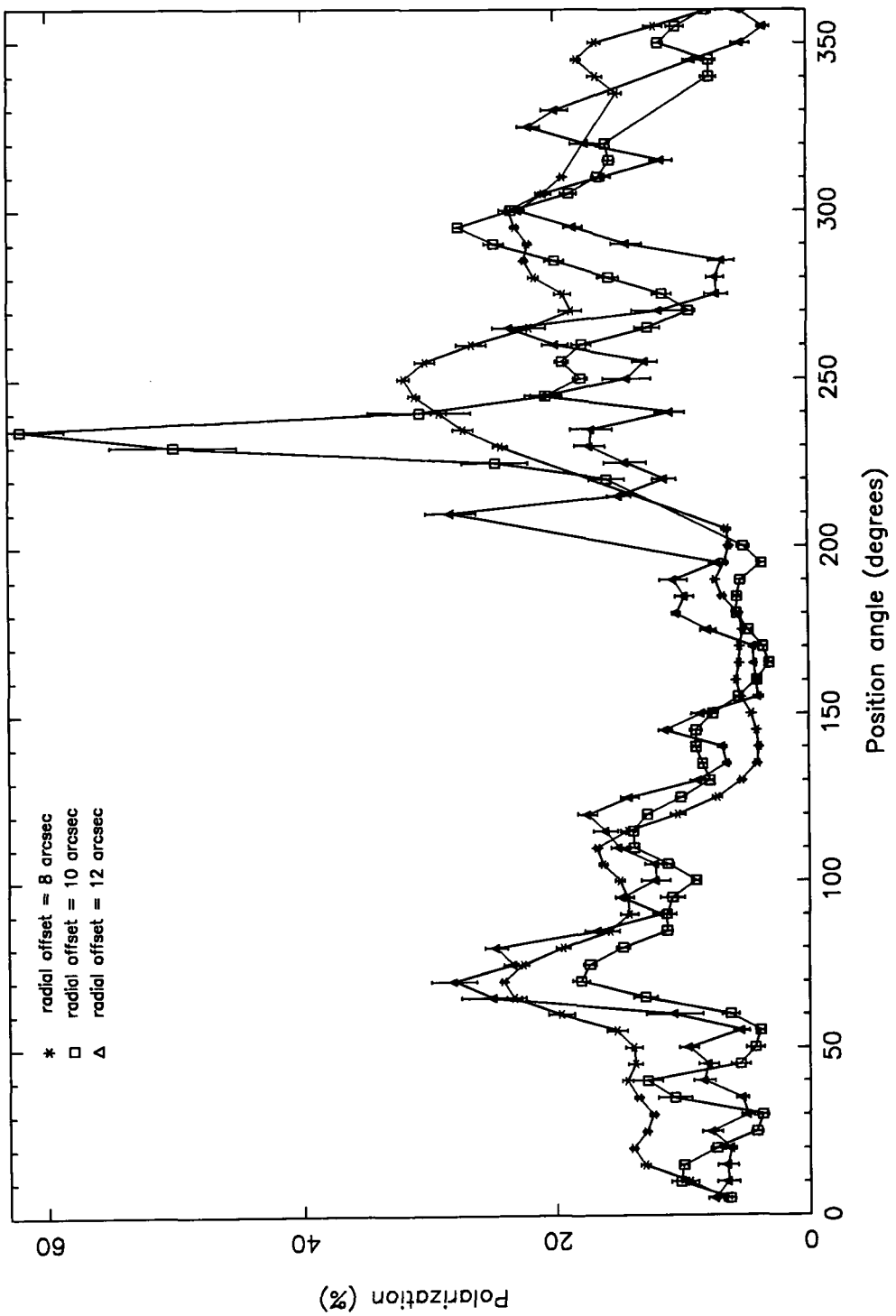

Figure 3.9: A trace of linear polarization for M 1-16 in the V-waveband as a function of position angle and radial offsets of 8,10 and 12 arcseconds

The high polarization of $\sim 60\%$ seen at position angle ~ 230 degrees in Figure 3.9 is most likely an anomaly in the data and is not representative of the levels of polarization which are observed over the nebula as a whole.

Figure 3.10 and Figure 3.11 profile the linear polarization and polarized intensity along the axis which lies at a position angle of 135 degrees. The values of the polarization and polarized intensity were again determined by applying a 1.5 arcsecond software aperture to a polarization image (corrected for the effects of interstellar polarization) with measurement positions separated by 0.67 arcseconds along the axis. The observed levels of polarization display features which strongly support both the presumed tilt of the nebula bipolar axis and the suggestion of a circumstellar disk. These features are discussed more fully in section §3.4.2

3.4 Discussion

The optical polarization data presented for M 1-16, in conjunction with the optical, IR and millimetre wave observations of Schwarz (1992), Aspin *et al.* (1993) and Sahai *et al.* (1994), permit additional inferences to be drawn concerning the structure and geometry of this object.

3.4.1 The bipolar lobes of M 1-16

The highly collimated outermost system of lobes in M 1-16 are confirmed as essentially pure line emission features, since both the V-band and Hα linear polarization data display no persuasive evidence for significant levels of scattered continuum light or scattered emission line radiation from the bright central object. This result implies that there is little to no dust mixed in with the shock-excited gas in, or along, the walls, or at the extremities, of the lobes (cf., King *et al.*, 1981; Aspin & McLean, 1984). The brightest emission, which is so prominent at the tips of these outermost bipolar lobes in the Hα line, is not detectable in the polarization data presented here, again presumably since the emission appears as a result of shocked gas and is not due to copious quantities of dust scattering centres congregated at these extremities. Presumably, dust which may have been ejected from the central system at earlier stages of the object's evolution has long since dissipated to sufficiently low density levels as to impart no significant polarization via scattering, with the intrinsic line emission in these regions overwhelming and diluting any low level polarization which may be present.

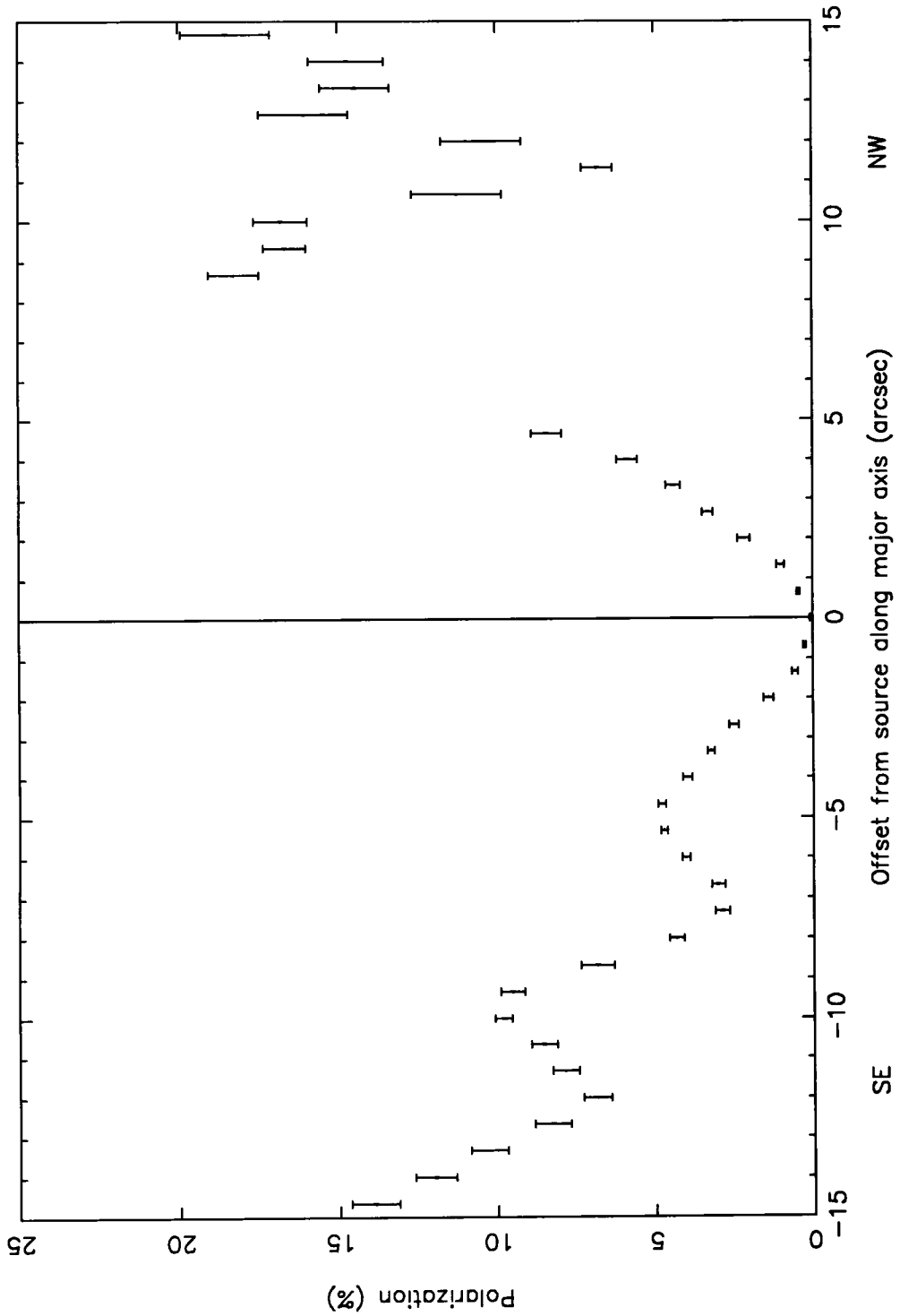

Figure 3.10: A profile of linear polarization (corrected for ISP), measured along the major axis at position angle 135 degrees, for M 1-16 in the V-waveband

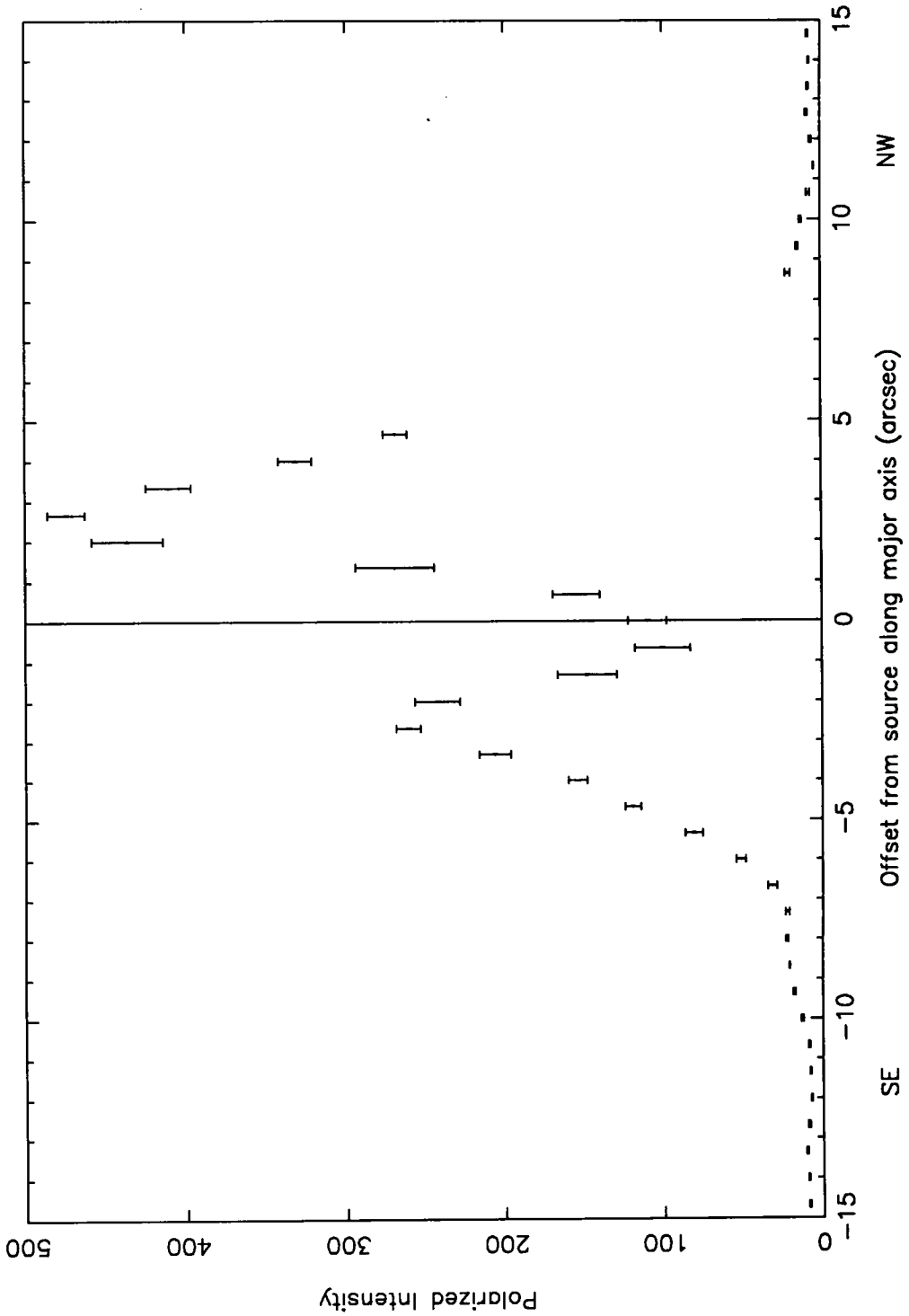

Figure 3.11: A profile of polarized intensity (corrected for ISP), measured along the major axis at position angle 135 degrees, for M 1-16 in the V-waveband

The probability of this being the case gains further support from the results of the linear polarization observations of the lobes in the Hα emission line. Electromagnetic radiation which is emitted by the excited gaseous material in the lobes will be intrinsically unpolarized. However, Hα radiation which has been scattered by dust in the lobes will be clearly revealed as such by the presence of an extensive centro-symmetric polarization pattern extending into the lobe regions. The observations of the young PN Mz 3, which are reported in Chapter 4 of this thesis, confirm that this would be the case (see also Scarrott, Scarrott & Wolstencroft 1993; Scarrott & Scarrott 1995).

The southern component of lobes **B** and **C** (Figure 3.2) also appear to be limb brightened (in both Hα and the continuum) which implies that they are hollow structures rather than a filled volume. The levels of linear polarization for the region of lobe **B** which lie outside of some 15 arcseconds offset from the central source are low and show no preferred orientation. Within 15 arcseconds radial distance from the source the polarization pattern is clearly centro-symmetric which implies the existence of an extensive, relatively intact remnant dust shell surrounding the central region. Lobe **C** is fully contained within this shell region. The radial measurements of the levels of polarization shown in Figure 3.8 and Figure 3.9, display local minima which coincide with the major axis of this lobe. It is clear that the lobe is the result of a stellar wind outflow which has blown a cavity in the surrounding dust shell.

The total intensity profile along the major axis of lobe **C** shown in Figure 3.3 indicated the existence of brightened knots at offsets of some 12 arcseconds both SE and NW of the source. The polarized intensity profile of Figure 3.11, however, shows no corresponding and significant level of polarized intensity at these same points. This implies that the knots appear solely in emission, are intrinsically unpolarized, and are therefore probably not the result of some localized density enhancement in the dust distribution. Indeed, the same locations coincide with points of local minima in the polarization profile of Figure 3.10 which strongly affirms their intrinsic emission nature. A similar, though less prominent, intensity enhancement occurs some $6 - 7$ arcseconds SE from the source which again coincides with a local minimum in the polarization profile. It is proposed that these intensity features are the result of shock excitation/ionization of material in the walls of lobe **C**, possibly at locations towards the tips of the lobe where the stellar wind entrained material becomes focussed (see below). Alternatively, the precession effect, which is clearly evident from the time varying position angle of the lobe axes, could

feasibly lead to material within the walls of lobe **C** colliding with previously ejected material which has been deposited along the wall(s) of lobe **B**. The complexity of the lobe system in M 1-16 renders it a very difficult task to differentiate with confidence between the various possibilities.

The apparent structure of the optical bipolar lobes in M 1-16 therefore appears to be generally consistent with the predictions of hydrodynamical stellar wind models (e.g. Cantó & Rodriguez, 1980; Cantó *et al.*, 1988; Icke *et al.*, 1989; Icke & Preston, 1989; Icke *et al.*, 1992). A supersonic stellar wind expanding into a molecular region (which possesses a density gradient) creates ovoidal cavities in the molecular material. Gas which is entrained to flow over the surface of a cavity will shock-excite the material in the cavity walls, producing regions of shock-excited line emission. The brightest emission region will be close to the tip of the cavity where the stellar wind entrained material becomes focussed. The appearance of M 1-16 is consistent with this type of model since the brightest optical line emitting regions are indeed seen to correspond to the tips of the outflow lobes, particularly in the outer lobes. The almost linear increase in the shock velocity which is observed in the optical spectra obtained by Schwarz (1992) would also be nicely explained in this manner. The work of Shu *et al.* (1991), mainly with young pre-main sequence stars and their outflows, raises the possibility of the velocity increase being a geometric effect as material is constrained to flow along the cavity walls in the lobes.

3.4.2 The geometry of M 1-16

Analysis of polarization data enables the placing of tighter constraints on the three-dimensional geometry of the system through the application of Mie scattering theory. The profile of polarization along the axis of lobe **C** (see Figure 3.10) displays a general trend for the levels of polarization to increase monotonically with offset distance from the source. This suggests that the scattering geometry, giving rise to the observed polarization, is becoming more favourable at greater offset distances such that the scattering angle is approaching 90 degrees. In Chapter 2.2, it was shown that smooth, homogeneous or core-mantle grains of diverse optical properties consistently impart maximum levels of polarization at scattering angles that are close to, or greater than 90 degrees. The asymmetrical nature of both the levels of polarization and scattered intensity which is observed in Mie scattering may be used as a diagnostic on the limits of the tilt of the scattering geometry, since for an inclination angle out of the plane of the sky ϕ, $P(90° + \phi) > P(90° - \phi)$.

If the dust grains in M 1-16 are assumed to be very small compared to the wavelength and therefore behave as Rayleigh-like scattering centres, then the observed maximum levels of polarization set a limit on the possible tilt angle of the nebula bipolar axis out of the plane of the sky. Along the axis and towards the extremities of lobe **C** (at angular offsets of some 10 arcseconds), polarization levels are found to reach a maximum level of $\sim 30\%$ in the NW as opposed to $\sim 10\%$ in the SE[5]. With reference to the Rayleigh scattering curve of Figure 2.1 and the diagram of Figure 3.12, the observed level of maximum polarization (30%) then implies a scattering angle (θ) of ~ 43 degrees under the assumptions of Rayleigh scattering. This value of θ limits the tilt of the bipolar axis to $\leqslant 47$ degrees from the plane of the sky regardless of which of the lobes is tilted towards us or away from us. The spectroscopic and CO data, of course, indicate that the northern bipolar axis is currently tilted away from us.

The polarization traces through lobe **C** (Figure 3.10) can be used to confirm that this is the case. Scattering from Mie particles composed of high-albedo materials produces a maximum in the polarization at scattering angles greater than 90 degrees. For the lobe tilted away from us, depending on the exact shape of the lobe, the scattering angle from the front face of the lobe increases upwards of 90 degrees with increasing offset from the source.

For the lobe tilted towards us, the scattering angle from the front face of the lobe increases upwards to 90 degrees with increasing offset distance. It would be expected that the levels of polarization would reflect this in that the polarization should be higher in the lobe tilted away. In the case of M 1-16, this implies the major axis of the nebula be tilted backwards out of the plane of the sky. The angle of tilt required to fit the polarization data from the Rayleigh assumptions ($\leqslant 48$ degrees) is consistent with the velocity measurements referred to in §3.1. However, there are differences in the levels of polarization at equivalent offset distances from the source which indicate an asymmetric nature to the polarization curve rather than a symmetric Rayleigh scattering model. The Mie scattering curves presented in §2.5 enable further comment to be made.

[5] At these positions, the lobe system is assumed to be optically thin so that a single scattering approximation is acceptable, whereas within the central ~ 5 arcsecond region of the object this assumption would likely be inapplicable

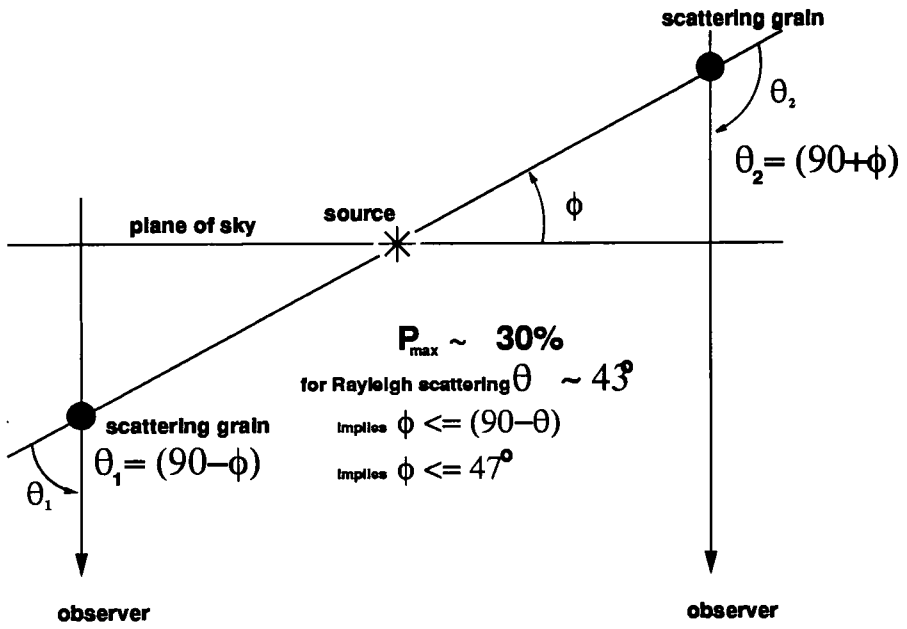

Figure 3.12: A simplified scattering geometry which demonstrates the relationship between the scattering angle and the tilt of the bipolar nebular axis out of the plane of the sky, assuming Rayleigh-like scattering

3.4.3 The nature of the dust grains in M 1-16

Initially, I consider the polarization properties of 'bare' grains under a normal power law size distribution. The observed levels of polarization to the NW and SE of the central region of the object place constraints upon the character of the dust grains responsible for the scattered light. Taking into account the discussion of the previous section, the polarization from the dust grains should possess the following properties

- $P_{max} \sim 30\%$
- $P(90° + \phi) > P(90° - \phi)$
- $P(90° - \phi) \sim 10\%$

where P_{max} is the magnitude of the peak polarization obtainable with a particular set of dust grain parameters and ϕ is the angle of inclination of the nebula axis. For each of the dust grain materials considered, I compute a set of grain parameters which give an optimum fit to the observed levels of polarization. To this end, I define a fitting function

$$\Delta = \left\{ \frac{(P_{90°-\phi} - 10)^2}{10} + \frac{(P_{90°-\phi} - 30)^2}{30} \right\}^{\frac{1}{2}}$$

The grain parameters (a_{min}, a_{max} and γ) and the nebula inclination angle (ϕ) were allowed to vary over a suitable range of values and Δ computed for each parameter set. The results are presented in Tables 3.3 through 3.6. For each input parameter set, the values which give a minimum value of Δ are shown.

A number of conclusions may be drawn from these calculations for 'bare' grains.

1. Homogeneous amorphous carbon grains cannot reproduce the nature of the observed polarization in M 1-16. Table 3.4 clearly shows the very poor level of fit to the polarization data. The reason for this can be seen in Figure 7.5 which shows scattering from amorphous carbon grains under a power law size distribution with power law indices (γ) of between 3.5 and 6.0. The level of polarization is predicted to be far greater than is observed. Reducing γ below 3.5 moves the scattering angle of peak polarization to $< 90°$, that is, the grains become more forward scattering. If this were the case, however, then for a nebula inclination axis of ϕ, $P(90°+\phi) < P(90°-\phi)$ and again this is not what is observed. Removing the smallest grains from the distribution (a 'large grain model') also has the effect of making the amorphous carbon grains forward scattering. This can be seen from Figure 7.17

2. Dirty ice grains similarly cannot be considered as suitable candidates for the dust grain material in M 1-16. Again, the levels of polarization from this material are found to be far higher than is observed, resulting in a poor fit to the data. The results of Table 3.6 and reference to Figure 7.10 suggest that low values of the power law index γ and a large grain model would improve the fit but introduce negative polarization (the polarization **E** vector becomes parallel to the radius vector from

the source to the scattering point) and this is not seen in the observations. In addition, there is no spectroscopic evidence or support for the presence of ice in M 1-16.

3. Pure silicate grains (Table 3.3) are able to reproduce the observations fairly well with a moderate power law index of 4.4 and with the smallest grains removed from the distribution ($a_{min} = 0.05\,\mu$m; $a_{max} = 1.00\,\mu$m). A nebula inclination angle of 40° is also indicated which is consistent with the generally accepted value of 45° from the velocity data.

4. Silicon carbide grains, however, provide the best fit to the observed levels of polarization (Table 3.5). Again a nebula tilt of 40° is suggested and the grain distribution parameters are well defined as $a_{min} = 0.005\,\mu$m, $a_{max} = 1.00\,\mu$m with $\gamma = 4.9$. However, there is a strong dependence upon the presence of the smallest grains. Increasing the lower grain cut-off to increase the number of larger grains introduces negative polarization (Figure 7.18), which is not observed.

Turning now to core-mantle grain behaviour. I apply the same criteria as for the 'bare' grains except we now have to consider the effect of the mantle thickness as well as the combination of core and mantle materials and in addition to the grain parameters of a_{min}, a_{max} and γ. As above, I compute a set of grain parameters which give an optimum fit to the observed levels of polarization using the fitting function defined previously.

It was not deemed necessary to attempt to fit all possible combinations of core and mantle materials in the analysis. Certain grain types and combinations are justifiably excluded on the grounds of the observational data for M 1-16. There are no observations which would indicate the presence of water ice, for example, so both ice and dirty ice as mantles were not considered in detail. The evolution of AGB stars to PNs and the production of astrophysical solid material which occurs during this period (see §2.3) is believed to commence with a preponderance of silicate material which gradually becomes mixed with an increasing abundance of carbonaceous products. On this basis, only oxygen-rich silicate or silicon carbide cores with amorphous carbon mantles were evaluated.

Table 3.3: Mie scattering calculations for 'bare' oxygen-rich silicate grains fitting to the polarization data of M 1-16 in the V-band

a_{min} (μm)	a_{max} (μm)	dm (μm)	γ	ϕ (°)	Δ	a_{min} (μm)	a_{max} (μm)	dm (μm)	γ	ϕ (°)	Δ
0.005	1.000		4.30	50	1.3799	0.005	1.000		4.20	35	0.5010
0.050	1.000		4.50	50	1.3182	0.050	1.000		4.40	35	0.6095
0.100	1.000		6.00	50	2.9677	0.100	1.000		6.00	35	2.6551
0.005	0.500		4.30	50	1.4614	0.005	0.500		4.20	35	0.4080
0.005	0.250		4.00	50	1.3183	0.005	0.250		3.90	35	0.2892
0.050	0.250		4.20	50	1.2321	0.050	0.250		4.10	35	0.3232
0.005	1.000		4.30	45	0.8045	0.005	1.000		4.10	30	1.1664
0.050	1.000		4.50	45	0.7441	0.050	1.000		4.30	30	1.2448
0.100	1.000		6.00	45	2.7880	0.100	1.000		6.00	30	2.7207
0.005	0.500		4.30	45	0.8958	0.005	0.500		4.10	30	1.0819
0.005	0.250		4.00	45	0.8429	0.005	0.250		3.90	30	0.7462
0.050	0.250		4.20	45	0.7374	0.050	0.250		4.00	30	0.8393
0.005	1.000		4.30	40	0.2824	0.005	1.000		4.00	25	1.7714
0.050	1.000		4.40	40	0.1629	0.050	1.000		4.10	25	1.8427
0.100	1.000		6.00	40	2.6770	0.100	1.000		6.00	25	2.8471
0.005	0.500		4.30	40	0.3470	0.005	0.500		4.00	25	1.6986
0.005	0.250		4.00	40	0.3211	0.005	0.250		3.80	25	1.2270
0.050	0.250		4.20	40	0.2667	0.050	0.250		3.90	25	1.3250

Table 3.4: Mie scattering calculations for 'bare' amorphous carbon grains fitting to the polarization data of M 1-16 in the V-band

a_{min} (μm)	a_{max} (μm)	dm (μm)	γ	ϕ (°)	Δ	a_{min} (μm)	a_{max} (μm)	dm (μm)	γ	ϕ (°)	Δ
0.005	1.000		3.50	50	6.0003	0.005	1.000		3.50	35	9.2410
0.050	1.000		3.50	50	5.6626	0.050	1.000		3.50	35	8.9167
0.100	1.000		5.60	50	2.9089	0.100	1.000		5.10	35	6.3199
0.005	0.500		3.50	50	5.6035	0.005	0.500		3.50	35	8.7613
0.005	0.250		3.50	50	5.6002	0.005	0.250		3.50	35	8.5671
0.050	0.250		3.50	50	5.1143	0.050	0.250		3.50	35	8.1180
0.005	1.000		3.50	45	6.9515	0.005	1.000		3.50	30	10.452
0.050	1.000		3.50	45	6.6396	0.050	1.000		3.50	30	10.087
0.100	1.000		5.70	45	4.0645	0.100	1.000		4.70	30	7.1654
0.005	0.500		3.50	45	6.4783	0.005	0.500		3.50	30	9.9614
0.005	0.250		3.50	45	6.4308	0.005	0.250		3.50	30	9.7006
0.050	0.250		3.50	45	5.9809	0.050	0.250		3.50	30	9.2064
0.005	1.000		3.50	40	8.0414	0.005	1.000		3.50	25	11.626
0.050	1.000		3.50	40	7.7342	0.050	1.000		3.50	25	11.197
0.100	1.000		5.40	40	5.2438	0.100	1.000		4.50	25	7.6883
0.005	0.500		3.50	40	7.5677	0.005	0.500		3.50	25	11.131
0.005	0.250		3.50	40	7.4524	0.005	0.250		3.50	25	10.811
0.050	0.250		3.50	40	7.0176	0.050	0.250		3.50	25	10.244

Table 3.5: Mie scattering calculations for 'bare' silicon carbide grains fitting to the polarization data of M 1-16 in the V-band

a_{min} (μm)	a_{max} (μm)	dm (μm)	γ	ϕ (°)	Δ	a_{min} (μm)	a_{max} (μm)	dm (μm)	γ	ϕ (°)	Δ
0.005	1.000		4.90	50	1.1882	0.005	1.000		4.80	35	0.4758
0.050	1.000		5.60	50	1.2269	0.050	1.000		5.40	35	0.4087
0.100	1.000		3.50	50	5.8571	0.100	1.000		3.50	35	5.8571
0.005	0.500		4.90	50	1.2260	0.005	0.500		4.80	35	0.4530
0.005	0.250		4.90	50	1.1658	0.005	0.250		4.80	35	0.4464
0.050	0.250		5.60	50	1.2077	0.050	0.250		5.40	35	0.3975
0.005	1.000		4.90	45	0.6599	0.005	1.000		4.70	30	1.0326
0.050	1.000		5.60	45	0.7212	0.050	1.000		5.30	30	0.9393
0.100	1.000		3.50	45	5.8571	0.100	1.000		3.50	30	5.8571
0.005	0.500		4.90	45	0.6884	0.005	0.500		4.70	30	1.0044
0.005	0.250		4.90	45	0.6498	0.005	0.250		4.70	30	0.9805
0.050	0.250		5.60	45	0.7098	0.050	0.250		5.30	30	0.9241
0.005	1.000		4.90	40	0.1368	0.005	1.000		4.60	25	1.5393
0.050	1.000		5.30	40	0.6881	0.050	1.000		5.20	25	1.4441
0.100	1.000		3.50	40	5.8571	0.100	1.000		3.50	25	5.8571
0.005	0.500		4.90	40	0.1485	0.005	0.500		4.60	25	1.5041
0.005	0.250		4.90	40	0.1871	0.005	0.250		4.60	25	1.4672
0.050	0.250		5.50	40	0.1721	0.050	0.250		5.20	25	1.4199

Table 3.6: Mie scattering calculations for 'bare' dirty ice grains fitting to the polarization data of M 1-16 in the V-band

a_{min} (μm)	a_{max} (μm)	dm (μm)	γ	ϕ (°)	Δ	a_{min} (μm)	a_{max} (μm)	dm (μm)	γ	ϕ (°)	Δ
0.005	1.000		3.50	50	3.5804	0.005	1.000		3.50	35	3.8110
0.050	1.000		3.50	50	3.3846	0.050	1.000		3.50	35	3.5903
0.100	1.000		3.50	50	1.6650	0.100	1.000		3.50	35	1.3746
0.005	0.500		3.50	50	4.6321	0.005	0.500		3.50	35	5.2664
0.005	0.250		3.50	50	7.6696	0.005	0.250		3.50	35	9.5584
0.050	0.250		3.50	50	7.5049	0.050	0.250		3.50	35	9.3909
0.005	1.000		3.50	45	3.4136	0.005	1.000		3.50	30	4.5002
0.050	1.000		3.50	45	3.2042	0.050	1.000		3.50	30	4.2781
0.100	1.000		3.50	45	1.1903	0.100	1.000		3.50	30	2.1391
0.005	0.500		3.50	45	4.5452	0.005	0.500		3.50	30	6.0451
0.005	0.250		3.50	45	8.0393	0.005	0.250		3.50	30	10.708
0.050	0.250		3.50	45	7.8757	0.050	0.250		3.50	30	10.529
0.005	1.000		3.50	40	3.4539	0.005	1.000		3.50	25	5.5211
0.050	1.000		3.50	40	3.2351	0.050	1.000		3.50	25	5.2914
0.100	1.000		3.50	40	0.9666	0.100	1.000		3.50	25	3.1129
0.005	0.500		3.50	40	4.7471	0.005	0.500		3.50	25	7.0652
0.005	0.250		3.50	40	8.6642	0.005	0.250		3.50	25	12.074
0.050	0.250		5.50	40	8.5006	0.050	0.250		3.50	25	11.876

The grain parameters (a_{min}, a_{max}, γ and mantle thickness dm) and the nebula inclination angle (ϕ) were allowed to vary over a suitable range of values as before and Δ computed for each parameter set. The results are presented in Tables 3.7 through 3.10.

From an inspection of these results for core-mantle grains, it is found that the optimum fit to the polarization data is obtained with grains composed of a silicon carbide core and a thin amorphous carbon mantle. The grain parameters are $a_{min} = 0.005\,\mu$m, $a_{max} = 1.000\,\mu$m, power law index $\gamma = 4.1$, mantle thickness $dm = 0.005\,\mu$m and a nebula inclination of 45°. A not unreasonable level of fit can also be obtained with oxygen-rich silicate cores and amorphous carbon mantles with the same grain parameters and a nebula tilt of 40°. In both cases, the fit to the polarization data is better than that obtained with the 'bare' grains.

Other points worth mentioning are

1. The thickness of the grain mantle coating has a significant effect on the nature of the polarization. In both the silicate/carbon and silicon carbide/carbon combinations, optimum results were obtained with a very thin mantle of $0.005\,\mu$m and above a mantle thickness of $0.01\,\mu$m, the level of fit became progressively worse.

2. In all cases, reducing the tilt of the nebula axis below 40° appeared to significantly degrade the calculated fit to the polarization data.

Some of the grain combinations were applied to the other size distribution models outlined in §2.5.2.2. The results are not shown here, but both the modified power law and the exponential distribution were unable to fit the polarization data sufficiently to warrant further investigation. The modified power law (with a fixed core size and a distribution over mantle thickness) was unable to produce a reasonable fit except for nebula tilt angles greater than $55 - 60$ degrees, which may be discounted. In addition, there appeared to be an optimum core size of $0.08\,\mu$m, either side of which the scattering behaviour became too symmetric about a scattering angle of 90 degrees or dropped sharply into negative-positive oscillations of polarization. The exponential grain size distribution could not fit the data even approximately, either for power index (q) values of 2 or 3.

Table 3.7: Mie scattering calculations for grains with an oxygen-rich silicate core and an amorphous carbon mantle fitting to the polarization data of M 1-16 in the V-band

a_{min} (μm)	a_{max} (μm)	dm (μm)	γ	ϕ (°)	Δ	a_{min} (μm)	a_{max} (μm)	dm (μm)	γ	ϕ (°)	Δ
0.005	1.000	0.005	3.90	50	1.3023	0.005	1.000	0.005	3.80	35	0.6334
0.050	1.000	0.005	4.10	50	1.2155	0.050	1.000	0.005	4.00	35	0.6890
0.100	1.000	0.005	6.00	50	3.0496	0.100	1.000	0.005	6.00	35	2.8443
0.005	0.500	0.005	3.90	50	1.4711	0.005	0.500	0.005	3.80	35	0.4508
0.005	0.250	0.005	3.60	50	1.4170	0.005	0.250	0.005	3.50	35	0.2110
0.050	0.250	0.005	3.90	50	1.2890	0.050	0.250	0.005	3.80	35	0.2460
0.005	1.000	0.005	3.80	45	0.7399	0.005	1.000	0.005	3.70	30	1.2515
0.050	1.000	0.005	4.10	45	0.6225	0.050	1.000	0.005	3.90	30	1.3389
0.100	1.000	0.005	6.00	45	2.9014	0.100	1.000	0.005	6.00	30	2.9249
0.005	0.500	0.005	3.80	45	0.9414	0.005	0.500	0.005	3.70	30	1.0703
0.005	0.250	0.005	3.60	45	1.0155	0.005	0.250	0.005	3.50	30	0.3761
0.050	0.250	0.005	3.80	45	0.8530	0.050	0.250	0.005	3.70	30	0.5824
0.005	1.000	0.005	3.80	40	0.1102	0.005	1.000	0.005	3.60	25	1.8449
0.050	1.000	0.005	4.10	40	0.1116	0.050	1.000	0.005	3.80	25	1.9171
0.100	1.000	0.005	6.00	40	2.8305	0.100	1.000	0.005	6.00	25	3.0342
0.005	0.500	0.005	3.80	40	0.2929	0.005	0.500	0.005	3.60	25	1.6815
0.005	0.250	0.005	3.60	40	0.6082	0.005	0.250	0.005	3.50	25	1.0710
0.050	0.250	0.005	3.80	40	0.3746	0.050	0.250	0.005	3.60	25	1.0306
0.005	1.000	0.01	3.50	50	0.9711	0.005	1.000	0.01	3.50	35	1.4012
0.050	1.000	0.01	3.80	50	0.9076	0.050	1.000	0.01	3.70	35	1.0629
0.100	1.000	0.01	6.00	50	3.0908	0.100	1.000	0.01	6.00	35	3.0143
0.005	0.500	0.01	3.50	50	1.2767	0.005	0.500	0.01	3.50	35	1.1534
0.005	0.250	0.01	3.50	50	2.1745	0.005	0.250	0.01	3.50	35	2.2460
0.050	0.250	0.01	3.60	50	1.1436	0.050	0.250	0.01	3.50	35	0.2152
0.005	1.000	0.01	3.50	45	0.5359	0.005	1.000	0.01	3.50	30	2.2357
0.050	1.000	0.01	3.80	45	0.2909	0.050	1.000	0.01	3.60	30	1.6997
0.100	1.000	0.01	6.00	45	2.9840	0.100	1.000	0.01	6.00	30	3.1016
0.005	0.500	0.01	3.50	45	0.7618	0.005	0.500	0.01	3.50	30	1.9887
0.005	0.250	0.01	3.50	45	2.0121	0.005	0.250	0.01	3.50	30	2.7634
0.050	0.250	0.01	3.60	45	0.7274	0.050	0.250	0.01	3.50	30	0.8020
0.005	1.000	0.01	3.50	40	0.7130	0.005	1.000	0.01	3.50	25	3.1239
0.050	1.000	0.01	3.80	40	0.4028	0.050	1.000	0.01	3.50	25	2.2454
0.100	1.000	0.01	6.00	40	2.9625	0.100	1.000	0.01	6.00	25	3.1744
0.005	0.500	0.01	3.50	40	0.5802	0.005	0.500	0.01	3.50	25	2.8984
0.005	0.250	0.01	3.50	40	2.0099	0.005	0.250	0.01	3.50	25	3.5582
0.050	0.250	0.01	3.60	40	0.3000	0.050	0.250	0.01	3.50	25	1.5103

Table 3.8: Mie scattering calculations for grains with an oxygen-rich silicate core and an amorphous carbon mantle fitting to the polarization data of M 1-16 in the V-band (continued)

a_{min} (μm)	a_{max} (μm)	dm (μm)	γ	ϕ (°)	Δ	a_{min} (μm)	a_{max} (μm)	dm (μm)	γ	ϕ (°)	Δ
0.005	1.000	0.05	3.50	50	12.422	0.005	1.000	0.05	3.50	35	15.827
0.050	1.000	0.05	3.60	50	2.6175	0.050	1.000	0.05	3.50	35	5.8071
0.100	1.000	0.05	6.00	50	2.5161	0.100	1.000	0.05	3.50	35	3.5053
0.005	0.500	0.05	3.50	50	12.426	0.005	0.500	0.05	3.50	35	15.829
0.005	0.250	0.05	3.50	50	12.447	0.005	0.250	0.05	3.50	35	15.836
0.050	0.250	0.05	3.50	50	2.0613	0.050	0.250	0.05	3.50	35	5.1446
0.005	1.000	0.05	3.50	45	13.171	0.005	1.000	0.05	3.50	30	17.712
0.050	1.000	0.05	3.60	45	3.6898	0.050	1.000	0.05	3.50	30	6.6920
0.100	1.000	0.05	5.10	45	3.2479	0.100	1.000	0.05	6.00	30	3.5043
0.005	0.500	0.05	3.50	45	13.174	0.005	0.500	0.05	3.50	30	17.714
0.005	0.250	0.05	3.50	45	13.190	0.005	0.250	0.05	3.50	30	17.723
0.050	0.250	0.05	3.50	45	3.1125	0.050	0.250	0.05	3.50	30	6.0232
0.005	1.000	0.05	3.50	40	14.301	0.005	1.000	0.05	3.50	25	19.872
0.050	1.000	0.05	3.50	40	4.7773	0.050	1.000	0.05	3.50	25	7.3678
0.100	1.000	0.05	4.50	40	3.6427	0.100	1.000	0.05	6.00	25	3.5043
0.005	0.500	0.05	3.50	40	14.304	0.005	0.500	0.05	3.50	25	19.876
0.005	0.250	0.05	3.50	40	14.314	0.005	0.250	0.05	3.50	25	19.891
0.050	0.250	0.05	3.50	40	4.1587	0.050	0.250	0.05	3.50	25	6.7441
0.005	1.000	0.10	3.50	50	5.9693	0.005	1.000	0.10	3.50	35	8.8424
0.050	1.000	0.10	6.00	50	2.8174	0.050	1.000	0.10	3.90	35	5.6233
0.100	1.000	0.10	6.00	50	3.3938	0.100	1.000	0.10	3.50	35	3.1970
0.005	0.500	0.10	3.50	50	5.9689	0.005	0.500	0.10	3.50	35	8.8416
0.005	0.250	0.10	3.50	50	5.9679	0.005	0.250	0.10	3.50	35	8.8398
0.050	0.250	0.10	3.70	50	2.8124	0.050	0.250	0.10	3.50	35	5.2124
0.005	1.000	0.10	3.50	45	6.6396	0.005	1.000	0.10	3.50	30	10.243
0.050	1.000	0.10	3.90	45	4.0894	0.050	1.000	0.10	6.00	30	3.1636
0.100	1.000	0.10	6.00	45	3.8559	0.100	1.000	0.10	3.50	30	3.1970
0.005	0.500	0.10	3.50	45	6.6391	0.005	0.500	0.10	3.50	30	10.242
0.005	0.250	0.10	3.50	45	6.6377	0.005	0.250	0.10	3.50	30	10.241
0.050	0.250	0.10	3.50	45	4.0118	0.050	0.250	0.10	6.00	30	3.1637
0.005	1.000	0.10	3.50	40	7.6152	0.005	1.000	0.10	3.50	25	11.726
0.050	1.000	0.10	4.20	40	5.1037	0.050	1.000	0.10	6.00	25	3.1636
0.100	1.000	0.10	3.50	40	5.4988	0.100	1.000	0.10	3.50	25	3.1970
0.005	0.500	0.10	3.50	40	7.6146	0.005	0.500	0.10	3.50	25	11.725
0.005	0.250	0.10	3.50	40	7.6129	0.005	0.250	0.10	3.50	25	11.724
0.050	0.250	0.10	3.50	40	4.8395	0.050	0.250	0.10	6.00	25	3.1637

Table 3.9: Mie scattering calculations for grains with a silicon carbide core and an amorphous carbon mantle fitting to the polarization data of M 1-16 in the V-band

a_{min} (μm)	a_{max} (μm)	dm (μm)	γ	ϕ (°)	Δ	a_{min} (μm)	a_{max} (μm)	dm (μm)	γ	ϕ (°)	Δ
0.005	1.000	0.005	4.10	50	0.6121	0.005	1.000	0.005	4.20	35	0.7198
0.050	1.000	0.005	4.70	50	0.7858	0.050	1.000	0.005	4.80	35	0.8853
0.100	1.000	0.005	3.50	50	4.6108	0.100	1.000	0.005	3.50	35	6.0419
0.005	0.500	0.005	4.10	50	0.7686	0.005	0.500	0.005	4.20	35	0.7782
0.005	0.250	0.005	4.10	50	0.6966	0.005	0.250	0.005	4.20	35	0.8508
0.050	0.250	0.005	4.70	50	0.8009	0.050	0.250	0.005	4.80	35	0.9289
0.005	1.000	0.005	4.10	45	0.0395	0.005	1.000	0.005	4.20	30	0.3982
0.050	1.000	0.005	4.70	45	0.2286	0.050	1.000	0.005	4.80	30	0.4553
0.100	1.000	0.005	3.50	45	5.4318	0.100	1.000	0.005	3.50	30	6.0419
0.005	0.500	0.005	4.10	45	0.1584	0.005	0.500	0.005	4.10	30	0.3022
0.005	0.250	0.005	4.10	45	0.1598	0.005	0.250	0.005	4.10	30	0.3295
0.050	0.250	0.005	4.80	45	1.8641	0.050	0.250	0.005	4.80	30	0.5339
0.005	1.000	0.005	4.20	40	1.2099	0.005	1.000	0.005	4.10	25	0.3174
0.050	1.000	0.005	4.80	40	1.3746	0.050	1.000	0.005	4.70	25	0.1739
0.100	1.000	0.005	3.50	40	6.0419	0.100	1.000	0.005	3.50	25	6.0419
0.005	0.500	0.005	4.20	40	1.2754	0.005	0.500	0.005	4.10	25	0.2274
0.005	0.250	0.005	4.20	40	1.3046	0.005	0.250	0.005	4.10	25	0.2451
0.050	0.250	0.005	4.80	40	1.3986	0.050	0.250	0.005	4.80	25	0.5395
0.005	1.000	0.01	3.50	50	0.3422	0.005	1.000	0.01	3.50	35	2.2806
0.050	1.000	0.01	4.10	50	0.2013	0.050	1.000	0.01	4.00	35	1.7606
0.100	1.000	0.01	3.50	50	3.9122	0.100	1.000	0.01	3.50	35	5.0115
0.005	0.500	0.01	3.50	50	0.2432	0.005	0.500	0.01	3.60	35	1.9641
0.005	0.250	0.01	3.50	50	0.0889	0.005	0.250	0.01	3.50	35	1.8474
0.050	0.250	0.01	4.10	50	0.2641	0.050	0.250	0.01	3.90	35	1.5241
0.005	1.000	0.01	3.50	45	0.9555	0.005	1.000	0.01	3.50	30	2.9318
0.050	1.000	0.01	4.10	45	0.4921	0.050	1.000	0.01	3.90	30	2.3355
0.100	1.000	0.01	3.50	45	5.0115	0.100	1.000	0.01	3.50	30	5.0115
0.005	0.500	0.01	3.50	45	0.6114	0.005	0.500	0.01	3.50	30	2.6015
0.005	0.250	0.01	3.50	45	0.5580	0.005	0.250	0.01	3.50	30	2.4802
0.050	0.250	0.01	4.10	45	0.3670	0.050	0.250	0.01	3.60	30	1.9687
0.005	1.000	0.01	3.50	40	1.6125	0.005	1.000	0.01	3.50	25	3.5722
0.050	1.000	0.01	4.10	40	1.1301	0.050	1.000	0.01	3.50	25	2.8247
0.100	1.000	0.01	3.50	40	5.0115	0.100	1.000	0.01	3.50	25	5.0115
0.005	0.500	0.01	3.50	40	1.2976	0.005	0.500	0.01	3.50	25	3.2309
0.005	0.250	0.01	3.50	40	1.2057	0.005	0.250	0.01	3.50	25	3.1037
0.050	0.250	0.01	4.00	40	0.9657	0.050	0.250	0.01	3.50	25	2.2258

Table 3.10: Mie scattering calculations for grains with a silicon carbide core and an amorphous carbon mantle fitting to the polarization data of M 1-16 in the V-band (continued)

a_{min} (μm)	a_{max} (μm)	dm (μm)	γ	ϕ (°)	Δ	a_{min} (μm)	a_{max} (μm)	dm (μm)	γ	ϕ (°)	Δ
0.005	1.000	0.05	3.50	50	11.817	0.005	1.000	0.05	3.50	35	14.426
0.050	1.000	0.05	3.60	50	0.8103	0.050	1.000	0.05	3.60	35	2.8137
0.100	1.000	0.05	4.50	50	1.3678	0.100	1.000	0.05	4.50	35	3.9334
0.005	0.500	0.05	3.50	50	11.825	0.005	0.500	0.05	3.50	35	14.550
0.005	0.250	0.05	3.50	50	11.853	0.005	0.250	0.05	3.50	35	14.684
0.050	0.250	0.05	3.50	50	0.4141	0.050	0.250	0.05	3.50	35	2.4839
0.005	1.000	0.05	3.50	45	12.077	0.005	1.000	0.05	3.50	30	15.355
0.050	1.000	0.05	3.70	45	1.4038	0.050	1.000	0.05	3.60	30	3.2331
0.100	1.000	0.05	4.50	45	2.2417	0.100	1.000	0.05	4.50	30	3.5042
0.005	0.500	0.05	3.50	45	12.085	0.005	0.500	0.05	3.50	30	16.332
0.005	0.250	0.05	3.50	45	12.115	0.005	0.250	0.05	3.50	30	17.547
0.050	0.250	0.05	3.50	45	0.5688	0.050	0.250	0.05	3.60	30	2.7665
0.005	1.000	0.05	3.50	40	13.767	0.005	1.000	0.05	3.50	25	16.565
0.050	1.000	0.05	3.70	40	2.1181	0.050	1.000	0.05	3.60	25	3.7900
0.100	1.000	0.05	4.50	40	3.6427	0.100	1.000	0.05	4.50	25	3.8504
0.005	0.500	0.05	3.50	40	13.874	0.005	0.500	0.05	3.50	25	18.576
0.005	0.250	0.05	3.50	40	13.920	0.005	0.250	0.05	3.50	25	18.791
0.050	0.250	0.05	3.50	40	0.7321	0.050	0.250	0.05	3.60	25	3.0866
0.005	1.000	0.10	3.50	50	5.5301	0.005	1.000	0.10	3.50	35	6.7811
0.050	1.000	0.10	3.70	50	0.8625	0.050	1.000	0.10	3.60	35	1.3499
0.100	1.000	0.10	4.20	50	2.0170	0.100	1.000	0.10	4.30	35	4.2318
0.005	0.500	0.10	3.50	50	5.5302	0.005	0.500	0.10	3.50	35	7.6621
0.005	0.250	0.10	3.50	50	5.5304	0.005	0.250	0.10	3.50	35	7.6759
0.050	0.250	0.10	6.00	50	0.5875	0.050	0.250	0.10	6.00	35	0.7590
0.005	1.000	0.10	3.50	45	5.6424	0.005	1.000	0.10	3.50	30	7.3954
0.050	1.000	0.10	3.70	45	0.9655	0.050	1.000	0.10	3.50	30	1.8976
0.100	1.000	0.10	4.20	45	2.6555	0.100	1.000	0.10	4.30	30	5.2291
0.005	0.500	0.10	3.50	45	5.6478	0.005	0.500	0.10	3.50	30	11.343
0.005	0.250	0.10	3.50	45	5.6482	0.005	0.250	0.10	3.50	30	11.451
0.050	0.250	0.10	6.00	45	0.6105	0.050	0.250	0.10	6.00	30	1.1922
0.005	1.000	0.10	3.50	40	5.7602	0.005	1.000	0.10	3.50	25	7.9599
0.050	1.000	0.10	3.70	40	0.9788	0.050	1.000	0.10	3.50	25	4.1515
0.100	1.000	0.10	4.30	40	3.0144	0.100	1.000	0.10	4.30	25	3.1970
0.005	0.500	0.10	3.50	40	5.8799	0.005	0.500	0.10	3.50	25	13.775
0.005	0.250	0.10	3.50	40	5.8832	0.005	0.250	0.10	3.50	25	13.846
0.050	0.250	0.10	6.00	40	0.6341	0.050	0.250	0.10	6.00	25	1.3448

3.4.4 Evidence for a circumstellar disk?

A number of authors have suggested that M 1-16 might possess a large disk structure tilted with the bipolar axis and aligned along a position angle of about 225 degrees, in a direction normal to the bipolar axis (Aspin *et al.*, 1993). There is a definite impression of some distortion in the intensity isophotes along this same direction but this factor alone cannot be proof that such a disk exists. The CO data of Sahai *et al.* (1994) appears to confirm the earlier NIR imaging of Aspin *et al.* (1993) finding the kinematic signature of a disk structure expanding with a slow outflow.

There is no direct evidence in the optical polarimetry data presented here for the presence of a circumstellar disk. At such a high angle of axis inclination, it is probable that the usual signature of a 'polarization disc' would not be seen in the data anyway. However, the trace of polarization and polarized intensity along the main axis of lobe **C** reveals quite sharp peaks at offsets of some $3-5$ arcseconds both to the SE and NW. The NW peak is only tentatively identified as this position lies in the region for which there is no polarization data available. However, both peaks are present in polarized intensity, albeit slightly closer to the source position, and it seems reasonable to assume that a companion polarization peak in the NW position is likely. This behaviour in the trace of polarization is reminiscent of that seen in the young PN or PPN, M 2-9 (Scarrott, Scarrott & Wolstencroft, 1993). The authors invoke a disk structure from which scattering at the disk edges gives rise to very similar observed peaks in polarization at opposing offset positions. The limited spectral coverage of the present data and the complex morphology of the nebula structure do not enable further comment other than the possibility of such a disk structure is not ruled out.

3.5 Conclusions

M 1-16 is an evolved object in transition between the AGB phase of stellar evolution and the PN phase and is actively ejecting a nebula. The object displays extensive radially opposing, and apparently precessing, lobe structures for which I find no evidence for intrinsic polarization, and therefore confirm their expected emission nature. The inner emission region of the object completely masks the central source for which it has been proposed that a binary system is present. The precession of the lobe structures does appear to lend strong support to that idea. In addition, the low luminosity of the object makes it difficult to reconcile the evolution of M 1-16 with that of single stars and again a binary system may be the answer.

The nebula is generally believed to be tilted to the line of sight by some 45 degrees and the polarization data strongly supports this figure. It is expected that the nebula is tilted such that the southern lobes are directed towards us according to the velocity data. I find that the levels of polarization are somewhat higher towards the NW of the object than the SE which implies that the scattering angles involved are higher in the northern regions such that that the northern lobes would to be tilted away from us as expected. The derivation of a direction of tilt from this polarization data may not be as straightforward a matter as has been found in other nebulae. The complexity of the lobe structures and the apparent azimuthal orientation of the bipolar axis may conspire to suggest a misleading result. However, the polarization data does confirm that the angle of tilt is very close to 45 degrees. Although there is no direct evidence for a circumstellar disk, the general morphology and structure of the nebula argue strongly for its existence.

Comparison with the results of Mie scattering calculations for a variety of dust grain materials leads to the conclusion that the dust in M 1-16 is most likely composed of core-mantle type grains, with a silicon carbide core and an thin amorphous carbon mantle. The size distribution appears to be well represented by a standard power law with an index of the order of 4.1, slightly above that usually assumed for models of the ISM . In addition, the amorphous carbon mantle can not be more than some 0.01 μm in thickness, probably only as much as half this value. The presence of both a silicate compound and carbon material grains in M 1-16 fits very well with the suggestion that the object has evolved from an R star or a rare J-type silicate-carbon star.

Figure 3.13 shows a possible geometry for the object based upon the collective observational data across the electromagnetic spectrum (adapted from Sahai *et al.* 1994).

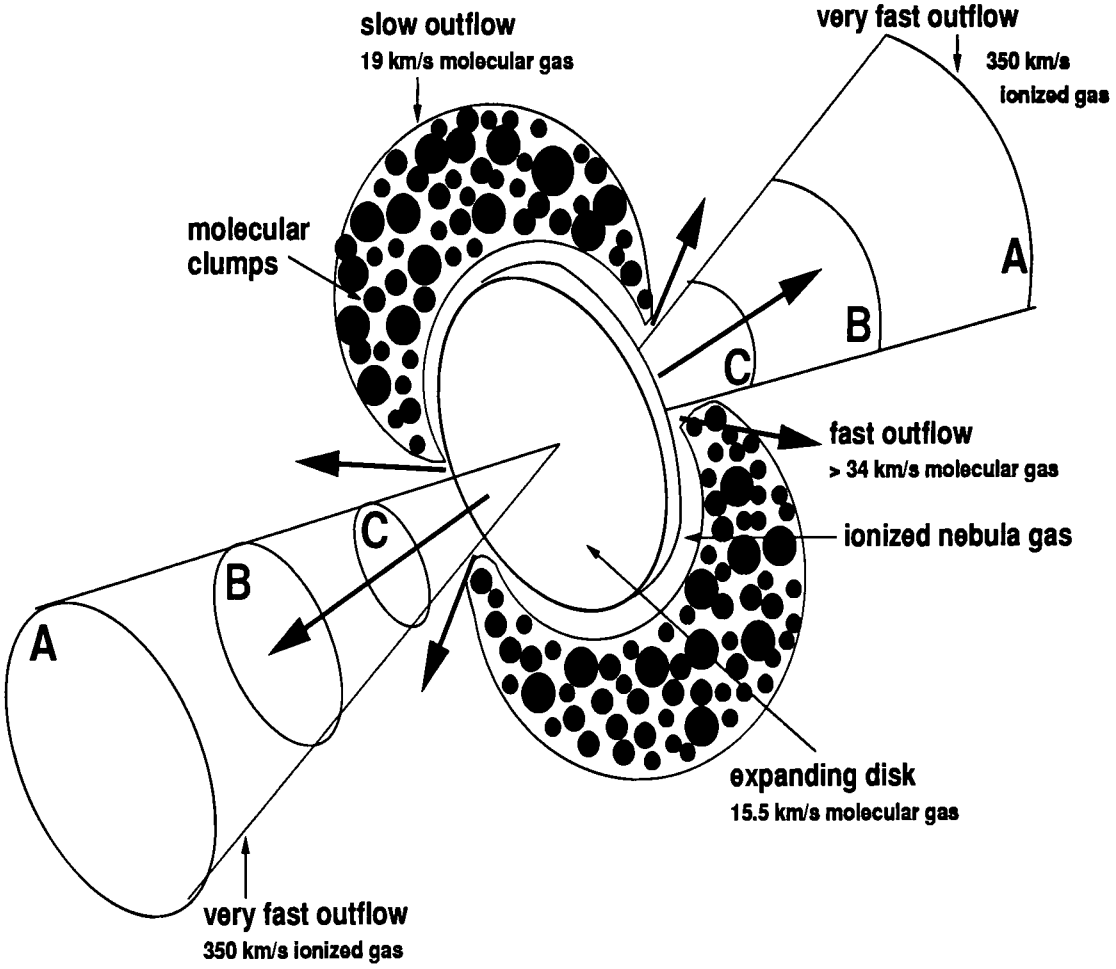

Figure 3.13: A schematic diagram of a possible geometry for M 1-16, showing the component outflows of the system.

Chapter 4

The planetary nebula Mz 3

Mz 3, at position RA $16^h\,17^m\,13^s.5$ Dec $-51°\,59'\,18''(2000.0)$ was discovered by Menzel in 1922 as a consequence of an emission Hα survey. The object is referenced as a true PN in the *Strasbourg-ESO Catalogue of Galactic Planetary Nebulae* (Acker *et al.*, 1992). In this chapter, optical polarimetry maps of Mz 3 are presented and discussed with reference to a number of previous observations of this object that have been carried out.

4.1 Previous studies of Mz 3

Figure 4.1 shows a Hα greyscale image of Mz 3 derived from the observational data presented later in this chapter. The orientation of the figure is north towards the top and east towards the left, with an approximate image scale of 27 arcseconds in the east-west direction by 43 arcseconds in the north-south direction.

This image of Mz 3 displays a prominent central source with relatively bright lobe structures extending some 11 arcseconds to the north and 15 arcseconds to the south. Beyond the inner lobes, there is fainter nebulosity visible out to distances of about 25 arcseconds. The central source is hot, $\sim$ 32000 K, of spectral type O9.5 according to Cohen *et al.* (1978), and is obscured from direct view. There is a distinct reduction in the nebulosity close to the core feature due to extinction by a dust lane. This results in an obvious narrow 'waist' in images of the nebula (Schwarz *et al.*, 1992), similar to that seen in M 2-9 (Calvet & Cohen, 1978; Balick, 1989) and IRAS 07131-0147 (Scarrott *et al.*, 1990). Indeed, the overall morphology of Mz 3 and IRAS 07131-0147 display significant similarities in the apparent distribution of material enshrouding their central sources and in the high levels of polarization (lower for Mz 3 however) found in the extended nebula regions.

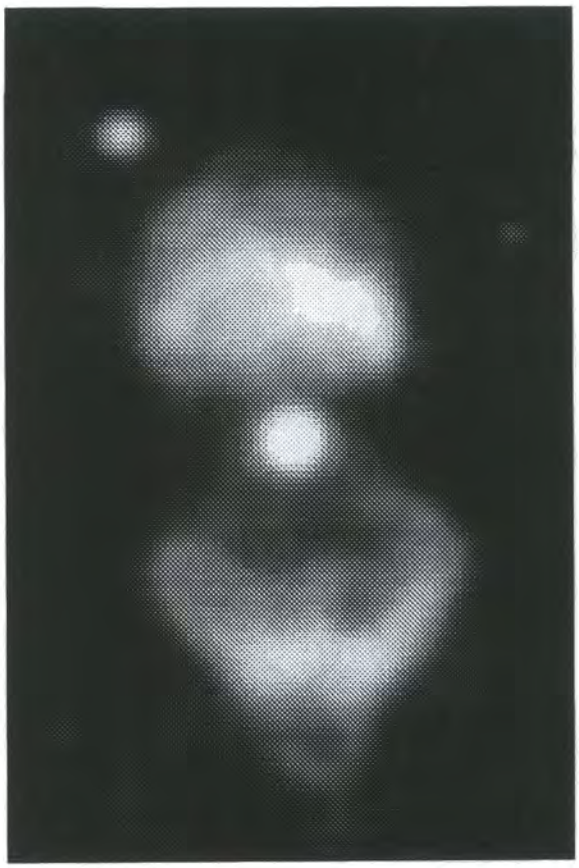

Figure 4.1: A greyscale intensity image of Mz 3 in Hα

The model of Lopez & Meaburn (1983) implies that the long axis of the nebula is tilted to our line of sight by about 30 degrees, with the northern lobe directed away from us. In addition, they also suggest that the bright lobes are the result of successive ejections of material from the outer layers of the central star and which now form radiatively ionized shells. Furthermore, there are two outer shells to the south of the central source containing a spherical cavity expanding at a rate of some $50\,\mathrm{km\,s^{-1}}$ as well as evidence for the existence of a disk of neutral material around the central source of Mz 3 expanding at a rate of $\sim 20\,\mathrm{km\,s^{-1}}$ (Meaburn & Walsh, 1985). To the north, there appears to be only one shell. The alternative steady state model of Lopez & Meaburn (1983) proposes that the lobes are the result of collision between an energetic particle wind and surrounding material. Adopting a stellar wind velocity of $1229\,\mathrm{km\,s^{-1}}$, the ejection and steady state models imply mass-loss rates of 1.7×10^{-4} and $3.9 \times 10^{-7}\,\mathrm{M_\odot\,yr^{-1}}$ respectively.

Scarrott & Scarrott (1995) report V-band imaging polarimetry data for Mz 3. They conclude from their analysis that, taken in conjunction with the velocity measurements, the bright lobes are seen by a combination of emission and reflected light from the central source. The southern lobe, particularly, is revealed as a spherical cavity, or bubble, filled with hot ionized gas and surrounded with dusty material which lines the surface of the cavity. The dust is believed to have been swept up from the outer layers of the stellar envelope by a fast stellar wind. Beyond the inner lobes, the nebula is seen mainly in reflected light from the central source which has been scattered by dust, forming a large scale reflection nebula.

Aitken & Roche (1982) performed a mid-infrared spectrophotometry study of Mz 3. Their results display an essentially featureless $8 - 13\,\mu$m spectrum apart from the presence of an emission line at a wavelength of $12.8\,\mu$m, believed to be due to Ne[II]. They obtained a good fit to their $10\,\mu$m spectrum with a featureless continuum affected by absorption due to overlying colder silicate grains. Quinn *et al.* (1996) carried out $10\,\mu$m imaging of Mz 3 in an effort to determine the spatial distribution of warm dust around the central source and within the lobes. Their $10\,\mu$m image shows the bright central source together with extended emission to the north ($\sim 270\,\mathrm{mJy\,arcsec^{-2}}$) and fainter ($\sim 100\,\mathrm{mJy\,arcsec^{-2}}$) emission to the south, both corresponding essentially with the spatial position of the emission seen in the optical images of Cohen *et al.* (1978), Schwarz *et al.* (1992), Scarrott & Scarrott (1995) and this present work. The obvious correlation between the visible and infrared images suggests that the dust regions which are seen in emission at $10\,\mu$m

are the same as are seen by reflection/scattering at visible wavelengths. The 10 μm data also appears to display an apparent maximum in the emission located some 7 arcseconds to the north and extending up to 3.5 arcseconds to the west.

No significant levels of polarization at 10 μm were detected by Quinn *et al.* (1996). In a 5 arcsecond circular software aperture, the reported values are 1.2 ± 1.2 per cent at a position angle of $69° \pm 29°$, consistent with the derived value for polarization position angle in the bright inner regions of nebulosity and central source reported in the V-band (Scarrott & Scarrott, 1995).

Mz 3 is likely to be optically thin at 10 μm with dust grains heated both radiatively and as a result of trapped Lyman-α photons in the ionized gas which fills the prominent bipolar lobes. Quinn *et al.* (1996) derive a value for the dust temperature at a distance of some 7 arcseconds from the source as around 110 – 130 K. The 10 μm surface brightness at this position requires the blackbody-equivalent temperature of the dust to be ≥ 95 K to effect this magnitude of emission and, assuming low optical depth, indeed implies both radiative and trapped Lyman-α heating of the dust. In addition, there is the implication of an extended shell of dust, surrounding the central star, whose inner edge lies between ~ 0.02 and ~ 0.2 arcseconds from the star and whose outer edge lies at a distance of some 1.5 arcseconds.

The central stars of PNs and PPNs are often not directly observable, as is the case for all the nebulae in this thesis, and so molecular line studies are often used to investigate PN envelopes. Bujarrabal & Bachiller (1991) studied Mz 3 for ^{12}CO and ^{13}CO emission and analysed their data within the framework of a model for CO excitation (Bujarrabal *et al.*, 1989). In the envelopes of oxygen-rich AGB stars, a CO abundance of $\sim 2 \times 10^{-4}$ is expected. However, this value can be significantly reduced through the process of photodissociation by the stellar UV (Bachiller *et al.*, 1988; Bujarrabal *et al.*, 1988). This is reckoned to be an efficient process in PPNs which have left the AGB more than about 300 years ago. ^{12}CO is very weak in Mz 3, and since the central star is very hot, the implication is that UV photodissociation of the molecules is an important factor in this nebula, more so than in the other PPNs studied by Bujarrabal & Bachiller (1991). The result of this is that the CO relative abundance is much lower than predicted, $\sim 0.5 \times 10^{-6}$, a factor of roughly 100 times smaller than that found in CO-rich PPNs and AGB envelopes. They find a total ionized mass of some 0.025 $M_\odot$, but this is dependent upon the assumed

value for the distance. Alternatively, a mass of about $0.05\,M_{\odot}$ can be derived for the bright inner lobes by an analysis of spectral lines.

In common with most PNs, the distance to Mz 3 is uncertain. Table 4.1 lists a number of proposed values from the literature.

Table 4.1: Literature distance values for Mz 3

Distance (kpc)	Reference
1.80	Cohen *et al.* (1978)
< 1.00	Lopez & Meaburn (1983)
3.30	van der Veen *et al.* (1989)
0.68	Stanghellini *et al.* (1993)
~ 1.00	Bujarrabal & Bachiller (1991)

Mz 3 is catalogued as point source IRAS 16133-5151 with available flux data at 12, 25, 60 and 100 μm. The peak flux in this PN is at 25 μm. Table 4.2 gives the values of both the IRAS point source catalogue and the colour corrected flux densities for Mz 3.

Table 4.2: IRAS flux densities for Mz 3

	IRAS flux density (Jy)			Colour corrected (Jy)		
F_{12}	88.76	$\pm$	5.33	113.72	$\pm$	6.83
F_{25}	343.40	$\pm$	17.17	371.40	$\pm$	18.57
F_{60}	277.00	$\pm$	41.55	259.12	$\pm$	38.87
F_{100}	112.60	$\pm$	21.39	106.67	$\pm$	20.26

Applying the definitions of van der Veen & Habing (1988), Mz 3's IRAS colours (using the non-colour corrected flux densities in Jy) are

$$\begin{aligned}
[12]-[25] &= 2.5\log(F_{25}/F_{12}) &&= 1.47 \pm 0.09\\
[25]-[60] &= 2.5\log(F_{60}/F_{25}) &&= -0.23 \pm 0.17\\
[60]-[100] &= 2.5\log(F_{100}/F_{60}) &&= -0.98 \pm 0.26
\end{aligned}$$

Under the classification of van der Veen & Habing (1988), the object is a PN containing cool dust, with the probability that the PN formed from an oxygen rich environment.

With the slightly different definitions of Walker & Cohen (1988) and Walker *et al.* (1989), the colours of Mz 3 (again, non-colour corrected in Jy) are

$$\begin{aligned}
[12]-[25] &= 1.56+2.5\log(F_{25}/F_{12}) &&= 3.03 \pm 0.09\\
[25]-[60] &= 1.88+2.5\log(F_{60}/F_{25}) &&= 1.65 \pm 0.17\\
[60]-[100] &= 1.11+2.5\log(F_{100}/F_{60}) &&= 0.13 \pm 0.26
\end{aligned}$$

which places the object into the authors 'red planetary nebulae' category.

4.2 Observational details

Mz 3 was observed on 22 March 1994 at the f/15 Cassegrain focus of the 3.9 metre Anglo-Australian Telescope (AAT) using the Mark IV Durham imaging CCD polarimeter (Scarrott *et al.*, 1983; Scarrott, 1991) and a EEV P8603 CCD blue-coated detector. The observations were made using an interference filter of bandwidth 5 nm centred on the Hα emission line, but which also encompasses the [NII] lines. Exposures of 200 seconds were taken at each of the four half-waveplate positions, and this was repeated at 3 telescope positions to provide complete coverage of the object (12 CCD frames in total). In addition, a sequence of four short duration exposures (10 seconds) was taken in order to determine the polarization of the central star without saturation of the CCD detector. The effective seeing at the time of the observations was approximately 1.4 arcseconds (the mean seeing disk size determined from field star images). The data were reduced in the standard manner (Draper, 1988).

4.3 Results

4.3.1 Intensity images

The appearance of Mz 3 seen in the emission line of Hα is very similar to that observed in the V-band continuum. Figure 4.2 displays a V-band image of Mz 3 derived from data originally published in Scarrott & Scarrott (1995) alongside the Hα image of Figure 4.1 for comparison. The V-band data was also obtained with the Anglo-Australian telescope. The images are therefore displayed at the same image scale of 0.32 arcseconds per pixel. Accordingly, the approximate extent of each image is 17 arcseconds in the east-west direction by 37 arcseconds in the north-south direction. The images are orientated with north towards the top and east to the left. The almost identical appearance of the nebula in the V-band to that seen in the Hα line suggests that that brightest regions of the nebula are seen mainly by emission.

The nebula displays a very striking form. The bright inner lobes are positioned some 8 arcseconds north and 10 arcseconds south of the prominent central core. The northern lobe appears foreshortened somewhat and this is expected if the nebula is tilted with the northern lobe away from the line of sight as is believed (Lopez & Meaburn, 1983; Meaburn & Walsh, 1985). In the southern lobe particularly, a certain amount of structure and limb brightening around the edges of the lobe is detectable. The northern lobe displays less detail. There is an obvious waist around the centre of the nebula and the presumed central star is not directly visible but is enshrouded in circumstellar material. Beyond the bright inner lobes, there are extensive regions of fainter nebulosity which are less well defined and structured.

4.3.2 The effects of interstellar polarization

Mz 3 is positioned at Galactic coordinates of $l = 331.73, b = -1.01$. At this location, and with an assumed distance to the object of 1 kpc, the extinction and polarization effects of the ISM are likely to influence the data considerably. The catalogue of linear polarization made available by Axon & Ellis (1976) suggests an ISP component of magnitude $\sim 3-6\%$ at a position angle $\sim$ 80 – 90 degrees. Scarrott & Scarrott (1995) assumed that their measured polarization (4.5% at 75°) of the central core in Mz 3 (in the V-band) was solely due to the effects of the ISM and the same assumption is made in correcting the polarization data that is presented in this section. For the Hα data presented here, I find a value of the ISP contribution to be $6.20\% \pm 0.22\%$ at a position angle of $66°.0 \pm 0°.9$, somewhat higher in magnitude than in the V-band.

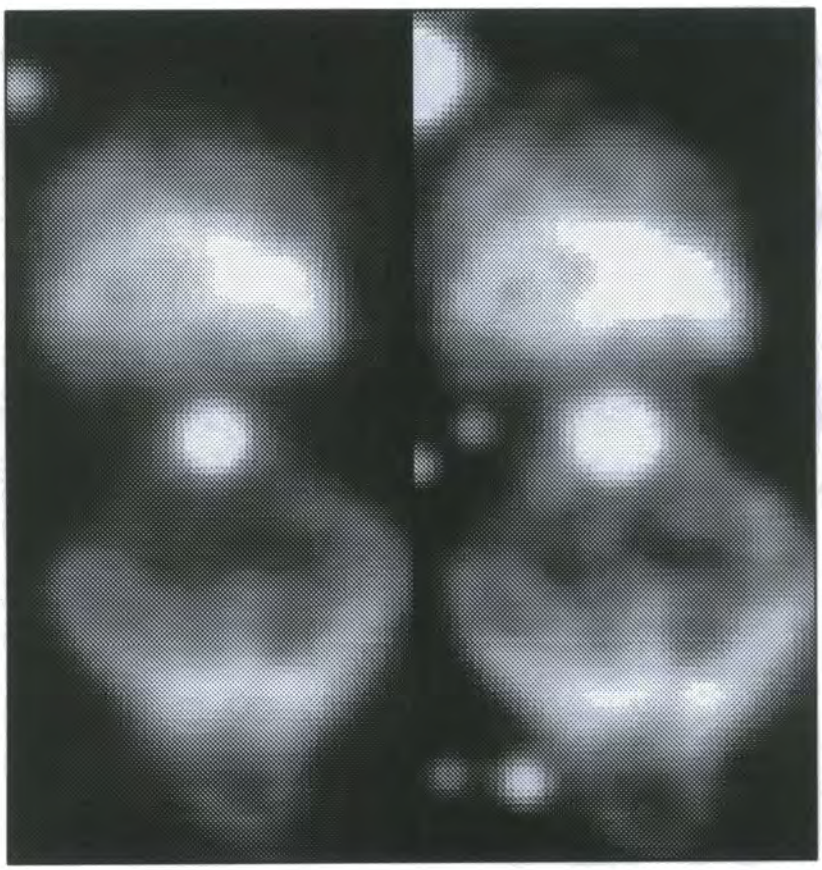

Figure 4.2: Comparative images of Mz 3 in the Hα emission line (left hand image) and the V-band (right hand image)

4.3.3 Polarization Maps

Figure 4.3 displays a Hα linear polarization map of Mz 3 alongside an intensity contour image, derived from the data obtained with the Anglo-Australian Telescope. The image coordinate system is in arcseconds. At the adopted distance to Mz 3, (1.0 kpc), one arcsecond in the image corresponds to a distance of some 0.005 parsecs or $\sim$ 1000 AU in the plane of the sky. The intensity contours highlight the brighter regions of the inner lobe structures. The contours are spaced logarithmically at intervals of 0.48 magnitudes. The vectors representing the magnitude and position angle of the linear polarization correspond to data which has been placed into square bins of dimensions 7 pixels (2.24 arcseconds) and spaced at intervals of 5 pixels (1.6 arcseconds). Uncertainties in the levels of polarization and position angle are of the order of $1-2$ percent and $6-8$ degrees respectively.

The polarization map, corrected for the effects of interstellar polarization (ISP) is very similar in form to the V-band map of Scarrott & Scarrott (1995). The regions outside of the bright inner lobes show the familiar centro-symmetric polarization pattern typical of a reflection nebula illuminated by a single, central source and observed via a combination of emission line radiation and reflected central starlight. The levels of polarization in the surrounding, fainter nebulosity range over values of $\sim$ 5 to $\sim$ 15% at various positions around the core, somewhat less than that observed in the V-band.

Within both of the bright inner lobes, the levels of polarization are observed to be much lower, only some 1 or 2 percent. The lobe interiors correspond with the regions that are seen by emission rather than reflection.

Across the centre of the object, running from a point some 7 arcseconds east of the core to 7 arcseconds west and one or two arcseconds north, there are a swathe of polarization vectors which appear to be orientated more parallel to the east-west direction. This sort of effect is seen in other PPNs and young PNs, as well as pre-main sequence objects. The effect is believed to be due to the presence of a circumstellar disk structure (Scarrott *et al.*, 1990; Kastner & Weintraub, 1990; Scarrott & Scarrott, 1994, 1995).

Figure 4.4 displays a greyscale intensity contour and a greyscale polarized intensity image which has been corrected for the effects of interstellar polarization. The southern lobe appears as a ring of enhanced polarization surrounding a region of effectively zero polarization.

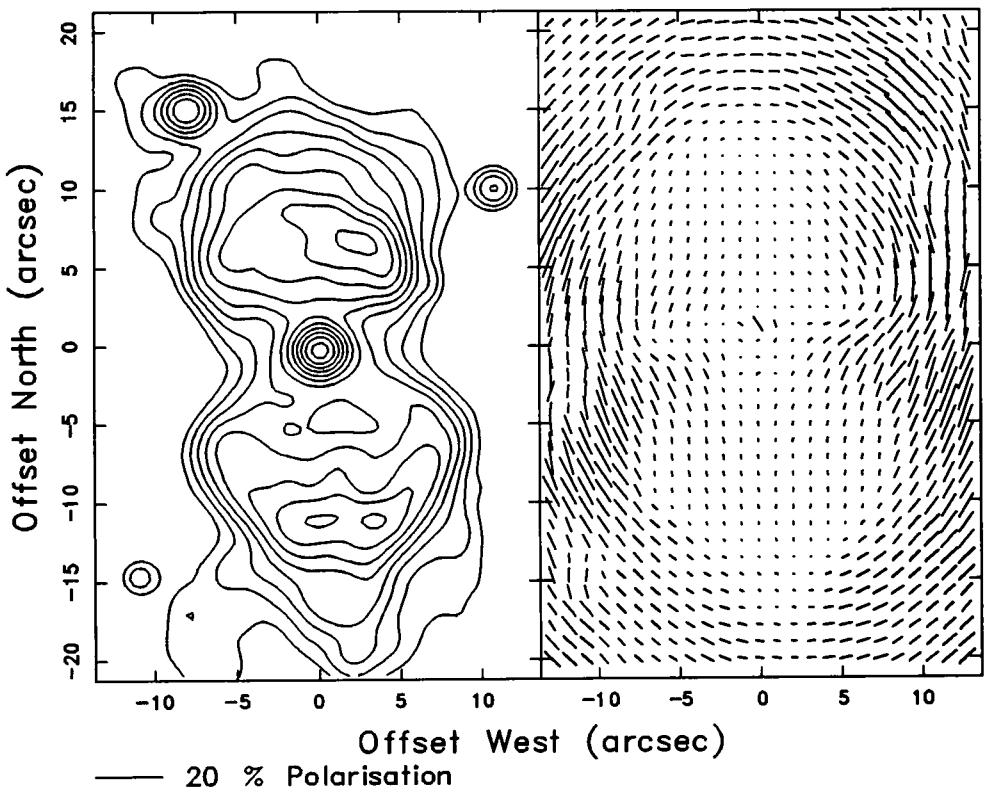

Figure 4.3: An intensity contour and linear polarization map of Mz 3 in the Hα emission line

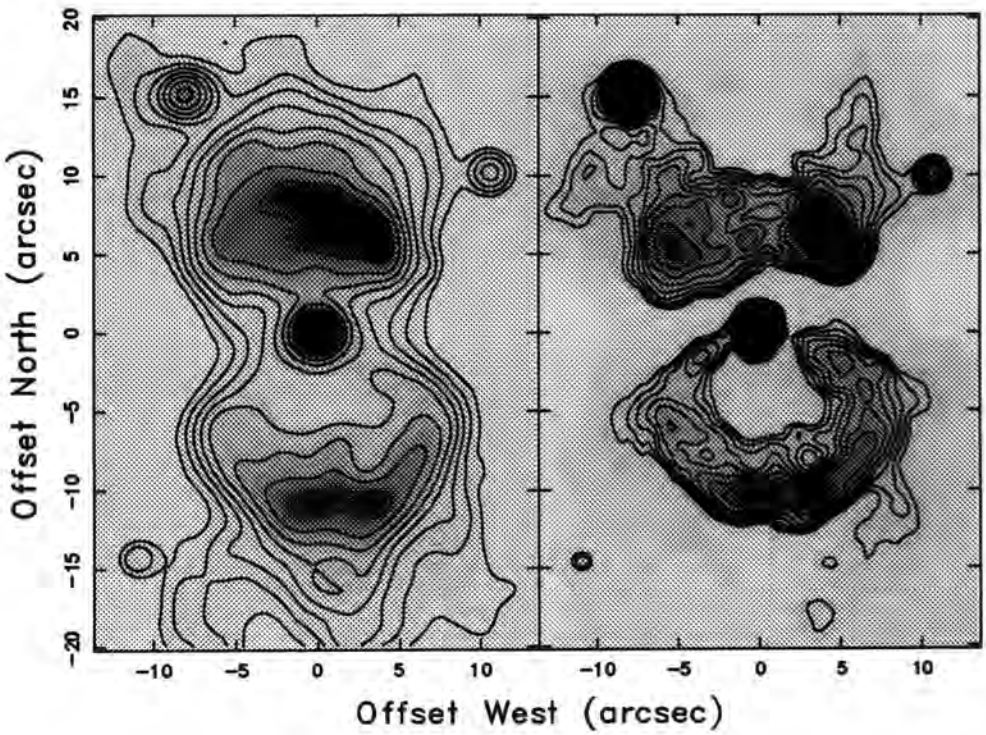

Figure 4.4: A greyscale intensity contour and polarised intensity contour (corrected for the effects of ISP) image of Mz 3 in the Hα emission line

Scarrott & Scarrott (1995) also see this effect in their V-band data and conclude that the southern lobe exists as a hollow spherical bubble with scattering dust distributed over its surface. This is also what is seen in the emission line data presented here. The northern lobe, again in accordance with the V-band data of Scarrott & Scarrott (1995), does not show the same morphology and this is presumably due to the combined obscuration effects of the supposed tilt of the nebula and an overlying circumstellar disk structure. There are regions in both the northern and southern lobes where the polarized intensity reaches some maximum value. In the southern lobe, this appears to be at positions corresponding to the brightest patches of intensity at the tip of the lobe. This may represent the effects of material which has been focussed and shocked at the extremity of the lobe by high-velocity stellar winds or mass ejecta similar to that seen in the large emission lobes of M 1-16 (Cantó & Rodriguez, 1980; Cantó *et al.*, 1988; Icke *et al.*, 1989; Icke & Preston, 1989; Icke *et al.*, 1992; Schwarz, 1992). A similar effect is seen in the northern lobe but here the brightest emission points are located on the east and west edges of the lobe. Again, gas which is entrained to flow along the walls of a hollow cavity will shock excite material in the walls. The enhanced patch of polarized intensity seen at offsets of 5 arcseconds east and north is not as prominent as the western counterpart and is not seen in the V-band data of Scarrott & Scarrott (1995). There is a striking absence of polarized emission running east-west across the object 2 to 3 arcseconds north of the core. This corresponds in position with the swathe of polarization vectors which are orientated parallel to the east-west direction and again coincides with the obscuration from a presumed disk structure.

Figure 4.5 is a trace of the polarization, corrected for ISP, along a line running N-S and 3.57 arcseconds west of the central core passing through the regions of highest intensity which exist at offsets of 7.5 and 10 arcseconds to the north and south respectively. The values of the polarization were determined by applying a 1.5 arcsecond software aperture to a polarization image (corrected for the effects of interstellar polarization) with measurement positions separated by 0.67 arcseconds.

Similarly, Figure 4.6 is trace of the polarization (applying the same method as for Figure 4.5), corrected for ISP, along a line running N-S and 5.00 arcseconds east of the central core, again passing through the patch of enhanced polarized intensity which exists at an offset of 7.5 arcseconds north and 5 arcseconds east respectively.

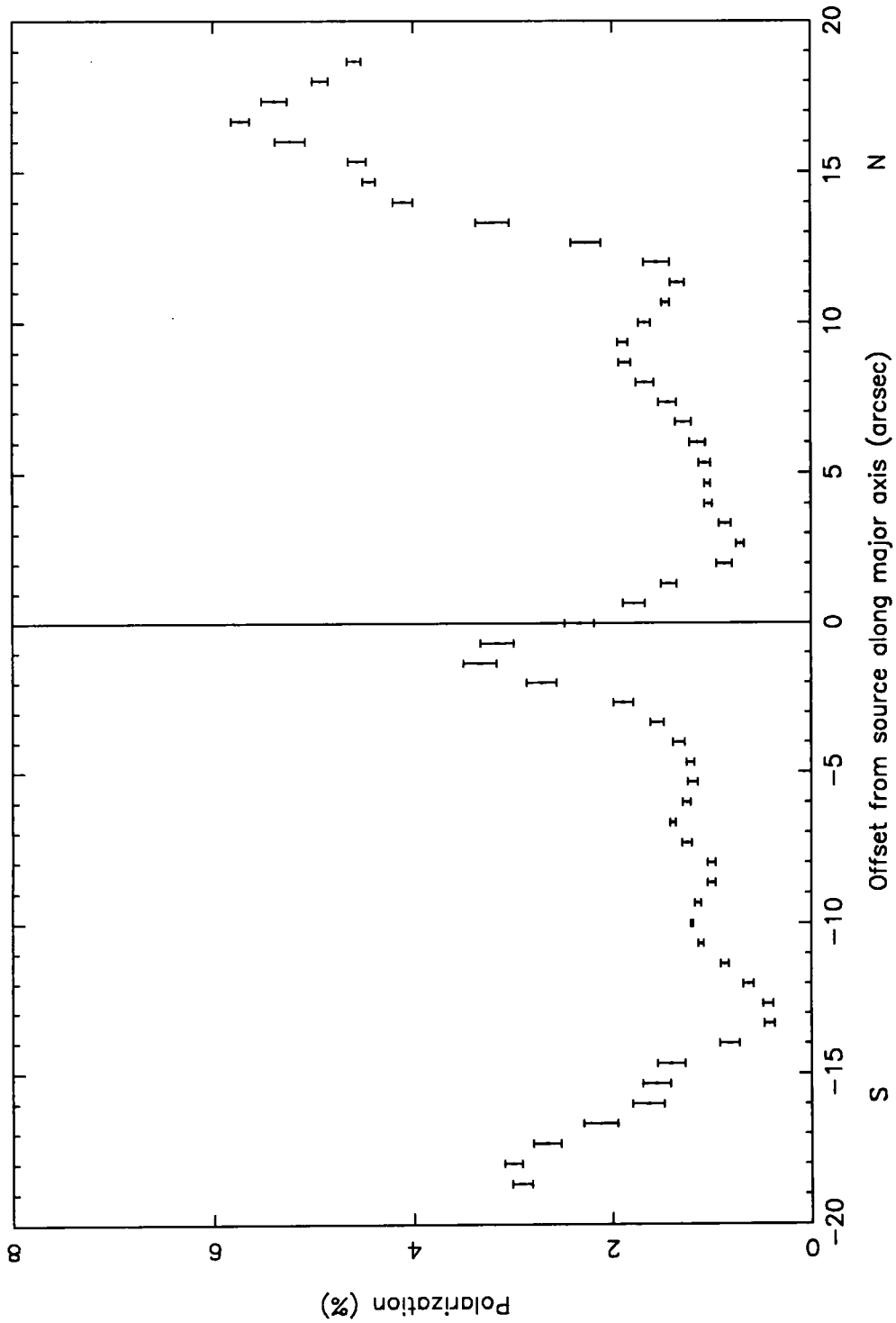

Figure 4.5: A trace of polarization (corrected for the effects of ISP) along a line 3.57 arcseconds west of the central core

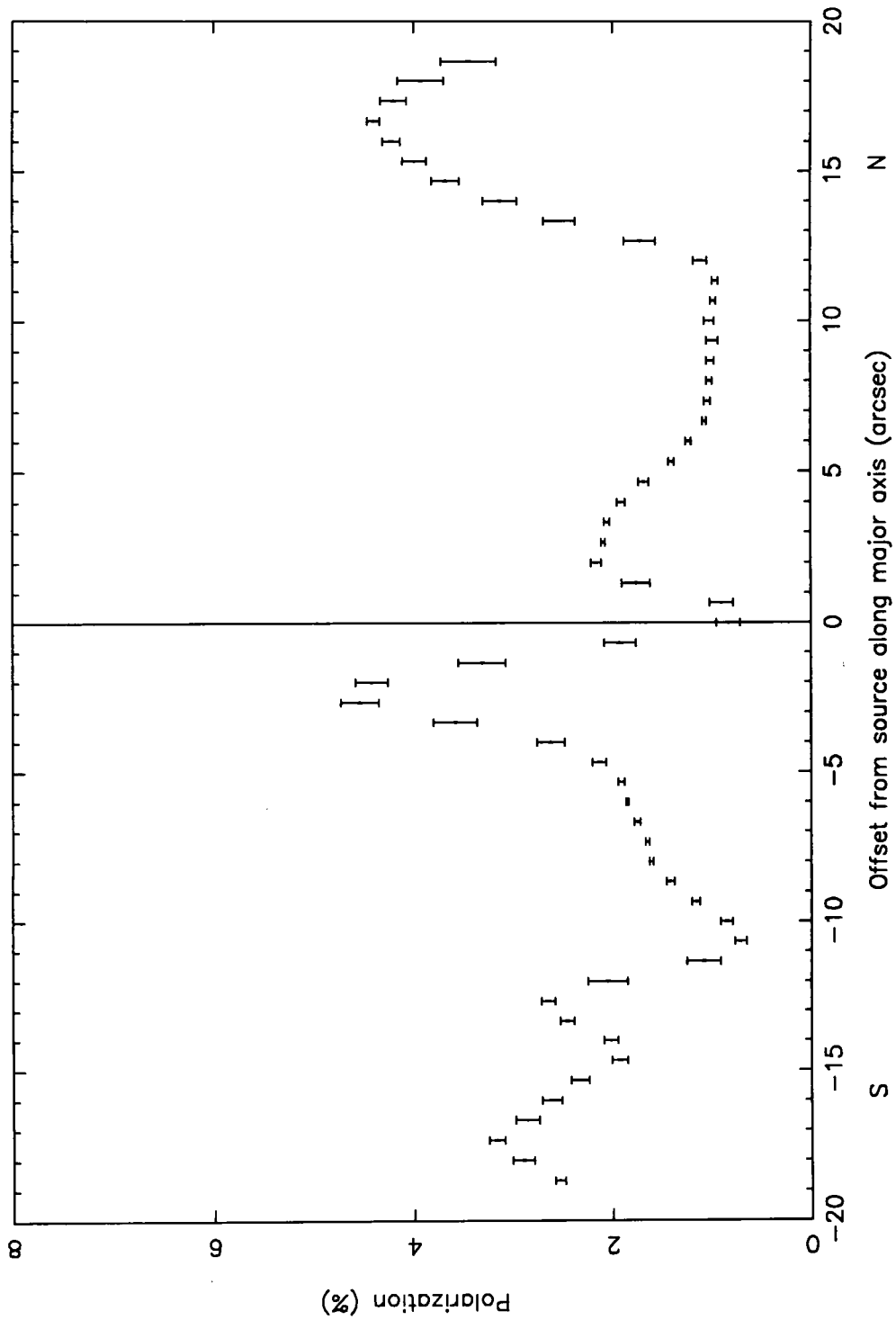

Figure 4.6: A trace of polarization (corrected for the effects of ISP) along a line 5.00 arcseconds east of the central core

There is a sharp peak in both plots some 2 to 3 arcseconds south of the central core and increasing levels of polarization occur as the measurement position moves outside of the inner lobe structures beyond 15 arcsecond offsets both to the north and south. The measured levels of polarization are not very high, averaging over some 2 to 6% maximum with the northern points consistently greater. The points at offsets of $\sim$ 15 arcseconds represent the positions where the edges of the hollow cavities, which comprise the inner lobes, end and we begin to measure the polarization which is due to scattering from the extensive surrounding envelope and which is comprised of neutral and dusty material. The inner 10 arcsecond region essentially covers the areas of the emission lobes.

Figure 4.7 and Figure 4.8 trace the polarized intensity along positions corresponding to the polarization plots of Figure 4.5 and Figure 4.6. The same apertures and measurement positions were used as for the polarization trace.

The plots show sharp peaks in polarized intensity corresponding to the offset positions of the intersection points with the hollow lobe structures. In addition, the correspondence between the high peaks in polarized intensity and the bright emission knots seen in the intensity images, but with no corresponding effect on the levels of polarization, would suggest that these points indeed coincide with locations along the walls of hollow spherical cavities on which dusty material is being shocked or excited, presumably by the action of a stellar outflow from the central core. This could be in the form of a high-velocity wind.

Figure 4.9 shows a greyscale polarization image which has been corrected for the effects of ISP. The scaling of the image is such that darker regions represent lower polarization levels, whereas the lighter parts are more highly polarized. Immediately obvious is the line of low polarization stretching across the object at a position which is coincident with the previously mentioned swathe of polarization vectors, some 1 to 2 arcseconds north of the central core, seen in Figure 4.3. This feature could certainly be linked with the supposed disk structure which is also believed to pass some 2 to 3 arcseconds north of the central core.

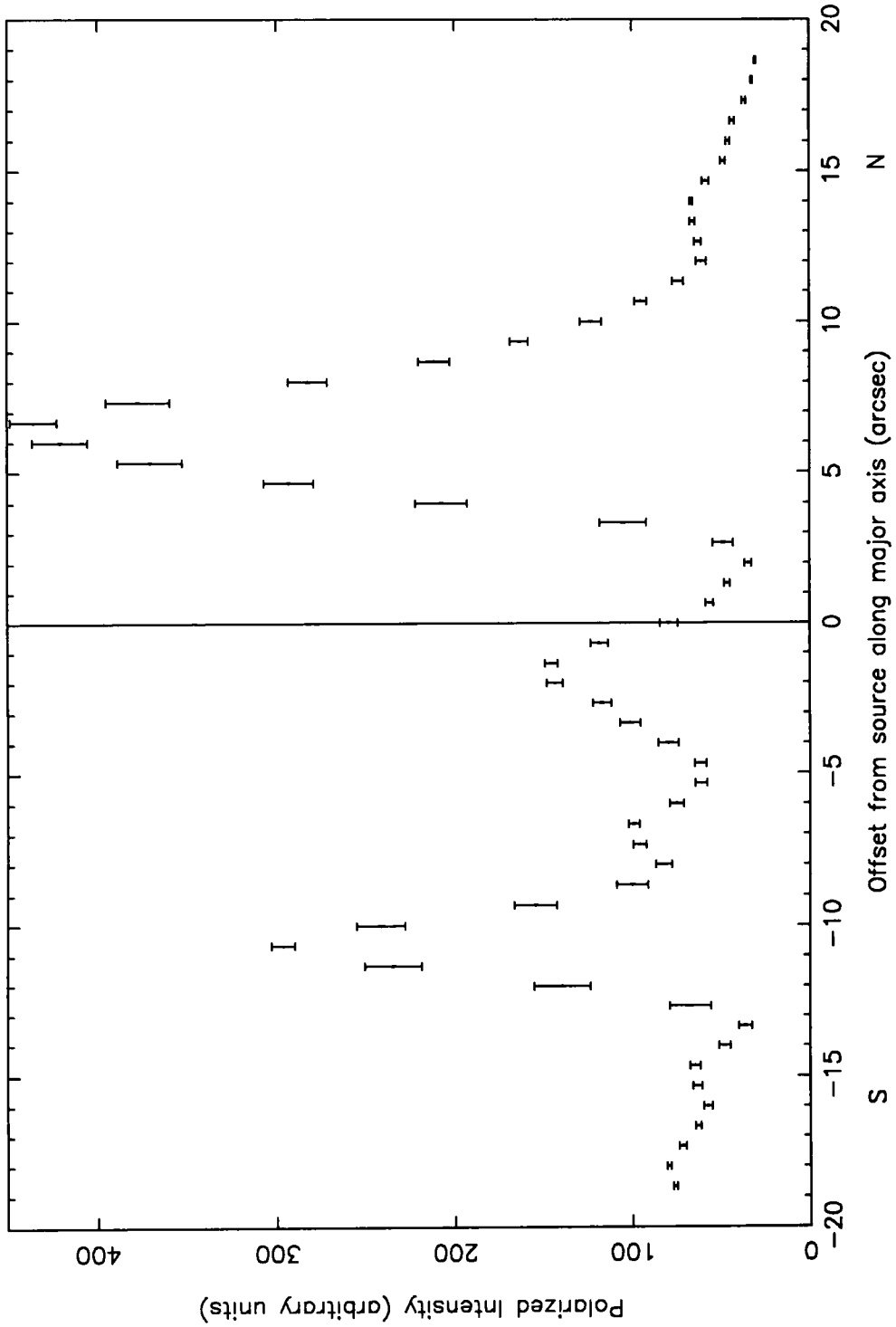

Figure 4.7: A trace of polarized intensity (corrected for the effects of ISP) along a line 3.57 arcseconds west of the central core

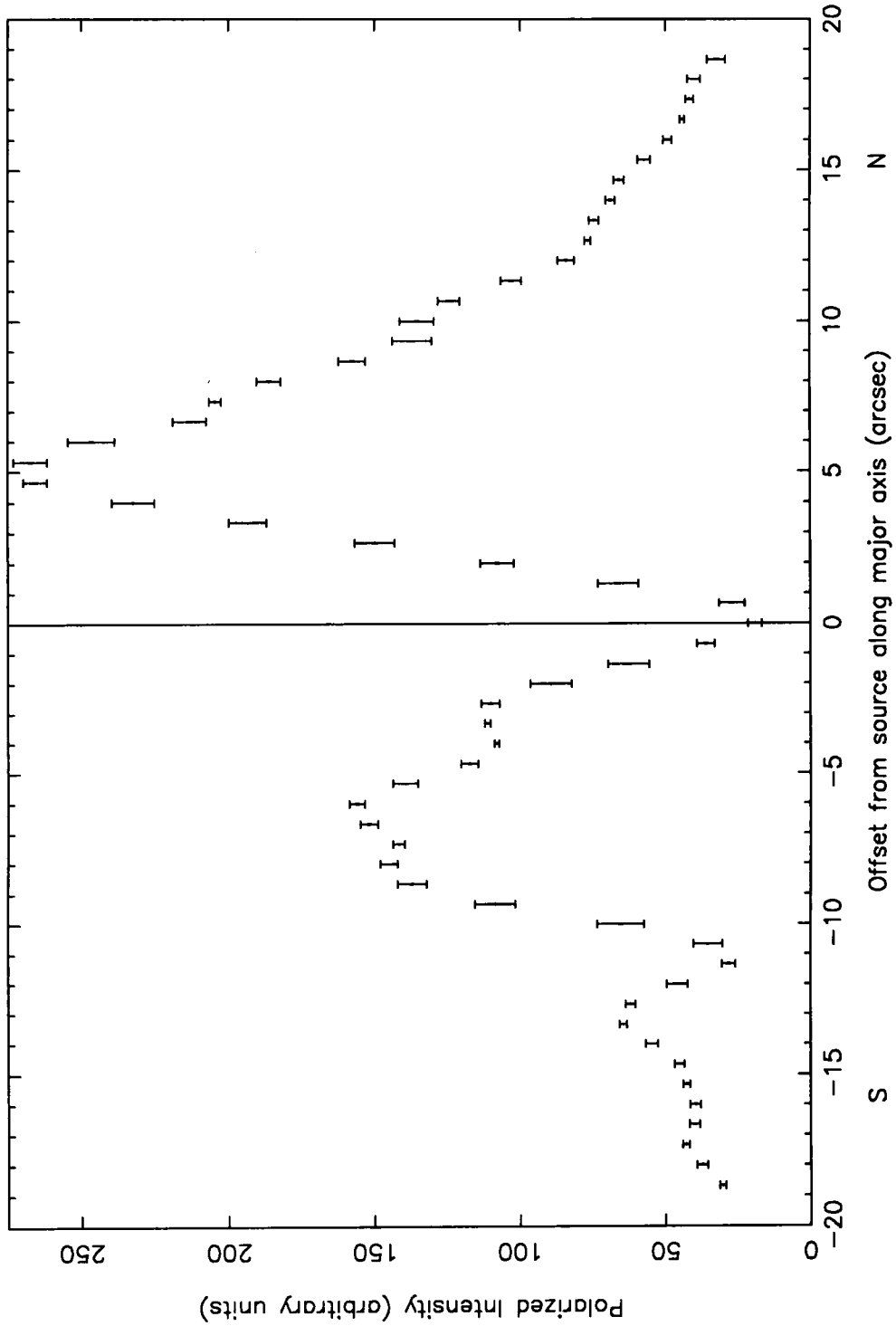

Figure 4.8: A trace of polarized intensity (corrected for the effects of ISP) along a line 3.57 arcseconds west of the central core

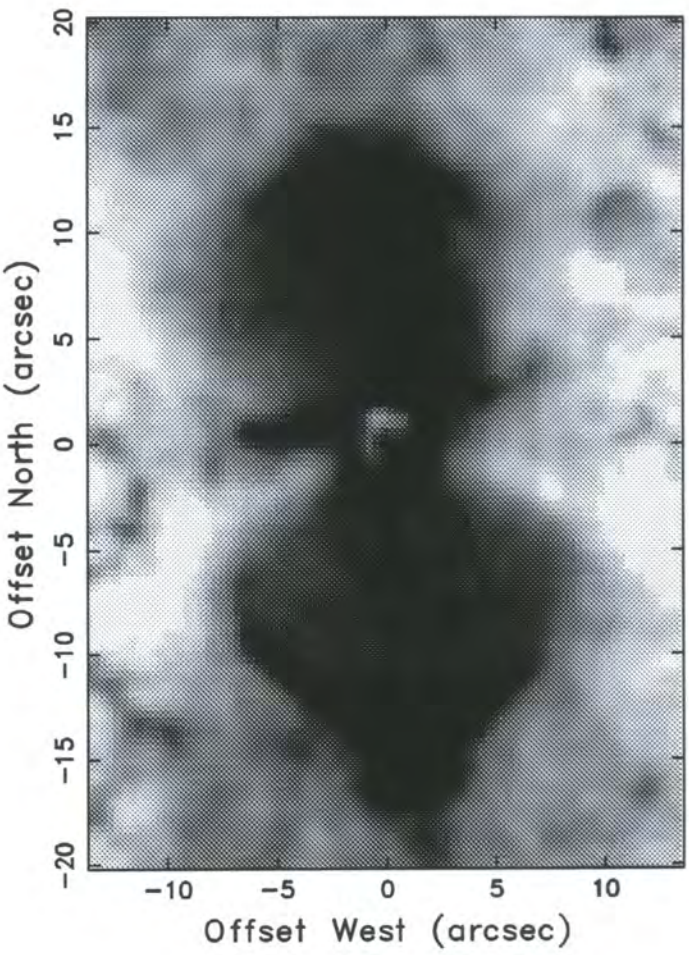

Figure 4.9: Greyscale polarization image of Mz 3 in Hα (corrected for the effects of ISP)

4.4 Discussion

4.4.1 The inner bipolar lobes

It is known with some certainty that Mz 3 is tilted with respect to the line of sight. The value of the tilt angle is thought to be of the order of 30 degrees. The expected presence of a circumstellar disk in such a system would imply that the disk structure also be tilted accordingly, and obscure to some degree part of the visible nebula. The spectroscopic data imply that the nebula is tilted with the southern lobe directed toward us, so that a disk structure would overlie and obscure the northern lobe. This is consistent with what is observed in that the northern lobe is foreshortened and not so clearly defined as the southern lobe. There are regions of enhanced emission at certain points around the bright lobe perimeter. In particular, the bright emission region some 7.5 arcseconds north and 3 arcseconds west also corresponds with a maximum in the 10 μm data of Quinn *et al.* (1996) but is not polarized to any significant degree above the level of the surrounding regions.

This suggests that it is the result of shock excitation on the walls of a cavity filled with hot ionized gas. Indeed, the polarization data given here in conjunction with the earlier V-band data of Scarrott & Scarrott (1995), does reinforce the idea that all the bright knotted regions seen around the perimeter of the inner lobes are the result of ionizing material constrained to flow over the hollow cavity walls of the lobes and, in doing so, shock exciting material in the walls. The appearance of the brightest emission towards the tips of the southern lobes suggests that a hydrodynamic stellar wind model would be an appropriate mechanism for the creation of the hollow 'bubbles' which comprise the bright bipolar lobes. The northern lobe is not so clearly defined or explainable by the same logic.

It is possible, however, that the extremities of this lobe, being tilted away from the line of sight, are obscured to direct viewing and instead we see only shock excitation in the walls of the lobe in less obscured locations to the northeast and northwest of the central region.

4.4.2 Evidence for a circumstellar disk?

There are morphological pointers to the existence of a circumstellar disk around the central region of Mz 3. The narrow waist, particularly, suggests the presence of some obscuring matter surrounding the central core. For a tilted nebula, the disk will also be

tilted, and presumably at the same angle. The polarization data presented here suggests that such a disk is indeed present. The levels and orientation of the observed polarization in the east-west direction some 2 to 3 arcseconds north of the central core, coinciding with the belt of low polarization seen in Figure 4.9 imply the presence of some large scale structure at that location. There seems to be no persuasive argument to forbid the assumption of a disk structure, which certainly seems to be required by the general morphology of the object, and that affects the nature of the polarization in this region. The structure is not noticeable in the V-band data presented by Scarrott & Scarrott (1995), which suggests that we are seeing emission from the disk structure in this narrow-band data rather than scattering from the edges of the disk after the fashion of that observed in other PNs such as M 2-9 (Scarrott, Scarrott & Wolstencroft, 1993).

4.4.3 The nature of the dust grains in Mz 3

Within the inner lobe structures, the levels of polarization are very low. It has been shown that these regions are essentially devoid of dusty material, being hollow cavities filled with ionized gas. Dust is present along the walls of the inner lobes and appears to be uniformly distributed in the regions surrounding the cavities. Shock excitation of material focussed at the tips of the lobes is evident, probably as a result of the continued effect of a supersonic stellar wind from the central source.

However, outside of this region, the object is surrounded by a large scale reflection nebula where scattering from dust is prevalent and becomes obvious via the levels and orientations of the polarization. In the V-band, the differentials in degree of polarization between the north and south of the object are of the order of 30% to 17%. Such levels of polarization are not observed in the Hα data presented here. The levels are much reduced at 8% and 6% respectively. However, the fact that there is a clear difference in the levels of polarization between north and south may enable a further estimate of the nebular tilt angle and suggestions as to the possible nature of the dust grains present in the object.

Following a similar analysis to that applied for M 1-16 (see Chapter 3.4), there is again a suggestion that the scattering geometry, which defines the levels of observed polarization for a scattering process, is becoming more favourable at greater offset distances such that the scattering angle is approaching 90 degrees. Under the same considerations as before, that is, the Rayleigh scattering curve (Figure 2.1) and a simplified scattering geometry

model (Figure 3.12), in conjunction with the observed maximum levels of polarization of some 30% in the V-band and $\sim$ 8% in Hα, a limit on the possible tilt angle of the bipolar axis in the nebula can be tentatively set[1]. It has been shown already (§3.4) that an observed polarization of 30% implies a scattering angle of 43 degrees. This value again limits the tilt of the bipolar axis to $\leqslant$ 47 degrees from the plane of the sky. This is not inconsistent with the value of 30° quoted earlier, but does not enable us to place a tighter constraint on the tilt angle.

However, levels of polarization are higher in the north than the south and scattering from Mie particles composed of high-albedo materials produces a maximum in the polarization at scattering angles greater than 90 degrees. The Mie scattering curves presented in Chapter 2.5 again enable further comments to be made.

Considering first the polarization properties of 'bare' grains under a normal power law size distribution. The observed levels of polarization to the north and south of the central region of the object place constraints upon the character of the dust grains responsible for the scattered light. In this case, the polarization from the dust grains should possess the following properties in the V-band

- $P_{max} \sim 30\%$
- $P(90° + \phi) > P(90° - \phi)$
- $P(90° - \phi) \sim 17\%$

where P_{max} is the magnitude of the peak polarization obtainable with a particular set of dust grain parameters and ϕ is the angle of inclination of the nebula bipolar axis.

Accordingly, for each of the dust grain materials considered, I compute a set of grain parameters which give an optimum fit to the observed levels of polarization using the fitting function

$$\Delta = \left\{ \frac{(P_{90°-\phi} - 17)^2}{17} + \frac{(P_{90°-\phi} - 30)^2}{30} \right\}^{\frac{1}{2}}$$

[1] At these positions, the lobe system is assumed to be optically thin so that a single scattering approximation is acceptable, whereas within the central $\sim$ 5 arcsecond region of the object this assumption would likely be inapplicable

The grain parameters (a_{min}, a_{max} and γ) and the nebula inclination angle (ϕ) were again allowed to vary over a suitable range of values and Δ computed for each parameter set. The results are presented in Tables 4.3 through 4.5. In this instance, dirty ice grains were not considered a likely candidate for inclusion in this case as there is no evidence from the observational database that ice is present in Mz 3. As before, for each input parameter set, the values which give a minimum value of Δ are shown.

Table 4.3: Mie scattering calculations for 'bare' oxygen-rich silicate grains fitting to the polarization data of Mz 3 in the V-band

a_{min} (μm)	a_{max} (μm)	dm (μm)	γ	ϕ (°)	Δ
0.005	1.000		4.30	35	1.1886
0.050	1.000		4.50	35	1.1144
0.100	1.000		6.00	35	2.9427
0.005	0.500		4.30	35	0.9288
0.005	0.250		4.10	35	1.0344
0.050	0.250		4.30	35	1.2817
0.005	1.000		4.30	30	1.4210
0.050	1.000		4.50	30	1.2434
0.100	1.000		6.00	30	3.0101
0.005	0.500		4.30	30	1.0655
0.005	0.250		4.10	30	1.2462
0.050	0.250		4.30	30	1.5853
0.005	1.000		4.30	25	1.8996
0.050	1.000		4.60	25	2.1005
0.100	1.000		6.00	25	3.1287
0.005	0.500		4.30	25	1.5602
0.005	0.250		4.10	25	1.2677
0.050	0.250		4.30	25	1.6856

Table 4.4: Mie scattering calculations for 'bare' amorphous carbon grains fitting to the polarization data of Mz 3 in the V-band

a_{min} (μm)	a_{max} (μm)	dm (μm)	γ	ϕ (°)	Δ
0.005	1.000		3.50	35	6.3311
0.050	1.000		3.50	35	6.0056
0.100	1.000		5.00	35	3.2421
0.005	0.500		3.50	35	6.0243
0.005	0.250		3.50	35	5.8744
0.050	0.250		3.50	35	5.5843
0.005	1.000		3.50	30	6.7648
0.050	1.000		3.50	30	6.5373
0.100	1.000		5.00	30	4.6201
0.005	0.500		3.50	30	6.6742
0.005	0.250		3.50	30	6.4996
0.050	0.250		3.50	30	6.0433
0.005	1.000		3.50	25	7.5429
0.050	1.000		3.50	25	7.4995
0.100	1.000		5.10	25	5.0356
0.005	0.500		3.50	25	7.4571
0.005	0.250		3.50	25	7.0350
0.050	0.250		3.50	25	6.8943

Table 4.5: Mie scattering calculations for 'bare' silicon carbide grains fitting to the polarization data of Mz 3 in the V-band

a_{min} (μm)	a_{max} (μm)	dm (μm)	γ	ϕ (°)	Δ
0.005	1.000		5.00	35	1.4267
0.050	1.000		5.70	35	1.2906
0.100	1.000		3.50	35	6.4269
0.005	0.500		4.90	35	1.3566
0.005	0.250		4.90	35	1.2134
0.050	0.250		5.70	35	1.1782
0.005	1.000		5.00	30	1.0477
0.050	1.000		5.70	30	0.9612
0.100	1.000		3.50	30	6.4269
0.005	0.500		4.90	30	1.0360
0.005	0.250		4.90	30	0.9541
0.050	0.250		5.70	30	0.9500
0.005	1.000		5.00	25	1.5786
0.050	1.000		5.70	25	1.4112
0.100	1.000		3.50	25	6.4269
0.005	0.500		4.90	25	1.5012
0.005	0.250		5.00	25	1.3679
0.050	0.250		5.70	25	1.3423

The calculations for 'bare' grains permit the following conclusions

1. Homogeneous amorphous carbon grains cannot reproduce the nature of the observed polarization in Mz 3. Table 4.4 shows the poor level of fit to the polarization data. As was seen in the case of M 1-16, pure carbon grains display such a high level of polarization, greater than is observed. Varying the value of γ only serves to move the scattering angle of peak polarization to $< 90°$ and the grains become more forward scattering which is not compatible with the observational data. Removing the smallest grains from the distribution (a 'large grain model') also has the effect of making the amorphous carbon grains forward scattering.

2. Pure silicate grains are able to reproduce the observations reasonably well with a moderate power law index of 4.3 and with the largest grains removed from the distribution ($a_{min} = 0.005\,\mu$m; $a_{max} = 0.50\,\mu$m). A nebula inclination angle of $\sim 35°$ is also indicated which is consistent with the generally accepted value of 30° from velocity measurements.

3. Silicon carbide grains can also provide a good fit to the observed levels of polarization. A nebula tilt of 30° is suggested and the grain distribution parameters are well defined as $a_{min} = 0.05\,\mu$m, $a_{max} = 0.25\,\mu$m with $\gamma = 5.7$. The range of grain sizes

is reduced compared to the silicate result with no large ($\sim 1.00\,\mu$m) grains and, in addition, no very small grains. The distribution is weighted strongly towards the smaller grains however.

Turning to the core-mantle grain combinations. Although not reproduced here, it was not possible to obtain a better fit to the data using core-mantle grain combinations of oxygen-rich silicate/amorphous carbon and silicon carbide/amorphous carbon than that given by the uncoated grains. Under the constraints set out above, the predicted levels of polarization from these core-mantle combinations, as well as the predicted tilt of the nebula, are found to be higher than that observed.

The presence of pure silicate grains, as suggested by the Mie scattering models to the polarization data also agrees well with the prediction of the *IRAS* two-colour diagram categorization of van der Veen & Habing (1988) which expects that the object will have formed from an oxygen-rich environment (see section 4.1). The Mie scattering calculations are therefore quite consistent with this view.

4.5 Conclusions

Mz 3 is a young, strikingly bipolar PN displaying two opposing bright lobes either side of the central core which is believed to be obscured from direct view by a circumstellar disk. The V-band polarization data of Scarrott & Scarrott (1995) and the Hα data presented in this chapter, confirm and agree that the nebula is seen by a combination of emission and scattered light. The lobe structures are seen to be hollow cavities, blown in a surrounding dusty shell by presumed hydrodynamic wind processes, upon the surface of which, dusty material is dispersed.

The nebula is believed to be tilted with respect to the line of sight by some 30 degrees and the polarization data available, in conjunction with the results of Mie scattering calculations, confirms this figure. I find that the inclination of the nebula axis is between 30 and 35 degrees. It would be possible to perform further calculations at a higher resolution in nebula tilt angle but it is unlikely that this would produce any worthwhile, or more accurate, results.

I find no convincing evidence in the data for scattering from the edges of the presumed circumstellar disk structure and cannot therefore confirm that the nebula is tilted with the northern lobe directed towards or away from us. The foreshortening and obscuration of the northern lobe, however, strongly suggests that the northern lobe is inclined away from the line of sight. The levels and orientation of the polarization running in a band some $2-3$ arcseconds north of the central core argues strongly for the presence of a circumstellar disk. This could also imply that the northern lobe is tilted away from us as the observed structure must belong to the front edge of the disk, and it's position above the central core argues for the backward tilt of the northern lobes.

I find no support in the polarization data for the extended shell of dust surrounding the central core as suggested by Quinn *et al.* (1996). The outer edge of the shell is reckoned to lie at some 1.5 arcseconds from the core and it is probable that the resolution of the present data is insufficient to detect such a structure. In addition, the relative brightness of the central core makes it very difficult to isolate features which are in such close proximity.

The observed levels of polarization in Mz 3, again in conjunction with Mie scattering models, strongly suggest that the dust material in the object is formed from oxygen-rich silicate. This is in excellent agreement with what might be expected from an *IRAS* two-colour diagram analysis in that the nebula is believed to have evolved from an oxygen-rich environment. I find that the dust exists as a wide range of sizes with a power law size distribution similar to that often applied in models of the ISM. The power law index, in this case, is found to be somewhat higher than the canonical 3.5 at a value of ~ 4.3. It is not necessary to invoke the possibility of core-mantle grains in explaining the levels of polarization in this object, indeed, it was not possible to obtain a physically realistic combination of core-mantle grain materials which gave a better fit to the observational data than that obtained with the 'bare' silicate grains.

Chapter 5

The protoplanetary nebula IRAS 09371+1212

The bipolar nebula IRAS 09371+1212, located at position RA $09^h\,39^m\,53^s.6$ Dec $+11°\,58'\,54''$ (2000.0), is a beautiful representative example of those objects which are undergoing the transition between AGB and PN stages, or PPNs. This particular object precipitated considerable interest through the observation that its IRAS colour temperatures were exceptionally cold, eventually leading to it being nicknamed the "Frosty Leo" nebula. High resolution adaptive optics imaging of the nebula strongly suggests that the central source of the bipolar outflow is an interacting binary system. In this chapter, multiwaveband optical polarimetry maps are presented, derived from data obtained with the Durham Imaging Polarimeter. An analysis of the data has previously been published (Scarrott & Scarrott, 1994, 1995), but the results given here are based upon a reappraisal of the data, particularly with regard to the nature of the dust material in the nebula.

5.1 Previous studies of IRAS 09371+1212

The luminosity of many objects which are at an early stage in their evolution from Asymptotic Giant Branch star to planetary nebula emerges mainly at IR wavelengths. As a consequence, it is often the case that such objects are initially noticed through the analysis of infrared survey data. This was indeed the case with IRAS 09371+1212, which was observed to possess an unusually large excess in its 60 μm faint source IRAS

flux. Forveille *et al.* (1987), via 2.6 millimetre CO observations, identified the object as an evolved star with a substantial CO outflow. In addition, they proposed that the unusual 60 μm IRAS flux was due to emission in the 46 μm ice band and this in turn was attributed to the presence of substantial grain material in the form of ice. This proposal led directly to the object receiving its apt nickname, the "Frosty Leo" nebula.

Near-IR observations (Rouan *et al.*, 1988; Hodapp *et al.*, 1988; Geballe *et al.*, 1988) have verified a strong 3.1 μm ice band absorption and strongly suggest the presence of an optically thick disk viewed almost edge on (Rouan *et al.*, 1988; Hodapp *et al.*, 1988). The same near-IR data suggests dust grain diameters up to 1.0 μm are present in the inner envelope of the nebula which is expanding at some 10 kms^{-1} (Dougados *et al.*, 1992).

Far-IR observations (Omont *et al.*, 1990) appear to confirm the hypothesis that the ice component is present as a crystalline coating of pure ice on very cold (< 50 K) silicate dust grains, contributing $\sim 66\%$ to the IRAS 60 μm flux.

Optical spectroscopy of the scattered light from the object identifies the central star as of spectral type K 7III or K 7II, with no evidence of line emission in the wavelength range 0.4-1.0 μm (Mauron *et al.*, 1989; Morris & Reipurth, 1990).

Millimetre observations suggest an expanding molecular envelope ($\sim 25\,\mathrm{kms}^{-1}$), corresponding to a mass loss rate of $2 \times 10^{-6}\, d^2(\mathrm{kpc})\ \mathrm{M}_\odot\,\mathrm{yr}^{-1}$ (Forveille *et al.*, 1987).

The distance to IRAS 09371+1212 is, however, uncertain. A lower limit of 1.0 kpc has been assigned by Mauron *et al.* (1989). This same value for the distance is alternatively given as an upper limit by Langill, Kwok & Hrivnak (1994) on the basis of its high Galactic latitude (b=42°.7). At this distance then, the rate of mass loss is of the order of $2 \times 10^{-6}\ \mathrm{M}_\odot\,\mathrm{yr}^{-1}$ from the result above.

Near-IR polarization data also infers a disk structure seen virtually edge on, and that single scattering from ice-coated silicate grains dominates the emission from the extended nebular envelope. There is also some evidence for a central cavity in the nebula (Dougados *et al.*, 1990).

Optical polarization (Scarrott & Scarrott, 1994, 1995) confirm the presence of an extensive, thin disk structure which completely obscures the central stellar source from view. The observed high levels of linear polarization ($\sim 60\%$) in the prominent *ansae* are believed to arise from ice-coated silicate grains with a lower size limit of $\sim 0.1\,\mu$m and a power-law size distribution index somewhat greater than that typically adopted for ISM grains. Bastien & Ménard (1990) have found that the disk is tilted to the line of sight at an angle of 15 degrees. However, Dougados *et al.* (1992) find in favour of an angle less than this and Scarrott & Scarrott (1994) suggest a tilt angle below 10 degrees is applicable.

K-band imaging (Beuzit *et al.*, 1994) of the inner 6 arcseconds shows that the source is not exactly at the center of the nebula image. It is located on the equatorial line of the pinched waist, but slightly offset to the west by 0.25 arcseconds from the centroid of the intensity isophotes.

The data does not confirm the presence of a companion star. The intensity isophotes do show pronounced deviation from circular symmetry, however, with an apparent narrowing in the equatorial plane direction and with two lobes extending NNW and SSE from the source (at a position angle of -14 degrees). Morris & Reipurth (1990) found a value of the position angle -25 degrees but this is based upon larger scale images and the inner isophotes are tilted slightly with respect to the outer ones. The inner lobes are asymmetric with the southern lobe intensity peak 0.8 arcseconds S of the source position. Dougados *et al.* (1990) and Forveille *et al.* (1987) find evidence for a central cavity extending over a few arcseconds from the star, probably due to interrupted mass loss. Radiative transfer models show that the brightness distribution within the cavity should be flat, peaking at the cavity radius and then dropping off as the radial distance squared. Beuzit *et al.* (1994) give supporting evidence for this at radial distance 0.9 arcseconds from star, but suggest that there cannot be a circular cavity as the ring of brightness would be circular around the star. That this is not seen could be due to obscuration by a disk or possibly the cavity is elongated in the polar direction and not spherical. Morris (1987) invokes a binary source to explain a possible disk presence. Since the star is not at the isophotal centre, either the scattering material comes from an unseen companion, or the star was located at a different location when the material was ejected (Beuzit *et al.*, 1994).

Near-IR adaptive optics imaging of the nebula (Roddier *et al.*, 1995) supports the binary model for the central source. The images, which the authors believe resolves the binary

system, imply that the two stars must be of similar spectral type (K7III) and shows evidence of absorption by a dust disk. Their bicone model argues for a nebula tilt of some 15 to 20 degrees and for the northern lobe of the object being tilted towards us, contrary to the view of Morris & Reipurth (1990) and Scarrott & Scarrott (1994).

IRAS 09371+1212 has available flux data at 12, 25, 60 and 100 μm with the peak flux at $\sim 60\,\mu$m. Table 5.1 gives the flux data values of the IRAS point source catalogue for the object.

Table 5.1: IRAS flux densities for IRAS 09371+1212

IRAS flux density (Jy)			
F_{12}	0.27[a]	±	.
F_{25}	4.59	±	0.28
F_{60}	70.70	±	8.48
F_{100}	28.21	±	3.39

[a]The 12 μm flux is of poor quality with no estimate of uncertainty

Applying the definitions of van der Veen & Habing (1988), IRAS 09371+1212's IRAS colours are

$$\begin{aligned} [12]-[25] &= 2.5\log(F_{25}/F_{12}) = 3.14 \pm 0.14 \\ [25]-[60] &= 2.5\log(F_{60}/F_{25}) = 2.97 \pm 0.15 \\ [60]-[100] &= 2.5\log(F_{100}/F_{60}) = -1.00 \pm 0.18 \end{aligned}$$

The above colours are well outside the main groupings in the classification of van der Veen & Habing (1988). However, extrapolating outwards implies that the object is of Type V or VIII. Both of these regions are associated with very cool objects containing very cold dust. This is consistent with the perceived nature of IRAS 09371+1212.

The different definitions of Walker & Cohen (1988) and Walker *et al.* (1989) yield the following colours for IRAS 09371+1212.

$$
\begin{aligned}
[12]-[25] &= 1.56+2.5\log(F_{25}/F_{12}) &= 4.70 \pm 0.14\\
[25]-[60] &= 1.88+2.5\log(F_{60}/F_{25}) &= 4.85 \pm 0.15\\
[60]-[100] &= 1.11+2.5\log(F_{100}/F_{60}) &= 0.11 \pm 0.18
\end{aligned}
$$

Walker *et al.* specifically mention IRAS 09371+1212 as being well isolated from the main concentration of objects in their survey. They suggest that IRAS 09371+1212 may be in a very transitory phase and may have evolved from an intermediate mass progenitor rather than a low mass star.

5.2 Observational details

IRAS 09371+1212 was observed between 15-18 April 1991 at the f/15 Cassegrain focus of the 3.9 metre Anglo-Australian Telescope (AAT) using the Mark IV Durham imaging CCD polarimeter (Scarrott *et al.*, 1983; Scarrott, 1991) and an EEV P8603 CCD blue-coated detector. *BVRI* broadband filters (refer to Table 5.2 for filter specifications) were used to image the object in seeing conditions of approximately 1-2 arcseconds. Short and long exposures (in order to obtain data on both the bright and faint regions of the nebula), ranging between 20 and 400 seconds, were made in each filter and at one single telescope position. The data were reduced in the standard manner (Draper, 1988).

Table 5.2: Specifications of broad-band filters for IRAS 09371+1212

Filter	Central Wavelength (μm)	FWHM (μm)
B	0.43	0.055
V	0.55	0.050
R	0.63	0.080
I	0.76	0.065

5.3 Results

5.3.1 Polarization maps

Some of the polarization data discussed in this Chapter has previously been published in Scarrott & Scarrott (1994, 1995). However, it would be useful and appropriate at this stage to review the morphology and general appearance of IRAS 09371+1212 in each of the four wavelength bands for which data is available. In fact, the object appears very similar in each of the wavebands. However, Figure 5.1 through Figure 5.4 display greyscale intensity contour and linear polarization maps for observations in the B, V, R and I filters respectively. A brief description of each image is warranted.

5.3.1.1 B filter observations

The greyscale contour image and polarization map of IRAS 09371+1212 in the B-waveband, derived from data obtained with the Anglo-Australian Telescope, is shown in Figure 5.1. The image coordinate system is in arcseconds. Adopting a distance to IRAS 09371+1212 of 1 kpc (Mauron *et al.*, 1989; Langill, Kwok & Hrivnak, 1994), one arcsecond in the image corresponds to a distance of some 0.005 parsecs or $\sim$ 1000 AU in the plane of the sky. Intensity contours are used to clarify the brightness distribution of the nebula. The contours are logarithmically spaced at intervals of 0.3 magnitudes. The magnitude and orientation of the linear polarization in the object is represented by vectors which have been placed into square bins of size 7 pixels (2.24 arcseconds) and spaced at intervals of $\sim$ 2.3 pixels ($\sim$ 0.75 arcseconds). The brightest intensity contours are also plotted beneath the polarization data for clarification.

The intensity image displays two barely resolved bright inner lobes[1], which are separated by some 3 arcseconds, by a narrow 'waist', or a line of local minimum in the flux, corresponding to the presumed location of an almost edge-on optically thick circumstellar disk of material which obscures the central source(s) from direct view. The southern lobe is some three times brighter than the northern lobe in the B-waveband. At offsets of $\sim$ 12 arcseconds to the north and south of the source, prominent *ansae* are clearly visible. The image displays point reflection symmetry in the intensity isophotes which is most striking when considering the shape of the ansae. These appear to be 'opposed' to

[1]The data displayed in this section is essentially that of Scarrott & Scarrott (1994) and in common with their analysis, the lobes are referred to as 'north' and 'south', although the main axis of the nebula as defined by a line joining the ansae is at a position angle of 157 degrees

each other in that they brighten in opposite directions. This form of reflection symmetry has been seen in other planetary nebulae, such as K 3 – 35 (Aaquist, 1993) for example. An satisfactory explanation for the 'cometary' appearance of the ansae remains elusive. If the ansae are local concentrations, or knots, of material which are moving rapidly in a clockwise direction (in relation to the central source), the tails could be the result of drag as the knots move through an ambient spherically symmetric medium. There are problems with this scenario, however, as the implication is that the ansae must have performed many rotations around the nebula in the time it has taken for them to expand out to their present radial distance. The knots must then have been of very high density originally and would now display a smoother intensity gradient with the inner regions of the nebula. The ansae are seen to be quite distinct from the inner nebula and this scenario seems therefore quite incompatible with the observations.

The levels of polarization throughout the object are high and the vectors display the familiar centro-symmetric pattern that results from simple scattering of the central starlight by an extensive reflection nebula. Within the central 6 arcsecond region, however, the polarization vectors are distorted from the circular pattern and display orientations which are believed to arise through the influence of the presumed disk structure. Similar 'polarization disks' are seen in other bipolar nebulae Scarrott *et al.* (1992); Bastien & Ménard (1988); Scarrott & Scarrott (1994).

The plane of the disk appears to bisect exactly the bright inner lobes. Langill, Kwok & Hrivnak (1994) have shown that the position angle of the plane of the disk increases with increasing wavelength. In the B-waveband, this angle is expected to be $\sim$ 71.5 degrees. The position angle appears to change with a rate of 18.4 ± 0.7 degrees per μm over the visual wavelengths through to the near-IR. The lobes and disk rotate in the same direction and become more perpendicularly aligned as wavelength is increased.

5.3.1.2 V filter observations

The greyscale contour image and polarization map of IRAS 09371+1212 in the V-waveband is shown in Figure 5.2. In this image, the intensity contours are logarithmically spaced at intervals of 0.32 magnitudes and the polarization vectors have again been placed into square bins of size 7 pixels (2.24 arcseconds) and spaced at intervals of $\sim$ 2.3 pixels ($\sim$ 0.75 arcseconds) as for the B-waveband.

The general morphology is very similar to that seen in the B-waveband image. Again the southern inner lobe appears brighter than the northern lobe by a factor of ~ 2.75.

The prominent ansae are clearly seen once again. The levels and pattern of polarization are very similar to that found in the B-waveband and the polarization disk is present. Langill, Kwok & Hrivnak (1994) showed that the separation of the ansae does not change with wavelength (at least over the visual part of the spectrum), but that the separation of the lobes does alter as a function of wavelength. It is seen that the lobes appear to move closer with increasing wavelength and that the position angle joining the lobes becomes more north-south aligned at longer wavelengths. The position angle of the lobes is seen to change at a rate of $22°.4 \pm 1°.4$ per μm. The lobes appear to 'spiral in' to the source position as they are viewed at longer wavelengths.

5.3.1.3 R filter observations

The greyscale contour image and polarization map of IRAS 09371+1212 in the R-waveband is shown in Figure 5.3. The intensity contours are logarithmically spaced at intervals of 0.4 magnitudes and the polarization vectors have been placed into square bins of size 7 pixels (2.24 arcseconds) and spaced at intervals of ~ 2.3 pixels (~ 0.75 arcseconds) as for the B-waveband and V-waveband data.

IRAS 09371+1212 is very red with the southern lobe being significantly brighter and bluer than the northern lobe. In this image, the southern lobe is brighter by ~ 1.75, so that the difference is not as great between the two lobes in this waveband. In contrast, the northern ansae is generally brighter than its southern companion (0.21 ± 0.03 in the V-band) but they have similar colours.

Again, the polarization data is comparable in terms of the polarization pattern and presence of the disk with the previous data. However, as the wavelength is increasing, it is clear that the magnitude of the polarization is increasing also.

5.3.1.4 I filter observations

The greyscale contour image and polarization map of IRAS 09371+1212 in the I-waveband is shown in Figure 5.4. The intensity contours are logarithmically spaced again at intervals of 0.4 magnitudes and the polarization vectors have been placed once more into square bins of size 7 pixels (2.24 arcseconds) and spaced at intervals of ~ 2.3 pixels (~ 0.75 arcseconds) as for the other data.

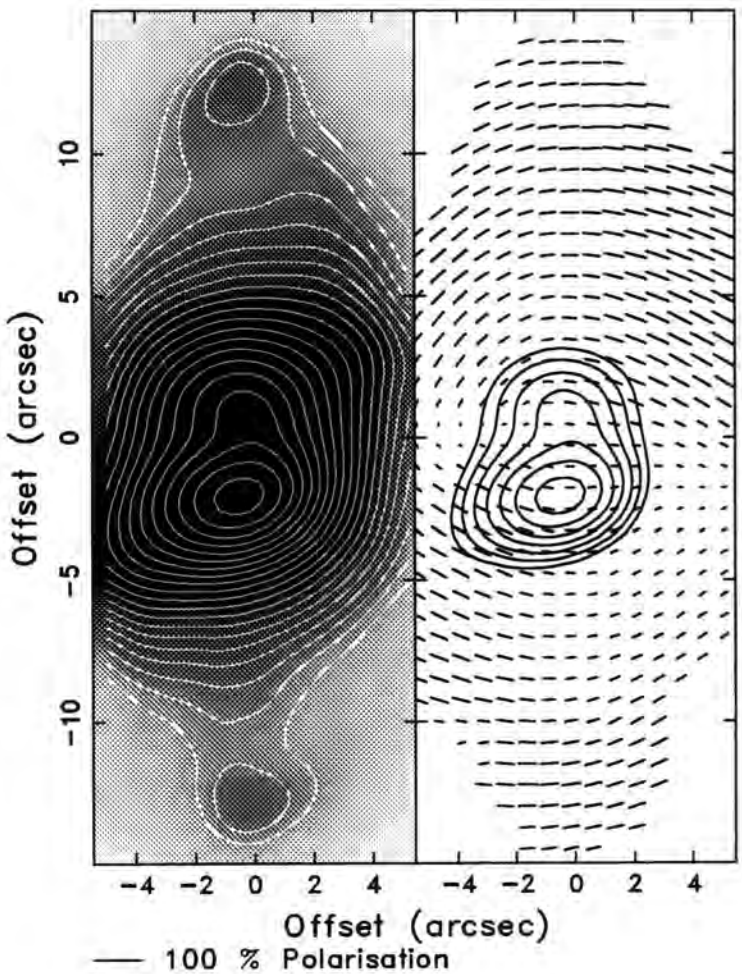

Figure 5.1: A greyscale intensity contour image and linear polarization map of IRAS 09371+1212 in the B-waveband

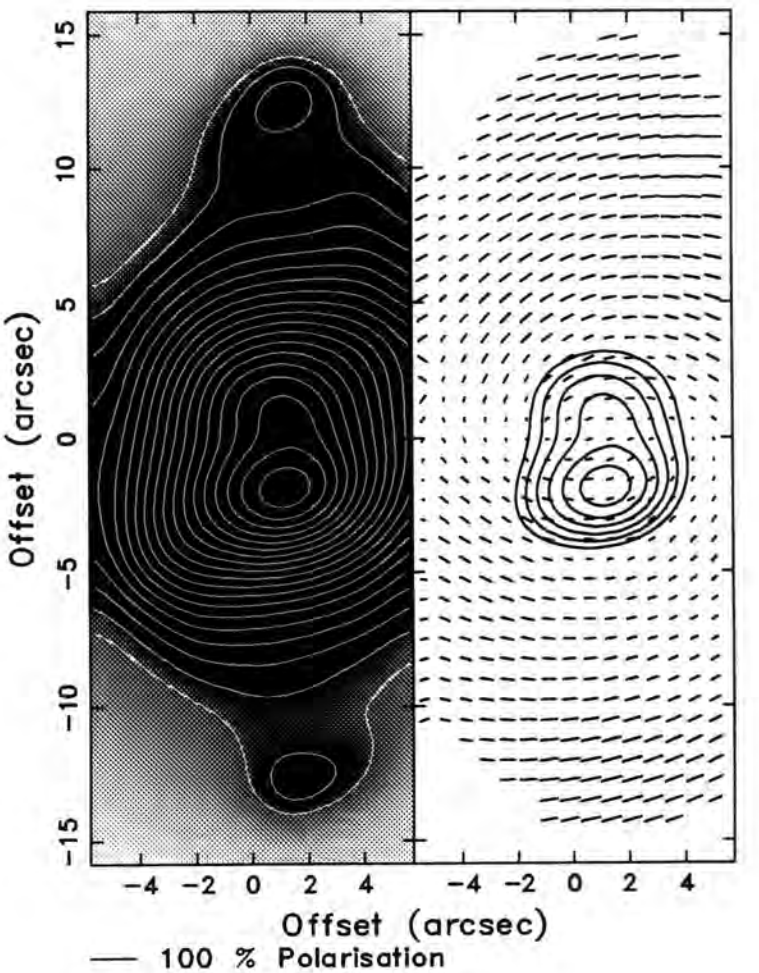

Figure 5.2: A greyscale intensity contour image and linear polarization map of IRAS 09371+1212 in the V-waveband

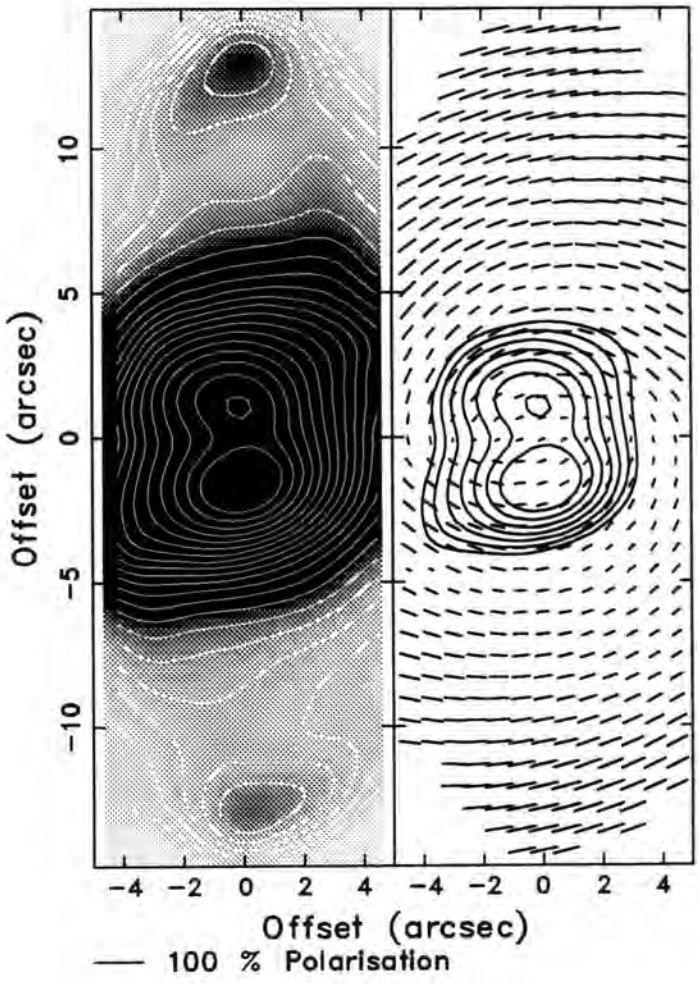

Figure 5.3: A greyscale intensity contour image and linear polarization map of IRAS 09371+1212 in the R-waveband

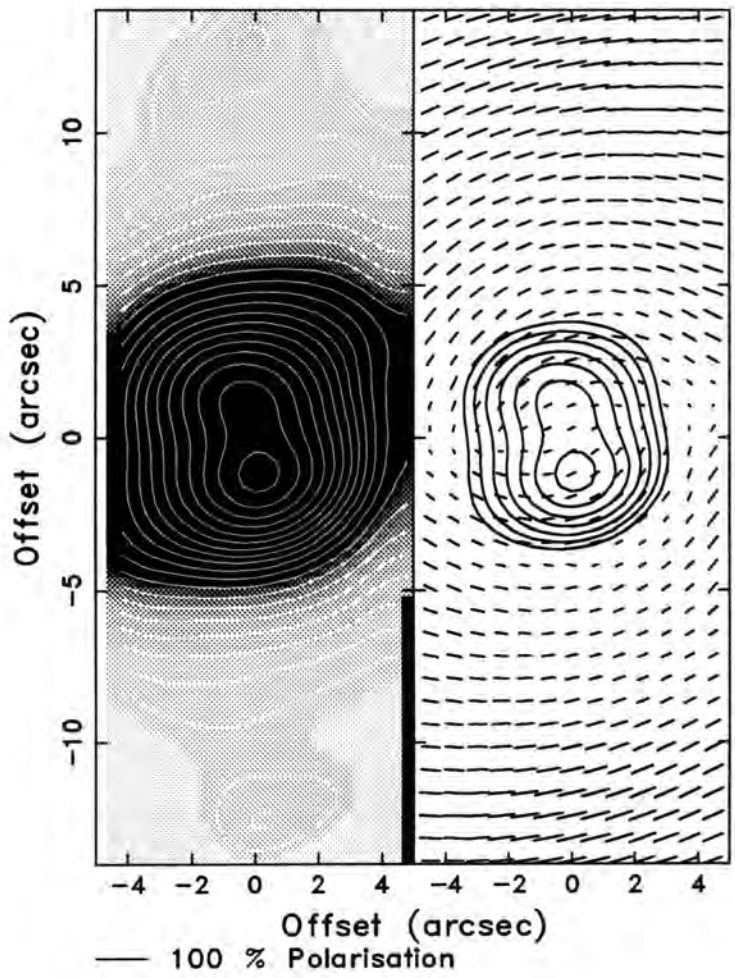

Figure 5.4: A greyscale intensity contour image and linear polarization map of IRAS 09371+1212 in the I-waveband

Once again, the southern lobe is brighter than the northern lobe by a factor of $\sim$ 1.8. The general appearance is consistent with the images in the other wavebands. Again the polarization vectors display strong centro-symmetry in the outer lobes and the polarization disk is evident bisecting the inner lobes.

Figure 5.5 through Figure 5.16 show traces of intensity, polarization and polarized intensity along an axis joining the ansae for data in each waveband. The zero position in each case is the point midway between the two bright inner lobes.

The traces of intensity, polarization and polarized intensity are very similar in appearance for each of the wavebands. The levels of polarization generally rise almost monotonically with radial offset from the central source reaching a maximum value close to the positions of the ansae. It is observed that the levels of polarization of the ansae are dependent upon the wavelength, with polarization increasing towards longer wavelengths. Measurements of the polarization of the ansae in each waveband, applying a 3 arcsecond diameter software aperture, results in the values given in Table 5.3.

Table 5.3: Polarization measurements of the ansae in IRAS 09371+1212

	Polarization (%)						Position angle (°)					
Filter	North			South			North			South		
B	36.2	±	12.8	36.2	±	10.6	150.1	±	9.8	149.3	±	8.1
V	47.2	±	1.1	45.3	±	0.8	142.9	±	0.6	141.2	±	0.4
R	60.0	±	2.9	61.1	±	2.4	145.2	±	0.8	143.3	±	0.7
I	58.1	±	1.7	57.2	±	1.4	145.2	±	0.7	142.8	±	0.5

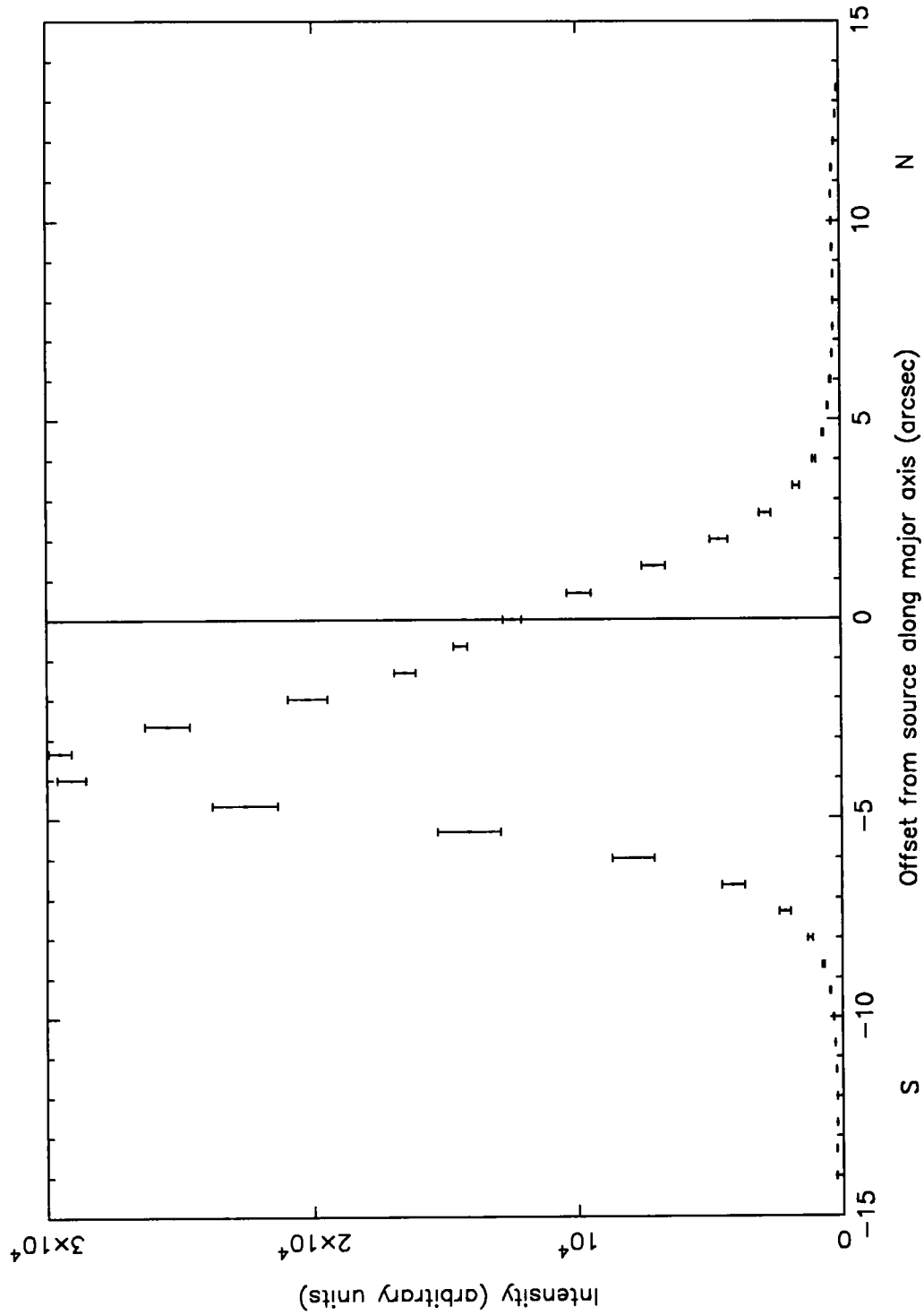

Figure 5.5: A trace of intensity along an axis connecting the ansae for IRAS 09371+1212 in the B-waveband

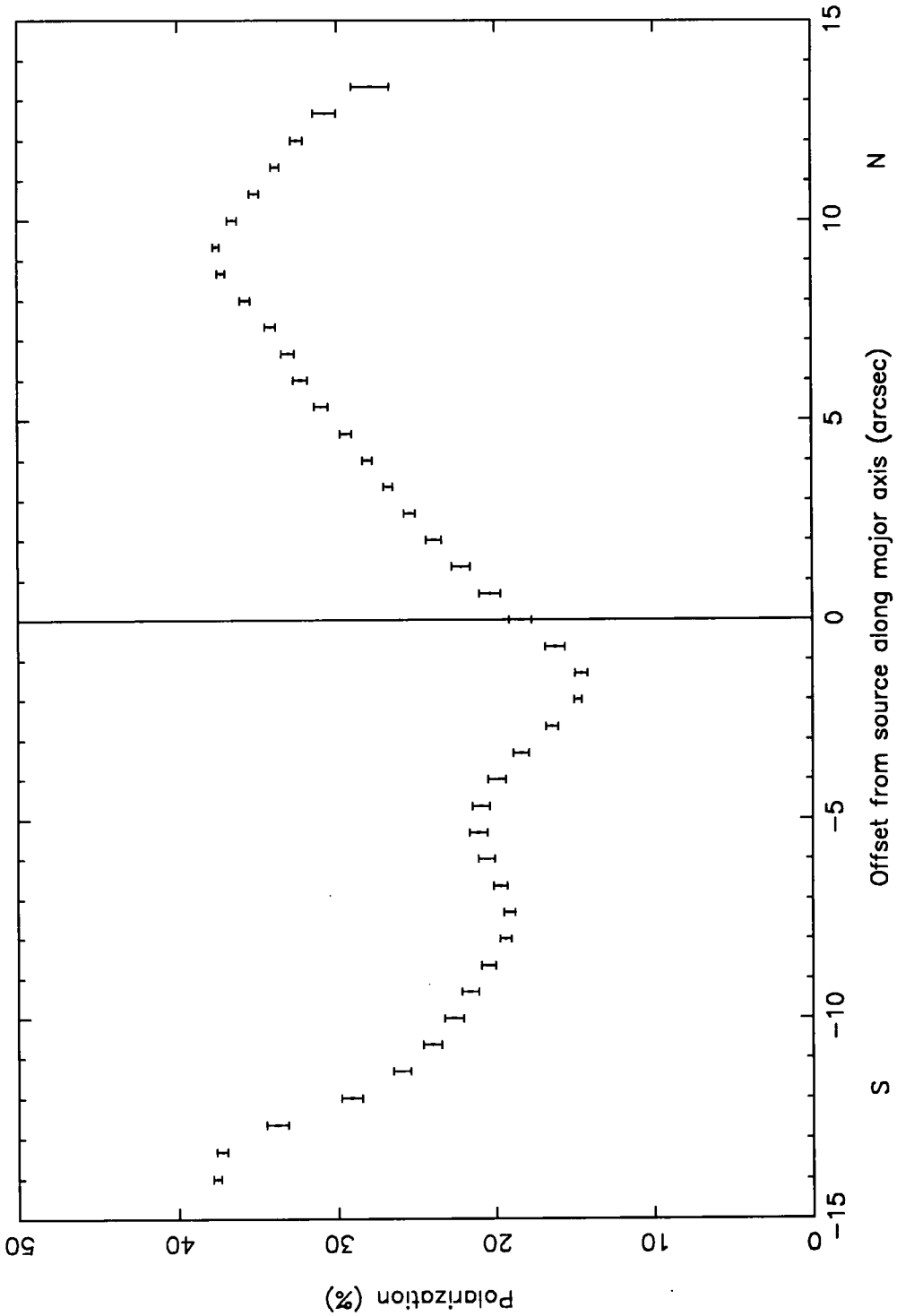

Figure 5.6: A trace of polarization along an axis connecting the ansae for IRAS 09371+1212 in the B-waveband

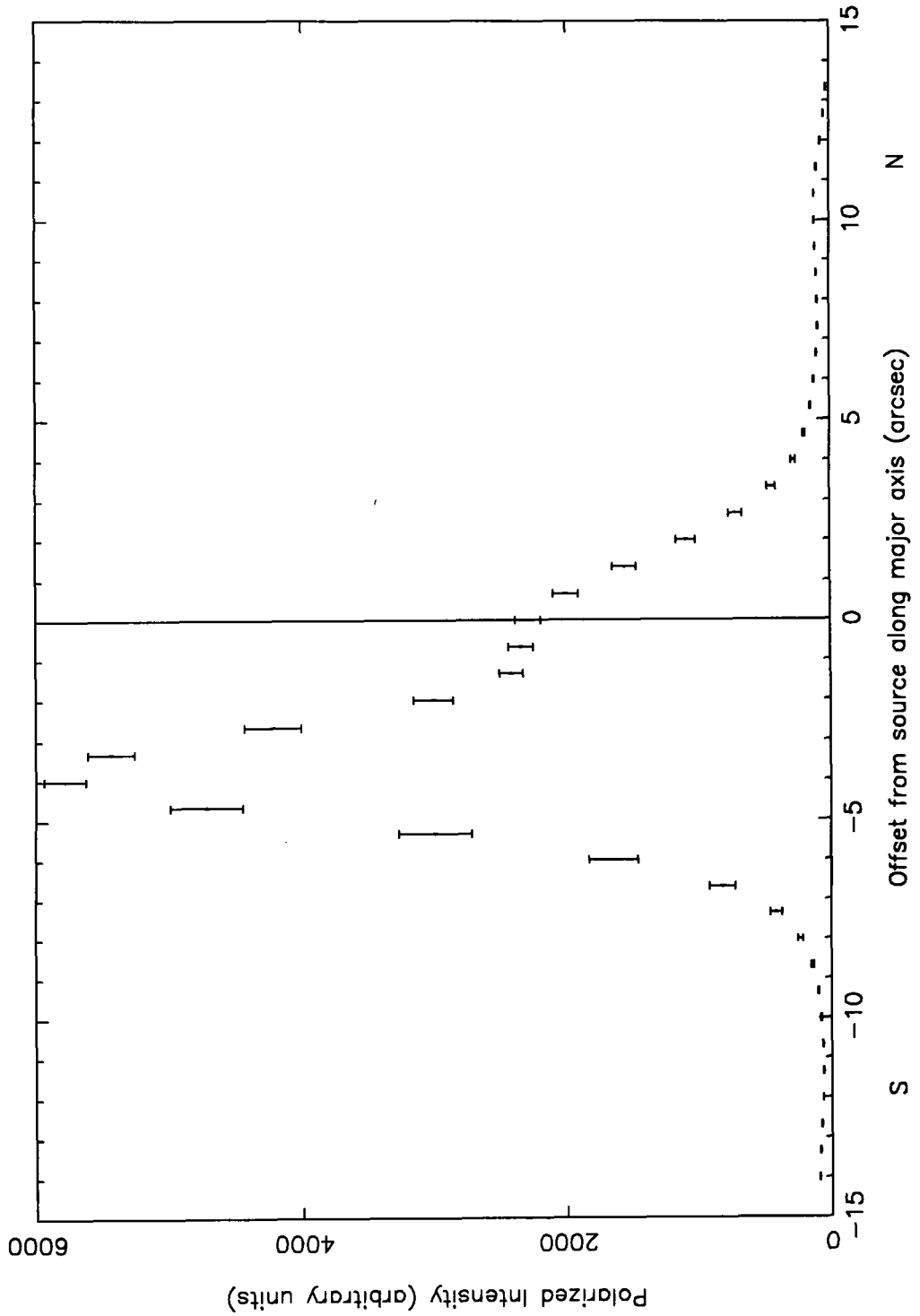

Figure 5.7: A trace of polarized intensity along an axis connecting the ansae for IRAS 09371+1212 in the B-waveband

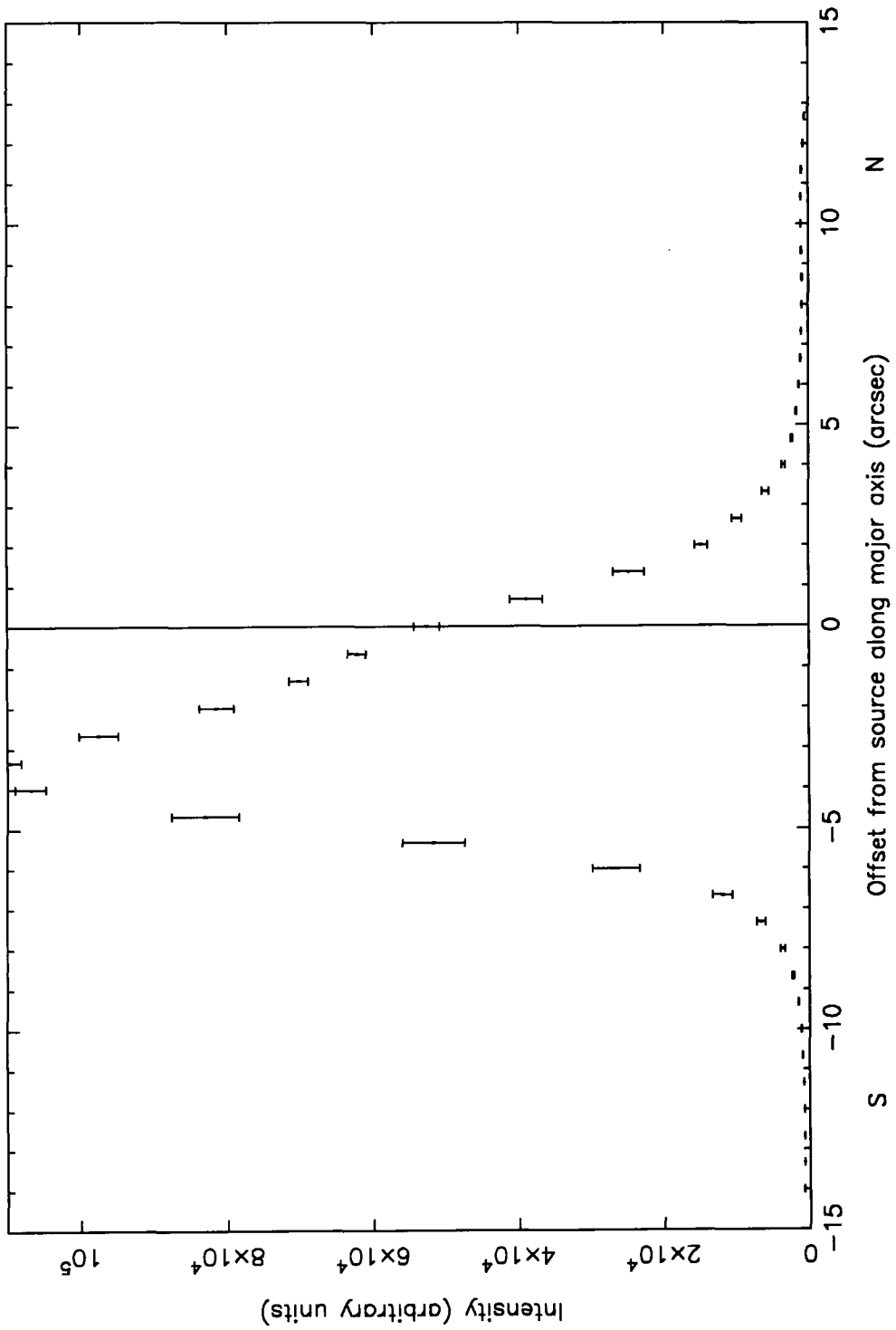

Figure 5.8: A trace of intensity along an axis connecting the ansae for IRAS 09371+1212 in the V-waveband

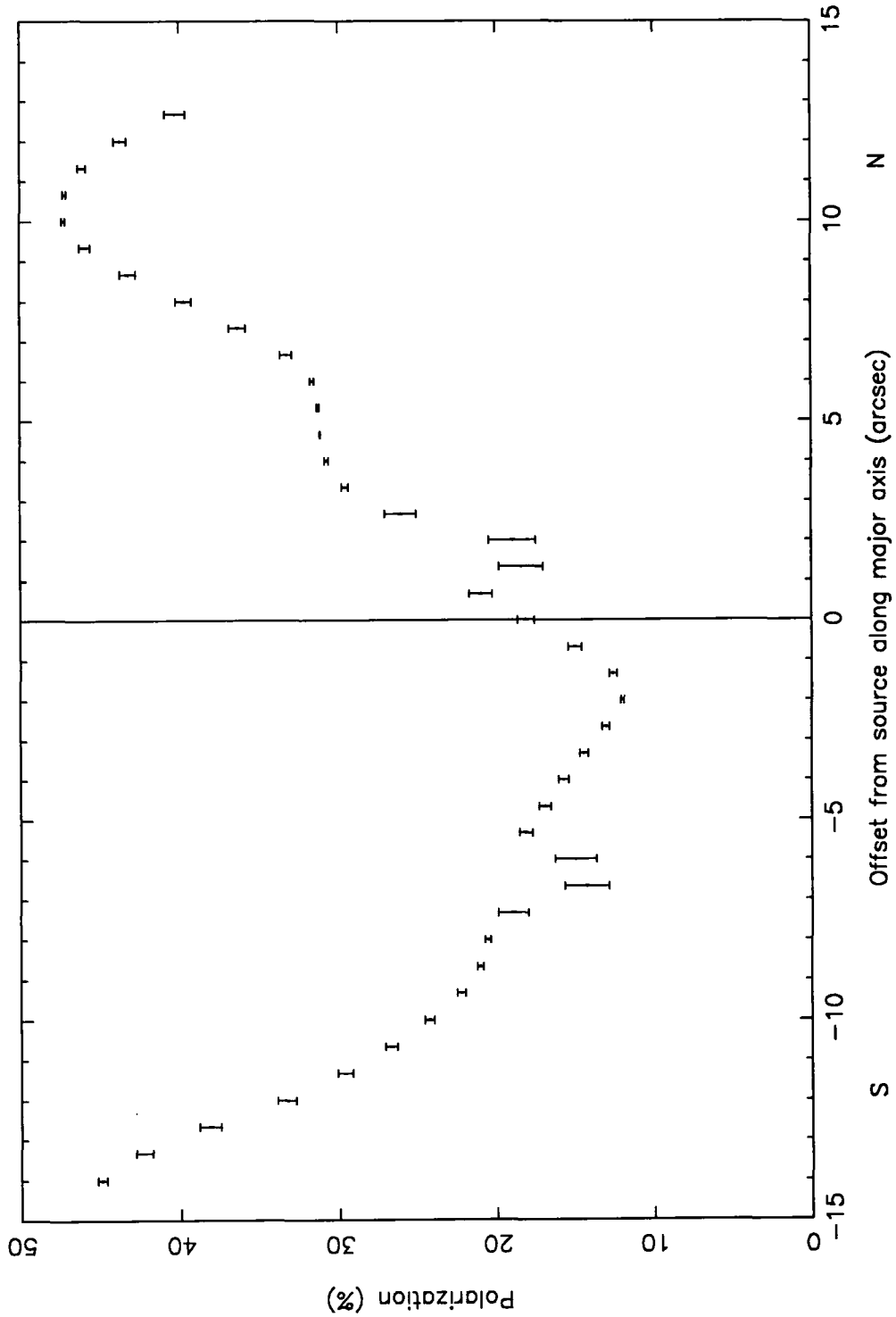

Figure 5.9: A trace of polarization along an axis connecting the ansae for IRAS 09371+1212 in the V-waveband

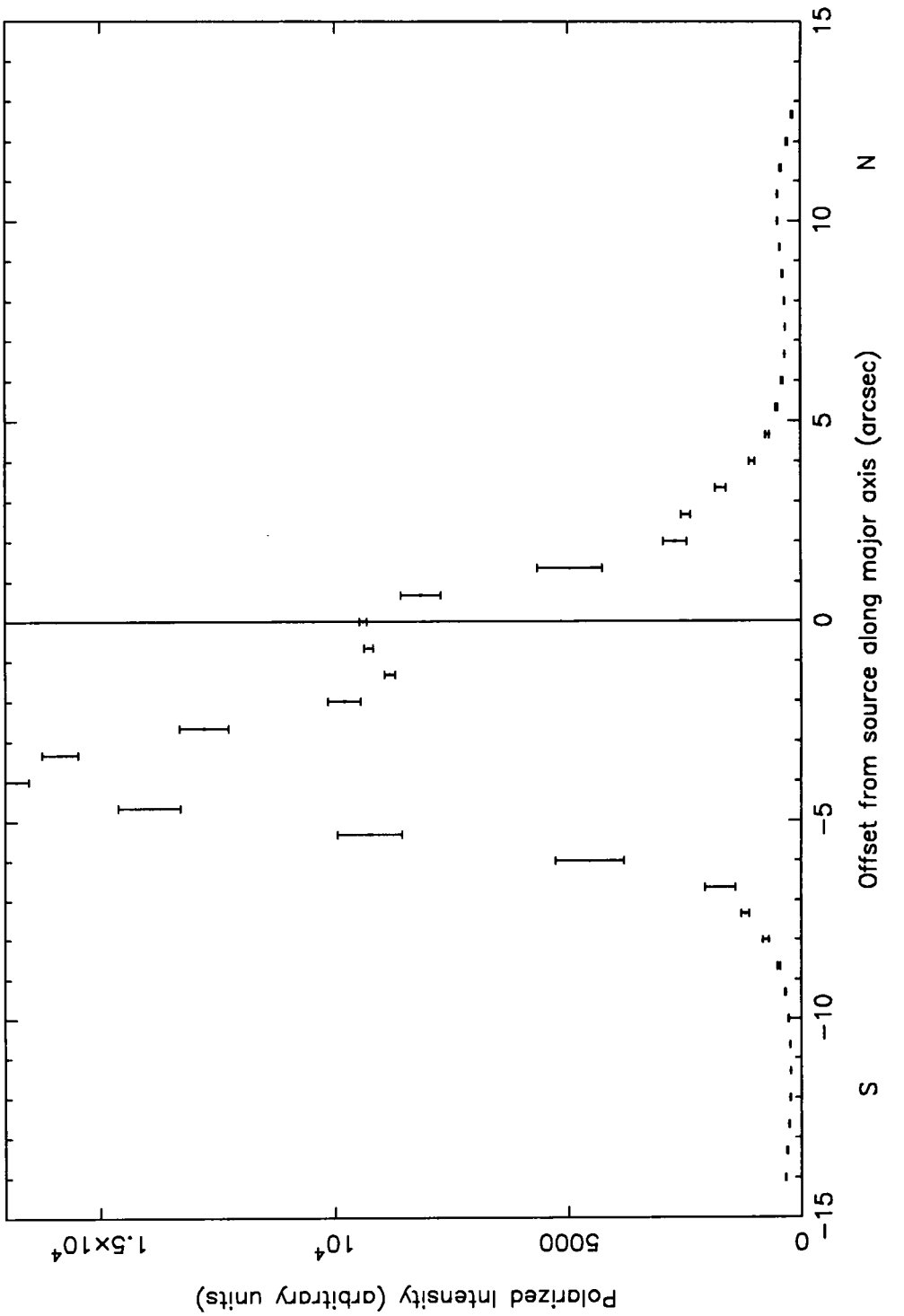

Figure 5.10: A trace of polarized intensity along an axis connecting the ansae for IRAS 09371+1212 in the V-waveband

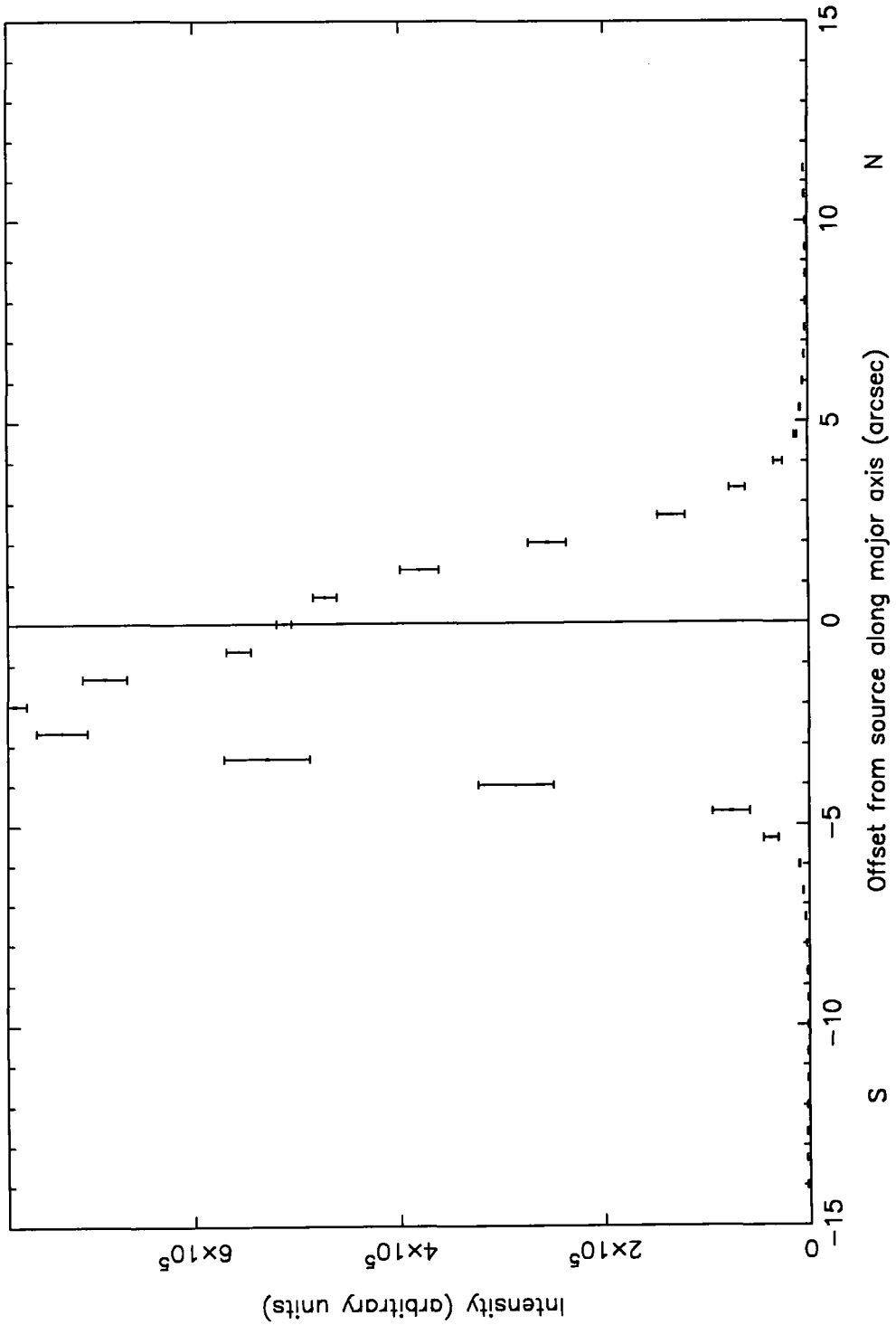

Figure 5.11: A trace of intensity along an axis connecting the ansae for IRAS 09371+1212 in the R-waveband

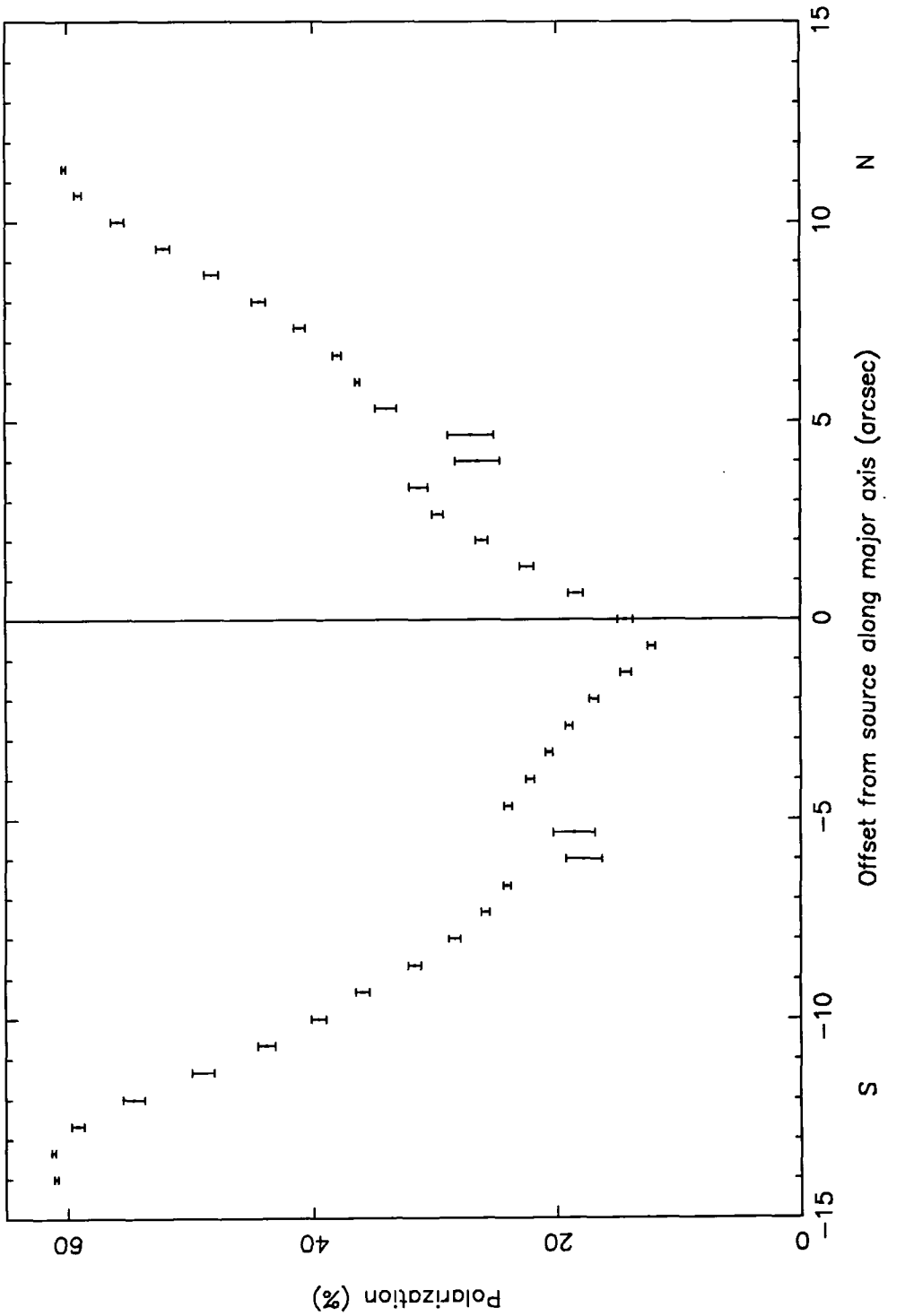

Figure 5.12: A trace of polarization along an axis connecting the ansae for IRAS 09371+1212 in the R-waveband

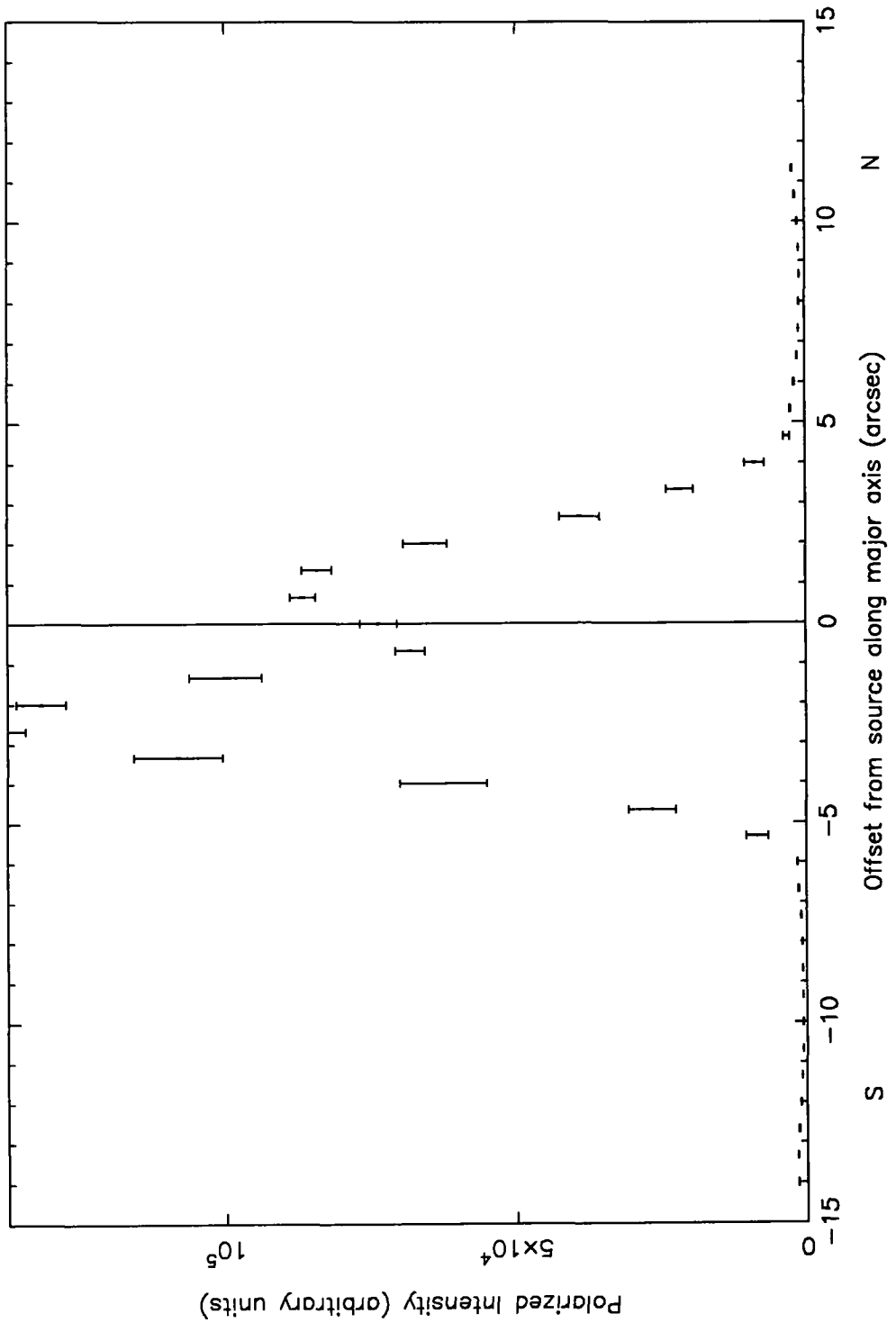

Figure 5.13: A trace of polarized intensity along an axis connecting the ansae for IRAS 09371+1212 in the R-waveband

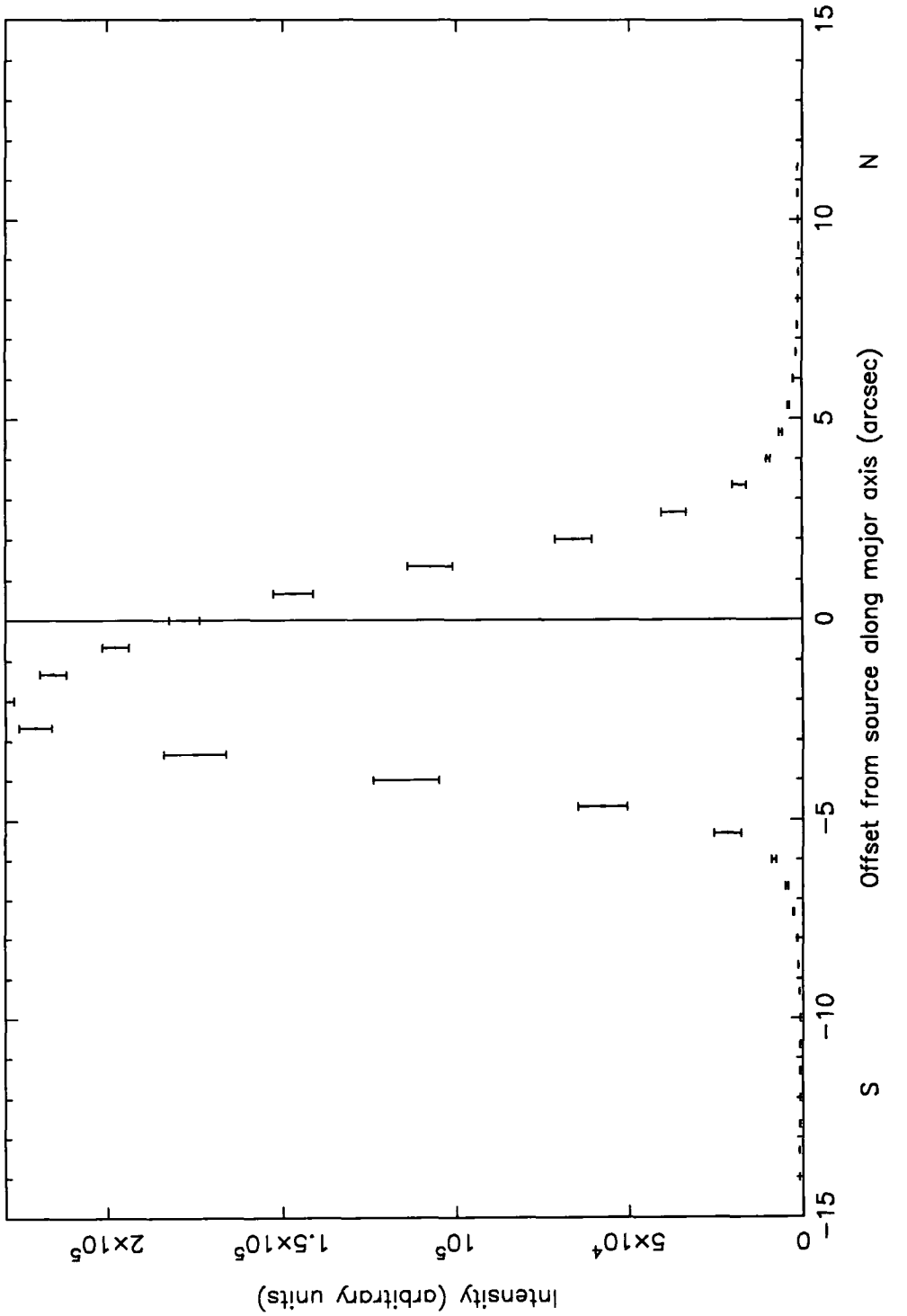

Figure 5.14: A trace of intensity along an axis connecting the ansae for IRAS 09371+1212 in the I-waveband

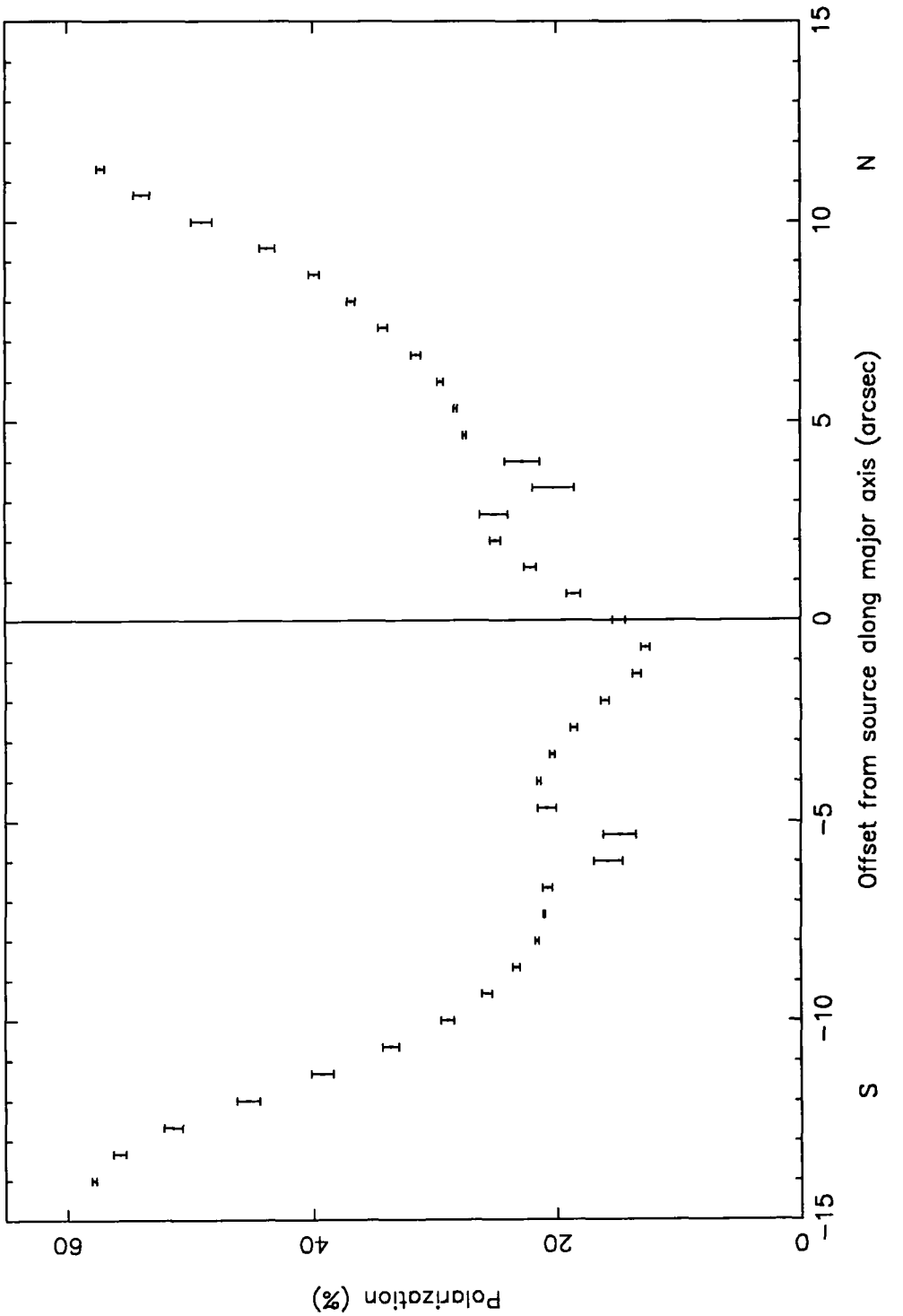

Figure 5.15: A trace of polarization along an axis connecting the ansae for IRAS 09371+1212 in the I-waveband

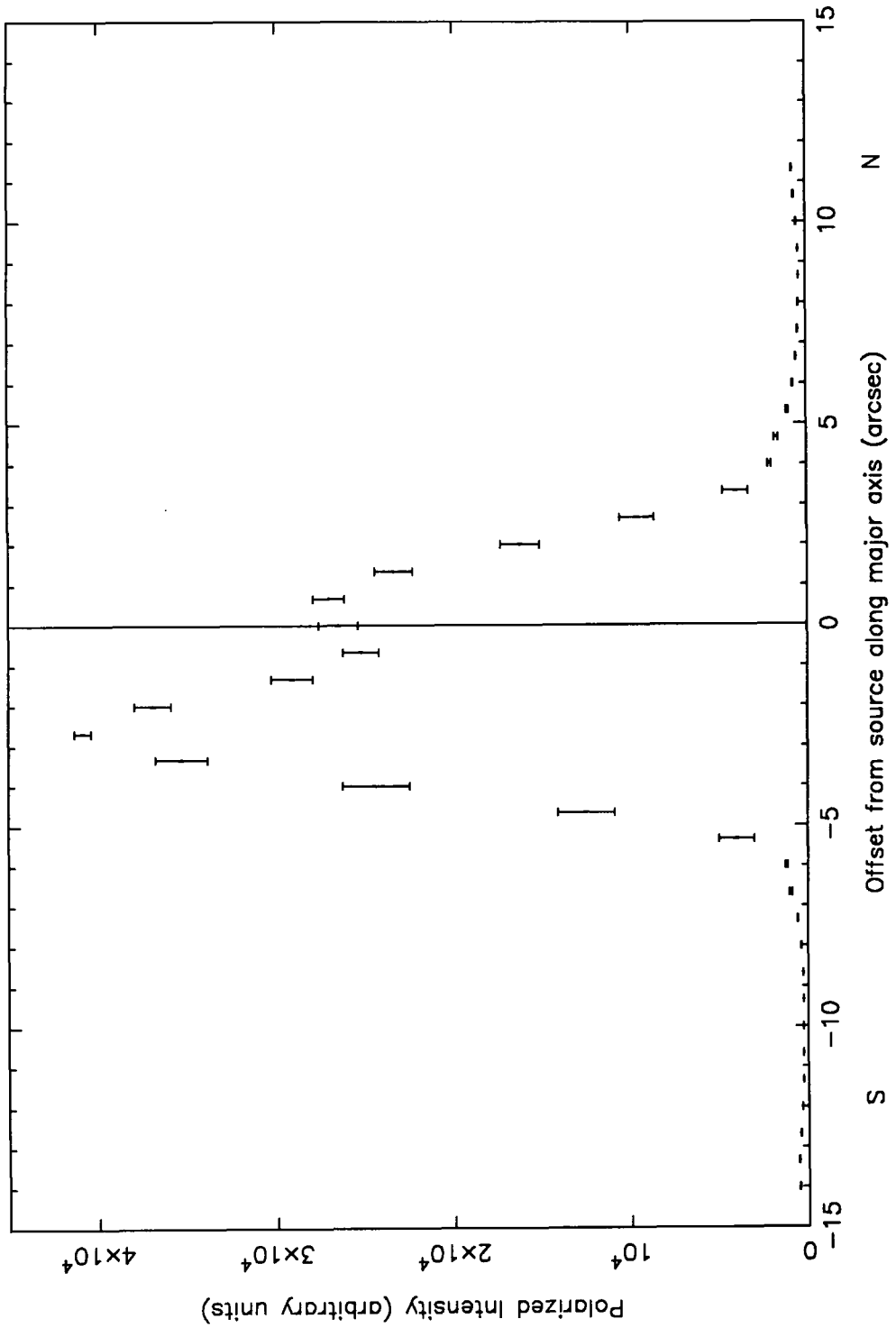

Figure 5.16: A trace of polarized intensity along an axis connecting the ansae for IRAS 09371+1212 in the I-waveband

5.4 Discussion

A full analysis of this data has already been carried out by Scarrott & Scarrott (1995). They propose a scattering geometry which explains the key features of the observed levels of polarization and the presence of the polarization disk. I have no evidence or basis for seeking other alternative explanations for the polarization features as their scattering model geometry achieves this very successfully and would not appear to require further modification. However, Roddier *et al.* (1995) did raise some questions as to the true nature of the nebula tilt. Is the northern lobe inclined towards us or away from us? Scarrott & Scarrott (1995) opt for the latter on the basis of the observed differences in colour and brightness between the northern and southern lobes. Roddier *et al.* (1995), however, seek to persuade us that the former orientation is the correct one from observations of radial velocities, nearby star positions and high resolution near-IR adaptive optics imaging.

The polarimetry data, in conjunction with scattering models for dust, can be used to investigate the nature of the dust material that inhabits IRAS 09371+1212. Since the object is clearly undergoing transition from the AGB phase, presumably towards a PN, dust matter should be expected to play an important role as the object evolves further. The introduction to this chapter showed that grains of silicate, which may be coated with ice, may be invoked to explain the observed IR spectral features. Additionally, the scattering properties of such grains are inextricably linked with the levels and nature of the polarization that results so that an analysis of the polarization is able to feed back key information on the dust grains themselves. Scarrott & Scarrott (1995) looked at the wavelength dependence of the observed polarization using Mie theory to deduce some of the grain parameters. The grains were presupposed to be ice-coated silicates under a power-law size distribution. In the following section I seek to apply the full Mie scattering routines, for core-mantle grains if necessary, that were described in Chapter Two with the intention of narrowing the range of possible grain parameters further.

5.4.1 The nature of the dust grains in IRAS 09371+1212

In a similar fashion to the analysis applied to M 1-16 and Mz 3, the variety of possibilities where the grain material is concerned were examined, under the restrictions that are incorporated in the polarization data.

The Mie scattering computations of Chapter 2 demonstrated the levels of polarization attainable by both 'bare' grains and core-mantle grains composed of materials which are expected to be found in the environments of PN and PPN, and with a distribution of sizes within the scattering volume. Bearing in mind the IR data which strongly suggests the presence of ice in some form, whether pure ice crystals or as a coating upon grains of a different material, the Mie scattering functions can be used to discriminate between certain material combinations and reject those that can never reproduce the observed levels of polarization.

For a specific wavelength and power law size distribution of bare, uncoated grains, a given level of polarization may be obtained by choosing a suitable value for the power law index or by adjusting the refractive index of the grain material. The same applies for the core-mantle grains but in addition we are also able to choose the core and mantle materials and the thickness of the mantle. With reference to the Mie scattering results for core-mantle grains following a normal power law distribution of core sizes and for silicate grains with a thin, say 0.01 μm, water ice mantle (refer to Figure 7.32), it is seen that to achieve the levels of polarization observed in IRAS 09371+1212 requires power law indices above the canonical ISM value of 3.5, in agreement with Scarrott & Scarrott (1995). A power law index of between 4.0 and 4.5 is required to fit the V-band data, for example. However, the IRAS 09371+1212 data extends over four wavebands and it is required that the levels of polarization be accounted for in each waveband.

With a range of grain core sizes which includes very small grains (0.005 μm) as well as larger grains (1.000 μm), the wavelength dependence of the polarization is one of decreasing polarization with increasing wavelength. This is not what is observed in IRAS 09371+1212, where the measurements of the ansae display a trend for increasing polarization with increasing wavelength (Table 5.3). An increase in the power law index will increase the levels of polarization at each wavelength but will not produce the correct form of wavelength dependence. The Mie calculations show that only by removing the small grains from the distribution (making a_{min} larger) is it possible to achieve an increasing level of polarization with increasing wavelength (see Tables 2.6, 2.7, 2.10 and 2.11). However, if further increases are made much beyond this value, the polarization curve begins to become too forward scattering, such that the peak polarization is found at scattering angles $\lesssim 70°$. Such asymmetry is not compatible with the observational data. It is seen that the differences in the levels of ansae polarization between the

north and south are small and therefore the scattering angle must be close to 90° for both the north and south. This implies that the major axis of the nebula lies almost in the plane of the sky. Reducing the upper cut-off size (a_{max}) of the grains does not appear to affect the levels of polarization significantly for moderate reductions.

An increase in the power law index (γ) will increase the predicted levels of polarization at each wavelength. This has the effect of weighting the distribution towards the smaller grain sizes within a particular size range.

However, there is also the mantle thickness parameter to consider. Calculations using the Mie theory and a normal power law indicate that a small increase in the mantle thickness greatly increases the magnitude of the peak polarization, so it might be expected that mantle thickness may be an important factor.

Following Scarrott & Scarrott (1995), I investigate the scattering behaviour of silicate grains coated with a water ice mantle. The polarization from the dust grains should possess the following properties

- $P_{max} \sim 36\%(B)$ $\quad (47\%(V), 61\%(R)$ and $58\%(I))$
- $P(90° + \phi) > P(90° - \phi)$
- $P(90° - \phi) \sim 36\%(B)$ $\quad (45\%(V), 60\%(R)$ and $57\%(I))$

where P_{max} is the magnitude of the peak polarization obtainable with the set of dust grain parameters and ϕ is the angle of inclination of the nebula axis. I compute a set of grain parameters which give an optimum fit to the observed levels of polarization in the ansae using a fitting function of similar form to that used in the analysis of M 1-16 and Mz 3.

The grain parameters (a_{min}, a_{max} and γ) and the nebula inclination angle (ϕ) were allowed to vary over a suitable range of values and the goodness of fit computed as before for each parameter set. The results are presented in Tables 5.4 through 5.7.

Table 5.4: Mie scattering calculations for grains with an oxygen-rich silicate core and a water ice mantle fitting to the polarization data of IRAS 09371+1212 in the B-waveband

a_{min} (μm)	a_{max} (μm)	dm (μm)	γ	ϕ (°)	Δ
0.100	1.000	0.005	4.1	10	0.1022
0.100	1.000	0.010	3.9	10	0.0847
0.100	2.000	0.010	3.9	10	0.0644
0.250	1.000	0.010	4.0	10	0.0535
0.250	1.000	0.025	3.5	10	0.0433

Table 5.5: Mie scattering calculations for grains with an oxygen-rich silicate core and a water ice mantle fitting to the polarization data of IRAS 09371+1212 in the V-waveband

a_{min} (μm)	a_{max} (μm)	dm (μm)	γ	ϕ (°)	Δ
0.100	1.000	0.005	4.3	10	0.1138
0.100	1.000	0.010	4.1	10	0.0477
0.100	2.000	0.010	4.1	10	0.0555
0.250	1.000	0.010	4.1	10	0.0764
0.250	1.000	0.025	3.7	10	0.0306

Table 5.6: Mie scattering calculations for grains with an oxygen-rich silicate core and a water ice mantle fitting to the polarization data of IRAS 09371+1212 in the R-waveband

a_{min} (μm)	a_{max} (μm)	dm (μm)	γ	ϕ (°)	Δ
0.100	1.000	0.005	4.4	10	0.1312
0.100	1.000	0.010	4.2	10	0.0456
0.100	2.000	0.010	4.2	10	0.0655
0.250	1.000	0.010	4.3	10	0.1574
0.250	1.000	0.025	3.9	10	0.0312

Table 5.7: Mie scattering calculations for grains with an oxygen-rich silicate core and a water ice mantle fitting to the polarization data of IRAS 09371+1212 in the I-waveband

a_{min} (μm)	a_{max} (μm)	dm (μm)	γ	ϕ (°)	Δ
0.100	1.000	0.005	4.5	10	0.2043
0.100	1.000	0.010	4.4	10	0.0361
0.100	2.000	0.010	4.4	10	0.0761
0.250	1.000	0.010	4.4	10	0.1855
0.250	1.000	0.025	4.1	10	0.0808

The results permit a number of points to be made

1. The minimum core grain size (a_{min}) is found to be of the order of 0.10 μm to fit the wavelength dependence of the observational data. In some cases, a higher value of 0.25 μm provides a better fit to the data under certain conditions but the important point to make is that there cannot be very small (0.005 μm) grains present, at least at the positions of the ansae. There is no reason to presuppose that the dust grains at the locations of the ansae are the same in character and composition with those throughout the rest of the object. However, it is difficult to assess the possibility that there exist different species of grains at different points in the nebula under the assumptions of low optical depth and single scattering. For the regions closer to the source(s), multiple scattering must become an important factor and an analysis of this region, in the manner of the above, requires that such processes be taken into account. It is likely, however, that grain species are correlated with their immediate environments such that the coldest material is located in these outer regions as well as the larger grain sizes (Scarrott & Scarrott, 1995; Dougados *et al.*, 1990).

2. The maximum core grain size is well defined at 1.000 μm. Raising this upper limit further (say to 2.000 μm) does not appear to influence the levels of polarization obtained significantly.

3. The thickness of the mantle coating on a grain does, however, appear to impact the nature of the polarization markedly. Scarrott & Scarrott (1995) found that a relatively high value for the power law index γ was necessary to obtain the magnitude of polarization seen in the data. As an alternative option, it appears that modifying the mantle thickness can gain the required fit to the observations without having

to invoke high values of γ. Only a relatively thin coating ($\sim 0.01 - 0.03\,\mu$m) may be required with a power law index of the order of $3.8 - 4.0$. However, running the scattering routines with thicker mantles than this value reduces the fit to the data, that is, mantle thicknesses of $0.05\,\mu$m and above do not appear to be suitable.

4. A number of angles of the nebula tilt were assumed, varying between 0 and 10 degrees. The results of the calculations appeared to be rather insensitive to the value adopted so most of the calculations were carried out at a nebula inclination of 10 degrees. The observational database of IRAS 09371+1212 would seem to support the general view that the inclination angle must be < 10 degrees and I find no evidence to the contrary from the scattering computations.

The scattering routines were also applied with other combinations of core and mantle material, specifically, silicon carbide and amorphous carbon cores with water ice mantles. In both cases, the grain parameters were not able to provide as good a fit to the observational data as that shown above for silicates and ice.

5.5 Conclusions

IRAS 09371+1212 is an unusual object which is presumed to be undergoing a transition between the AGB and PN phases. IR data for the nebula suggest it is cool and contains very cold dust. Evidence in favour of a binary system within the obscured central region is strong and it is possible that at least one of the binary components is an evolved star of somewhat higher mass than normal. There is good reason to suppose that a circumstellar disk surrounds the source. The observations support the presence of an optically thick disk seen almost edge-on. As a consequence of this, and the fact that the polarization and intensity of the ansae is almost identical between north and south, the nebula major axis must not be tilted out of the plane of the sky by a significant amount. This can be confirmed by a consideration of the predicted scattered intensity from core-mantle grains composed of silicate and water ice. The differences in intensity between the inner nebula lobes in each waveband are duplicated with scattering from silicate/ice grains with a size distribution following a normal power law and power law index of ~ 4.2 and a mantle thickness of $\sim 0.03\,\mu$m. The scattered intensity ratios strongly support a value for the nebula tilt as $< 10^\circ$ (in agreement with the general consensus).

A lower cut-off limit to the minimum grain size is also required to fit the polarization data wavelength dependency. With the new core-mantle calculations, this turns out to be $\sim 0.1\,\mu$m, which agrees with the earlier proposal of Scarrott & Scarrott (1995) based on an interpolation between the scattering properties of silicates and ice separately.

Determining the correct value for the power law index is another important factor. In the analysis of Scarrott & Scarrott (1995), the canonical value used for models of the ISM (3.5) does not weight in favour of the smaller grains sufficiently and it is found that a value more towards 5.0 to 5.5 is required. The Mie scattering routines using core-mantle grain combinations enable the thickness of the grain coating to be taken into account. It is found that lower values of the power law index may be retained if the mantle thickness is relatively thin ($\sim 0.03\,\mu$m). The canonical power law index of 3.5, however, still remains unable to account for the observed levels of polarization in IRAS 09371+1212, and it is clear that extra weighting towards the smaller grains in the distribution is required whatever the exact nature of the grains.

Adopting other materials for the core, such as amorphous carbon and silicon carbide, can increase the polarization over the silicate/ice combination, but also introduces more forward scattering behaviour which is not seen in the data.

With regard to IRAS 09371+1212, I have sought to concentrate mainly on the scattering properties of the dust material in the object. There remains much to discover concerning this unusual nebula, particularly in relation to the central regions and inner lobes. A model incorporating multiple scattering in a disk structure is required to investigate the scattering and radiative properties of this region. Such a model has been under construction but unfortunately has so far proved inconsistent in its predictions. It is hoped to improve the model in a number of ways in the near future in order to further explore the character of IRAS 09371+1212 more fully.

Chapter 6

Summary and Conclusions

I conclude this thesis with a general discussion of PPNs and PNs with regard to the polarization data presented in Chapters 3, 4 and 5, followed by a suggestion for further polarization observations on selected objects.

Planetary nebulae represent a fleeting transitionary period in a star's evolution which is a small fraction of the star's total lifetime. It has been shown how stars within a certain mass range, upon leaving the main sequence, progress through stages of considerable instability and structural change. As the star leaves the main sequence, mass-loss processes commence in the outer regions of the star. The theoretical understanding of this phenomenon is somewhat weak at the present time but it is plainly observed that stars evolving through the RGB and AGB stages lose a significant percentage of their total mass as they progressively evolve towards their final end state. The mechanisms which promote this behaviour are not completely understood but there are known to be complex processes of pulsation and inner mixing within the star which may be in part responsible. However, at the tip of the AGB stage, the star will have shed much of its outer envelope and in the cooler, outer regions, dust grain condensation becomes feasible. It is believed that this in turn promotes the development of radiatively-driven stellar winds from the central star which themselves cause further changes to the stars environment and behaviour. Chapter 1 of this thesis presented a detailed summary of the main processes involved during this stage of the stars evolution. The result of these complex processes is the formation of a shell of dust/gas around the rapidly evolving central star, which often hides the star from direct view, but which is an essential ingredient in the subsequent creation of a planetary nebula.

Observations of planetary nebulae reveal that these objects possess a wide range of morphologies and general properties and are considerably more diverse than an analysis of their common ancestry might suggest. It is clear that the effects of the mass-loss processes which occur during the RGB and AGB have a very strong influence on the morphology of a particular PN as it forms. Chapter 1 also dealt with the mechanisms behind the asymmetric nature of the dust distribution in the late AGB shell which is believed to eventually result in the many and varied shapes of PNs. The interacting stellar winds model for the formation and evolution of PNs has been viewed as having good success in explaining many features of these objects, but the question still remains as to exactly how the initial asymmetry in the stars envelope is created. Between the competing theories of the influence of magnetic fields, stellar rotation, fossil protostellar disks, the impact of a binary system is generally regarded as the most natural and convincing explanation. In the case of the bipolar nebulae, this is particularly appealing and presents a satisfactory mechanism for the phenomena of axial precession which is seen in some PNs (cf., M 1-16 in this thesis). In addition, the binary hypothesis also suggests that the formation of accretion/excretion disks in the system is not uncommon. This is reflected again in the observations of bipolar PNs, for which a circumstellar disk structure is a natural explanation for the bipolar appearance itself, rather than an isotropic ionization and excitation of the stars dusty shell. The disk constrains the ionizing winds to directions normal to its plane and the polar directions of the star. This results in the, often quite spectacular, bipolar morphologies seen in a number of PNs. It is clear from the predictions of the Interacting Stellar Winds models that bipolar morphology may be very common, but that various inclinations which the bipolar axis may present to the line of sight may distort our understanding of the true abundance of bipolar PNs somewhat.

Optical polarimetry of PNs by the Durham Polarimetry Group tend to confirm the impression that the bipolar PNs are often young objects with considerably asymmetric dust distributions and high levels of linear polarization. Data has been obtained by the author (not detailed in this thesis) on a number of PNs which show very low levels of polarization and are mainly seen purely by emission. It is suggested that these are older PNs in which the circumstellar dust has been blown away to sufficiently low levels so as to effect very little polarization through scattering. In most cases, this appears to be the case with the elliptical and symmetric PNs which display bright, ring-like morphologies and where the central star is usually visible. The nebula then essentially comprises an evolved, hot central star from which strong UV radiation ionizes the surrounding, almost exclusively

gaseous, shell. However, it is known that during the mass-loss processes from the evolving star, an extensive circumstellar envelope is formed. Such structures are seen in very deep images of planetary nebulae where the bright central regions have been masked out during the exposure. It would be expected that there should be a dust component of these envelopes which may become observable through the polarization imparted to scattered radiation from the central star. An investigation of these very faint envelopes would be useful. A number of attempts have been made previously to observe such objects, but the very low surface brightness of the envelope and the proximity of the overwhelming central object make successful data collection very difficult. However, I believe that it would be a worthwhile future project as there is very little currently known about these faint envelopes and their relationship to the evolution of the central star.

It is quite a different matter for the bipolar nebulae. The central star is often obscured and the bipolar lobe structures are seen by a combination of emission and scattered light from the central star which escapes out from the star along the polar directions. Relatively high levels of polarization suggest that the dust content of the stars shell is relatively intact. This in turn implies a younger stage of development as a PN. It could be argued that the dust may play a crucial role in the development of the PN structure. Supposing the progenitor star had not produced a large amount of dust in the mass-loss phase of its evolution, then the shell will be relatively dust free as the stellar winds begin to ionize the shell regions. This will result in an isotropic expansion of the nebula, rather than being constrained to the polar regions and a more elliptical or ring-like nebula. The higher symmetry and low dust density may be as a result of the progenitor being a single star rather than a binary system. In other words, it may be that binarity may strongly influence both the rate of mass-loss and the symmetry of the mass-loss. There are strong suggestions that all bipolar nebulae are formed from bipolar progenitor systems. Optical polarimetry cannot prove this point directly but can be used very effectively to investigate the dust distribution in PNs. This is useful in that the nature and distribution of the dust is a good diagnostic of the evolutionary stage of the object. The spatial distribution of the dust is linked directly to the nature of the central object. Comparison with scattering models also enables some insight into the chemistry of the circumstellar environment where the dust is formed.

The polarization data presented in this thesis concentrates upon bipolar nebulae. Of these, one (IRAS 09371+1212) is usually classed as a PPN whilst the other two (M 1-16

and Mz 3) are considered as young planetary nebulae. For each object, an analysis of the observed levels and character of the linear polarization enables certain deductions to be made about the nature and distribution of the dust within the nebula. All of the objects discussed herein display considerable deviations from spherical symmetry and, in each case, there is strong evidence for the presence of a circumstellar disk structure. The location of dust in PNs is still poorly known, so that the question remains as to whether a thick dusty equatorial disk, acting as a collimation mechanism for outflows, is a necessary prerequisite for the formation and evolution of bipolar PNs. A consistent theoretical picture of the early phases of planetary nebula evolution has to include an understanding of the bipolar outflow phenomena and its relationship to the central exciting source and the nature of any circumstellar disk, which presumably contributes significantly to the evolutionary mechanisms in the transient PPN stage.

It is the short-lived evolutionary phase of low and intermediate mass stars between the Asymptotic Giant Branch and the planetary nebula stage which is generally considered to be the least well understood area of current stellar evolution theory. Polarimetry at optical wavelengths is a powerful diagnostic tool for the detection and further analysis of the dusty tori which are believed to surround most, if not all, PPNs and young PNs, as well as the structure of the associated bipolar outflow lobes. The effects on the polarization vector of scattering from dust grains are strongly wavelength, grain size and grain material dependent. Combining the polarization data obtained at different optical wavelengths, the intensity and distribution of the linear polarization vector provides important information on the dust density distribution in the disk and lobes, dust grain composition and dust grain size distribution and shape. In conjunction with Monte Carlo scattering models (which can include the effects of multiple Mie scattering in the disk by core-mantle grains in a fairly straightforward manner), disk properties such as diameter, thickness, extinction and optical depth may be modelled in terms of their effect on linear polarization. On the basis of the observations carried out so far into PPNs and PNs, I suggest that the most worthwhile results from polarimetric observations will arise from a study of very young PPNs. There are a number of such objects which have been discovered as a result of analysis of the IRAS database combined with subsequent ground-based IR observations. These are small objects of low optical brightness but images show that they already possess highly axisymmetric bipolar morphologies. High-resolution imaging has provided some direct evidence for the presence of circumstellar disks in these objects, but observational data related to the composition and distribution of the dust, which comprises the bulk of the material in these disks, is severely lacking.

Finally, I present here a shortlist of possible objects which merit polarimetric observations on the basis of their PPN status.

IRAS 04296+3429	IRAS 05113+1347
IRAS 07134+1005	IRAS 20000+3239
IRAS 21282+5050	IRAS 22223+4327
IRAS 22272+5435	IRAS 17150-3224
IRAS 17441-2411	IRAS 19500-1709

Chapter 7

Mie scattering curves

This chapter contains a series of figures which represent the results of the Mie scattering calculations of Chapter 2. Reference should be made to that chapter for the details of the grain materials, size distributions and grain size parameters investigated.

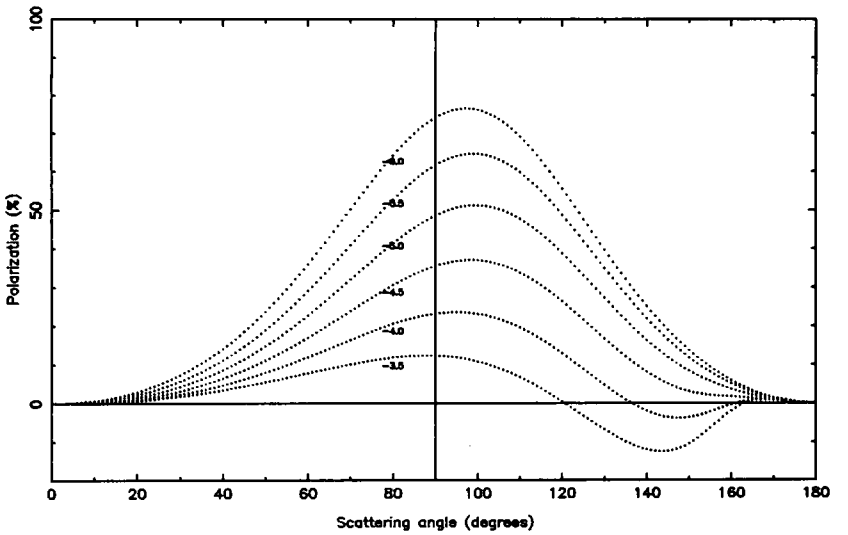

Figure 7.1: Mie scattering calculations for the polarization from oxygen-rich silicate grains as a function of scattering angle (θ) and power law index (γ). Grain size distribution $n(a) = n_o a^{-\gamma}$; $a_{min} = 0.005\,\mu$m $a_{max} = 1.000\,\mu$m

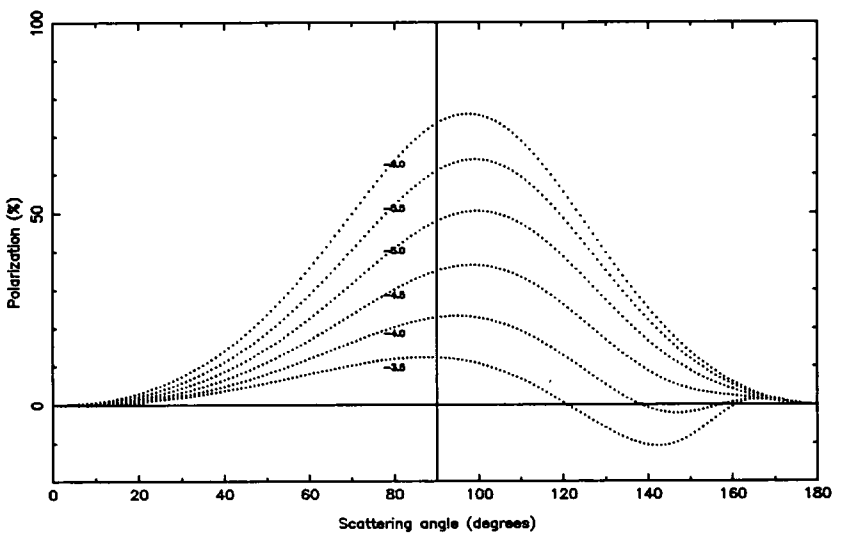

Figure 7.2: Mie scattering calculations for the polarization from oxygen-deficient silicate grains as a function of scattering angle (θ) and power law index (γ). Grain size distribution : $n(a) = n_o a^{-\gamma}$; $a_{min} = 0.005\,\mu$m $a_{max} = 1.000\,\mu$m

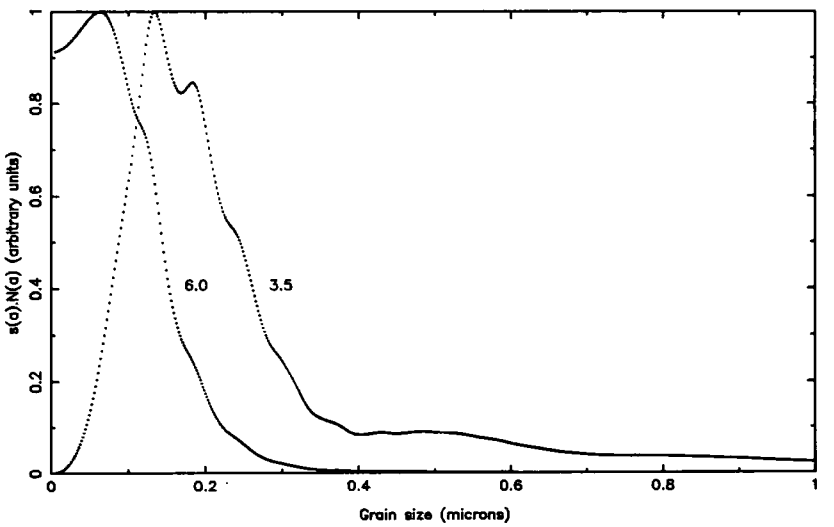

Figure 7.3: The product of the total scattering cross-section $s(a)$ and the grain size distribution $n(a)$ as a function of grain size (a) for oxygen-rich silicate grains at a wavelength of 0.515 μm. The size distribution function is $n(a) = n_o a^{-\gamma}$ and $\gamma = 3.5$ and 6.0.

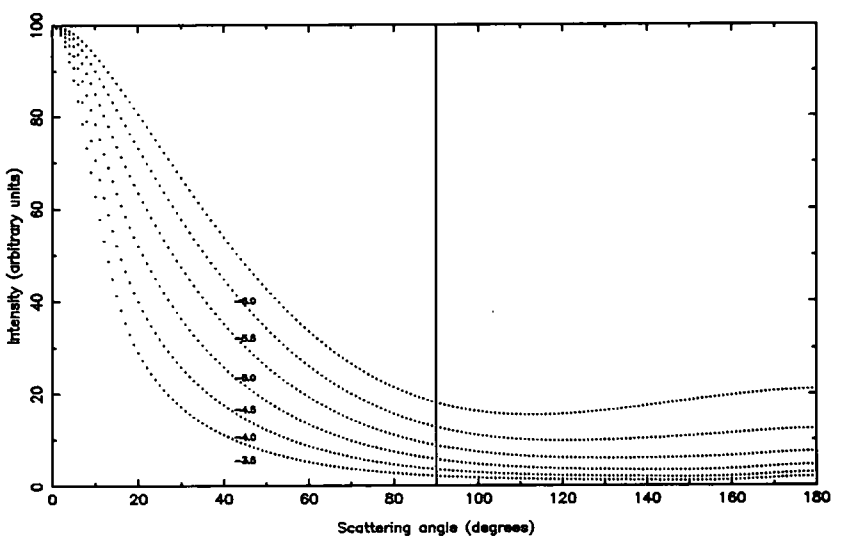

Figure 7.4: Mie scattering calculations for the scattered intensity from oxygen-rich silicate grains as a function of scattering angle (θ) and power law index (γ). Grain size distribution : $n(a) = n_o a^{-\gamma}$; $a_{min} = 0.005\,\mu$m $\quad a_{max} = 1.000\,\mu$m

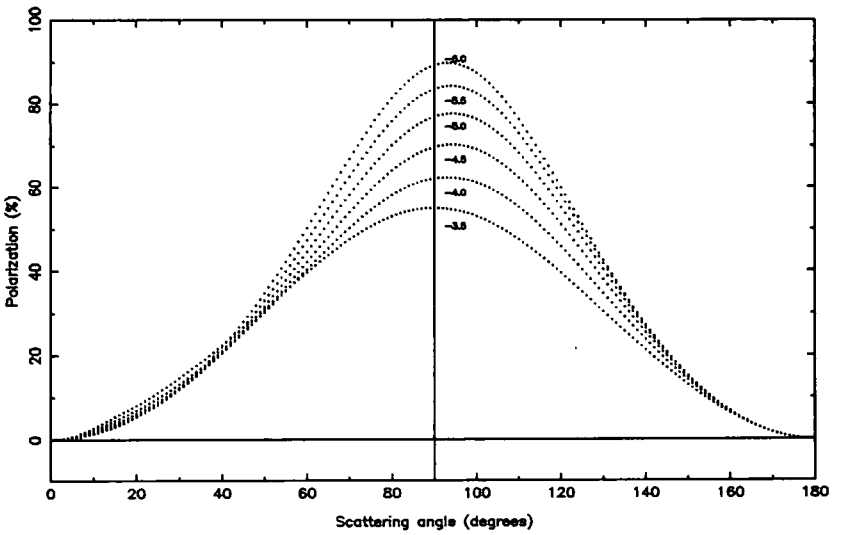

Figure 7.5: Mie scattering calculations for the polarization from amorphous carbon grains grains as a function of scattering angle (θ) and power law index (γ). Grain size distribution $n(a) = n_o a^{-\gamma}$; $a_{min} = 0.005\,\mu$m $a_{max} = 1.000\,\mu$m

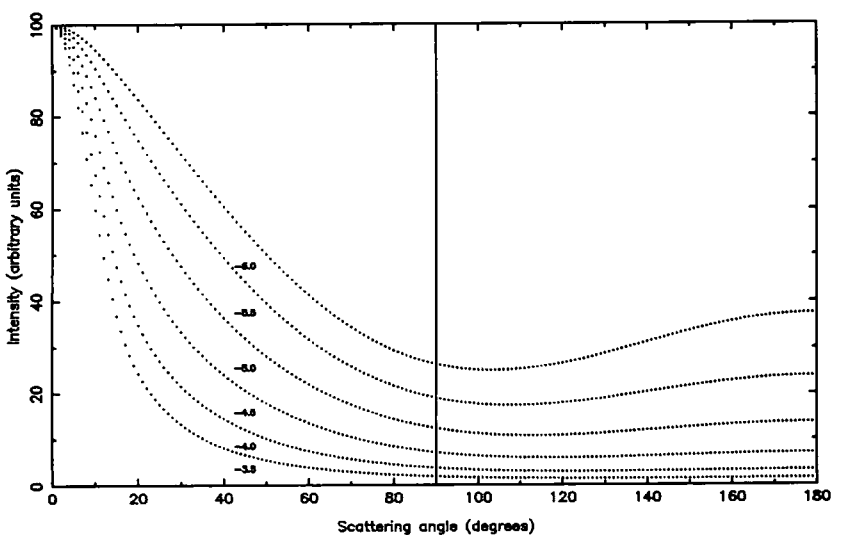

Figure 7.6: Mie scattering calculations for the scattered intensity from amorphous carbon grains as a function of scattering angle (θ) and power law index (γ). Grain size distribution : $n(a) = n_o a^{-\gamma}$; $a_{min} = 0.005\,\mu$m $a_{max} = 1.000\,\mu$m

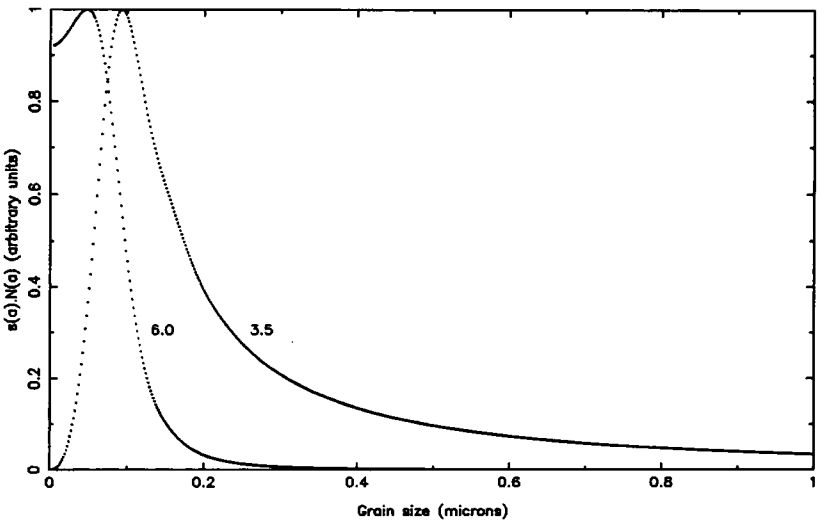

Figure 7.7: The product of the total scattering cross-section $s(a)$ and the grain size distribution $n(a)$ as a function of grain size (a) for amorphous carbon grains at a wavelength of 0.515 μm. The size distribution function is $n(a) = n_o a^{-\gamma}$ and $\gamma = 3.5$ and 6.0.

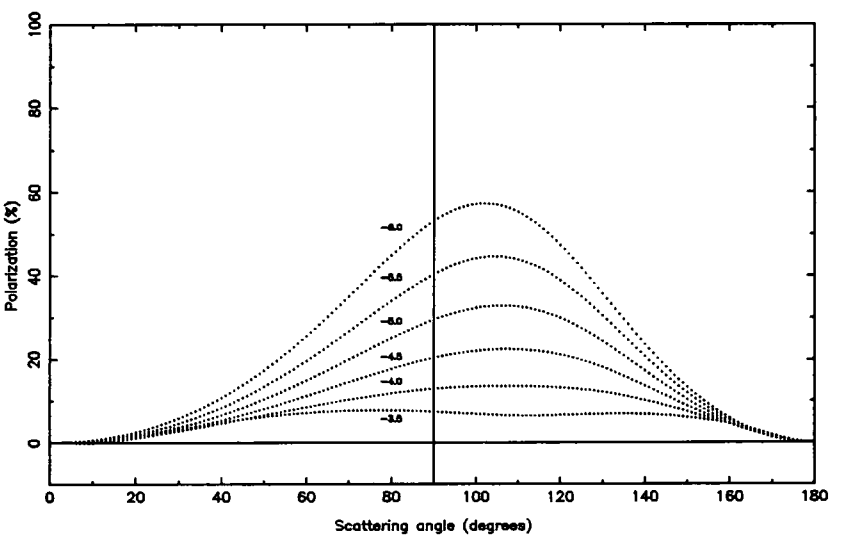

Figure 7.8: Mie scattering calculations for the polarization from silicon carbide grains as a function of scattering angle (θ) and power law index (γ) Grain size distribution : $n(a) = n_o a^{-\gamma}$

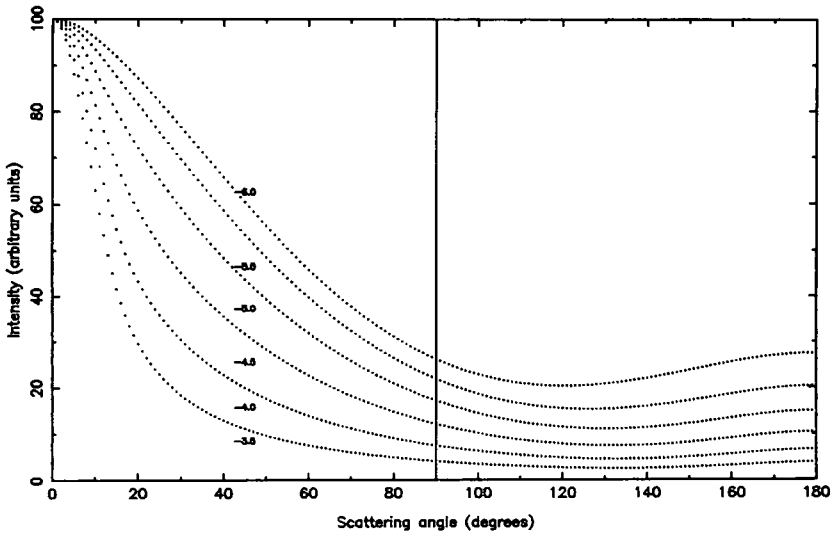

Figure 7.9: Mie scattering calculations for the scattered intensity from silicon carbide grains as a function of scattering angle (θ) and power law index (γ) Grain size distribution : $n(a) = n_o a^{-\gamma}$

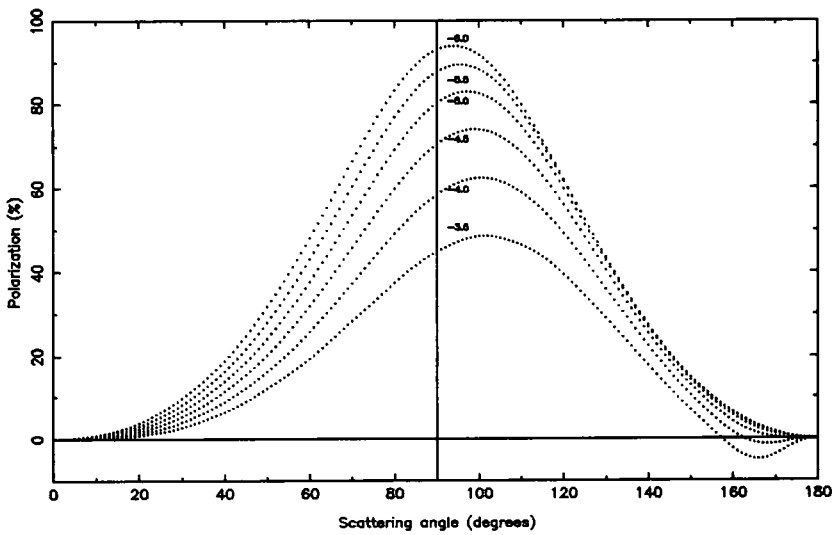

Figure 7.10: Mie scattering calculations for the polarization from dirty ice grains as a function of scattering angle (θ) and power law index (γ) Grain size distribution : $n(a) = n_o a^{-\gamma}$

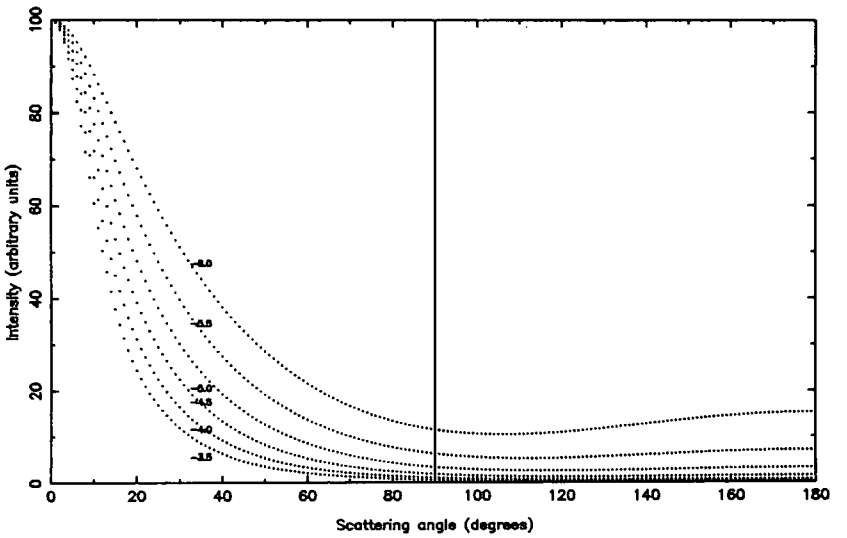

Figure 7.11: Mie scattering calculations for the scattered intensity from dirty ice grains as a function of scattering angle (θ) and power law index (γ) Grain size distribution : $n(a) = n_o a^{-\gamma}$

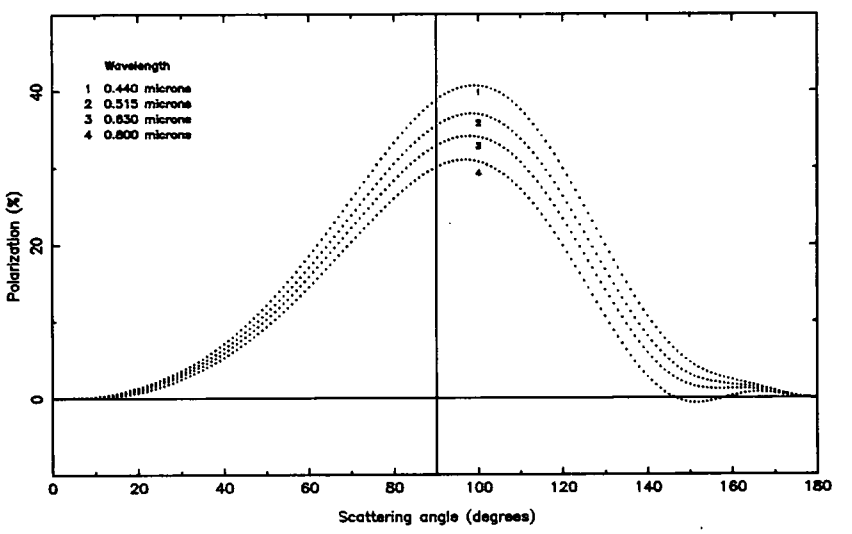

Figure 7.12: Mie scattering calculations for the polarization from oxygen-rich silicate grains as a function of scattering angle (θ) and wavelength (λ). Grain size distribution : $n(a) = n_o a^{-4.5}$

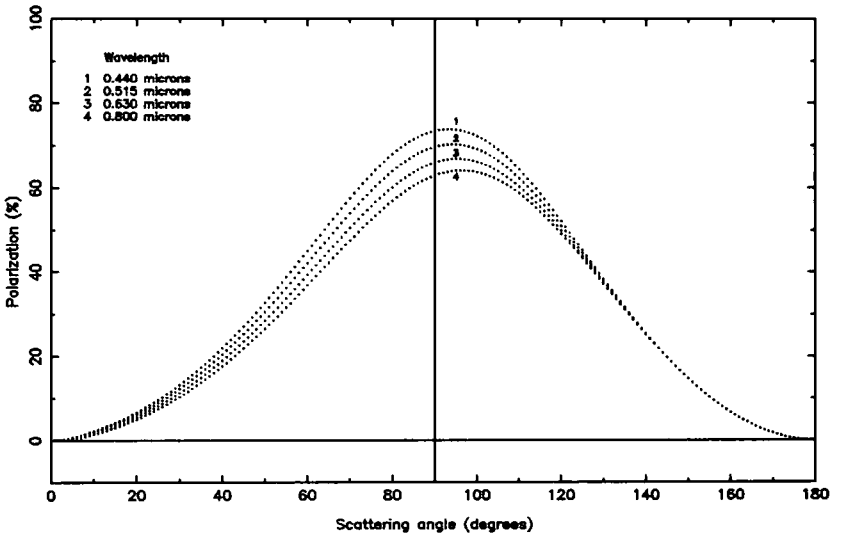

Figure 7.13: Mie scattering calculations for the polarization from amorphous carbon grains as a function of scattering angle (θ) and wavelength (λ). Grain size distribution : $n(a) = n_o\, a^{-4.5}$

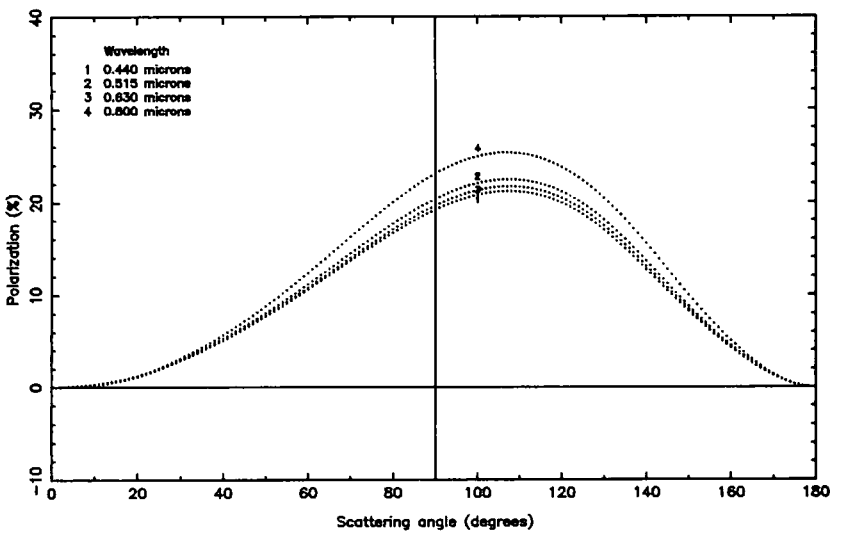

Figure 7.14: Mie scattering calculations for the polarization from silicon carbide grains as a function of scattering angle (θ) and wavelength (λ). Grain size distribution : $n(a) = n_o\, a^{-4.5}$

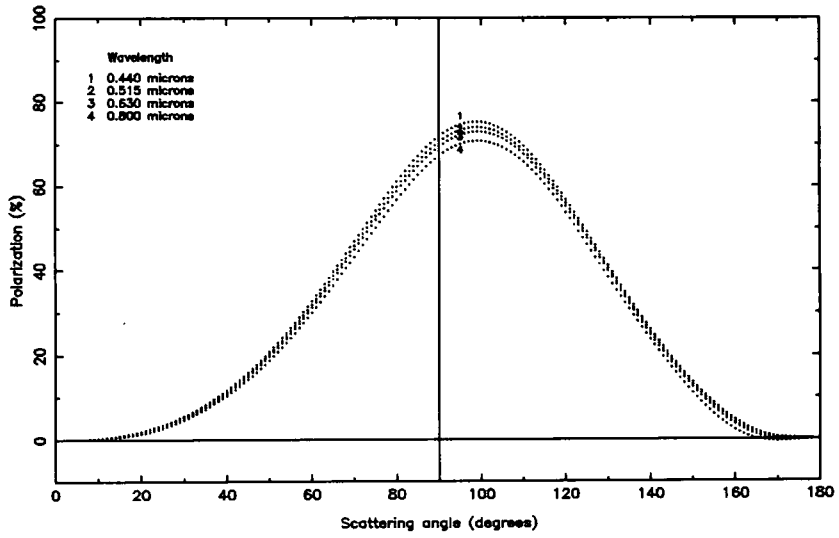

Figure 7.15: Mie scattering calculations for the polarization from dirty ice grains as a function of scattering angle (θ) and wavelength (λ). Grain size distribution : $n(a) = n_o\, a^{-4.5}$

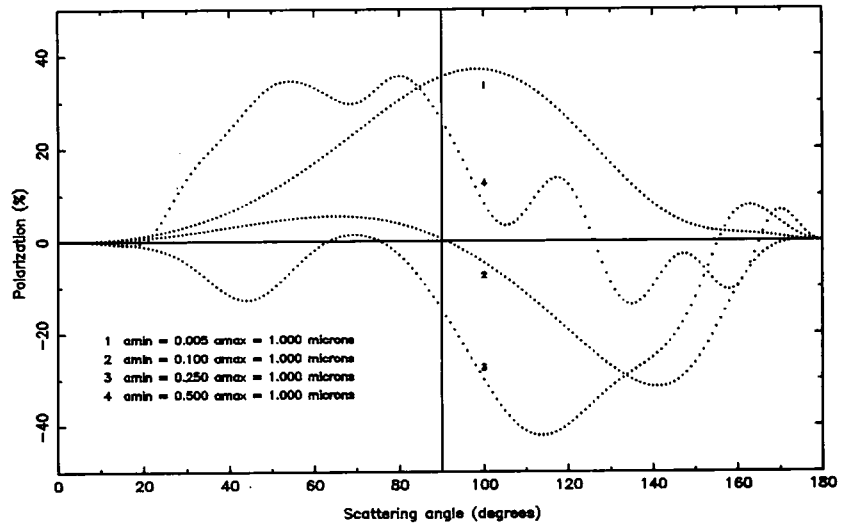

Figure 7.16: Mie scattering calculations for the polarization from oxygen-rich silicate grains as a function of scattering angle (θ) and minimum grain core size (a_{min}). Grain size distribution : $n(a) = n_o\, a^{-4.5}$

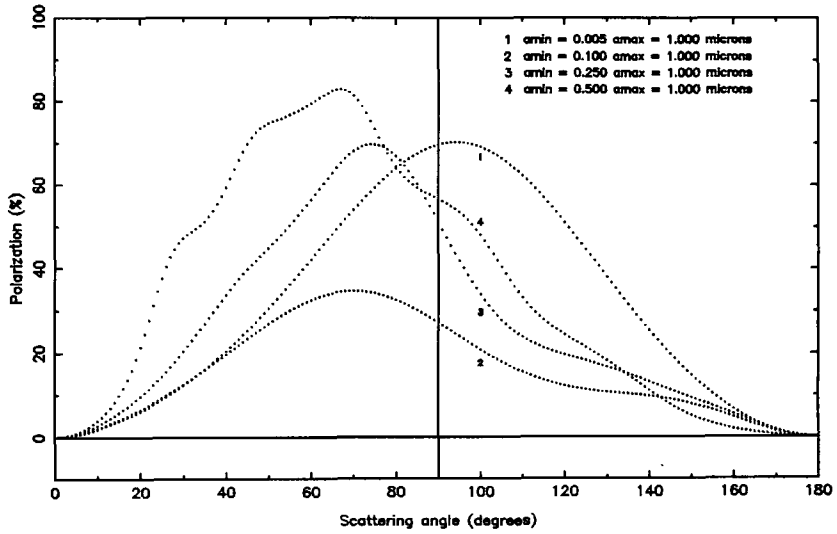

Figure 7.17: Mie scattering calculations for the polarization from amorphous carbon grains as a function of scattering angle (θ) and minimum grain core size (a_{min}). Grain size distribution : $n(a) = n_o a^{-4.5}$

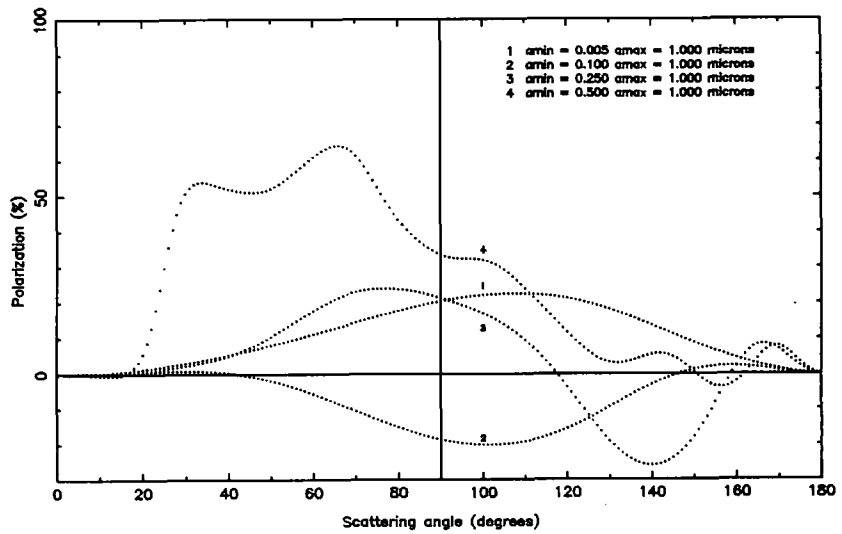

Figure 7.18: Mie scattering calculations for the polarization from silicon carbide grains as a function of scattering angle (θ) and minimum grain core size (a_{min}). Grain size distribution : $n(a) = n_o a^{-4.5}$

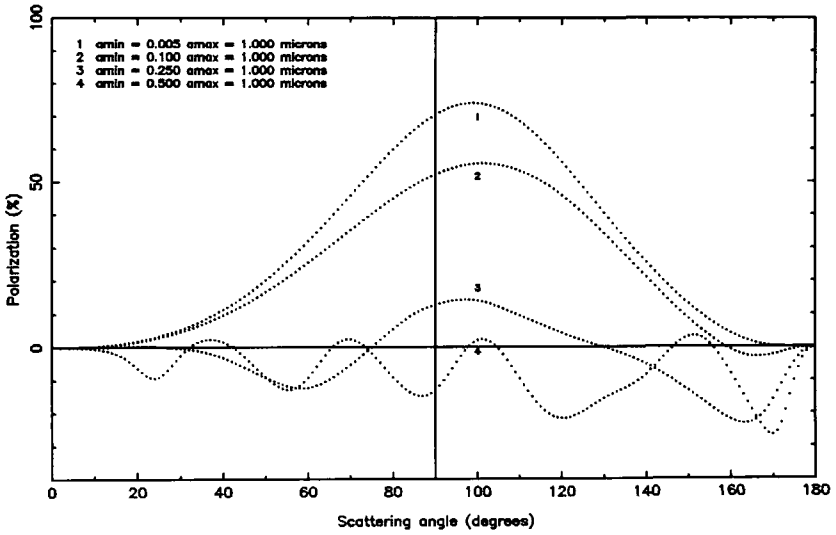

Figure 7.19: Mie scattering calculations for the polarization from dirty ice grains as a function of scattering angle (θ) and minimum grain core size (a_{min}). Grain size distribution : $n(a) = n_o\, a^{-4.5}$

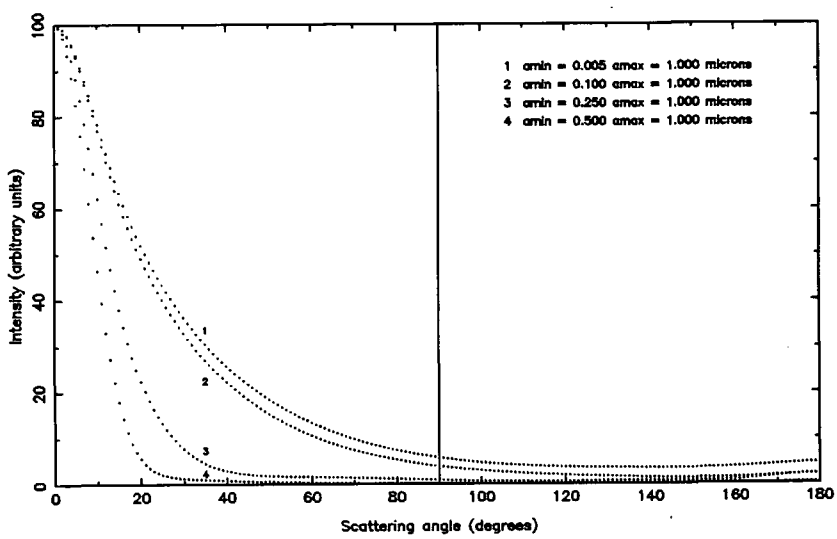

Figure 7.20: Mie scattering calculations for the scattered intensity from oxygen-rich silicate grains as a function of scattering angle (θ) and minimum grain core size (a_{min}). Grain size distribution : $n(a) = n_o\, a^{-4.5}$

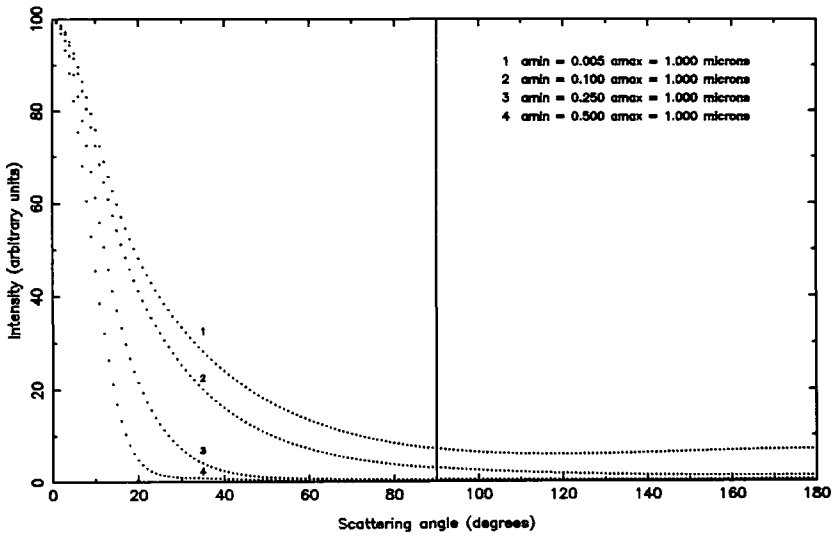

Figure 7.21: Mie scattering calculations for the scattered intensity from amorphous carbon grains as a function of scattering angle (θ) and minimum grain core size (a_{min}). Grain size distribution : $n(a) = n_o a^{-4.5}$

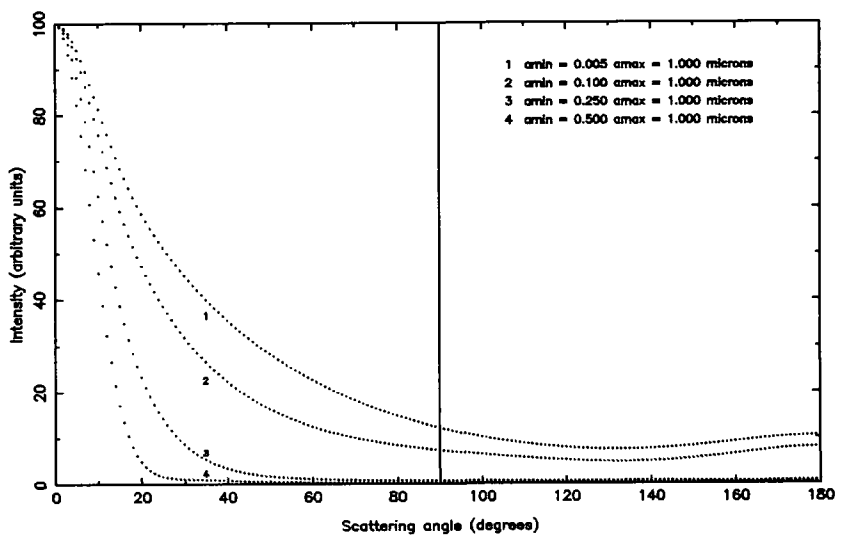

Figure 7.22: Mie scattering calculations for the scattered intensity from silicon carbide grains as a function of scattering angle (θ) and and minimum grain core size (a_{min}). Grain size distribution : $n(a) = n_o a^{-4.5}$

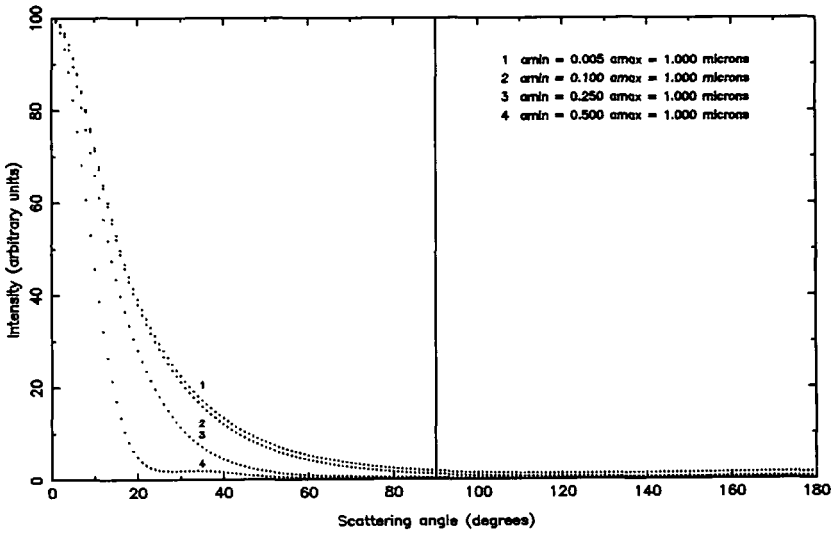

Figure 7.23: Mie scattering calculations for the scattered intensity from dirty ice grains as a function of scattering angle (θ) and minimum grain core size (a_{min}). Grain size distribution : $n(a) = n_o\, a^{-4.5}$

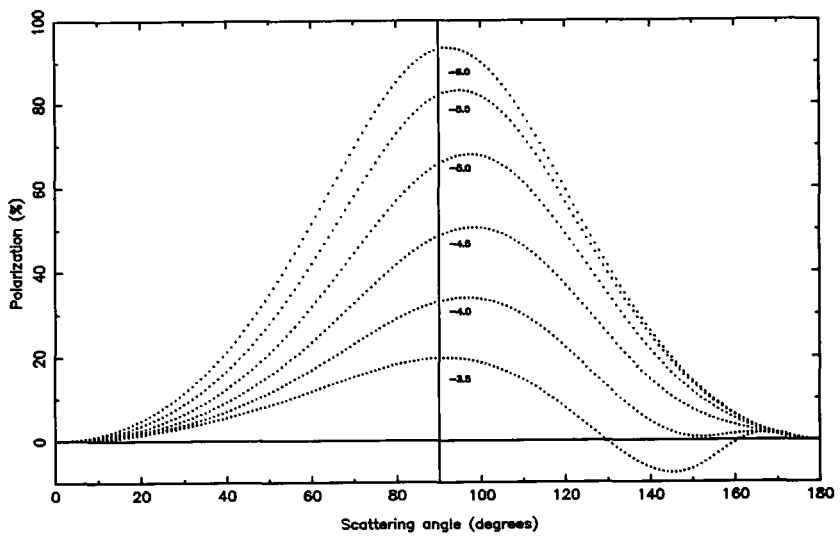

Figure 7.24: Mie scattering calculations for the polarization from oxygen-rich silicate grains with a 0.01 μm water ice mantle as a function of scattering angle (θ) and power law index (γ). Grain size distribution : $n(a) = n_o\, a^{-\gamma}$

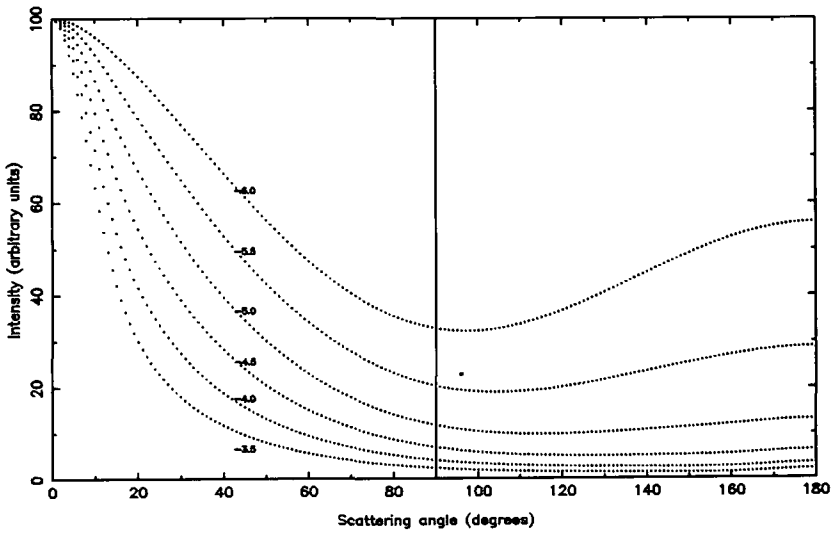

Figure 7.25: Mie scattering calculations for the scattered intensity from oxygen-rich silicate grains with a 0.01 μm water ice mantle as a function of scattering angle (θ) and power law index (γ). Grain size distribution : $n(a) = n_o\, a^{-\gamma}$

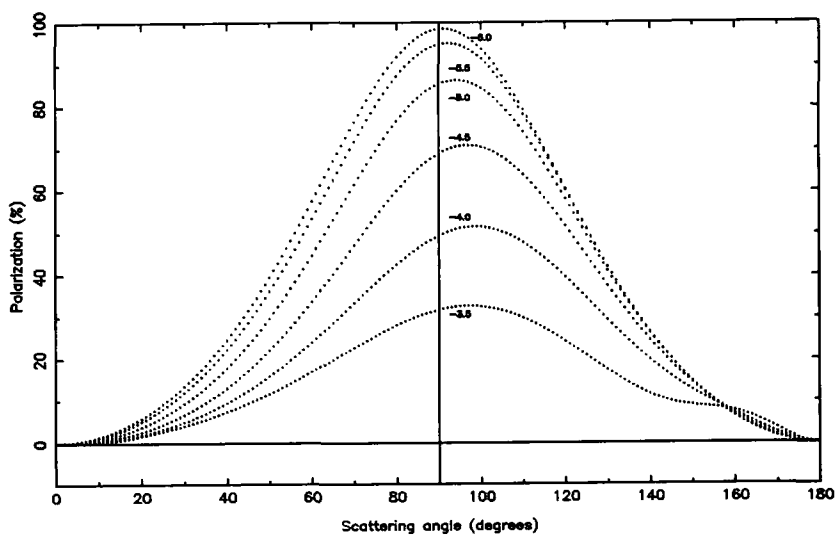

Figure 7.26: Mie scattering calculations for the polarization from oxygen-rich silicate grains with a 0.01 μm amorphous carbon mantle as a function of scattering angle (θ) and power law index (γ). Grain size distribution : $n(a) = n_o\, a^{-\gamma}$

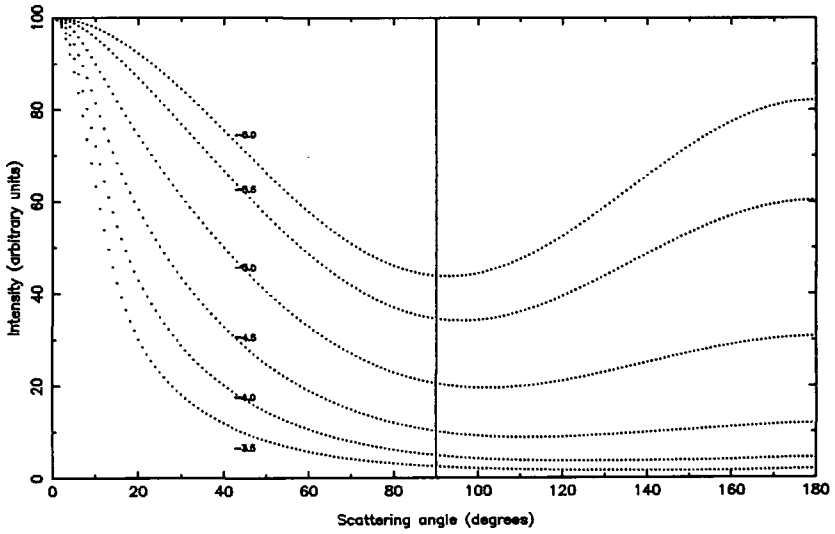

Figure 7.27: Mie scattering calculations for the scattered intensity from oxygen-rich silicate grains with a 0.01 μm amorphous carbon mantle as a function of scattering angle (θ) and power law index (γ). Grain size distribution : $n(a) = n_o\, a^{-\gamma}$

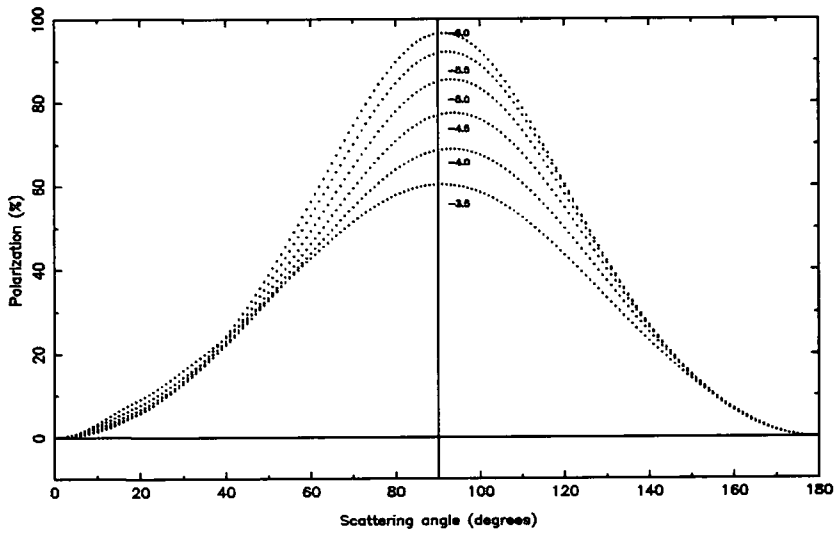

Figure 7.28: Mie scattering calculations for the polarization from amorphous carbon grains with a 0.01 μm water ice mantle as a function of scattering angle (θ) and power law index (γ) Grain size distribution : $n(a) = n_o\, a^{-\gamma}$

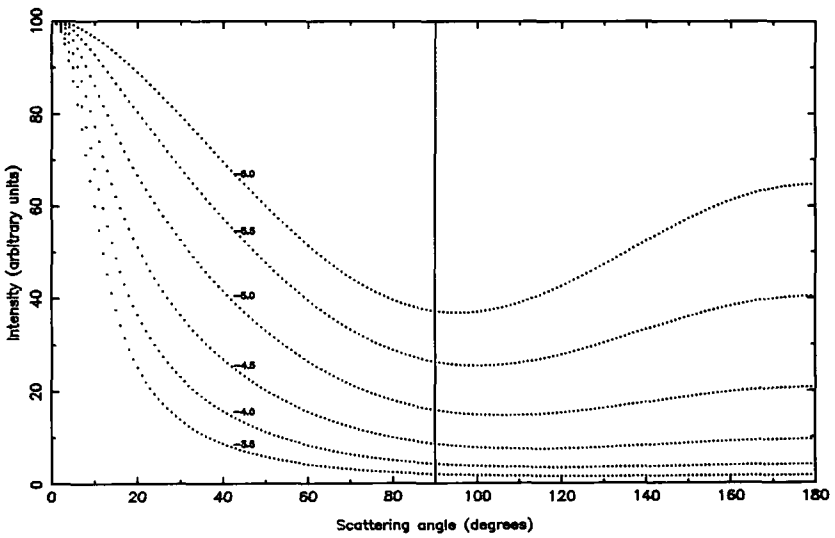

Figure 7.29: Mie scattering calculations for the scattered intensity from amorphous carbon grains with a 0.01 μm water ice mantle as a function of scattering angle (θ) and power law index (γ). Grain size distribution : $n(a) = n_o a^{-\gamma}$

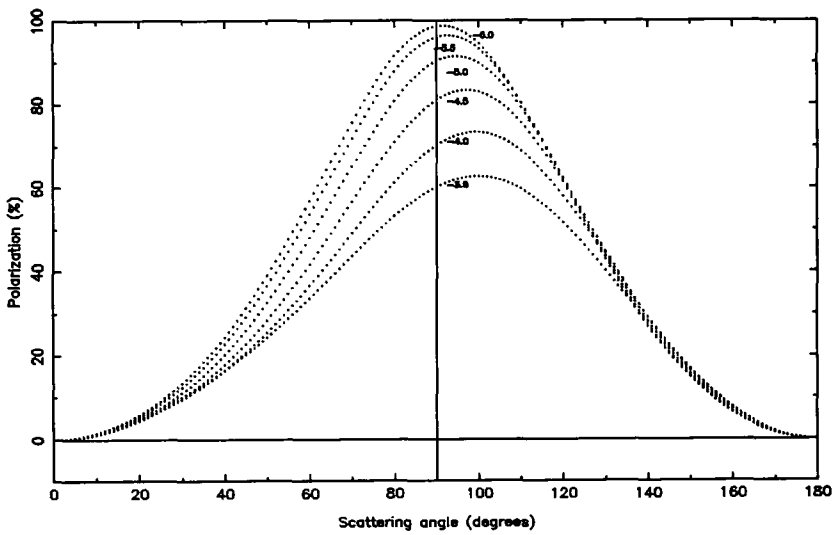

Figure 7.30: Mie scattering calculations for the polarization from amorphous carbon grains with a 0.01 μm silicon carbide mantle as a function of scattering angle (θ) and power law index (γ) Grain size distribution : $n(a) = n_o a^{-\gamma}$

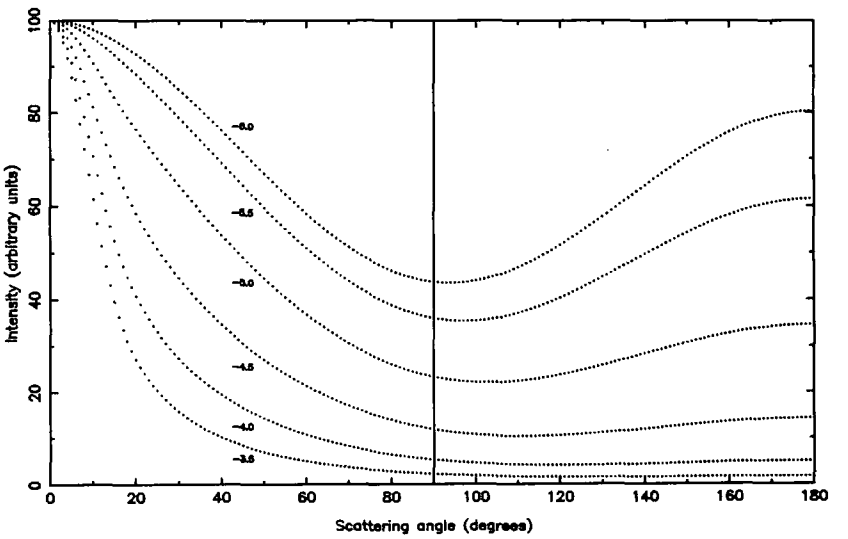

Figure 7.31: Mie scattering calculations for the scattered intensity from amorphous carbon grains with a 0.01 μm silicon carbide mantle as a function of scattering angle (θ) and power law index (γ) Grain size distribution : $n(a) = n_o a^{-\gamma}$

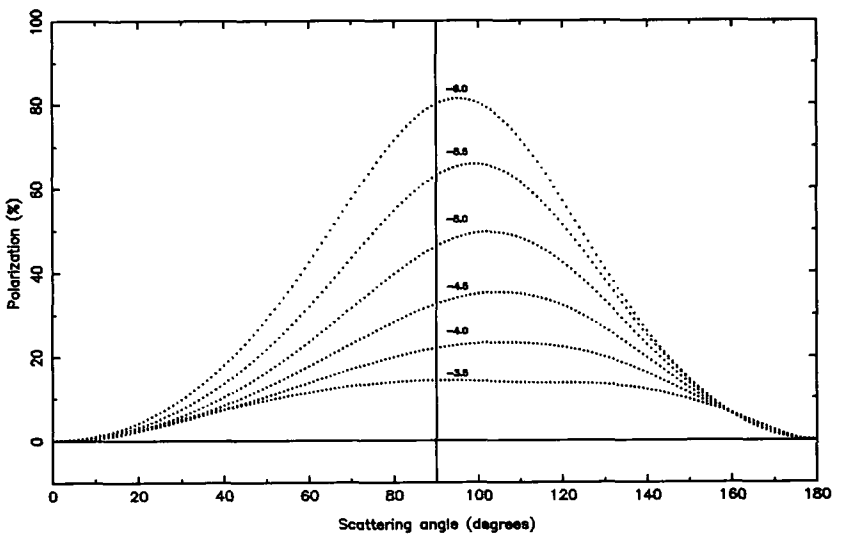

Figure 7.32: Mie scattering calculations for the polarization from silicon carbide grains with a 0.01 μm water ice mantle as a function of scattering angle (θ) and power law index (γ). Grain size distribution : $n(a) = n_o a^{-\gamma}$

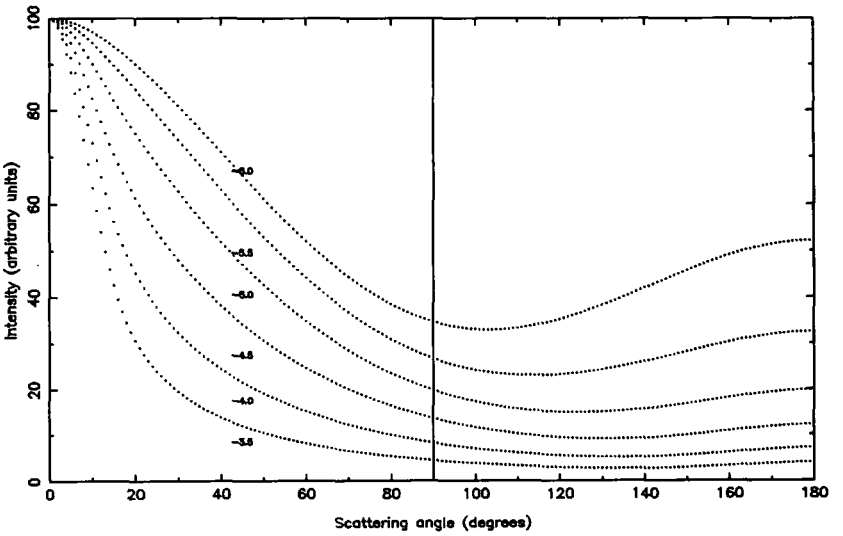

Figure 7.33: Mie scattering calculations for the scattered intensity from silicon carbide grains with a 0.01 μm water ice mantle as a function of scattering angle (θ) and power law index (γ). Grain size distribution : $n(a) = n_o\, a^{-\gamma}$

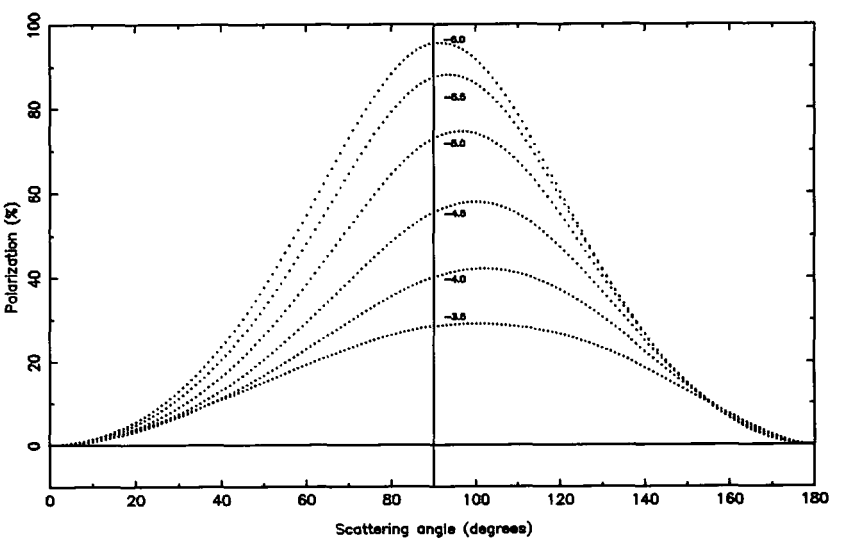

Figure 7.34: Mie scattering calculations for the polarization from silicon carbide grains with a 0.01 μm amorphous carbon mantle as a function of scattering angle (θ) and power law index (γ). Grain size distribution : $n(a) = n_o\, a^{-\gamma}$

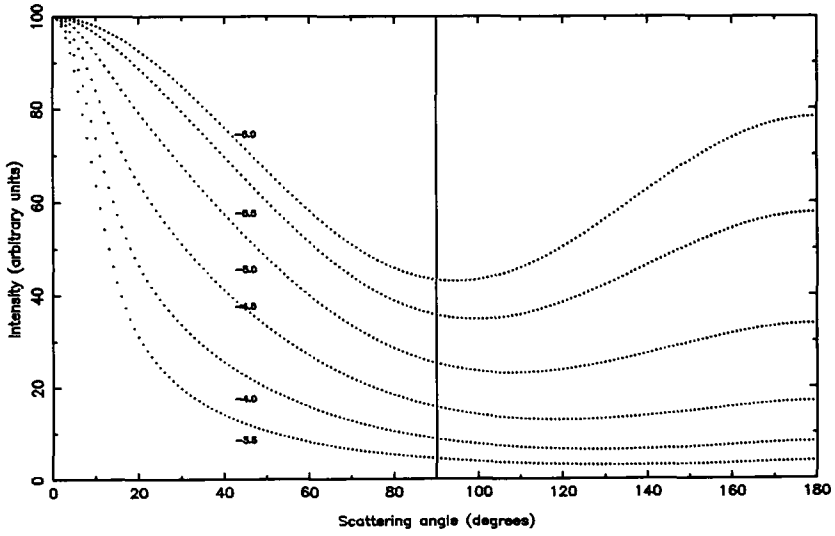

Figure 7.35: Mie scattering calculations for the scattered intensity from silicon carbide grains with a 0.01 μm amorphous carbon mantle as a function of scattering angle (θ) and power law index (γ). Grain size distribution : $n(a) = n_o a^{-\gamma}$

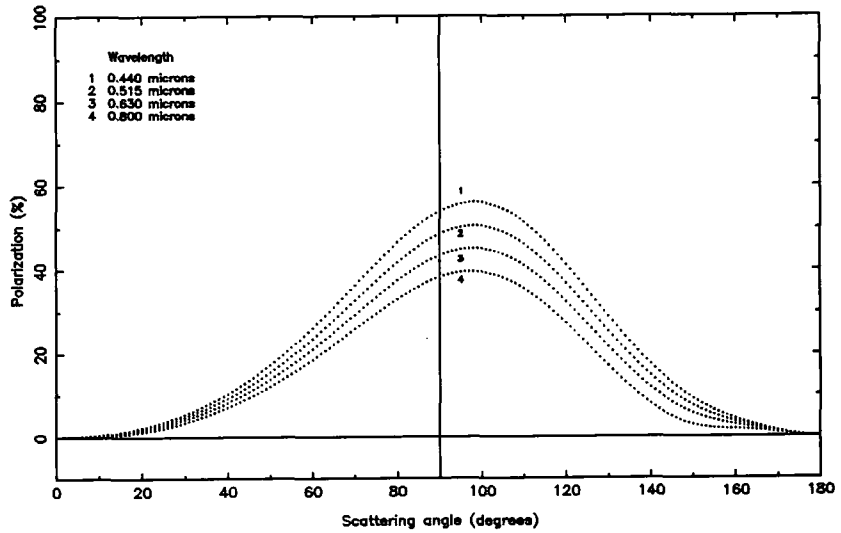

Figure 7.36: Mie scattering calculations for the polarization from oxygen-rich silicate grains with a thin water ice mantle as a function of scattering angle (θ) and wavelength (λ). Grain size distribution : $n(a) = n_o a^{-4.5}$

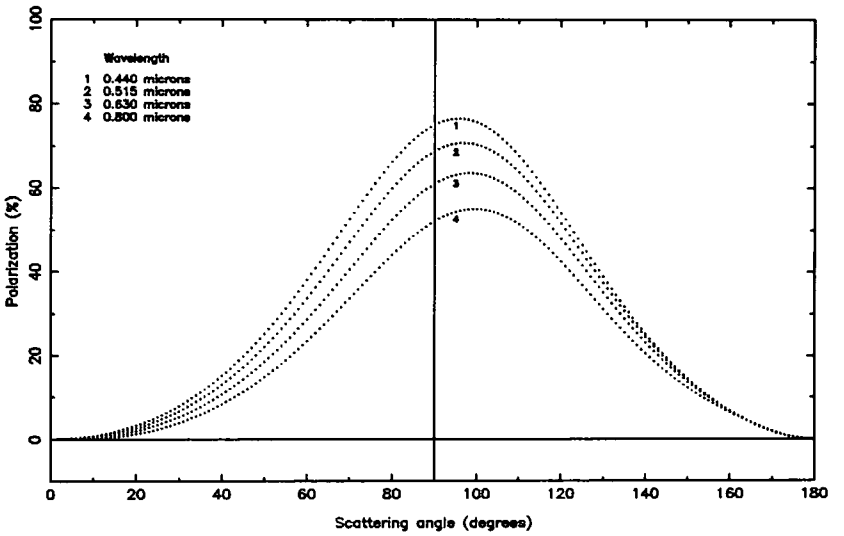

Figure 7.37: Mie scattering calculations for the polarization from oxygen-rich silicate grains with a thin amorphous carbon mantle as a function of scattering angle (θ) and wavelength (λ). Grain size distribution : $n(a) = n_o a^{-4.5}$

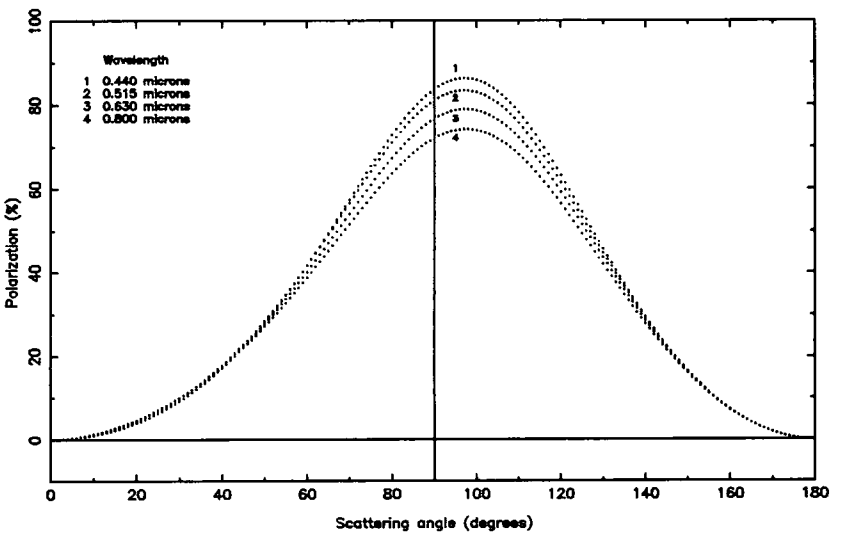

Figure 7.38: Mie scattering calculations for the polarization from amorphous carbon grains with a thin silicon carbide mantle as a function of scattering angle (θ) and wavelength (λ). Grain size distribution : $n(a) = n_o a^{-4.5}$

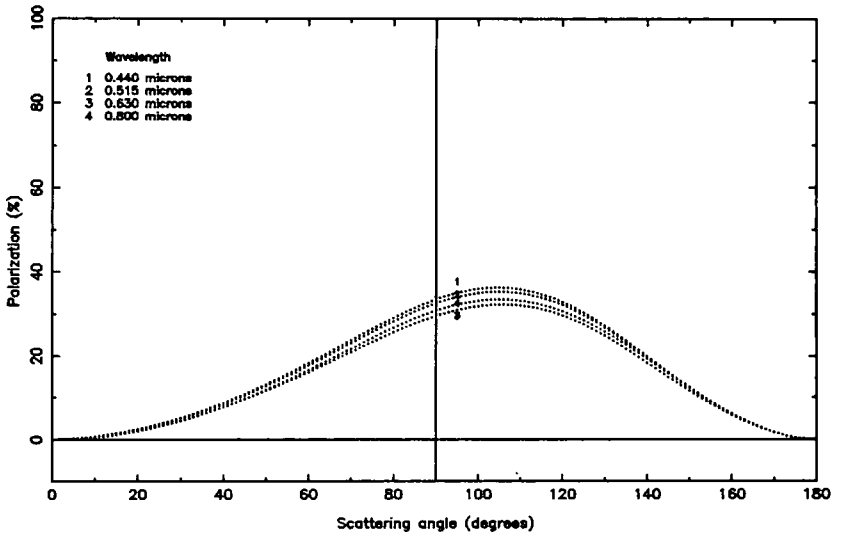

Figure 7.39: Mie scattering calculations for the polarization from silicon carbide grains with a 0.01 μm water ice mantle as a function of scattering angle (θ) and wavelength (λ). Grain size distribution : $n(a) = n_o\, a^{-4.5}$

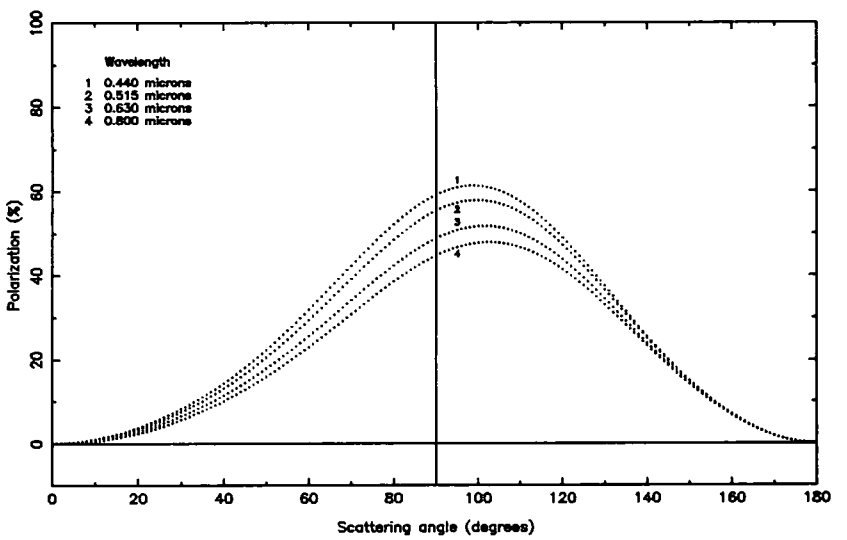

Figure 7.40: Mie scattering calculations for the polarization from silicon carbide grains with a thin amorphous carbon mantle as a function of scattering angle (θ) and wavelength (λ). Grain size distribution : $n(a) = n_o\, a^{-4.5}$

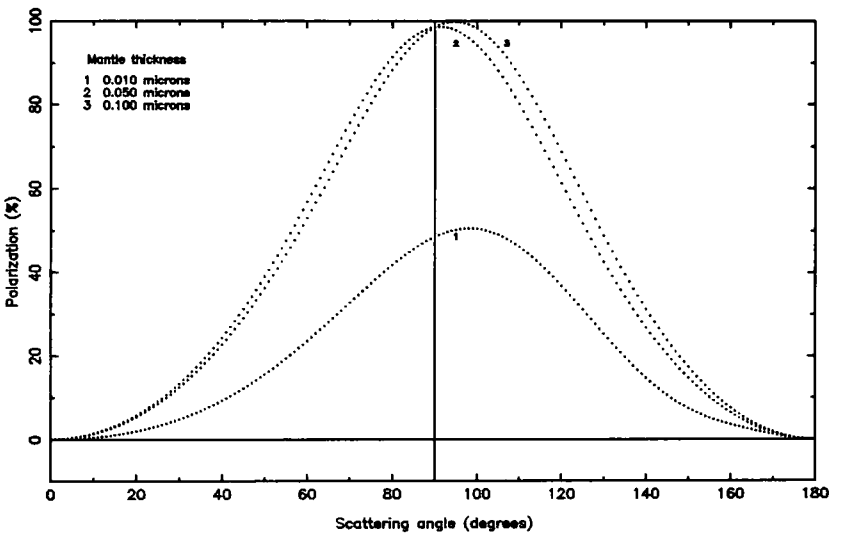

Figure 7.41: Mie scattering calculations for the polarization from oxygen-rich silicate grains with a water ice mantle as a function of scattering angle (θ) and mantle thickness. Grain size distribution : $n(a) = n_o a^{-4.5}$

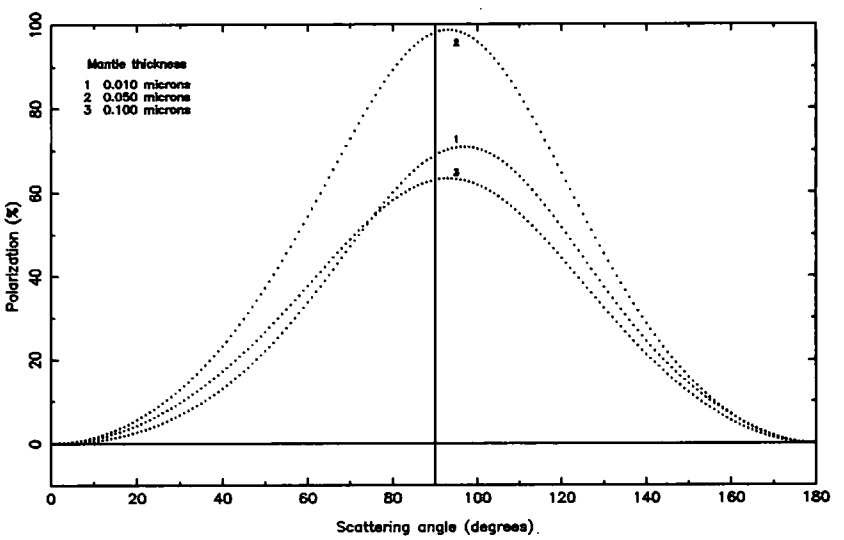

Figure 7.42: Mie scattering calculations for the polarization from oxygen-rich silicate grains with an amorphous carbon mantle as a function of scattering angle (θ) and mantle thickness. Grain size distribution : $n(a) = n_o a^{-4.5}$

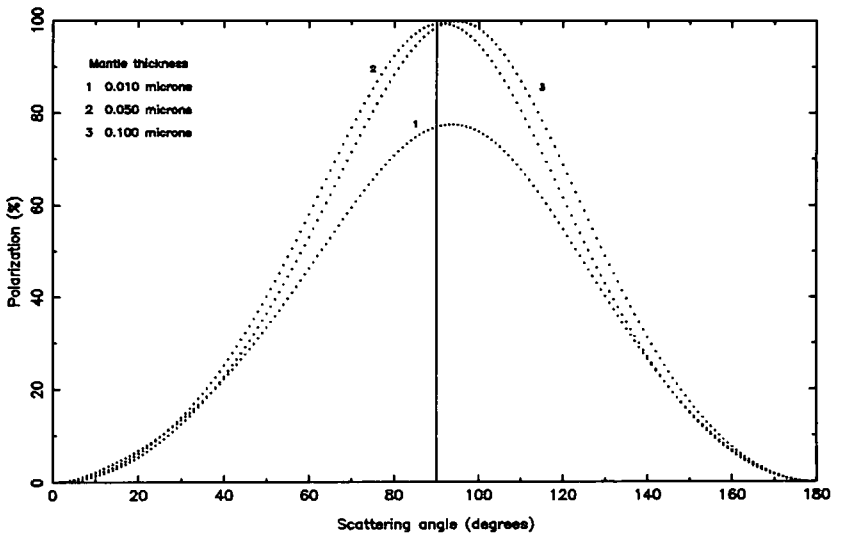

Figure 7.43: Mie scattering calculations for the polarization from amorphous carbon grains with a water ice mantle as a function of scattering angle (θ) and mantle thickness. Grain size distribution : $n(a) = n_o a^{-4.5}$

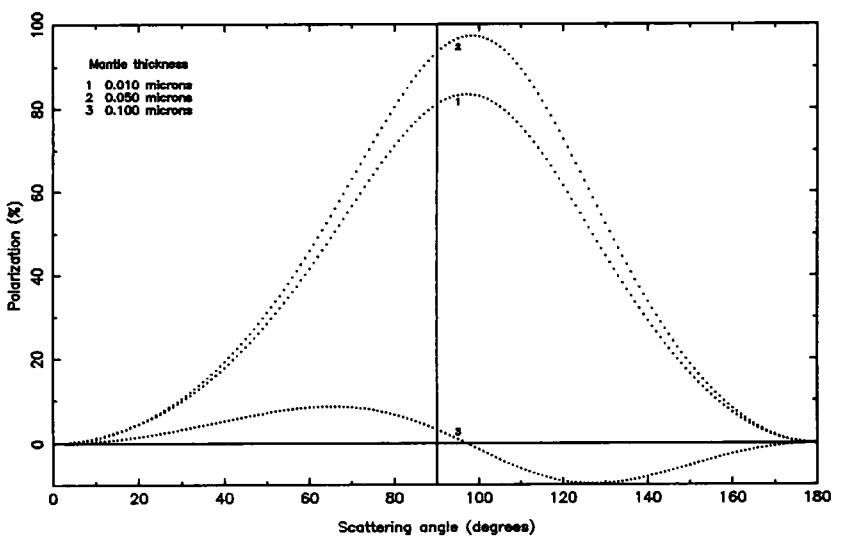

Figure 7.44: Mie scattering calculations for the polarization from amorphous carbon grains with a silicon carbide mantle as a function of scattering angle (θ) and mantle thickness. Grain size distribution : $n(a) = n_o a^{-4.5}$

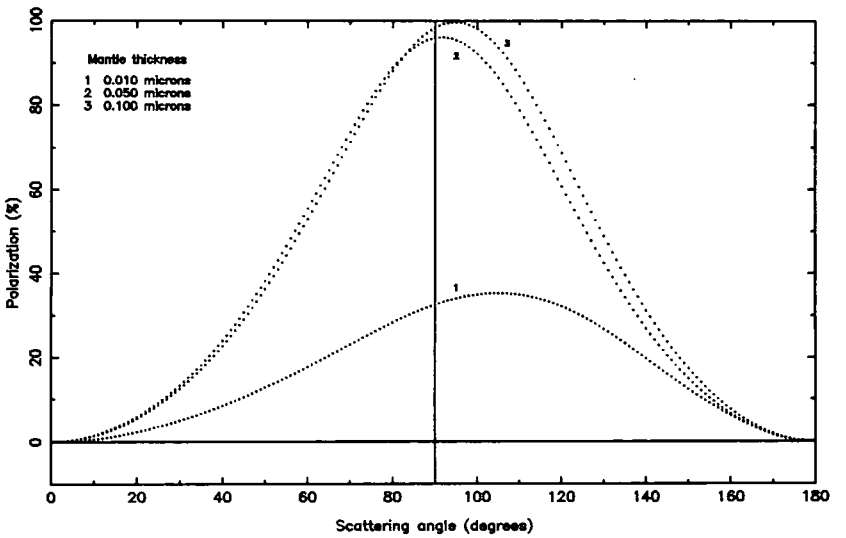

Figure 7.45: Mie scattering calculations for the polarization from silicon carbide grains with a water ice mantle as a function of scattering angle (θ) and mantle thickness. Grain size distribution : $n(a) = n_o\, a^{-4.5}$

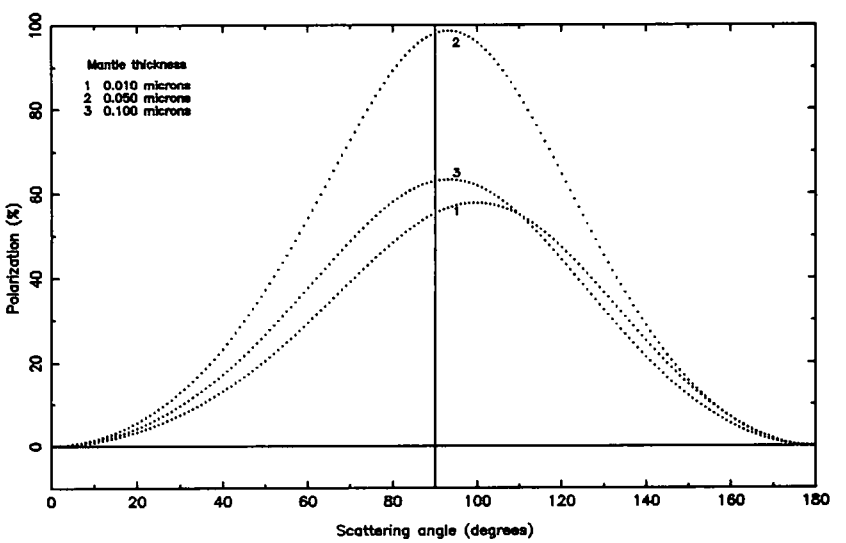

Figure 7.46: Mie scattering calculations for the polarization from silicon carbide grains with an amorphous carbon mantle as a function of scattering angle (θ) and mantle thickness. Grain size distribution : $n(a) = n_o\, a^{-4.5}$

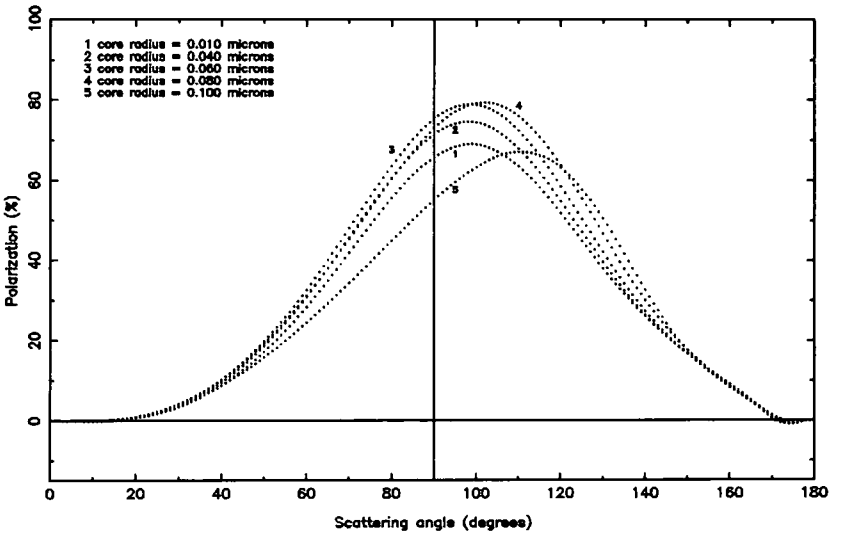

Figure 7.47: Mie scattering calculations for the polarization from oxygen-rich silicate grains with a water ice mantle as a function of scattering angle (θ) and core radius (a_{core}). Grain size distribution : $n(a) = n_o\, a^{-4.5}$ Power law with distribution of mantle thickness.

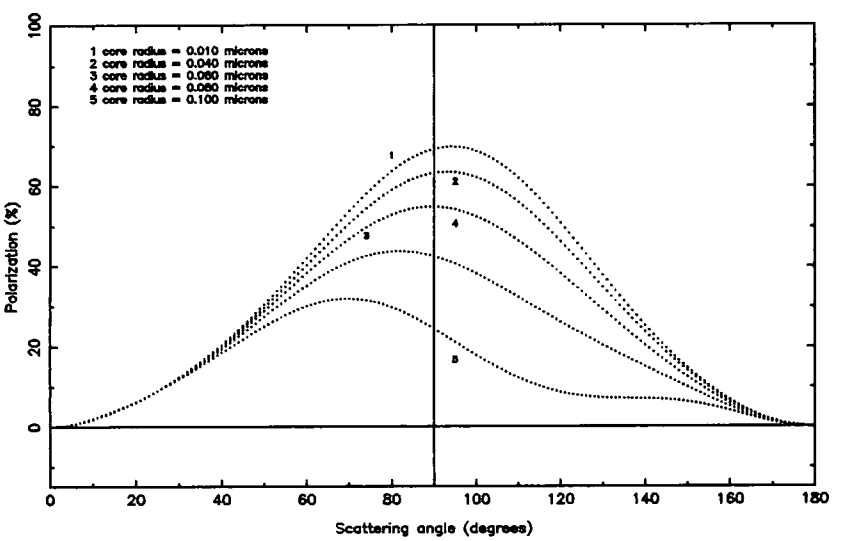

Figure 7.48: Mie scattering calculations for the polarization from oxygen-rich silicate grains with an amorphous carbon mantle as a function of scattering angle (θ) and core radius (a_{core}). Grain size distribution : $n(a) = n_o\, a^{-4.5}$ Power law with distribution of mantle thickness.

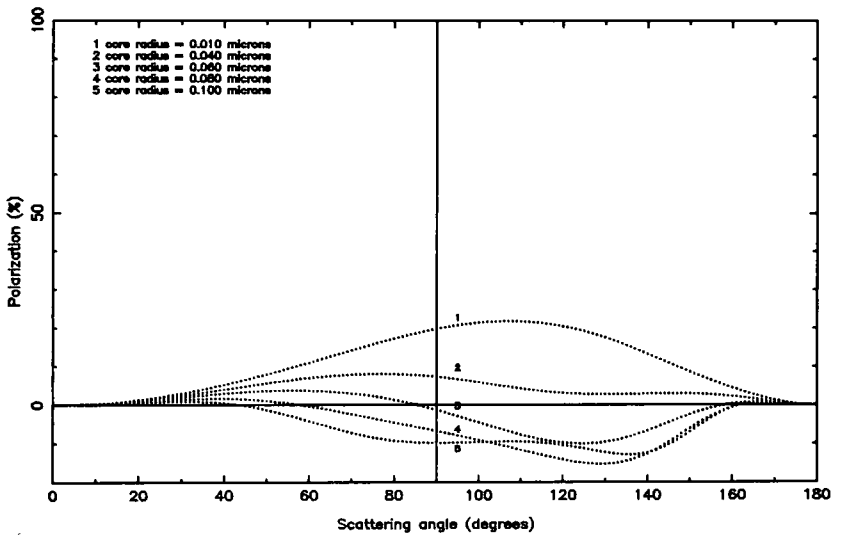

Figure 7.49: Mie scattering calculations for the polarization from amorphous carbon grains with a silicon carbide mantle as a function of scattering angle (θ) and core radius (a_{core}). Grain size distribution : $n(a) = n_o a^{-4.5}$ Power law with distribution of mantle thickness.

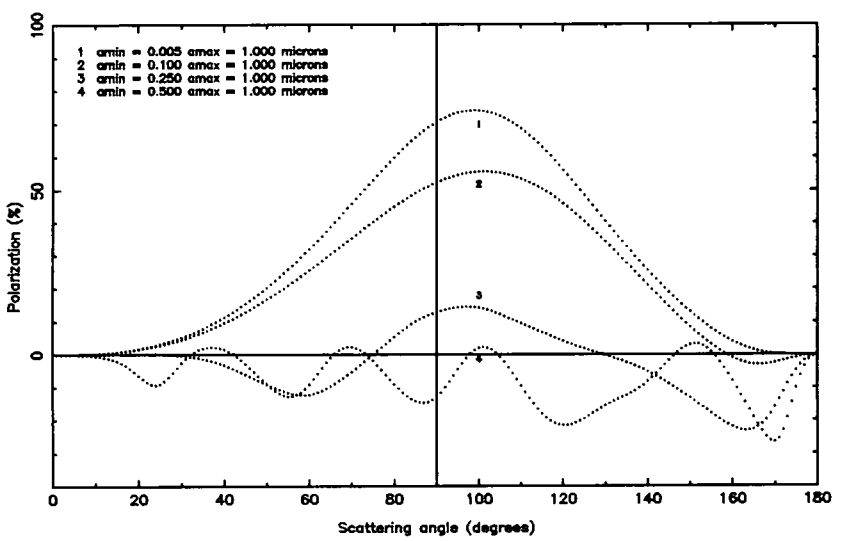

Figure 7.50: Mie scattering calculations for the polarization from silicon carbide grains with a water ice mantle as a function of scattering angle (θ) and core radius (a_{core}). Grain size distribution : $n(a) = n_o a^{-4.5}$ Power law with distribution of mantle thickness.

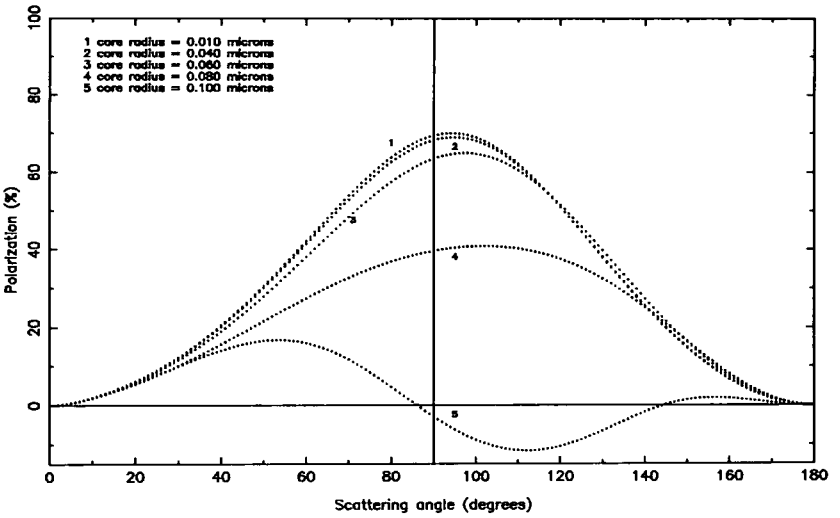

Figure 7.51: Mie scattering calculations for the polarization from silicon carbide grains with an amorphous carbon mantle as a function of scattering angle (θ) and core radius (a_{core}). Grain size distribution : $n(a) = n_o a^{-4.5}$ Power law with distribution of mantle thickness.

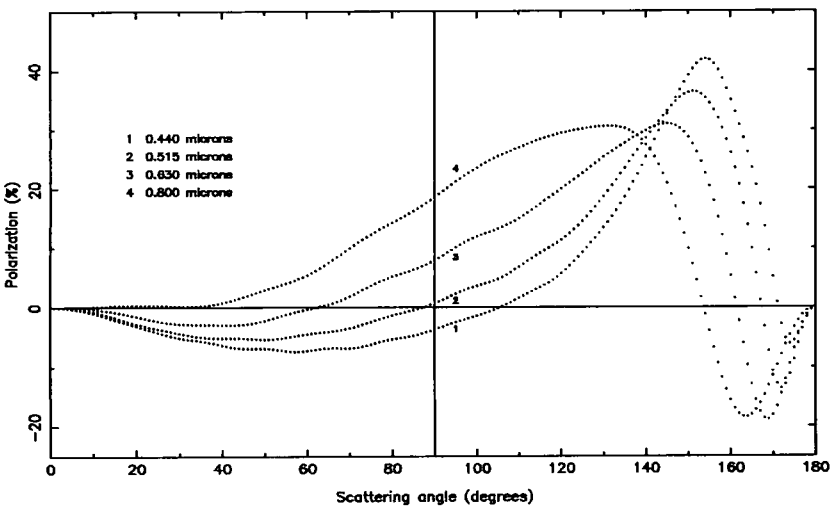

Figure 7.52: Mie scattering calculations for the polarization from oxygen-rich silicate grains with a water ice mantle as a function of scattering angle (θ) and wavelength (λ) for a given core radius (a_{core}). Grain size distribution : $n(a) \propto \exp\left[-5\left(\frac{a-a_c}{a_o}\right)^q\right]$ Exponential function with a distribution of mantle thickness.

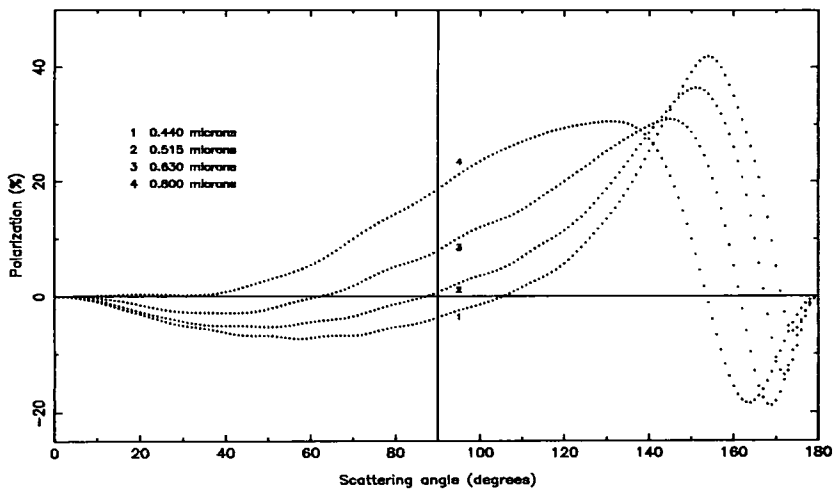

Figure 7.53: Mie scattering calculations for the polarization from silicon carbide grains with a water ice mantle as a function of scattering angle (θ) and wavelength (λ) for a given core radius (a_{core}). Grain size distribution : $n(a) \propto \exp\left[-5\left(\frac{a-a_c}{a_o}\right)^q\right]$ Exponential function with a distribution of mantle thickness.

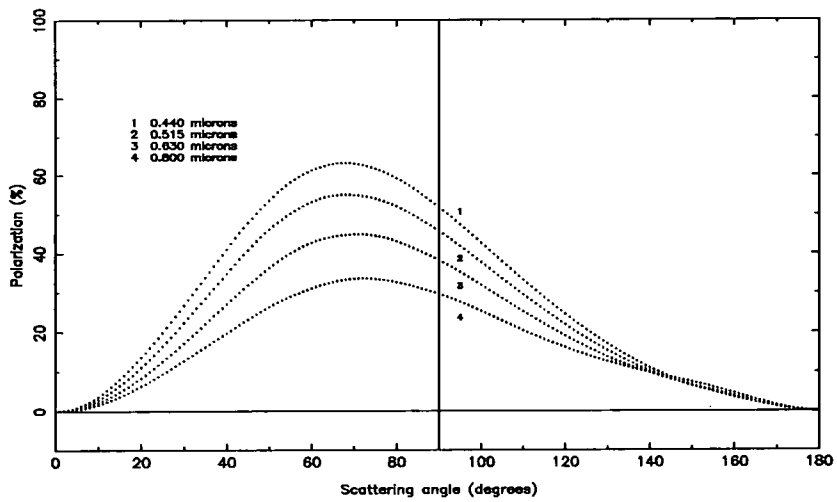

Figure 7.54: Mie scattering calculations for the polarization from silicon carbide grains with an amorphous carbon mantle as a function of scattering angle (θ) and wavelength (λ) for a given core radius (a_{core}). Grain size distribution : $n(a) \propto \exp\left[-5\left(\frac{a-a_c}{a_o}\right)^q\right]$ Exponential function with a distribution of mantle thickness.

Bibliography

Aaquist, O. B., Kwok, S., 1990, Astron. Astrophys., 84, 229

Aaquist, O. B., 1993, Astron. Astrophys., 267, 260

Abbott, D. C., 1982, Astrophys. J., 259, 282

Abell, G. O., Goldreich, P., 1966, Publ.Astron.Soc.Pac., 78, 232

Acker, A. *et al.*, 1978, Astron. Astrophys. Suppl., 33, 811

Acker, A., 1980, Astron. Astrophys., 89, 33

Acker, A., Gleizes, F., Chopinet, M., Marcout, J., Ochsenbein, F., Roques, J. M., 1982, Catalogue of the central stars of true and possible planetary nebulae

Acker, A., 1983, IAU Symp., 103 Planetary Nebulae, ed D R Flower (Dordrecht: Reidel) p 241

Acker, A., Marcout, J., Ochsenbein, F., Stenholm, B., Tylenda, R., Schohn, C., 1992, The Strasbourg-ESO Catalogue of Galactic Planetary Nebulae (Munich: ESO)

Ageorges, N., Fischer, O., Stecklum, B., Eckart, A., Henning, Th., 1996, Astrophys. J., 463, L101

Aitken, D. K., Roche, P. F., Spenser, P. M., Jones, B., 1979, Astrophys. J., 233, 925

Aitken, D. K., Roche, P. F., 1982, MNRAS, 200, 217

Allen, C. W., 1973, Astrophysical Quantities

Aller, L. H., Ross, J. E., O'Mara, B. J., Keyes, C. D., 1981, MNRAS, 197, 95

Aller, L. H., 1993, IAU Symp., 155 Planetary Nebulae, ed R Weinberger & A Acker (Dordrecht: Kluwer) p 1

Alton, P., 1996, PhD Thesis, University of Durham

Amnuel, P. R. *et al.*, 1984, Astrophys. Sp. Sci., 107, 19

Amnuel, P. R. *et al.*, 1989, Astrophys. Sp. Sci., 14, 21

Asano, S., Yamamoto, G., 1975, Appl. Opt., 14, 29

Ashley, M. C. B., Hyland, A. R., 1988, Astrophys. J., 331, 538

Aspin, C., McLean, I. S., 1984, Astron. Astrophys., 134, 333

Aspin, C., Schwarz, H. E., Smith, M. G., Corradi, R. L. M., Mountain, C. M., Wright, G. S., Ramsay, S. K., Robertson, D., Beard, S. M., Pickup, D. A., Geballe, T. R., Bridger, A., Laird, D., Montgomery, D., Glendinning, R., Pentland, G., Griffin, J. L., Aycock, J., 1993, Astron. Astrophys., 278, 255

Axon, D. J., Ellis, R. S., 1976, MNRAS, 177, 499

Bachiller, R., Gómez-González, J., Bujarrabal, V., Martin-Pintado, J., 1988, Astron. Astrophys., 196, L5

Baessgen, M., Grewing, M., 1989, Astron. Astrophys., 218, 273

Balick, B., 1987, Astron. J., 94, 671

Balick, B., Preston, H. L., 1987, Astron. J., 94, 958

Balick, B., Preston, H. L., Icke, V., 1987, Astron. J., 94, 1641

Balick, B., 1989, Astron. J., 97, 476

Barnbaum, C., Morris, M., Kahane, C., 1995, Astrophys. J., 450, 862

Bastien, P., Ménard, F., 1988, Astrophys. J., 326, 334

Bastien, P., Ménard, F., 1990, Astrophys. J., 364, 232

Baud, B., Habing, H. J., 1983, Astron. Astrophys., 127, 73

Berry, D. S., 1985, PhD Thesis, University of Durham

Beuzit, J.-L., Thebault, P., Perrin, G., Rouan, G., 1994, Astron. Astrophys., 291, L1

Bianchi, S., Ferrara, A., Giovanardi, C., 1996, Astrophys. J., 465, 127

Biermann, P., Harwit, M., 1979, Astrophys. J., 241, L33

Blöcker, T., 1995, Astron. Astrophys., 299, 755

Bond, H. E., Livio, M., 1990, Astrophys. J., 355, 568

Boothroyd, A. I., Sackmann, I. J., Ahern, S. C., 1993, Astrophys. J., 416, 762

Bohren, C. F., Huffman, D. R., 1983, Absorption and Scattering of Light by Small Particles, Wiley, New York

Bowen, G. H., Willson, L. A., 1991, Astrophys. J., 375, L53

Bujarrabal, V., Gómez-González, J., Bachiller, R., Martin-Pintado, J., 1988, Astron. Astrophys., 204, 242

Bujarrabal, V., Gómez-González, J., Planesas, P., 1989, Astron. Astrophys., 219, 256

Bujarrabal, V., Bachiller, R., 1991, Astron. Astrophys., 242, 247

Cahn, J. H., Kaler, J. B., Stanghellini, L., 1992, Astron. Astrophys. Suppl., 94, 399

Calvet, N., Cohen, M., 1978, MNRAS, 182, 687

Cantó, J., Rodriguez, L. F., 1980, Astrophys. J., 239, 982

Cantó, J., Tenario-Tagle, G., Rozycka, M., 1988, Astron. Astrophys., 192, 287

Chandrasekhar, S., Schönberg, ?. ?., 1942, Astrophys. J., 96, 161

Cherchneff, I., Barker, J. R., 1992, Astrophys. J., 416, 769

Capriotti, E. R., 1978, IAU Symp., 76 Planetary Nebulae, ed Y Terzian (Dordrecht: Reidel) p263

Cohen, M., Barlow, M. J., 1974, Astrophys. J., 193, 401

Cohen, M., FitzGerald, M. P., Kunkel, W., Lasker, B. M., Osmer, P. S., 1978, Astrophys. J., 221, 151

Cohen, M., Barlow, M. J., 1980, Astrophys. J., 238, 585

Cohen, M., Dopita, M. A., Schwartz, R. D., Tielens, A. G. G. M., 1985, Astrophys. J., 297, 702

Corradi, R. L. M., Schwarz, H. E., 1993, Astron. Astrophys., 268, 714

Corradi, R. L. M., Schwarz, H. E., 1993, Astron. Astrophys., 278, 247

Corradi, R. L. M., Schwarz, H. E., 1993, Astron. Astrophys., 273, 247

Corradi, R. L. M., 1995, MNRAS, 276, 521

Cudworth, K. M., 1974, Astron. J., 79, 1384

Cuesta, L., Phillips, J. P., Mampaso, A., 1995, Astron. Astrophys., 304, 475

Daniel, J. Y., 1980, Astron. Astrophys., 87, 204

Daub, C. T., 1982, Astrophys. J., 260, 612

Debye, P., 1909, Ann. Physik., 1909, 30, 59

Duley, W. W., Williams, D. A., 1981, MNRAS, 196, 269

de Rooij, W. A., van der Stap, C. C. A. H., 1984, Astron. Astrophys., 131, 237

Dominik, C., Sedlmayr, E., Gail, H.-P., 1993, Astron. Astrophys., 277, 578

Dominy, J. F., 1984, Astrophys. J. Suppl., 55, 27

Donn, B., Wickramasinghe, N. C., Hudson, J. P., Stecher, T. P., 1968, Astrophys. J., 153, 451

Dorfi, E. A., Hoefner, S., 1996, Astron. Astrophys., 313, 605

Dougados, C., Rouan, D., Lacombe, F., Forveille, T., Tiphene, D., 1990, Astron. Astrophys., 227, 437

Dougados, C., Rouan, D., Léna, P., 1992, Astron. Astrophys., 253, 464

Draine, B. T., Lee, H. M., 1984, Astrophys. J., 285, 89

Draine, B. T., 1985, Protostars and Planets II, ed D Black, M Mathews, (Tucson: University of Arizona Press) p621

Draine, B. T., 1988, Astrophys. J., 333, 848

Draper, P. W., 1988, PhD thesis, University of Durham

Duley, W. W., Williams, D. A., 1981, MNRAS, 196, 269

Duley, W. W., 1993, IAU Symp., 135 Interstellar Dust, ed L J Allamandola (Dordrecht: Kluwer) p141

Dutra, C. M., Maciel, W. J., 1990, Rev. Mexicana Astron. Astrof., 21, 264

Dwarkadas, V. V., Chevalier, R. A., Blondin, J. M., 1996, Astrophys. J., 457, 773

Egan, M. P., Leung, C. M., 1995, Astrophys. J., 444, 251

Faúndez-Abans, M., Maciel, W. J., 1987a, Astron. Astrophys., 183, 324

Felli, M., Perinotto, M., 1979, Astron. Astrophys., 76, 69

Fischer, O., Henning, Th., Yorke, H. W., 1994, Astron. Astrophys., 284, 187

Forrest, W. J., Houck, J. R., McCarthy, J. F., 1981, Astrophys. J., 248, 195

Forveille, T., Morris, M., Omont, A., Likkel, L., 1987, Astron. Astrophys., 176, L13

Frank, A., Mellema, G., 1994, Astrophys. J., 430, 800

Frank, A., Balick, B., Livio, M., 1996, Astrophys. J., 471, L53

Friend, D. B., Abbot, D. C., 1986, Astrophys. J., 311, 701

Garcia Lario, P., Manchado, A., Riera, A., Mampaso, A., Pottasch, S. R., 1991, Astron. Astrophys., 249, 223

Gathier, R., Pottasch, S. R., Goss, W. M., van Gorkum, J. H., 1983, Astron. Astrophys., 128, 325

Gathier, R., Pottasch, S. R., Goss, W. M., 1986, Astron. Astrophys., 157, 191

Gathier, R., Pottasch, S. R., Pel, J. W., 1986, Astron. Astrophys., 157, 171

Geballe, T., Kim, Y. H., Knacke, R. F., Noll, K. S., 1988, Astrophys. J., 326, L65

Gehrz, R. D., Woolf, N. J., 1971, Astrophys. J., 165, 285

Gehrz, R. D., 1989, IAU Symp., 135 Interstellar Dust, ed L J Allamandola & A G G M Tielens, (Dordrecht: Kluwer) p 445

Gillett, F. C., Low, F. J., Stein, W. A., 1967, Astrophys. J., 149, L97

Gilman, R. C., 1969, Astrophys. J., 155, L185

Gilman, R. C., 1972, Astrophys. J., 178, 423

Gledhill, T. M., 1987, PhD thesis, University of Durham

Goebel, J. H., Moseley, S. H., 1985, Astrophys. J., 290, L35

Goodrich, R. W., 1991, Astrophys. J., 366, 163

Gorny, S. K., Stasinska, G., Tylenda, R., 1997, Astron. Astrophys., 318, 256

Greenberg, J. M., Mendoza-Gómez, C. X., de Groot, M. S., Breukers, R., 1993, Dust and Chemistry in Astronomy, ed T J Millar & D A Williams (London: IOP) p 271

Greig, W. E., 1971, Astron. Astrophys., 10, 161

Greig, W. E., 1972, Astron. Astrophys., 18, 70

Groenewegen, M. A. T., de Jong, T., 1994, Astron. Astrophys., 283, 463

Gurzadyan, G. A., 1996, Astron. Astrophys., 311, 997

Heap, S. R., Augensen, H. J., 1987, Astrophys. J., 313, 268

Hartigan, P., Raymond, J., Hartmann, L., 1987, Astrophys. J., 316, 323

Howe, D. A., Millar, T. J., Williams, D. A., 1992, MNRAS, 255, 217

Hodapp, K., Sellgren, K., Nagata, T., 1988, Astrophys. J., 326, L61

Huggins, P. J., Healey, A. P., 1989, Astrophys. J., 346, 201

Iben, I. Jr., Renzini, A., 1984, Ann. Rev. Ast. Astr., 21, 271

Iben, I. Jr., Renzini, A., 1984, Phys. Rep., 105(6), 329

Iben, I. Jr., Rood, R. T., 1970, Astrophys. J., 159, 605

Iben, I. Jr., Tutukov, A. V., 1989, IAU Symp., 131 Planetary Nebulae, ed S Torres-Peimbert (Dordrecht: Kluwer) pp 505-22

Icke, V., 1988, Astron. Astrophys., 202, 177

Icke, V., Preston, H. L., Balick, B., 1989, Astron. J., 97, 462

Icke, V., Preston, H. L., 1989, Astron. Astrophys., 211, 409

Icke, V., 1991, Astron. Astrophys., 251, 369

Icke, V., Balick, B., Frank, A., 1992, Astron. Astrophys., 253, 224

Iyengar, K. V. K., 1986, Astron. Astrophys., 158, 89

Jewitt, D. C., Danielson, G. E., Kupferman, P. N., 1986, Astrophys. J., 302, 727

Jones, A. P., Duley, W. W., Williams, D. A., 1990, QJRAS, 31, 567

Johnson, J. J., Jones, T. J., 1991, Astron. J., 101, 1735

Judge, P. G., Stencel, R. E., 1991, Astrophys. J., 371, 357

Jura, M., 1986, Astrophys. J., 303, 327

Jura, M., 1994, Astrophys. J., 434, 713

Jura, M., 1996, Astrophys. J., 472, 806

Justtanont, K., Tielens, A. G. G. M., Skinner, C. J., Haas, M. R., 1997, Astrophys. J., 476, 319

Kahane, C., Maizels, C., Jura, M., 1988, Astrophys. J., 328, L25

Kahane, C., Audinos, P., Barnbaum, C., Morris, M., Astron. Astrophys., 314, 871

Kahn, F. D., 1983, IAU Symp., 103 Planetary Nebulae, ed D R Flower (Dordrecht: Reidel) p 305

Kahn, F. D., West, K. A., 1985, MNRAS, 212, 837

Kaler, J. B., 1970, Astrophys. J., 160, 887

Kaler, J. B., 1983b, Astrophys. J., 271, 188

Kaler, J. B., 1985, Ann. Rev. Ast. Astr., 23, 89

Kaler, J. B., Lutz, J. H., 1985, Publ.Astron.Soc.Pac., 97, 700

Kastner, J. H., Weintraub, D. A., 1990, Astron. J., 109, 1211

Kim, S.-H., Martin, P. G., Hendry, P. D., 1994, Astrophys. J., 422, 164

King, D. J., Perkins, H. G., Scarrott, S. M., Taylor, K. N. R., 1981, MNRAS, 196, 45

Kolesnik, I. G., Pilyugin, L. S., 1986, Soviet Astronomy, 30, 169

Krishna Swamy, K. S., O'Dell, C. R., 1968, Astrophys. J., 151, L61

Kwok, S., 1975, Astrophys. J., 198, 583

Kwok, S., Purton, C. R., FitzGerald, M. P., 1978, Astrophys. J., 219, L125

Kwok, S., 1980, Astrophys. J., 236, 592

Kwok, S., 1982, Astrophys. J., 258, 280

Kwok, S., Bignell, R. C., 1984, Astrophys. J., 276, 544

Kwok, S., 1985, Astron. J., 90, 49

Kwok, S., 1986, Astron. J., 290, 568

Kwok, S., Hrivnak, B. J., Milone, E. F., 1986, Astrophys. J., 303, 451

Kwok, S., 1993, Ann. Rev. Astron. Astrophys., 31, 63

Kwok, S., 1994, Publ.Astron.Soc.Pac., 106, 344

Lambert, D. L., Gustafsson, B., Eriksson, K., Hinkle, K. H., 1986, Astrophys. J. Suppl., 62, 373

Lambert, D. L., Hinkle, K. H., Smith, V., 1990, Astron. J., 99, 1612

Langill, P. P., Kwok, S., Hrivnak, B. J., 1994, Publ.Astron.Soc.Pac., 106, 736

Lefèvre, J., Daniel, J. Y., 1988, Polarized Radiation of Circumstellar Origin, eds G V Coyne *et al.* (Tuscon Univ. Arizona Press) p 523

Leger, A., Puget, J. L., 1984, Astron. Astrophys., 137, L5

Lequeux, J., Jourdain de Muizon, M., 1990, Astron. Astrophys., 240, L19

Leroy, J. L., Le Borgne, J. F., Arnaud, J., 1986, Astron. Astrophys., 160, 171

te Lintel Hekkert, P., Chapman, J. M., 1996, Astron. Astrophys. Suppl., 119, 459

Livio, M., Salzman, J., Shaviv, G., 1979, MNRAS, 188, 1

Livio, M., Soker, N., 1988, Astrophys. J., 329, 764

Lloyd-Evans, T., 1990, MNRAS, 243, 336

Lopez, J. A., Meaburn, J., 1983, MNRAS, 204, 203

Lopez, B., Mékarnia, D., Lefèvre, J., 1995, Astron. Astrophys., 296, 752

Lutz, J. H., 1973, Astrophys. J., 181, 135

Lutz, J. H., 1989, IAU Symp., 131 Planetary Nebulae, ed S Torres-Peimbert (Dordrecht: Kluwer) pp 65-72

Maciel, W. J., Pottasch, S. R., 1980, Astron. Astrophys., 88, 1

Maciel, W. J., 1984, Astron. Astrophys. Suppl., 55, 253

Maciel, W. J., 1989, IAU Symp., 131 Planetary Nebulae, ed S Torres-Peimbert (Dordrecht: Kluwer) pp 73-82

Marten, H., Schönberner, D., 1991, Astron. Astrophys., 248, 590

Martin, P. G., 1989, IAU Symp., 135 Interstellar Dust, ed L J Allamandola & A G G M Tielens, (Dordrecht: Kluwer) p 55

Masson, C. R., 1986, Astrophys. J., 302, L27

Mathis, J. S., Rumpl, W., Nordsieck, K. H., 1977, Astrophys. J., 217, 425

Mathis, J. S., 1989, IAU Symp., 135 Interstellar Dust, ed L J Allamandola & A G G M Tielens, (Dordrecht: Kluwer) p 360

Matsumura, M., Seki, M., 1991, Ap&SS, 176, 283

Mauron, N., Le Borgne, J.-F., 1986, Astron. Astrophys., 168, 217

Mauron, N., Le Borgne, J.-F., Picquette, M., 1989, Astron. Astrophys., 218, 213

Mathis, J. S., Rumpl, W., Nordsieck, K. H., 1977, Astrophys. J., 217, 425

Mckee, C. F., Hollenbach, D. J., Seab, C. G., Tielens, A. G. G. M., 1987, Astrophys. J., 318, 674

Meaburn, J., Walsh, J. R., 1985, MNRAS, 215, 761

Meixner, M., Skinner, C. J., Temi, P., Rank, D., Bregman, J., Ball, J. R., Keto, E., Arens, J. F., Jernigan, J. G., 1993, Astrophys. J., 411, 266

Meixner, M., Graham, J. R., Skinner, C. J., Hawkins, G. W., Keto, E., Arens, J. F., Jernigan, J. G., 1994, Experimental Astronomy, 3, 1-4, 53

Meixner, M., Skinner, C. J., Graham, J. R., Keto, E., Jernigan, J. G., Arens, J. F., 1997, Astrophys. J., 482, 897

Mellema, G., Eulderink, F., Icke, V., 1991, Astron. Astrophys., 252, 718

Mellema, G., 1994, Astron. Astrophys., 290, 915

Mellema, G., Frank, A., 1995, MNRAS, 273, 401

Mellema, G., 1995, MNRAS, 277, 173

Méndez, R. H., 1975, Astrophys. J., 199, 411

Méndez, R. H., Kudritzki, R. P., Herrero, A., Husfeld, D., Groth, H. G. G., 1988, Astron. Astrophys., 190, 113

Méndez, R. H., Kudritzki, R. P., Herrero, A., 1992, Astron. Astrophys., 260, 329

Merrill, K. M., Stein, W. A., 1976, Publ.Astron.Soc.Pac., 88, 874

Meyers, P. C. *et al.*, 1987, Astrophys. J., 319, 340

Mie, G., 1908, Ann. Physik., 25, 377

Minkowski, R., 1946, Publ.Astron.Soc.Pac., 58, 305

Miranda, L. F., 1995, Astron. Astrophys., 304, 531

Morris, M., Bowers, P. F., 1980, Astron. J., 85, 724

Morris, M., 1981, Astrophys. J, 249, 572

Morris, M., Bowers, P. F., Turner, B. E., 1982, Astrophys. J., 259, 702

Morris, M., 1987, Publ.Astron.Soc.Pac., 99, 1115

Morris, M., Reipurth, B., 1990, Publ.Astron.Soc.Pac., 102, 446

Morris, M., Guilloteau, S., Lucas, R., Omont, A., 1987, Astrophys. J., 321, 888

Moseley, H., 1980, Astrophys. J., 238, 892

O'Keefe, J. A., 1939, Astrophys. J., 90, 294

Olofsson, H., Carlstrom, U., Eriksson, K., Gustafsson, B., Willson, L. A., 1990, Astron. Astrophys., 230, L13

Omont, A., 1986, Astron. Astrophys., 164, 159

Omont, A., Moseley, S. H., Forveille, T., Glaccum, W. J., Harvey, P. M., Likkel, L., Loewenstein, R. F., Lisse, C. M., 1990, Astrophys. J., 355, L27

Ossenkopf, V., Henning, Th., Mathis, J. S., 1992, Astron. Astrophys., 261, 567

Osterbrock, D. E., 1989, Astrophysics of Gaseous Nebulae and Active Galactic Nuclei (California: University Science Books)

Paczynski, B., 1970, Acta Astron., 20, 47

Paczynski, B., 1971, Acta Astron., 21, 417

Papoular, R., Pégourié, B., 1983, Astron. Astrophys., 128, 335

Pascoli, G., Leclercq, J., Poulain, B., 1992, Publ.Astron.Soc.Pac., 104, 182

Pauldrach, A., Puls, J., Kudritzki, R. P., Mendéz, R. H., Heap, S. R., 1988, Astron. Astrophys., 207, 123

Pégourié, B., Papoular, R., 1985, Astron. Astrophys., 142, 451

Pégourié, B., 1988, Astron. Astrophys., 194, 335

Peimbert, M., 1978, IAU Symp., 76 Planetary Nebulae, ed Y Terzian (Dordrecht: Reidel) pp 215-23

Peimbert, M., Torres-Peimbert, S., 1983, IAU Symp., 103 Planetary Nebulae, ed D R Flower (Dordrecht: Reidel) pp 233-42

Peimbert, M., 1990, Observational Astrophysics, ed R E White (IOP Publishing Ltd) pp 1-64

Perinotto, M., 1989, IAU Symp., 131 Planetary Nebulae, ed S Torres-Peimbert (Dordrecht: Kluwer) p293

Pilyugin, L. S., 1987, Soviet Astronomy, 31, 282

Pottasch, S. R., 1984, Planetary Nebulae (Dordrecht: Reidel)

Pottasch, S. R., 1989, IAU Symposium, 131, 481

Preibisch, Th., Ossenkopf, V., Yorke, H. W., Henning, Th., 1993, Astron. Astrophys., 279, 577

Pringle, J. E., 1989, MNRAS, 238, 37P

Puget, J. L., Léger, A., 1989, Ann. Rev. Ast. Astr., 27, 261

Quinn, D. E., Moore, T. J. T., Smith, R. G., Smith, C. H., Fujiyoshi, T., 1996, MNRAS, 283, 1379

Renzini, A., 1981, Physical Processes in Red Giants, ed I Iben Jr. & A Renzini, (Dordrecht: Reidel), p 431

Renzini, A., 1983, IAU Symp., 103 Planetary Nebulae, ed D R Flower (Dordrecht: Reidel) p 267

Renzini, A., Fusi-Pecci, F., 1988, Ann. Rev. Astron. Astrophys., 26, 199

Roche, P. F., Aitken, D. K., 1986 MNRAS, 221, 63

Roddier, F., Roddier, C., Graves, J. E., Northcott, M. J., 1995, Astrophys. J., 443, 249

Rouan, D., Omont, A., Lacombe, F., Forveille, T., 1988, Astron. Astrophys., 189, L3

Rowlands, N., Houck, J. R., Herter, T., 1994, Astrophys. J., 427, 867

Sabbadin, F., 1986, Astron. Astrophys., 160, 31

Sahai, R., Wootten, A., Clegg, R. E. S., 1990, Astron. Astrophys., 234, L1

Sahai, R., Wootten, A., Schwarz, H. E., Clegg, R. E. S., 1991, Astron. Astrophys., 251, 560

Sahai, R., Wootten, A., Schwarz, H. E., Wild, W., 1994, Astrophys. J., 428, 237

Scarrott, S. M., Warren-Smith, R. F., Pallister, W. S., Axon, D. J., Bingham, R. G., 1983, MNRAS, 204, 1163

Scarrott, S. M., Rolph, C. D., Wolstencroft, R. D., 1990, MNRAS, 243, 462

Scarrott, S. M., Rolph, C. D., Wolstencroft, R. D., Walker, H. J., Sekiguchi, K., 1990, MNRAS, 245, 484

Scarrott, S. M., 1991, Vistas Astron., 34, 163

Scarrott, S. M., Draper, P. W., Gledhill, T. M., 1992, in Proc. RAL Workshop Astron. Astrophys., Dusty Discs, Rutherford Appleton Laboratory, Chilton, UK, ed P M Gondhalekar, p 8

Scarrott, R. M. J., Scarrott, S. M., Wolstencroft, R. D., 1993, MNRAS, 264, 740

Scarrott, S. M., Scarrott, R. M. J., 1994, MNRAS, 268, 615

Scarrott, S. M., Scarrott, R. M. J., 1995, MNRAS, 277, 277

Schönberner, D., 1990, From Miras to Planetary Nebula: Which Path for Stellar Evolution?, ed M O Menessier & A Omomt (Paris: Edition Frontires), p 355

Schwarz, H. E., 1988, IAU Coll., 103, 123

Schwarz, H. E., Aspin, C., Lutz, J. H., 1989, Astrophys. J., 344, L29

Schwarz, H. E., 1991, Astron. Astrophys., 243, 469

Schwarz, H. E., 1992, Astron. Astrophys., 264, L1-L4

Schwarz, H. E., Corradi, R. L. M., Melnick, J., 1992, Astron. Astrophys. Suppl., 96, 23

Schwarz, H. E., Corradi, R. L. M., 1992, Astron. Astrophys., 265, L37-L40

Schwarz, H. E., Corradi, R. L. M., Stanghellini, L., 1993, IAU Symp., 155 Planetary Nebulae, ed R Weinberger, A Acker p 214

Seab, C. G., Snow, T. P., 1989, Astrophys. J., 347, 479

Seaton, M. J., 1983, IAU Symp., 103 Planetary Nebulae, ed D R Flower (Dordrecht: Reidel) p 129

Shirt, J. V., 1984, PhD Thesis, University of Durham

Shaw, R. A., Kaler, J. B., 1989, Astrophys. J. Suppl. Ser., 69, 495

Shields, G. A., 1983, IAU Symp., 103 Planetary Nebulae, ed D R Flower (Dordrecht: Reidel) p 259

Shklovsky, I. S., 1956, Astron. Zh., 33, 315

Shu, F. H., Ruden, S. P., Lada, C. J., Lizano, S., 1991, Astrophys. J., 328, L19

Skinner, C. J., Whitmore, B., 1988, MNRAS, 237, 79

Slijkhuis, S., Hu, J. Y., de Jong, T., 1991, Astron. Astrophys., 248, 547

Soker, N., Livio, M., 1989, Astrophys. J., 339, 268

Soker, N., 1989, Astrophys. J., 340, 921

Solf, J., Ulrich, H., 1985, Astron. Astrophys., 148, 274

Stanghellini, L., Kaler, J. B., 1989, Astrophys. J., 343, 811

Stanghellini, L., Corradi, R. L. M., Schwarz, H. E., 1993, Astron. Astrophys., 279, 521

Stasińska, G., 1989, Astron. Astrophys., 213, 274

Straniero, O., Gallino, R., Busso, M., 1995, Astrophys. J., 440, L85

Telesco, C. M., Harper, D. A., 1977, Astrophys. J., 211, 475

Thronson, H. A., Latter, W. B., Black, J. H., Bally, J., Hacking, P., 1987, Astrophys. J., 322, 770

Thronson, H. A., Latter, W. B., Black, J. H., Bally, J., Hacking, P., 1988, Publ.Astron.Soc.Pac., 100, 1446

Tielens, A. G. G. M., 1993, Dust and Chemistry in Astronomy, ed T J Millar & D A Williams (London: IOP) pp 103-141

Treffers, R., Cohen, M., 1974, Astrophys. J., 188, 545

Tylenda, R., Stasinska, G., 1994, Astron. Astrophys., 288, 897

van de Hulst, H. C., 1957, Light Scattering by Small Particles, Wiley, New York

van de Steene, G. C., Zijlstra, A. A., 1995, Astron. Astrophys., ???, ???

van de Steene, G. C., Zijlstra, A. A., 1995, Astron. Astrophys. Suppl., 108, 485

Vassiliadis, E., Wood, P. R., 1993, Astrophys. J., 413, 641

Vassiliadis, E., Wood, P. R., 1994, Astrophys. J. Suppl. Ser., 92, 125

van der Veen, W. E. C. J., Habing, H. J., 1988, Astron. Astrophys., 194, 125

van der Veen, W. E. C. J., Habing, H. J., Geballe, T. R., 1989, Astron. Astrophys., 226, 108

Volk, K., Kwok, S., 1987, Astrophys. J., 315, 654

Voshchinnikov, N. V., Grinin, V. P., Karjukin, V. V., 1995, Astron. Astrophys., 294, 547

Walker, H. J., Cohen, M., 1988, Astron. J., 95, 1801

Walker, H. J., Cohen, M., Volk, K., Wainscoat, R. J., Schwartz, D. E., 1989, Astron. J., 98, 2163

Warren-Smith, R. F., 1979, PhD Thesis, University of Durham

Waters, L. B. F. M., 1986, Astron. Astrophys., 162, 121

Weaver, J., McCray, R., Castor, J., Shapiro, P., Moore, R., 1977, Astrophys. J., 218, 377

Weidemann, V., 1987, Astron. Astrophys., 188, 74

Weidemann, V., 1989, Astron. Astrophys., 213, 155

Weiss, A., 1989, Astron. Astrophys., 209, 135

Whitelock, P. A., 1985, Mon.Not.R.Astron.Soc., 213, 59

Whitney, B, A., Hartmann, L., 1992, Astrophys. J., 395, 529

Wickramasinghe, N. C., 1973, Light Scattering Functions for Small Particles with Applications in Astronomy, Hilger, London

Willems, F. J., de Jong, T., 1986, Astrophys. J., 309, L39

Witt, A. N., 1977, Astrophys. J. Suppl. Ser., 35, 1

Wood, P. R., Bessel, M. S., Fox, M. W., 1983, Astrophys. J., 272, 99

Woodward, C. E., Forrest, W. J., Pipher, J. L., Moneti, A., Shure, M. A., 1989, Astrophys. J., 337, 754

Woolf, N. J., Ney, E. P., 1969, Astrophys. J. Letters, 155, L181

Yusef-Zadah, F., Morris, M., White, R. L., 1984, Astrophys. J., 278, 186

Zhang, C. Y., Kwok, S., 1990, Astron. Astrophys., 237, 479

Zhang, C. Y., 1995, Astrophys. J. Suppl. Ser., 98, 659

Zijlstra, A. A., 1990, Astron. Astrophys., 234, 387

Zijlstra, A. A., Pottasch, S. R., 1991, Astron. Astrophys., 243, 478

Zuckerman, B., Aller, L. H., 1986, Astrophys. J., 301, 772

Zuckerman, B., Dyck, H. M., 1986, Astrophys. J., 311, 345

List of Abbreviations

AGB Asymptotic Giant Branch

CSE circumstellar envelope

CE common envelope

HR Hertzsprung-Russell

IRAS Infrared Astronomical Satellite

ISM interstellar medium

ISW interacting stellar winds

LMC Large Magellanic Cloud

NIR near infrared

PAHs Polycyclic Aromatic Hydrocarbons

PN planetary nebula

PNs planetary nebulae

PPN protoplanetary nebula

PPNs protoplanetary nebulae

RGE red giant envelopes

RGB Red Giant Branch

SMC Small Magellanic Cloud

TP the thermal pulse

TP-AGB thermally-pulsing AGB

Acknowledgements

It is with great pleasure that I would like to acknowledge the support, friendship, guidance and many skills of those with whom I have worked during these past few years as a postgraduate research student in the Physics Department of the University of Durham. My thanks first of all to the Particle Physics and Astronomy Research Council for the financial means to undertake the major part of this work. Prof. D. Bloor and Prof. B. K. Tanner are also acknowledged for all the facilities provided by the Physics Department.

My sincere thanks go to the inimitable Dr. Mike Scarrott, who allowed me the opportunity to pursue astronomical research and through whose masterful guidance and oversight, my understanding of the 'black art' of polarimetry has gradually developed. Bus driving was never as much fun as this.

A great measure of thanks and appreciation to my fellow polarimeterist, office companion and friend, Dr. David Stockdale, whose sound knowledge of the Durham Polarimeter and whose expert technical abilities enable all things polarimetric to run so smoothly. Thanks to him also for the companionship, fun, beer and curries shared in distant lands during many observing runs. Likewise to Dr. Peter Draper, whose excellent computing skills, software management and clear, understandable answers to my questions, helped to make some sort of sense out of all these numbers. Thanks also to Mr Alan Lotts. His skillful and proficient support and management of the Starlink computing facilities deserves great credit and appreciation.

I would also like to acknowledge others who have helped me, hindered me or bought me drinks - Paul Alton (now moth recording at the University of Cardiff), Jamie Holder, Steve Fullerton and Steve Lishman.

Finally, I acknowledge all the support and strength that my immediate family have given me throughout the whole period of my studies and research. Thank you Mum for all the love, understanding and financial aid that you and Dad provided over the years. It's taken a long time and there's been many trials and tribulations but you were always there for me. Thanks also to my daughter Jackie for all her encouragement. A special loving thank you to my wife Karen who has sacrificed so much in order that I might pursue my dreams. Your love, understanding, motivation and inspiration is behind all that I do.